Diss. ETH. No. 20093

Continuous non-invasive blood pressure estimation

A dissertation submitted to

ETH Zurich

for the Degree of

Doctor of Sciences

presented by

Josep Maria Solà i Carós

M. Sc. Telecommunications, Universitat Politècnica de Catalunya

born on the 6th of June, 1980

citizen of Catalonia, Spain

accepted on the recommendation of

Prof. Dr. Ralph Müller, examiner

Dr. Olivier Chételat, co-examiner

Prof. Dr. Hans-Andrea Loeliger, co-examiner

2011

Pell de gallina inaugural (1928)

The cardiovascular system seen by Salvador Dalí

Table of Contents

Acknowledgements

As a metaphor of life, advancing in the preparation of a PhD thesis requires the personal investment of large amounts of energy,… and the active support of a great group of people.

For this I deeply want to thank:

My advisor at CSEM, Dr. Olivier Chételat, for giving me the happiness of free research. Since the very first day of this PhD he has encouraged me to freely move within the biomedical research jungle, stimulating with the right advices at the right moment, supporting the fruitful ideas, and criticizing the wrong ones. His personal support to these research activities has been the key element of the survival of my thesis within CSEM.

My advisor at ETHZ, Prof. Dr. Ralph Müller, for opening me the door to the ETHZ. I extremely appreciate Prof. Müller for having accepted this free bird in his nest: making proof of a generous open-mindedness to new adventures. His rational and synthetic view of my research has wisely guided this PhD thesis through a scientific path, asking the precise questions when required, and pruning secondary branches when needed. Prof. Müller has helped me in translating a research and development work into a scientific dissertation.

My co-advisor at ETHZ, Prof. Dr. Andrea Loeliger, for his structured and synthetic understanding of real-life problems. A series of long discussions with Prof. Loeliger during the first months of research led to the generation of a simplified model of the cardiovascular system that supported the entire thesis work.

Jens Kraus, my primary boss at CSEM that actively constructed the conditions for a PhD thesis within an ETHZ-CSEM consortium. His full support to my research and life activities has been the main cause of my commitment to research, and CSEM.

My colleagues Dr. Philippe Renevey and Dr. Rolf Vetter for their valuable expertise in signal processing, and their ability to come up with the brilliant idea when everything is dark.

My colleagues Dr. Stephan Böhm and Prof. Dr. Andy Adler for sharing with me their deep knowledge in EIT and cardio-respiratory physiology. Only the moon knows how many nights we have spent discussing about new challenges… and creating solutions.

The team of doctors at the Inselspital and the CHUV: Dr. Stefano F. Rimoldi, Prof. Dr. Claudio Sartori and Prof. Dr. Yves Alemann, for their fruitful and active support to my research activities. Their theoretical and practical knowledge on cardiovascular pathophysiology have undeniably guided my research work.

The worldwide “team of EIT doctors”: Prof. Dr. Fernando Suárez Sipmann, Prof. Dr. Daniel Reuter, Gerardo Tusman, Arnoldo Santos and Dr. Stefan Maisch for accepting a Swiss engineer into their animal operating rooms, and for the dozens of hours of passionate discussions.

The CSEM team, including all the people at the signal and processing group, the electronics team, our secretaries and all the staff. Without their support in terms of electronics, firmware, and software developments, discussions, general support, and “good-morning smiles” this thesis would have never been possible. Working in such a multidisciplinary environment with great doses of humor has been a real stimulating pleasure.

My family, for seeding me with the need of knowledge, and teaching me the strength to persevere in the adversity… and Myriam for travelling in life with me.

Josep,

Neuchâtel, the 21st of July 2011

Summary

Elevated Blood Pressure (BP) is a human-specific illness affecting a quarter of the worldwide population. Clinically known as hypertension, elevated BP is considered the major risk factor for cardiovascular disease: the most common cause of death in developed countries. Detecting, treating and controlling hypertension are major goals of modern medicine.

For more than one century, the non-invasive measurement of BP has relied on the inflation of pneumatic cuffs around a limb, typically the upper arm. In addition to being occlusive, and thus cumbersome, clinical cuff-based methods provide intermittent BP readings, *i.e.* every twenty minutes, hence impeding the suitable monitoring of short-term BP regulation mechanisms. In addition, cuff-based methods may not yield representative BP during sleep as repeated inflations induce arousal reactions, leading to non-representative overestimated BP values. Therefore, the development of novel technologies that reduce the recurrent use of pneumatic cuffs is clearly justified.

The goal of this thesis is to investigate novel non-invasive technologies for the continuous measurement of BP. Particular emphasis is given to non-occlusive technologies that can be used in ambulatory scenarios, during daily life activities and not only within hospitals or physicians' offices. This thesis addresses thus the challenge of ambulatory BP monitoring from four different perspectives: cardiovascular physiology, clinical applicability, system integration, and signal/information processing.

The thesis starts by reviewing basic concepts of cardiovascular physiology related to the control of BP in humans: this analysis aims at setting the background knowledge for the understanding of the challenges faced by the BP monitoring field. Currently existing approaches for the non-invasive monitoring of BP are then reviewed systematically: their principles of work and their respective advantages/limitations are identified from both, clinical and ambulatory perspectives. The studied approaches are the auscultatory, oscillometric, tonometric, volume-clamp and pulse wave velocity techniques. The introductory part of this thesis is completed with a comprehensive review of the metrological means for the non-invasive and non-occlusive monitoring of cardiovascular parameters that have been used for this research, namely: electro-cardiography (ECG), photo-plethysmography (PPG), phono-cardiography (PCG), impedance-cardiography (ICG) and electrical impedance tomography (EIT).

The thorough appraisal of the state of the art identifies the Pulse Wave Velocity (PWV) technique as the most promising track to follow, since it provides the best trade-off between clinical and ambulatory compliances. PWV-based techniques rely on the fact that the velocity at which arterial pressure pulses propagate along the arterial tree depends on the underlying BP. Therefore, by continuously measuring PWV along the arterial tree one obtains beat-by-beat surrogate values of mean BP. However, this principle can only be exploited reliably if PWV is measured along central elastic arteries, where no vasomotion phenomenon exists. State-of-the-art metrological techniques to measure PWV are either unable to assess central PWVs, or not adapted for ambulatory monitoring. Therefore, to date the potential of PWV has not been fully exploited.

The major contribution of this thesis is thus the development and testing of new PWV-based techniques for the continuous, non-invasive and non-occlusive measurement of BP. In particular this thesis explores two new strategies to assess the Pulse Transit Time (PTT) of pressure pulses along central segments of the arterial tree. These techniques are based on 1) the use of the EIT technology, and 2) a chest sensor implementing mature sensing technologies such as ECG, PPG, ICG and PCG.

Electrical Impedance Tomography (EIT) is a non-invasive monitoring technology based on the analysis of bioimpedance signals. This thesis provides first proof that EIT applied at the chest skin is capable of providing information on the pulsatility of the aortic arterial wall, as if a virtual catheter was placed into the descending aorta. After constructing a novel algorithm for the identification of EIT pixels providing functional information on pulsatility of the descending aorta, and describing a method to estimate aortic Pulse Transit Times (PTT), experimental data on animal models is provided. Accordingly, EIT-derived PTT estimates show to highly correlate with invasive BP measurements ($r=-0.967$, $p<0.00001$) for a wide range of mean BP values (from 60 to 150 mmHg).

A chest sensor for the measurement of central PWV values integrating multiple non-occlusive technologies is introduced by this thesis as well. The novel sensing approach relies on the detection of the opening of the aortic valve (genesis of pressure pulses) by the joint analysis of ECG, ICG and PCG time series, and the detection of the arrival time of the pulses at the subcutaneous vessels of the chest by the joint analysis of ECG and multi-channel PPG time series. This thesis describes the integration of the depicted sensing technologies in a single chest sensor, introduces new dedicated multi-parametric signal processing routines, and provides experimental data on humans. Accordingly, chest sensor-derived PWV estimates show to positively correlate with reference carotid-to-femoral PWV measurements ($r=0.88$, $p<10^{-9}$) for a population of 31 normo- and hypertensive male subjects.

The second contribution of this thesis is the introduction of a novel signal processing tool enabling the reliable determination of the arrival time of arterial pressure pulses even under noisy measurement conditions. Called parametric estimation of Pulse Arrival Times (PAT), this technique is a key element for the deployment of novel technologies aiming at measuring PWV at central arterial locations by means of non-invasive measuring means. This thesis introduces thus the new concept of PAT estimation via the fitting of parametric models to non-invasive arterial time series, and tests its agreement with state-of-the-art approaches. Accordingly, when evaluated on 200 hours of intensive care unit PPG signals, PAT values determined by the novel technique show to particularly correlate with PAT values determined by the state-of-the-art first derivative technique ($r=0.99$, $p<0.001$), while increasing its robustness to real motion noise and simulated multiplicative colored Gaussian noise.

In conclusion, this thesis introduces a collection of novel technological and algorithmic strategies paving the way towards the deployment of devices for the ambulatory, continuous, non-invasive and non-occlusive measurement of BP.

Zusammenfassung

Erhöhter Blutdruck (BD) ist eine menschlich-spezifische Krankheit von welcher ein Viertel der Weltbevölkerung betroffen ist. Die klinisch als Hypertonie bekannte Krankheit gilt als Hauptrisikofaktor für die Herz-Kreislauf-Erkrankung und ist somit die häufigste Todesursache in den entwickelten Ländern. Das Erkennen, Behandeln und die Kontrolle des Bluthochdrucks sind wichtige Ziele der modernen Medizin.

Die Standard-Methode zur nicht-invasiven Messung des BD ist seit mehr als einem Jahrhundert die Inflation von pneumatischen Manschetten um eine Gliedmasse, in der Regel um den Oberarm. Nicht nur sind manschetten-basierte Methoden okklusiv und damit umständlich, sie liefern auch nur lückenhafte Blutdruckmessungen in Intervallen von 20 Minuten. Sie stellen damit nur ein ungeeignetes Mittel zur dauerhaften Überwachung der Regulierungsmechanismen des BDs dar. Darüber hinaus können manschetten-basierte Methoden keine repräsentativen BD-Werte während des Schlafs ermitteln, da wiederholte Inflationen Weck-Reaktionen auslösen, was zu überhöhten BD-Werten führt. Aus diesen Gründen ist die Entwicklung neuartiger Technologien zur kontinuierlichen BD-Überwachung ohne dauerhaft notwendige pneumatische Manschetten eindeutig gerechtfertigt.

Das Ziel dieser Arbeit ist es, neue nicht-invasive Technologien für die kontinuierliche Messung des BDs zu finden und zu untersuchen. Ein besonderer Schwerpunkt liegt auf nicht-okklusiven Technologien, welche sich neben dem Einsatz in Krankenhäusern oder Arztpraxen auch für den Gebrauch in ambulanten Umgebungen sowie während Aktivitäten des täglichen Lebens eignen. Diese Arbeit beleuchtet damit die Herausforderung der ambulanten BD-Überwachung aus vier verschiedenen Perspektiven: Herz-Kreislauf-Physiologie, klinische Anwendbarkeit, Systemintegration sowie die Signal- und Informationsverarbeitung.

Die These beginnt mit einer Einführung in die grundlegenden Konzepte der menschlichen Herz-Kreislauf-Physiologie mit speziellem Schwerpunkt auf der Regelung des BDs: Diese Darstellung zielt darauf ab, das Hintergrundwissen für das Verständnis der Herausforderungen auf dem Gebiet der BD-Überwachung näher zu erläutern. Daraufhin werden derzeit bekannte Ansätze für die nicht-invasive BD-Überwachung systematisch überprüft: ihre grundlegenden Arbeitsweisen und ihre jeweiligen Vor- und Nachteile werden sowohl aus klinischen als auch ambulanten Perspektiven beschrieben. Im Speziellen werden der auskultatorische, der oszillatorische und der tonometrische Ansatz sowie die Volumen-Klemme und Methoden basiert auf der Pulswellengeschwindigkeit analysiert. Die Einleitung schliesst mit einer umfassenden Darstellung der verwendeten messtechnischen Methoden für die nicht-invasive und nicht-okklusive Überwachung von Herz-Kreislauf-Parametern, welche in dieser Arbeit verwendet wurden. Namentlich sind dies Elektro-Kardiographie (ECG), Photo-Plethysmographie PPG), Phono-Kardiographie (PCG), Impedanz-Kardiographie (ICG) und Elektrische Impedanz-Tomographie (EIT).

Nach der grundlegenden Beurteilung des aktuellen Stands der Technik kristallisiert sich die Pule Wave Velocity-Technik (PWV) als der vielversprechendste Weg heraus, da sie den besten Kompromiss zwischen den klinischen und ambulanten Anforderungen bietet. PWV-basierte Techniken beruhen auf der Tatsache, dass die Geschwindigkeit arterieller Druckwellen entlang der Blutgefässe direkt mit dem zugrundeliegenden BD zusammenhängt. Daher ist es möglich durch kontinuierliche Messung der PWV entlang der Blutgefässe einen pulsschlag-genauen Surrogat-Wert des mittleren BDs zu erhalten. Einschränkend ist zu erwähnen dass dieses Prinzip nur zuverlässig genutzt werden, wenn die PWV entlang der zentralen elastischen Arterien gemessen wird, in denen keine Vasomotion-Effekte auftreten. Die zu diesem Zeitpunkt bekannten PWV-Messtechniken sind entweder nicht in der Lage diese zentralen PWVs zu messen, oder aber wurden sie nicht für die ambulante Überwachung angepasst. Aus diesem Grund ist das Potenzial der PWV zurzeit nicht voll ausgeschöpft.

Der wichtigste Beitrag dieser Arbeit ist daher die Entwicklung und Erprobung neuer PWV-basierter Techniken für die kontinuierliche, nicht-invasive und nicht-okklusive BD-Messung. Insbesondere, diese These befasst sich mit zwei Strategien, um die Pulse Transit Time (PTT) von Druckimpulsen entlang der zentralen Segmente der arteriellen Blutgefässe zu ermitteln. Diese Techniken basieren auf 1) der Verwendung der EIT-Technologie, und 2) einem Brust-Sensor, welcher erprobte Sensortechnologien wie ECG, PPG, ICG und PCG zur Anwendung bringt.

Elektrische Impedanz-Tomographie (EIT) ist eine nicht-invasive Überwachungstechnologie welche auf der Analyse von Bioimpedanz-Signalen basiert. Diese Arbeit erbringt den ersten Beweis, dass EIT, angewendet auf der Brust, in der Lage ist, Informationen über den Puls in der absteigenden Aorta zu ermitteln. Das Ergebnis ist das Gleiche als ob ein virtueller Katheter in die Aorta platziert worden wäre. Ein neuartiger Algorithmus zur Identifizierung von EIT-Pixeln wurde entwickelt um funktionale Informationen über den Puls in der absteigenden Aorta zu gewinnen. Desweitern wird eine Methode präsentiert, um die Pulslaufzeiten in der Aorta zu schätzen. Diese Methoden wurden dann mit experimentellen Daten an Tiermodellen evaluiert. Es zeigte sich, dass EIT-basierte PTT-Schätzungen signifikant mit invasiven Blutdruckmessungen ($r = -0.967$, $p < 0{,}00001$) korrelieren, dies für eine breite Palette von mittleren BD-Werten (60 bis 150 mmHg).

Des Weiteren wird in dieser Arbeit ein Brust-Sensor für die Messung der zentralen PWV-Werte mittels verschiedener nicht-okklusiver Technologien vorgestellt. Der neuartige Sensor-Ansatz fundiert auf zwei Methoden. Erstens, die Öffnung der Aortenklappe (Ursprung der Druckimpulse) wird durch die gemeinsame Analyse von EKG-, ICG- und PCG-Zeitreihen ermittelt. Zweitens, die Ankunftszeit der Impulse an den subkutanen Gefäßen der Brust wird durch die gemeinsame Analyse der EKG- und Multi-Channel-PPG-Zeitreihen erfasst. Diese Arbeit beschreibt die Integration dieser Sensor-Technologien in einem einzigen Brust-Sensor, stellt neue dedizierte multi-parametrische Signalverarbeitungsroutinen vor und präsentiert experimentelle Daten, aufgenommen an menschlichen Probanden. Es zeigte sich, dass Brust-Sensor-basierte PWV-Schätzungen positiv mit Referenz-PWV-Messungen (Karotis-Femora) korrelieren ($r = 0{,}88$, $p < 10\text{-}9$). Die Ergebnisse stammen von Experimenten mit 31 normal- und hypertensiven männlichen Personen.

Der zweite Beitrag dieser Arbeit ist die Einführung eines neuen Signalverarbeitungs-Instruments, genannt parametrische Schätzung der Puls-Ankunftszeiten (PAT). Ziel dieses Instruments ist die zuverlässige Bestimmung der Ankunftszeit des arteriellen Druckpulses, auch unter rauschhaften Messbedingungen. Diese Technik ist ein wesentliches Element der neuartigen Technologien zur Messung der PWV an zentralen arteriellen Orten mit Hilfe von nicht-invasiven Messungen. Diese These stellt somit das neue Konzept der PAT-Schätzung mittels der Optimierung von parametrischen Modellen basiert auf nicht-invasiven arteriellen Zeitreihen vor. Weiterhin wird die Übereinstimmung des neuen Instruments mit aktuellen Ansätzen verifiziert. Dazu wurden PPG-Signale ausgewertet, welche zuvor während 200 Stunden auf einer Intensivstation aufgenommen wurden. Die PAT-Werte, welche mittels der neuen Technik ermittelt wurden, korrelieren mit den PAT-Werten welche durch eine aktuelle Referenz-Methode basiert auf der ersten Ableitung ($r = 0{,}99$, $p < 0{,}001$) bestimmt wurden. Gleichzeitig erhöhte sich die Robustheit gegenüber Bewegungs-Rauschen und gegenüber simuliertem, multiplikativem, farbigem Rauschen.

Im Ergebnis stellt diese These eine Sammlung von neuen technologischen und algorithmischen Strategien vor und bereitet den Weg für den Einsatz von Geräten für die ambulante, kontinuierliche, nicht-invasive und nicht-okklusiven Messung von BD.

Chapter 1

Introduction

1. Introduction

1.1. Motivation

"*Four days ago my doctor gave me this inflating device, and since then I didn't sleep a single full night… and neither did my wife!*"

For the last decades the ambulatory measurement of Blood Pressure (BP) has been prescribed to patients suspected to suffer from nocturnal hypertension, or any other type of 24h-hypertensive pattern. The procedure is simple: a patient leaves the doctor's office with a cuff around the upper arm. During the following days, an automatic device records BP values every 20 minutes by inflating the pneumatic cuff, fully occluding the arm's blood circulation. Finally, the patient returns to the doctor's office where his hypertensive profile is evaluated, and an appropriate treatment is proposed.

When discussing with patients participating to such ambulatory programs, one realizes that automatic BP monitors are perceived as cumbersome, noisy and even painful. And this is particularly true during night, where periodic inflations of brachial cuffs create sleep arousals: affecting sleep quality and interestingly, altering BP itself.

When discussing with physicians and cardiovascular physiologists, the unanimous criticism to current brachial cuff devices resides on the fact they are only capable of providing intermittent BP readings, preventing medical staff from assessing fast BP changes occurring in any living cardiovascular system.

There is currently in the market no available ambulatory technology to measure BP in a continuous, non-occlusive, and reliable way.

A candidate technique to perform continuous non-occlusive BP measurements has been known since 1905. Commonly depicted as Pulse Wave Velocity (PWV), this technique exploits the fact that the velocity at which arterial pressure pulses propagate along the arterial tree depends on the underlying BP. Hence, after a preliminary calibration maneuver, one is able to obtain indirect measurements of BP by continuously measuring PWV values on a given arterial segment. A major restriction of this technique is the fact that the BP-PWV dependency is only exploitable in central elastic arteries, *e.g.* the aorta, limiting the implantation of PWV-based techniques: to assess PWV of central arteries is not an easy task by itself, and the development of a non-invasive and non-occlusive technique that could be used in ambulatory remains an unsolved technological problem.

To date, little has been advanced in this direction. On the one side, clinically-validated technologies have been developed to measure PWV of central arteries non-invasively… but they are not adapted to ambulatory uses. And on the other side, experimental works have been performed allowing the ambulatory continuous measurement of PWV of peripheral arteries… but their clinical relevance has been *de facto* limited, since they don't rely on central pressure pulse propagation analyses. Hence, the bridge linking the clinical demand and the technological development is not built yet.

1.2. Specific aims

This thesis aims at investigating novel continuous and non-occlusive techniques to measure BP values of living cardiovascular systems in ambulatory. In particular, this thesis aims at developing and testing new techniques based on the measurement of the propagation velocity of pressure pulses along central elastic arteries. Special emphasis is thus given to the investigation of novel metrological and signal processing techniques. The *in-vivo* experimental assessment of the performances of the novel techniques is a major aim of this research work as well. Specifically, the aims of this thesis are:

Thesis aim #1: to analyze the existing gap between the clinical demand for continuous non-occlusive techniques to measure ambulatory BP, and the technological capabilities proposed in the state of the art.

Thesis aim #2: to identify the causes that have lead PWV-techniques to fail in solving the BP clinical-technological gap, and to provide solution guidelines.

Thesis aim #3: to propose novel noise-robust signal-processing approaches to the measurement of PWV that can be implemented in ambulatory scenarios.

Thesis aim #4: to develop novel metrological concepts that allow measuring in ambulatory the propagation velocity of pressure pulses along central arteries.

Thesis aim #5: to test *in vivo* the ability of the developed metrological and signal-processing approaches to measure BP and central PWV.

1.3. Outline of the thesis

The current thesis is organized as it follows:

Chapter 1 provides an introduction to the thesis by describing its motivation and major research aims.

Chapter 2 consists on the compilation of the background information required for the understanding of the research works performed within the thesis. In particular this chapter reviews physiology concepts related to living cardiovascular systems, it reviews the history and state of the art in the field of non-invasive BP measurement and it introduces the concept of PWV and its relationship with continuous non-occlusive BP measurement. Finally, this chapter reviews the working principles and limitations of those non-invasive and non-occlusive metrological technologies used in this thesis. The material provided by this chapter has been partly published as a book chapter.

Chapter 3 presents the conception, development and evaluation of a novel signal processing approach to measure PWV in ambulatory scenarios. Based on the parametric modeling of arterial pressure pulses, this technique has been shown to outperform all state-of-the-art techniques in terms of noise robustness. Performance evaluation is provided based on both, simulated data, and *in-vivo* arterial pressure time series. The material provided by this chapter has been entirely published as a peer-reviewed journal paper.

Chapter 4 introduces a novel non-invasive and non-occlusive technique to measure BP based on the use of the Electrical Impedance Tomography (EIT) technology. By analyzing sequences of EIT images recorded at the chest level, this technique tracks the propagation of arterial pressure pulses from the right ventricle towards the descending aorta, and provides thus estimates on aortic PWV. EIT image acquisition is performed at high imaging rates (up to 50 images/second) and simply requires the use of a non-occlusive chest belt. The ability of the novel technique to measure BP is assessed *in vivo* on a pig model under several hemodynamic conditions. The material provided by this chapter has been entirely published as a peer-reviewed journal paper.

Chapter 5 presents a novel technique to measure central PWV values based on the use of a non-occlusive chest belt that performs simultaneous electro-cardiographic, impedance-cardiographic, phono-cardiographic and photo-plethysmographic measurements on the sternum. This technique tracks the propagation of arterial pressure pulses from their genesis at the aortic valve until their arrival at the sternum subcutaneous vascular bed. The performance of the novel technique in providing ambulatory estimates of central PWV is evaluated in a study involving up to 31 normo- and hypertensive human subjects. The material provided by this chapter has been entirely published as a peer-reviewed journal paper.

Chapter 6 concludes this thesis by summarizing the performed research, underlining the main limitations and setting guidelines for future work.

Four annexes provide unpublished data that complement the main body of this thesis:

Annex 1 suggests, from a theoretical perspective, a novel technique to improve PWV-based estimations of BP by introducing measurements of an additional cardiovascular variable, *i.e.* the cardiac output.

Annex 2 revisits a signal processing technique extensively used during this thesis, *i.e.* ensemble averaging, form a novel frequency perspective.

Annex 3 provides experimental evidence on the orders of magnitude of the electrical properties of tissues and organs within the thoracic cavity.

Annex 4 provides first experimental evidence on the use of the chest sensor introduced in Chapter 5 to monitor continuous BP changes in a subject during a one-hour experimental protocol involving several cardiovascular stresses.

Chapter 2

Background

Partly adapted from postprint version of:

Ambulatory monitoring of the cardiovascular system: the role of Pulse Wave Velocity

Josep Solà[1], Yves Allemann[2] and Stefano F. Rimoldi[2]

[1]CSEM – Centre Suisse d'Electronique et de Microtechnique, Neuchâtel, Switzerland

[2]Swiss Cardiovascular Center Bern, University Hospital Bern, Bern, Switzerland

Published in:

New Developments in Biomedical Engineering

Book Chapter

I-Tech Education and Publishing (2010), Vienna, Austria

ISBN 978-953-7619-57-2

Contributions by Yves Allemann and Stefano F. Rimoldi are in Section 2.6.3.

2. Background

This background section aims at providing the physiologic and technologic concepts required for the understanding of the research works performed during this thesis.

Section 2.1 starts by providing useful information on cardiovascular physiology, and in particular on the regulation of blood pressure. Section 2.2 provides an overview of the state of the art in non-invasive blood pressure measurement techniques, as well as reviewing the existing international criteria for the assessment of accuracy of blood pressure measurement devices. Section 2.4 revisits the history of non-invasive blood pressure measurement, and describes in detail the existing non-occlusive measurement techniques (auscultatory and oscillometric techniques). Section 2.5 provides a state of the art of semi-occlusive measurement techniques (tonometric and volume-clamp techniques). Section 2.6 focuses on the measurement of blood pressure by means of Pulse Wave Velocity techniques. After describing the biomechanical implications of the pulse wave velocity parameter, this section provides a review on its clinical applications, and justifies its use as a surrogate measurement of blood pressure. Finally, Section 2.7 provides a review on the non-invasive monitoring technologies that will be used along the thesis research works, namely electro-cardiography, impedance-cardiography, phono-cardiography, photo-plethysmography and electrical impedance tomography.

2.1. Cardiovascular physiology

This introductory section provides background concepts on the anatomy of the cardiovascular system (section 2.1.1), the cardiovascular mechanisms for the control of blood pressure (section 2.1.2), and the definition and stratification of hypertension (2.1.3). A final sub-section provides typical order of magnitude values for parameters of healthy cardiovascular systems (section 2.1.4).

2.1.1. Cardiovascular anatomy

Since this thesis copes with the measurement of blood pressure in humans, the understanding of the underlying physiology is of uttermost importance. In particular, the anatomy and functioning of the blood-pressure supporting system, *i.e.* the Cardio Vascular System (CVS), are to be comprehended.

For humans, as well as for all warm-blooded animals, the CVS is a life-maintaining system whose primary functions are [1]:

1. The rapid convective transport of oxygen, nutrients and water to organs and tissues, and the wash out of waste products,
2. The generation and distribution of hormones,
3. And the regulation of body temperature

The central pillar of the current thesis is related to the first of the depicted functions: the transport of fluids along the CVS to control the arterial systemic Blood Pressure (BP). Defined as the pressure exerted by arterial blood upon vessel walls, BP is controlled within a

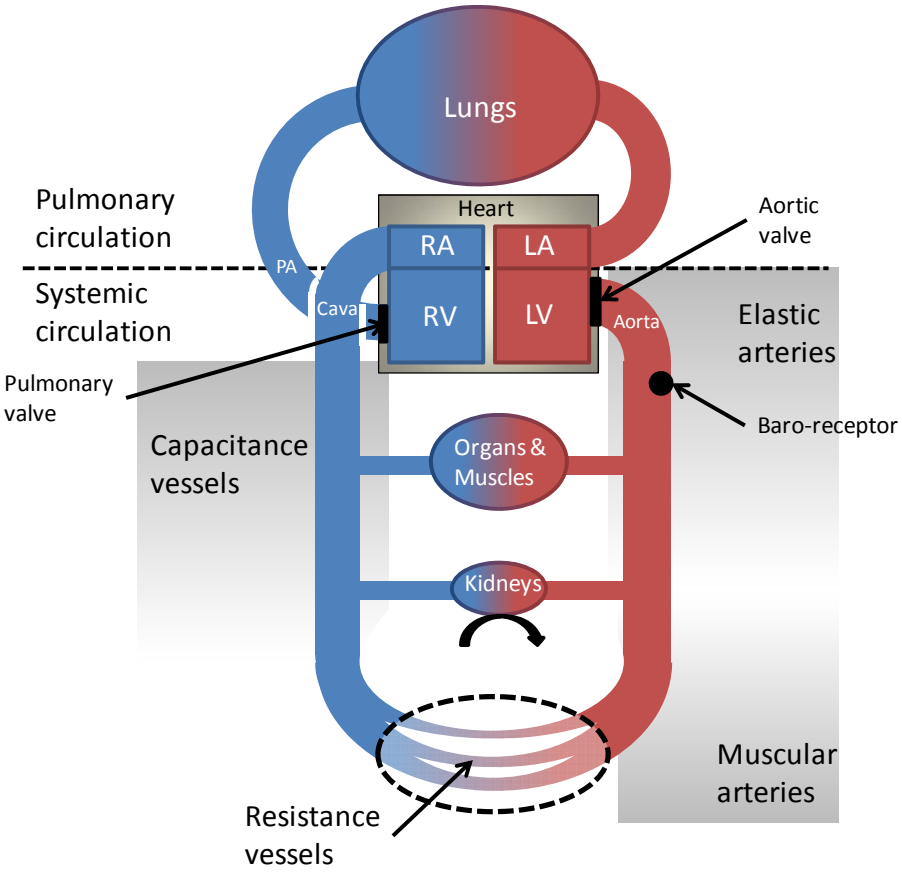

Figure 2.1: Sketch of the cardiovascular system, suggesting the anatomical location and interconnection of those organs and structures intervening in the regulation of blood pressure. RA: Right Atrium, RV: Right Ventricle, LA: Left Atrium, LV: Left Ventricle, PA: Pulmonary Artery.

very precise range in any healthy CVS: the establishment of correct BP values ensures the optimal perfusion of critical organs such as the brain, the heart or the kidneys.

Figure 2.1 illustrates a sketched description of the CVS, including the most relevant organs and anatomical structures participating in the control of BP. In summary, one differentiates between pulmonary and systemic circulations. The Pulmonary circulation is in charge of transporting blood from the right heart (Right Ventricle, RV) through the lungs in order to perform a gas exchange at the alveolar level (release of carbon-dioxide, and capture of oxygen). Oxygenated blood is recalled by the Left Atrium, LA. The Systemic circulation distributes then the oxygenated blood through all the body (starting at the left ventricle, LV) and recalls the de-oxygenated blood at the right auricle, RA.

The flow of blood through the pulmonary and systemic circulations is orchestrated by the cardiac cycle (see Section 2.7.1): following a complex synchronized contraction of the left and right ventricles, the aortic and pulmonary valves open, and a certain amount of blood is released into the aorta and the Pulmonary Arteriy (PA). The Aortic blood flow is initially buffered by central elastic arteries, and immediately distributed to the whole CVS via a complex network of conduct, or muscular arteries. Perfusion of organs, muscles and kidneys

is performed via subsequent branches of main conduit arteries. The last segment of the muscular arterial branching corresponds to the so-called resistance vessels: a large network of diameter-changing small vessels. Baro-receptors are pressure sensing mechanoreceptors transmitting information about blood flow and blood pressure to the Central Nervous System (CNS). De-oxygenated blood is recalled by the venous system and transported via the vena cava into the RA. Note that because of their ability to store large amounts of blood, veins are typically depicted as capacitance vessels.

2.1.2. Blood pressure control mechanisms

A crucial function of the CVS is thus to perform the homeostatic control of BP in order to ensure the optimal blood perfusion of critical organs: daily common activities such as standing-up, or jogging are possible thanks to this very sophisticated control mechanism that regulates BP within a very narrow range in some fractions of seconds. The current section studies the mechanisms though which the continuous control of BP is performed in healthy CVS.

Figure 2.2 provides a summary of the two available BP control mechanisms, organized according to their response time:

- The baroreflex is in charge of the instantaneous and fast regulation of BP: a set of pressure mechanosensors send messages to the CNS informing about the current hemodynamic status. Via electrical impulses sent through the Autonomic Nervous System (ANS) the baroreflex instantaneously modifies the functionality of heart and vessels in order to achieve target BP values, respectively varying the cardiac output and the vascular resistance.
- The control of extra-cellular fluid volume performed by the kidneys is responsible for maintaining normal BP in the long term. When the efficiency of the baroreflex starts decreasing, for instance after some hours of challenge or in chronic hypertension, this slower but more long-lasting mechanism takes over the homeostatic control of BP. In particular, the renal excretion of salt and water adjusts the running volume of blood, and modifies thus the amount of cardiac refilling and venous return.

The processes through which both BP control mechanisms actuate are summarized in Figure 2.3. From a BP control perspective, the two crucial variables determining systemic arterial blood pressure are cardiac output (CO, the flow of blood ejected by the heart into the aorta, in l/min) and systemic vascular resistance (SVR, the fluidic resistance opposed by the arterial system to the flow of blood, in mmHg.min/l), *i.e.*

$$\mathrm{BP}=\mathrm{CO}\cdot\mathrm{SVR}$$

Equation 1

The achievement of a given CO depends on two variables as well, heart rate (HR, the amount of cardiac contractions per unit of time, in beats/min) and stroke volume (SV, the amount of blood ejected by the heart at each contraction, in L), *i.e.*

$$\mathrm{CO}=\mathrm{HR}\cdot\mathrm{SV}$$

Equation 2

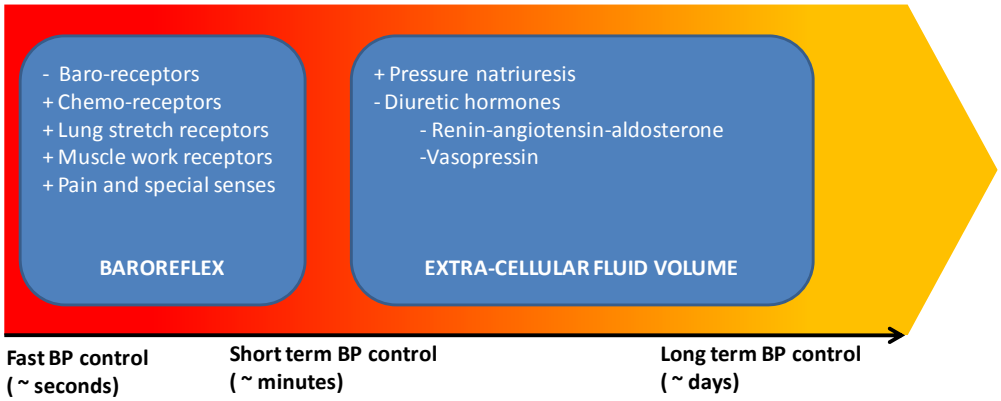

Figure 2.2: Blood pressure control mechanisms, according to their response time.

In healthy CVS, the determination of heart rate is performed by the triggering frequency of the sinus node (the natural pacemaker of the heart), which responds to the stimulus of the para-sympathetic nerve. The achievement of a determined stroke volume depends on the one side on the cardiac contractibility as commanded by the cardiac branch of the sympathetic nervous system, and on the other side on the venous return. Understood as the amount of cardiac refilling, the venous return depends on four main variables: the sympathetic tone innervation (inducing venous vasoconstriction of splanchnic and cutaneous veins), the extra-cellular fluid volume (as controlled by the kidneys, see Figure 2.2), the body position (modifying venous return via orthostatic pressure changes), and the muscle activity (increasing venous return by pumping blood out of skeletal muscle veins).

A crucial element of the blood pressure regulation is thus the ANS. Actuating via two opposite branches (the sympathetic and para-sympathetic systems) the ANS is capable of either achieving fast increases of BP (innervation of cardiac muscle contractibility, innervation of resistance vessel tone, and innervation of venous tone) or performing very fast decreases of BP (enervation of the sinus node, and thus, lowering of the heart rate). The amount of ANS nerve electrical activity is controlled by the cerebral cortex: by comparing the balance of pressor and depressor reflexes to a central set-point, electrical commands are continuously delivered to the CVS via the different ANS pathways.

Baro-receptors are stretch receptors located at main elastic arteries signaling pulse pressure and mean pressure levels to the cerebral cortex via a depressor reflex (negative feedback). A resetting mechanism allows baro-receptors to adapt their working point at different pressure values, for instance, when blood pressure is to be regulated at higher values during physical exercise periods or chronic hypertension situations. Sensitivity of baro-receptors is also modified (decreased) by aging and chronic hypertension, reducing the global feedback gain of the baroreflex system.

Pressor reflexes, or pressure-rising reflexes, are a set of mechanisms that interfere into the baro-reflex system inducing an increase of blood pressure. They are namely the chemo-receptors (stimulated by arterial blood hypoxemia, hypercapnia, acidosis and hyperkalemia), lung stretch receptors (mechanoreceptors located at the lung stimulated at each breath, and partly responsible of sinus arrhythmia: increase of heart rate at each inspiration), muscle work receptors located at the muscle (either mechanoreceptors that

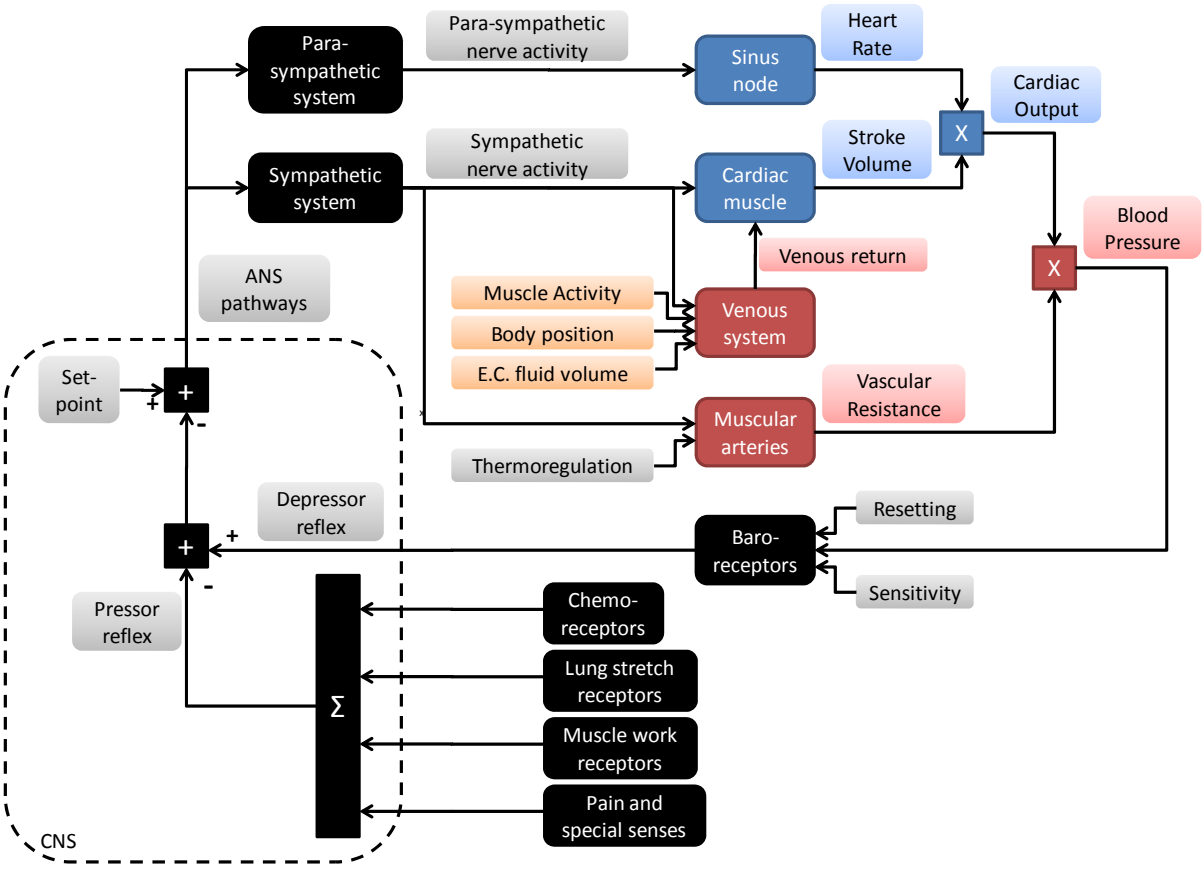

Figure 2.3: Overview of blood pressure control mechanisms, including baroreflex control and extra-cellular fluid volume control. Black boxes depict elements corresponding to the nervous system, blue boxes to the heart, red boxes to vessels, and orange boxes depict elements external to the baroreflex control.

contribute to the rapid increase of heart rate in the first few seconds of exercise, or metaboreceptors activated by chemicals released particularly during isometric exercise) and pain and special sense receptors (activated by somatic or visceral pain, cold, alerting situations and sexual stimulation).

The BP control overview provided by Figure 2.3 aims at being a simplified model of the reality, facilitating the understanding of the physiology underlying the works of the current thesis. A comprehensive model of CVS control was proposed by Guyton in 1972. For a detailed physiological, electro-physiological and bio-chemical description of CVS control see [1, 2].

2.1.3. Blood pressure and hypertension

As it has been described above, the entire cardiovascular system (CVS) is dedicated to the regulation of BP within a certain range even during strong physiological challenges. However due to the beating mechanism of the heart, arterial BP is not a single value but a continuum series of values. In clinical practice four representative indicators of BP status are generally provided (see Figure 2.4) [3]:

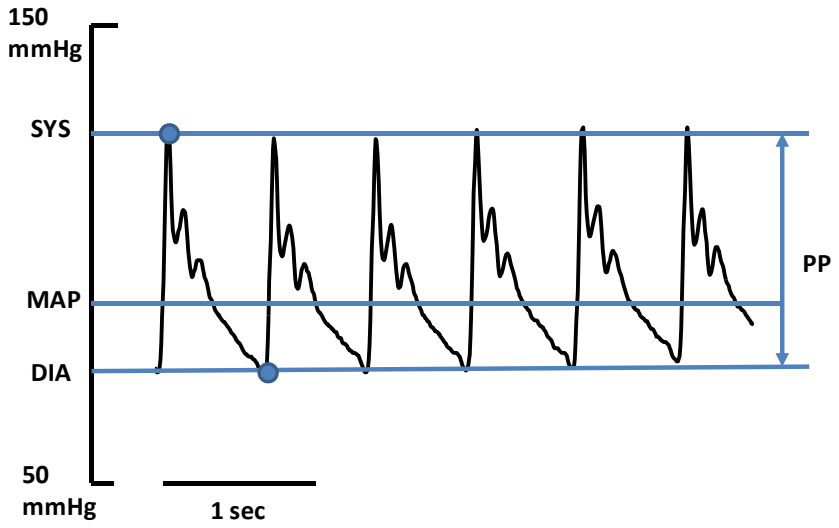

Figure 2.4: Six beats of an arterial blood pressure tracing recorded at the finger, including the definitions of Systolic pressure (SYS), Diastolic pressure (DIA), Mean Arterial Pressure (MAP) and Pressure Pulse (PP).

- **Systolic pressure (SYS):** defined as the maximum value of an arterial pressure tracing.
- **Diastolic pressure (DIA)**: defined as the minimum value of an arterial pressure tracing.
- **Mean Arterial pressure (MAP)**: defined as the average value of an arterial pressure tracing. MAP is commonly approximated as:

$$MAP = \frac{SYS+2\ DIA}{3}$$

Equation 3

- **Pressure Pulse (PP)**: defined as the difference between SYS and DIA.

The high prognostic and diagnostic value of BP is nowadays incontestable [4], and since several decades now BP measurements are a routine task of any medical examination. As a diagnostic screening tool, BP is by definition the optimal means to identify hypertension. Affecting around 26% of the worldwide population [5], hypertension is a human-specific illness chronically increasing arterial blood pressure above normal values. The interest in detecting, treating and controlling hypertension relies on the fact that elevated blood pressure is considered one of the major risk factors for Cardiovascular Disease (CVD): the most common cause of death in developed countries [6].

Hypertension is thus defined as BP levels being above normality. As a matter of fact, the definition of hypertensive BP thresholds evolves continuously according to new empirical data recorded worldwide. Currently, the guidelines [7] of the European Society of Hypertension (ESH) propose to classify blood pressure levels according to optimal, normal, high normal and hypertensive groups using as thresholds the values provided by Table 2.1.

Table 2.1: Blood pressure thresholds (in mmHg) for the stratification of hypertension according to the European Society of Hypertension (ESH), 2007 [7].

Category	Systolic		Diastolic
Optimal	< 120	and	< 80
Normal	120-129	and/or	80-84
High normal	130-139	and/or	85-89
Grade 1 Hypertension	140-159	and/or	90-99
Grade 2 Hypertension	160-179	and/or	100-109
Grade 3 hypertension	≥ 180	and/or	≥ 110
Isolated systolic hypertension	≥ 140	and	< 90

Table 2.2: Blood pressure thresholds (in mmHg) for the stratification of ambulatory hypertension according to the European Society of Hypertension (ESH), 2007 [7].

Hypertension category	Systolic	Diastolic
Office (see Table 2.1)	> 140	> 90
24-hour	125-130	>80
Day	130-135	> 80
Night	> 120	> 70
Home	130-135	> 85

Blood pressure levels as characterized in Table 2.1 are those measured in the office or in the clinic during a physical examination, *i.e.* office or clinic BP. However, as described above, blood pressure of a living cardiovascular system is a continuously changing vital parameter. For this reason single sporadic office BP measurements provide, at the best, only a partial view of the nature of the hypertension. A full clinical picture is to be achieved only by measuring BP throughout a full day of cardiovascular events. Accordingly, ambulatory BP measurement is defined as the measurement of BP out of the office while subjects perform their daily life activities. In the state of the art, ambulatory measurements typically provide BP values every 20 to 30 minutes using brachial oscillometric BP cuffs (see Section 2.4.3). Although the precision of such ambulatory automatic readings might be somehow lower than office measurements, it has been recently accepted that "although office BP should be used as a reference, ambulatory BP may improve prediction of cardiovascular risk in untreated and treated patients" [7]. As an example of the importance of performing BP measurements in a 24h setup, Figure 2.5 reproduces some typical hypertensive patterns that can be easily identified by ambulatory monitoring, but that single office examinations would omit [8]. According to the principles of ambulatory monitoring, guidelines for the stratification of ambulatory hypertension have been defined as well (see Table 2.2). The guidelines include a *home hypertension* category, depicting those isolated self-measurements performed by patients at home. Standard recommendations on when office, ambulatory or home BP measurements should be performed are provided in Table 2.3.

According to the data and evidences provided by this section, the ambulatory measurement of BP appears to be a key element for the identification and diagnosis of a large spectrum of hypertension cases. Unfortunately, the only measurement means made nowadays available to clinicians to perform such measurements is the so-called oscillometric technique (see Section 2.4.3). Although being unsupervised, *i.e.* BP is measured automatically without the supervision of the clinician, oscillometric measurements suffer of two main limitations:

- Because of its intermittent nature, oscillometric BP measurements are obtained only every 20-30 minutes providing a discontinuous view of BP regulation mechanisms.
- Because of its occlusive nature, oscillometric devices interfere with patients life style creating discomfort during measurements (occluding cuff), and biasing measured BP values especially during night time.

Therefore, the need of a new technique allowing the unsupervised, continuous, and non-occlusive measurement of BP is justified, being the main target of the current thesis.

Table 2.3: European Society of Hypertension (ESH) criteria for the recommendation of office, ambulatory or home BP measurement strategies [7].

Measurement type	Recommended when:
Office BP	• Main screening tool
Ambulatory BP	• Large office BP variability • High office BP in subjects with low cardiovascular risk • Office and home BP disagree • Resistance to drug treatment • Hypotensive episodes are suspected • Pre-clampsia is suspected in pregnant women
Home BP	• Additional information is needed on the BP lowering effect of treatment throughout dose-to-dose intervals • Doubts exists on the reliability of ambulatory BP

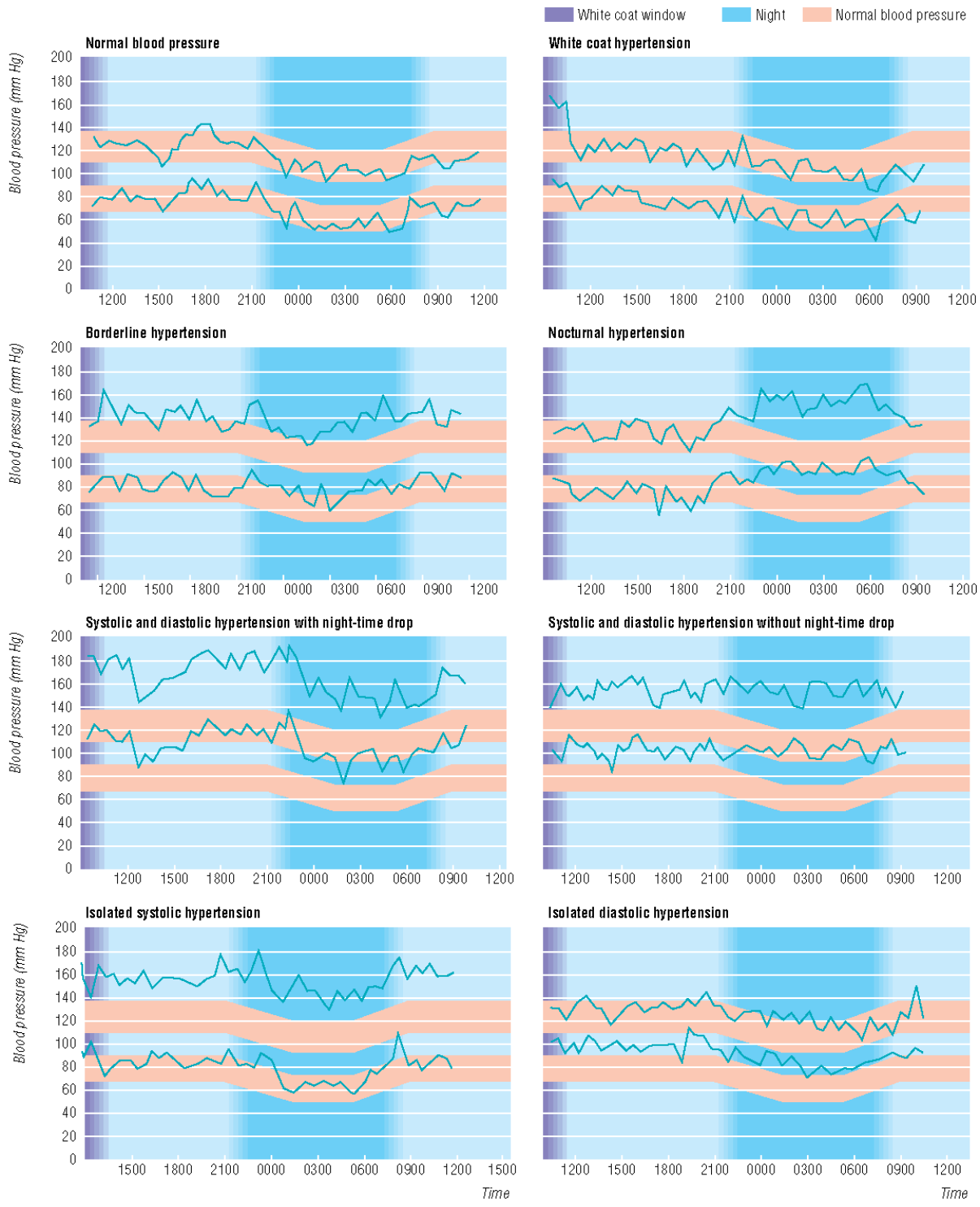

Figure 2.5: Typical hypertensive patterns, as measured by 24h ambulatory monitoring, according to the definitions by the British Hypertension Society (BHS), from [8]. Illustrated patterns are white coat hypertension, borderline hypertension, nocturnal hypertension, isolated systolic hypertension and isolated diastolic hypertension.

2.1.4. Orders of magnitude of the CVS

In order to complete the current section, Table 2.4 provides a summary of typical values for the most relevant cardiovascular variables involved in the regulation of blood pressure.

Table 2.4: Typical values for timing and biomechanical cardiovascular parameters.

		Typical value
Cardiac timing	Heart rate	50 – 100 bpm
	Heart rate, maximum	180 – 220 bpm
	Isovolumetric contraction (pre-ejection period, PEP)	50 ms
	Left Ventricular Ejection time (LVET)	300 ms
Volumes	Total blood volume	5 L
	Venous blood volume	3 L
	Pulmonary blood volume	0.6 L
	Stroke volume at rest	70-80 cm^3
	Stroke volume, maximum	110-120 cm^3
Flows	Cardiac output at rest	4-7 L/min
	Cardiac output, maximum	20-35 L/min
Pressures	Systemic blood pressure	120/80 mmHg
	Pulmonary blood pressure	25/10 mmHg
	Central venous pressure	0-10 mmHg
Resistances	Systemic vascular resistance	20 mmHg/L/min
	Pulmonary vascular resistance	3 mmHg/L/min
	Aorta cross-sectional area	4 cm^2
Areas	Capillary total cross-sectional area	1000 cm^2
	Vena cava cross-sectional area	7 cm^2
Velocities	Aortic blood velocity at rest	20 cm/s
	Aortic blood velocity during exercise	250 cm/s
	Aortic Pulse Wave Velocity in young	4-5 m/s
	Aortic Pulse Wave Velocity in elderly	10-15 m/s
Blood properties	Blood density	1.06 g/cm^3
	Blood viscosity	2.76 mPa s

2.2. Overview of non-invasive blood pressure measurement techniques

The non-invasive, *i.e.* transcutaneous, measurement of blood pressure has been the target of clinical investigations and technological developments since the end of the 19th century [9]. The goal of the current section is to sketch a landscape of those techniques that have had enough clinical relevance to prevail until nowadays.

A graphical overview of the constellation of relevant techniques is provided by Figure 2.6. Each technique has been positioned in a 2D space, where the horizontal axis depicts clinical compliance, and the vertical axis depicts ambulatory compliance. According to the scope of this thesis, an ideal BP measurement technique should be placed on the upper right region of this constellation, *i.e.* depicting perfect ambulatory and clinical compliances. As it will be demonstrated further, none of the existing technique matches these two criteria nowadays.

The specific criteria used in the generation of the constellation of techniques illustrated above are now described. Measurement techniques have been analyzed according to five sub-criteria grouped as it follows (see Table 2.5):

- Ambulatory compliance: three sub-criteria assess whether or not a technique is compliant to be implemented in ambulatory scenarios. First, does a measurement require the full occlusion of the arterial flow of blood? Possible answers are: yes, partly or no. Second, does the technique require human supervision to be performed? Possible answers are: the technique is supervised, or the technique is unsupervised. Third, is the technique prone to be used in 24h monitoring measurement campaigns? Possible answers are: yes, partly or no.
- Clinical compliance: two sub-criteria assess the compliance of the measured BP values with clinical requirements. First, does the technique provide intermittent measurements of BP, does it provide a single BP value par heart beat, or does it measure a continuous BP waveform? Possible answers are: intermittent, beat by beat or continuous. Second, are the measured values accurate enough when compared against an arterial catheter measurement of BP? Possible answers are: the accuracy of the technique is gold standard, good, controversial, or poor.

Recalling the information provided by both Table 2.5 and Figure 2.6 one realizes that there is currently no technique providing both optimal ambulatory and clinical performances. On the one side both occlusive techniques (oscillometric and auscultatory) depict good clinical compliance, but their ambulatory performance is rather limited (in particular for auscultatory measurements). On the other side, partly-occlusive techniques (volume clamp and tonometric) depict better ambulatory compliance, but their clinical performance remains rather low (in particular for tonometry measurements).

Finally, Pulse Wave Velocity (the central pillar technique of the present thesis) depicts an optimal ambulatory compliance, while maintaining fairly good clinical performances. Appearing thus as a potential candidate for ambulatory monitoring of BP, PWV techniques are currently the target of a large amount of research works worldwide. This thesis aims at

providing novel theoretical and experimental support to both the clinical and ambulatory features of PWV techniques when used in the assessment of BP.

Table 2.5: Detailed analysis of clinically-relevant non-invasive techniques for the measurement of blood pressure. A graphical interpretation of this analysis is provided in Figure 2.6.

	Ambulatory compliance criteria			Clinical compliance criteria	
Technique	**Occlusive**	**Supervision**	**24h-prone**	**Periodicity**	**Accuracy**
Auscultation	Yes	Supervised	No	Intermittent	Gold standard
Oscillometric	Yes	Unsupervised	Yes	Intermittent	Good
Volume-clamp	Partly	Unsupervised	Partly	Continuous	Controversial
Tonometric	Partly	Unsupervised	Fairly	Continuous	Poor
Pulse Wave Velocity	No	Unsupervised	Yes	Beat by beat	Controversial

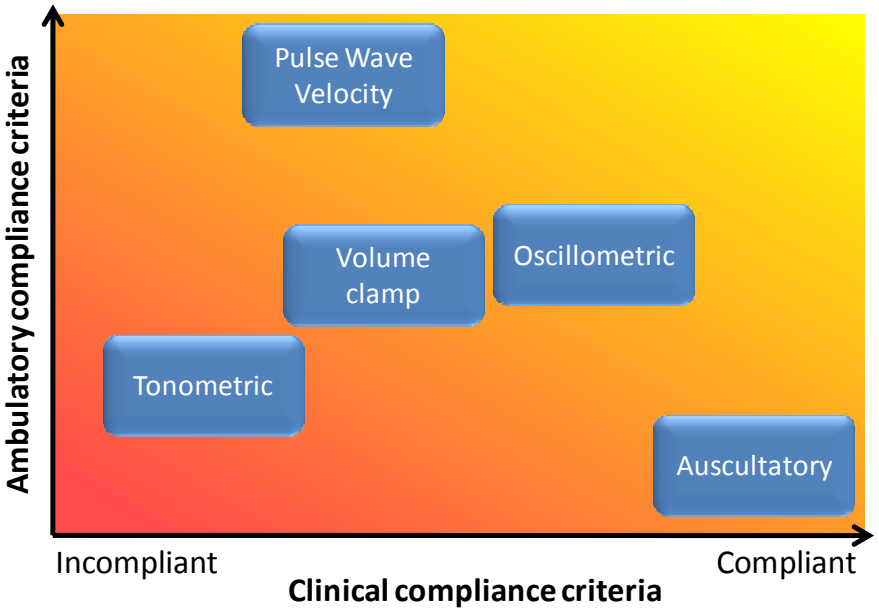

Figure 2.6: Graphical overview of existing techniques for the non-invasive measurement of Blood Pressure (BP). Evaluation criteria are clinical compliance (horizontal axis) and ambulatory compliance (vertical axis), as defined by Table 2.5.

2.3. International standards for blood pressure measurement accuracy

The assessment of measurement accuracy for a given BP device is regulated by two international standards, respectively proposed by the British Hypertension Society (BHS) and the US Association for the Advancement of Medical Instrumentation (AAMI) [10]. Both standards define a maximum tolerated error when comparing BP measurements performed by a given technique, with BP measurements performed by the auscultation of Korotkoff sounds and a mercury sphygmomanometer. Table 2.6 describes the standardized accuracy criteria. Note that grading criteria for the BHS are defined as cumulative percentage of readings falling within a certain BP range, *e.g.* Grade A is achieved if at least 60% of the systolic and diastolic measurements performed with a new device fall within the gold standard measurement ±5mmHg.

Table 2.6: BHS and AAMI validation standards for BP measurement devices. Grading criteria are as compared to BP measurements by auscultation of Korotkoff sounds and a mercury sphygmomanometer.

BHS	**Cumulative percentage of readings falling within**		
	5 mmHg	**10 mmHg**	**15 mmHg**
Grade A	60%	85%	95%
Grade B	50%	75%	90%
Grade C	40%	65%	85%
Grade D	otherwise		
AAMI	**Statistical comparison**		
	Mean difference	**Mean stdev**	
AAMI	< 5 mmHg	< 8 mmHg	

2.4. Blood pressure measurement by occlusive techniques

The analysis of the state of the art on non-invasive blood pressure measurement starts with the study of currently existing occlusive means, namely the auscultatory and the oscillometric techniques. See Figure 2.6 for an overall view of the benefits and limitations of these techniques.

2.4.1. The pioneers of occlusive blood pressure measurement

The history [9, 11] of occlusive measurement of blood pressure in humans started in 1855 when Vierordt developed a pioneer pulse recorder, *i.e.* a device capable of recording on a paper the beatings of a radial artery pulse. During the following decades different researchers improved Vierordt's method (Etienne Jules Marey and Samuel Siegfried Karl Ritter von Basch) testing new families of sphygmomanometers, *i.e.* devices to measure the pressure (-manometer) of a pulse (sphygmo-, in Greek). Those sphygmomanometers required precisely localizing an artery, and placing a mechanical device onto it (see Figure 2.7).

At the end of that century Scipione Riva-Rocci moved one step further introducing the first sphygmomanometer with an inflation cuff. The cumbersome need of seeking for specific arteries was overcome by simply occluding the whole upper arm with a brachia cuff (Figure 2.8). Harvey Cushing, an American doctor, spotted this Italian approach and imported it to the US in 1901, where modern sphygmomanometers based on inflation cuffs were spread into clinical practice.

Unfortunately, the Riva-Rocci sphygmomanometer was only able of measuring systolic pressures: by palpating the arterial pulse distally from the inflation cuff, and by simultaneously increasing the pressure at the cuff, one determined systolic pressure as the pressure indicated by the manometer when no pulse was palpated anymore. Only some years later, in 1905, a Russian doctor named Nikolai Korotkoff observed that by listening at the sounds generated by the arteries with a stethoscope one could determine specific blood flowing sounds occurring at different cuff pressures [12]. By characterizing said sounds, Korotkoff established the basics of the modern auscultation measurement of blood pressure.

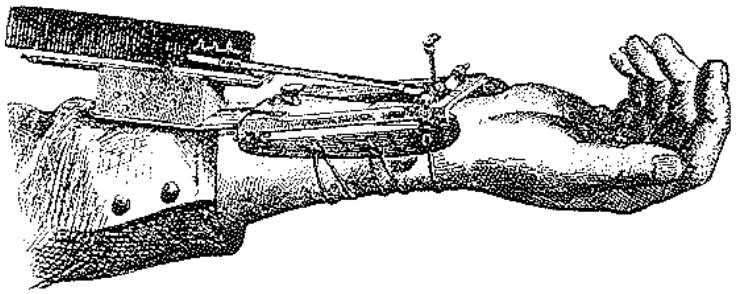

Figure 2.7: Radial artery sphygmomanometer developed by Etienne Jules Marey in 1860 (from [9])

2.4.2. Auscultatory measurement

Still considered as the gold standard method to measure blood pressure non-invasively [13], the auscultatory technique was developed by Riva-Rocci and Korotkoff in the beginnings of the 20th century (see section above for chronological issues).

The auscultatory technique consists of [13]:

1. Occluding the brachial artery with a cuff situated at the upper arm, at supra-systolic pressures, *i.e.* impeding any passage of blood flow through the brachial artery. Other limbs such as the upper leg might be used as well.
1. Placing a stethoscope over the artery just below (distally from) the cuff.
2. Gradually deflating the brachial cuff, until a first sound is heard at the stethoscope. Brachial cuff pressure is then associated to the systolic pressure (Figure 2.9).
3. Gradually deflating the brachial cuff, until any sound completely disappears from the stethoscope. Brachial cuff pressure corresponds is finally associated to the diastolic pressure (Figure 2.9).

The discussion on the genesis of Korotkoff sounds has motivated a large amount of theoretical and experimental research works [9]. Currently, the mixture of two phenomena is assumed to play a role: on the one side the turbulent flow of blood downstream from the occluding cuff, and on the other side the movement of vessel walls at the arrival of a pressure pulse at the occluding cuff.

The measurement of the pressure being actually applied to a brachial cuff is performed by either a mercury column (mercury sphygmomanometer), a mechanical transmission of the pressure to a circular scale (aneroid sphygmomanometer), or electronic pressure gauges (hybrid sphygmomanometer). However, after one century of clinical evidence, gold standard auscultation remains mercury sphygmomanometry [13].

Unfortunately, auscultatory measurements require the intervention of human operators (for both deflating the brachial cuff, and decoding Korotkoff sounds), inducing a large inter-operator variability, and compromising in several cases the accuracy of blood pressure readings. Regular training of operator is thus needed to achieve target measurement accuracies [13]. Cuff deflation rate as well as cuff size and positioning play an important role in the accuracy of the measurement too [9].

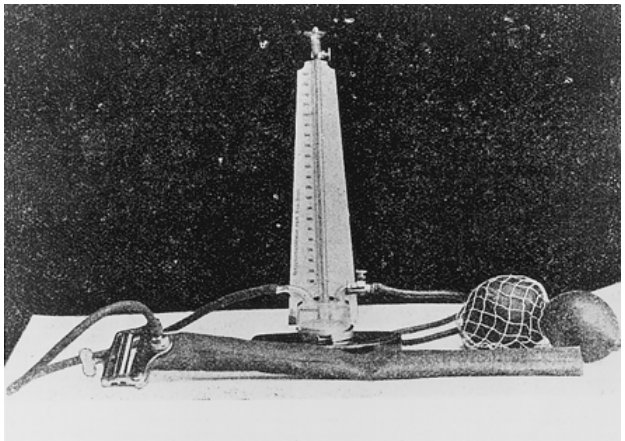

Figure 2.8: Riva-Rocci sphygmomanometer used by Nikolai Korotkoff in 1910 (from [12])

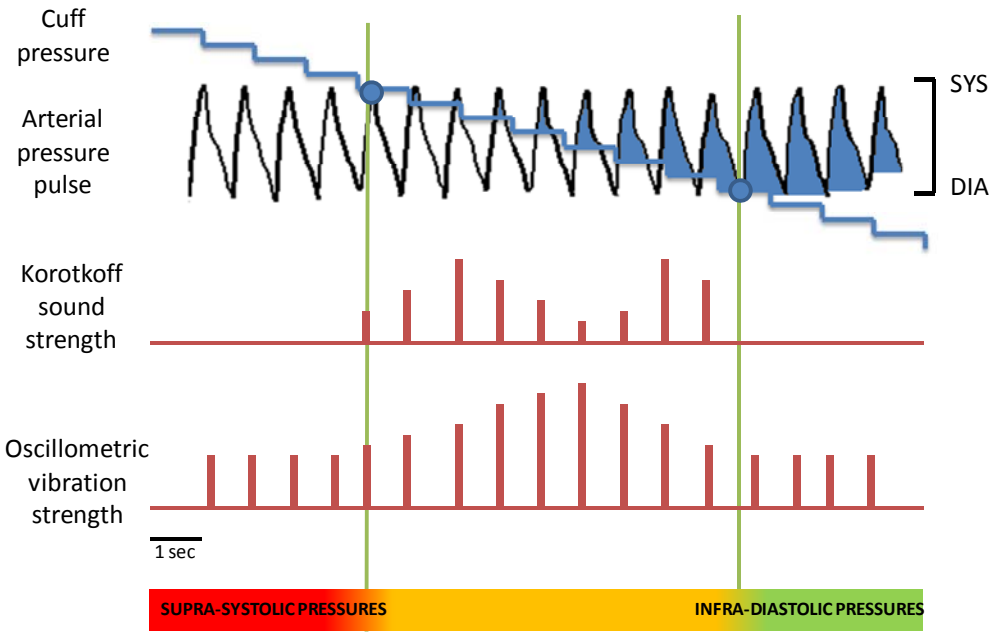

Figure 2.9: Strength of Korotkoff sounds and oscillometric vibrations for a brachial cuff deflating from supra-systolic towards infra-diastolic cuff pressures.

A revisited version of the auscultatory technique has been recently proposed [14] replacing the decoding of Korotkoff sounds by the analysis of photo-plethysmographic signals at the fingers. Such an approach is expected to provide a new family of auscultatory devices that reduce the amount of required human expertise.

2.4.3. Oscillometric measurement

Aiming at overcoming the operator-dependent nature of auscultatory measurements, a revolutionary family of automated unsupervised devices to measure blood pressure were released on the early 70s [15]. So-called oscillometric devices, these devices replaced the auscultation of Korotkoff sounds by the digital processing of pressure oscillations transmitted from the arteries to the cuff.

The oscillometric technique consists thus of [15]:

1. Placing an inflation cuff at the upper arm, similarly to the auscultatory method, and occluding the brachial artery at supra-systolic pressures.
2. Gradually deflating the brachial cuff until infra-diastolic pressures, and recording the pressure pulses transmitted from the brachial artery to the cuff.
3. Jointly processing the time series of pressure pulses recorded at the cuff, and the time series of occluding pressure applied to the cuff, in order to determine a systolic, a mean, and a diastolic pressure value.

The underlying phenomenon of oscillometric measurement was already described in 1876 by Etienne-Jules Marey [16]: oscillations measured at an inflation cuff reach their maximum amplitude when the applied pressure approximates the mean arterial pressure (Figure 2.9). Increasing or decreasing the cuff pressure will diminish the amplitude of the oscillations, and they will remain even at supra-systolic and infra-diastolic cuff pressures [13]. Hence, in contrast with the auscultatory method, oscillometry is not capable of providing an accurate measurement of neither systolic nor diastolic arterial pressures (see Figure 2.21): *add-hoc* signal processing strategies have been developed by oscillometric device manufacturers to overcome such limitation. The details and accuracy of these proprietary algorithms remain unknown [9, 13].

Nevertheless, oscillometric techniques have paved the way towards a fully unsupervised and repeatable measurement of blood pressure… opening a new dimension of cardiovascular monitoring: the ambulatory measurement of blood pressure [17, 18].

Oscillometric devices to be placed in alternative body locations such as wrist have been commercialized as well: unfortunately, measurement errors induced by orthostatic pressure changes at the wrist limit their use [13]. Therefore, although wrist devices are less cumbersome than traditional brachial cuffs, their use in clinical routine has been rather limited.

2.5. Blood pressure measurement by semi-occlusive techniques

Chronologically developed after the auscultatory and oscillometric techniques, a family of semi-occlusive techniques appeared during the 20th century. Based on the partial occlusion of an artery (blood flow is never fully impeded), these techniques allow the continuous measurement of arterial pressure waveforms to the expense of a critical placement of sensing probes. Recall that Figure 2.6 provides a graphical overview of the different measurement techniques.

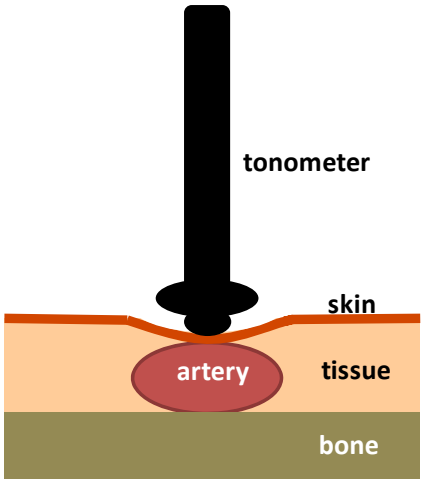

Figure 2.10: Principle of work of arterial applanation tonometry: a superficial artery is compressed against a flat bone. Arterial wall deformations are measured with a precise displacement sensor, *i.e.* a tonometer.

2.5.1. Tonometric measurement

Inspired by the pioneering developments by Vierordt and Marey (see Section 2.4.1), and by previous works in ocular monitoring, Pressman and Newgard introduced applanation tonometry in 1963 [19].

This method consists on applying a force over the center of a superficial artery (against an underlying bone) until the vessel starts distorting. At this point, and based on a linear spring model of the measurement setup, Pressman and Newgard demonstrated that the vertical displacements observed by the tonometer are proportional to the arterial pressure [20]. Finally, by keeping a constant positioning of the tonometer-artery-bone system (Figure 2.10), a sensor translates the sensed vertical displacements into electrical signals depicting arterial pressure waveforms. More sophisticated models describing the mechanics of applanation tonometry measurements were further developed by Drzewiecki during the 80s [19].

Although appealing because of its capability of providing accurate recordings of arterial waveforms, applanation tonometry suffers of three main limitations:

1. The positioning of the tonometer over the center of the artery is highly critical: the difference between correct and wrong placements is within fractions of millimeters [20]. Accordingly, wrong placements will lead to a non-linearity in the underlying displacement-pressure relationship. Self-positioning tonometers depicting either an array of sensing probes or a single pivoting probe have been released aiming at overcoming this limitation. An example of such a technology is the Vasotrac device (MedaWave Inc., St. Paul, USA), implementing a self-positioning pivoting wrist tonometer [21].
2. Applanation tonometry measures a vertical displacement that is proportional to arterial pressure [20]. Therefore, although this technology can be used to provide continuous recording of arterial pressure waveforms, no absolute BP value is obtained. Commercial tonometers require thus to calibrate the recorded waveforms via an occlusive cuff measurement of BP. An alternative approach to cuff calibration is that proposed by the Vasotrac device (MedaWave Inc., St. Paul, USA): by gently compressing and decompressing the radial artery during a period of 12 to 15 beats, a zero-load state of the artery wall is detected as the tonometer pressure providing maximum signal amplitude. This pressure is then assumed to be an absolute estimate of mean arterial pressure [21, 22].
3. The need of a continuous precise positioning of the sensor makes applanation tonometry highly sensitive to motion: subjects are required to remain still while measurements are being performed [23].

In spite of the enumerated limitations, applanation tonometry remains the gold standard method to assess arterial waveforms non-invasively. Recently, this technique has entered clinical routine via the commercialization of the SphygmoCor device (AtCor Medical, New South Wales, Australia): under expert supervision and operation, this device performs

applanation tonometry measurements at the radial artery, and further derives an estimate of the underlying central arterial pressure waveform (see Section 2.6) [24].

Figure 2.11: Two examples of commercialized applanation tonometry devices. Left figure, the supervised SphygmoCor (AtCor Medical, New South Wales, Australia): the gold-standard non-invasive method to assess central artery pressure waveform. Right figure, the unsupervised Vasotrac (MedaWave Inc., St. Paul, USA): a pioneer attempt to ambulatory tonometric monitoring.

2.5.2. Volume-clamp measurement

This method was introduced by Penaz in 1969 [25] based as well on the observation done by Marey in 1876 [16]: the pulsation of an artery reaches its maximum amplitude at the zero transmural state, *i.e.* when the pressure inside the artery equals the pressure of its surrounding tissues. The volume-clamp method consists thus on placing a small cuff incorporating a photo-plethysmographic (PPG) device around a finger [26]. The technique operates in two different phases (see Figure 2.12). During a calibration phase the cuff pressure is adjusted to maximize the amplitude of PPG pulsatility along the cardiac cycle. If the applied cuff pressure exceeded the intra-arterial pressure (positive transmural pressure) the artery would over-distend, become stiffer, and thus decrease its pulsatility. On the other side, if the applied cuff pressure was bellow the intra-arterial pressure (negative transmural pressure) the artery would collapse, decreasing pulsatility as well. Therefore, by clamping the volume of the artery at its maximum PPG pulsatility status, one ensures that the pressure generated at the cuff equals the intra-arterial pressure, the arterial wall being thus unloaded. In a running phase the cuff-pressure is servo-controlled around the calibrated unloaded pressure in order to maintain a constant PPG amplitude signal along the whole cardiac cycle. Accordingly, the instantaneously-applied pressure corresponds to the artery unloaded pressure at each phase of the cardiac cycle, providing thus a continuous estimate of the pressure pulse waveform (see Figure 2.12).

Although the accuracy and reproducibility of the volume-clamp method were initially demonstrated by several clinical studies [27, 28], it is nowadays recognized that it does not reach any of the BHS nor AAMI standard criteria [26] (see Table 2.6). Evidence exists, for instance, on problems associated to the automatic recalibration (physiocal) and the overestimation of systolic pressures [29, 30]. Even more, the volume-clamp method remains

a semi-occlusive method, leading to periods of venous congestion if used during prolonged time periods.

In spite of the identified limitations, the volume-clamp remains nowadays the only unsupervised method for the continuous non-invasive measurement blood pressure. A commercial device implementing the volume-clamp method is PORTAPRES (Finapres Medical Systems, Amsterdam, The Netherlands), as illustrated in Figure 2.13.

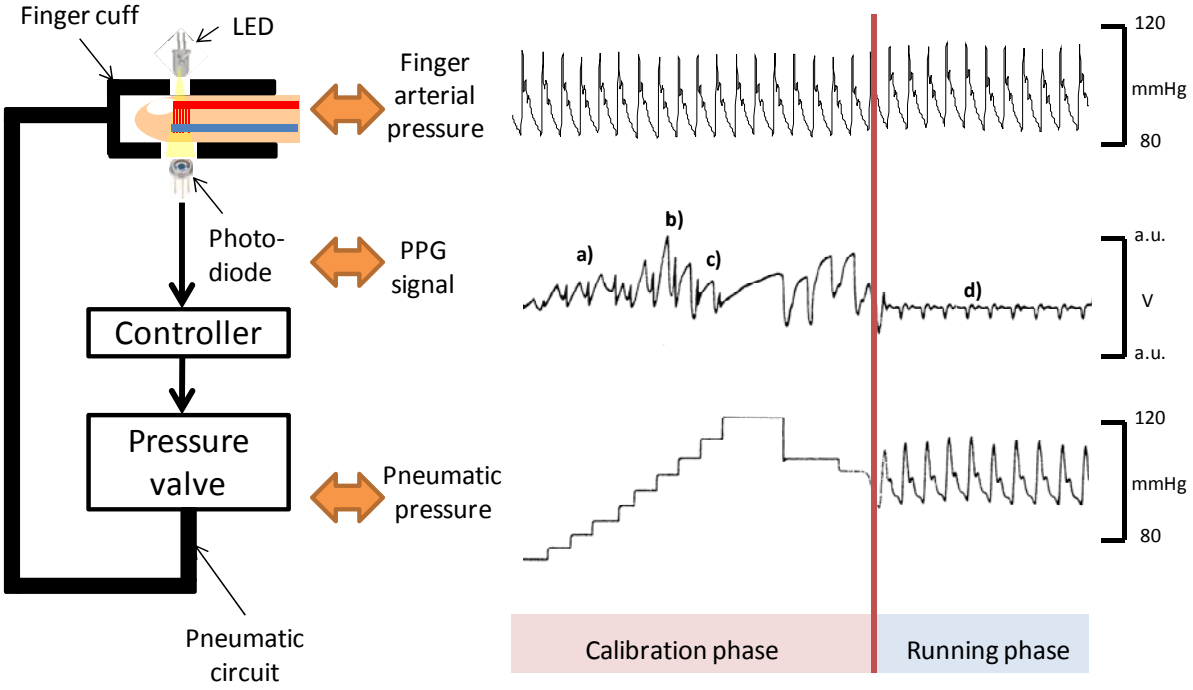

Figure 2.12: The Volume-clamp method to measure continuous blood pressure. Calibration phase: in a) cuff pressure is smaller than arterial pressure, leading to small PPG pulsatility. In b) cuff pressure reaches arterial pressure, leading to zero transmural pressure and thus, maximizing PPG pulsatility. In c) the artery is collapsed. Running phase: in d) the servo-controlling of the pressure valve continuously clamps the artery at its zero transmural state. Time series adapted from [31].

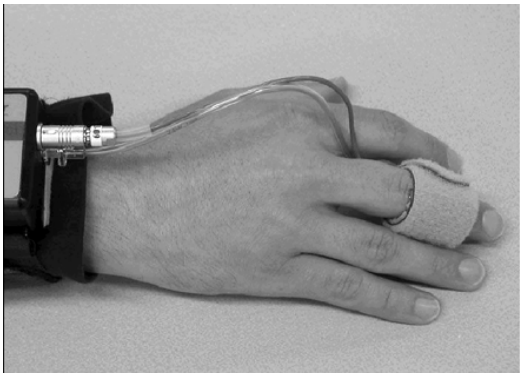

Figure 2.13: Implementation of the volume-clamp method in a commercial device (Finapres Medical Systems, Amsterdam, The Netherlands) [32].

2.6. Blood pressure measurement by Pulse Wave Velocity techniques

An alternative family of techniques to non-invasively assess blood pressure is that derived from Pulse Wave Velocity (PWV) measurements. As depicted by Figure 2.6 these techniques provide optimal performance in ambulatory scenarios: by being strictly non-occlusive, they create no disturbances to subjects and are thus perfectly adapted to 24h monitoring. Unfortunately the performance according to clinical criteria appear to be sub-optimal at the current development status of the technology.

Because PWV techniques will be at the center of this thesis research, a comprehensive analysis of the phenomena and clinical and technical implications of measuring PWV is now provided. Section 2.6.1 initiates the discussion with a formal definition of the PWV parameter. Section 2.6.2 provides theoretical evidence on the relationship between PWV and arterial stiffness. Section 2.6.3 studies clinical aspects and applications of PWV, going from the non-invasive assessment of arterial stiffness to the generation of cardiovascular risk factor markers. Section 2.6.4 provides a comprehensive summary of the state of the art in PWV measuring techniques, and Section 2.6.5 analyses how blood pressure estimates are to be derived from PWV measurements.

2.6.1. Definition of Pulse wave velocity

In cardiovascular research and clinical practice, PWV refers to the velocity of pressure pulses that propagate along the arterial tree. In particular, one is interested in those pressure pulses generated during left ventricular ejection: at the opening of the aortic valve, the sudden rise of aortic pressure is absorbed by the elastic aorta walls. Subsequently a pulse wave naturally propagates along the aorta exchanging energy between the aortic wall and the aortic blood flow (Figure 2.14).

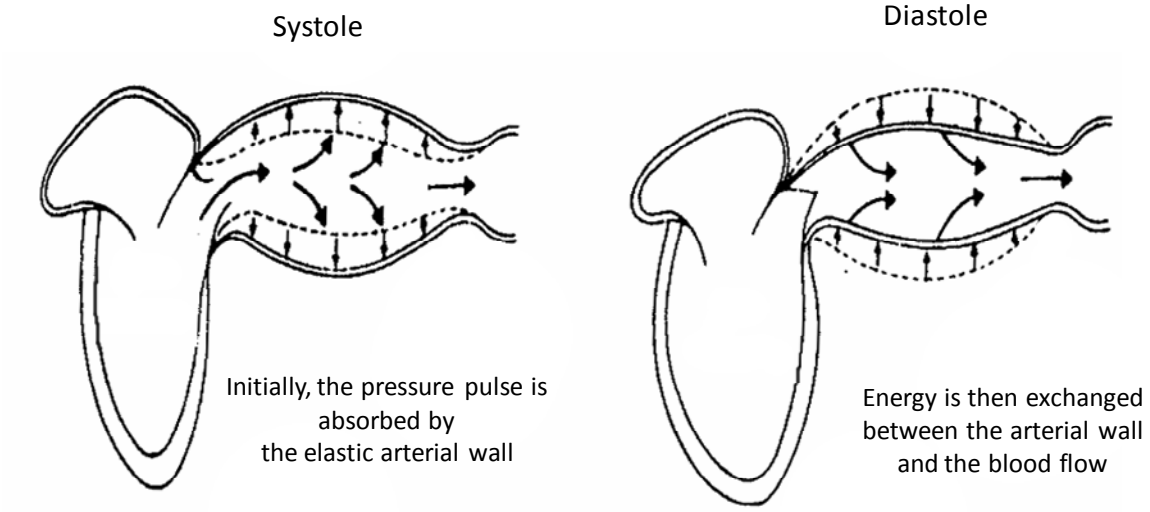

Figure 2.14: Genesis of pressure pulses: after the opening of the aortic valve the pulse propagates through the aorta exchanging energy between the aortic wall and the blood flow. Adapted with permission from [33].

At each arterial bifurcation, a fraction of the energy is transmitted to the following arteries, while a portion is reflected backwards. Note that one can easily palpate the arrival of arterial pressure pulses at any superficial artery, such as the temporal, carotid or radial artery: already in the year 1500, traditional chinese medicine performed clinical diagnosis by palpating the arrival of pressure pulses at the radial artery [34]. But why do clinicians nowadays gather interest in the velocity of such pulses, and especially in the aorta? The reason is that the velocity of propagation of aortic pressure pulses depends on the elastic and geometric properties of the aortic wall. We will show later that while arterial stiffness is difficult to measure non-invasively, PWV is nowadays available *in vivo* to clinicians. Hence, the PWV parameter is an easily-accessible potential surrogate for the constitutive properties of the arterial wall.

2.6.2. Pulse wave velocity and stiffness: the Moens-Korteweg equation

It has already been stated that modifications of the biomechanical properties of the arterial wall will induce changes at the velocity at which pressure pulses travel along it. The goal of the current section is to provide a simple mathematical model supporting this relationship. In particular, the proposed model [35] aims at establishing the relationship between PWV and biomechanical characteristics such as wall stiffness, wall thickness and arterial diameter via the commonly-known Moens-Korteweg equation.

The derivation of the equation relies on a mass model of a volume of blood moving through an arterial segment (Figure 2.15), as well as on a model of the biomechanics of the arterial wall (Figure 2.16). Both models assume that the volume of blood V induces a flow Q while undergoing a pressure P. The geometry of the models is defined by an arterial length dx, an internal arterial radius R, a constant internal area A, and an arterial wall thickness h. Blood density is assumed to be ρ, wall shear stress τ, and wall circumferential stress σ_θ.

The Moens-Korteweg derivation starts by imposing the law of mass conservation, *i.e.*:

$$Q_{in} - Q_{out} = \frac{dV}{dt}$$

$$Q - (Q + dQ) = \frac{d(Adx)}{dt}$$

$$-dQ = \frac{dA}{dt}dx$$

$$\frac{dQ}{dx} + \frac{dA}{dt} = 0$$

Equation 4

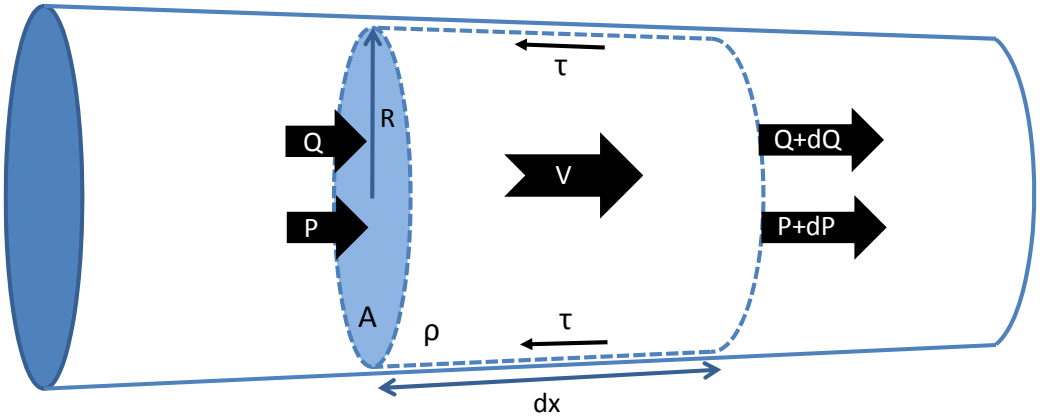

Figure 2.15: Geometrical and mass model of a volume of blood moving along an artery. R: arterial radius, dx: arterial length, P: influx pressure, $P + dP$: outflux pressure, Q: influx blood flow, Q+dQ: outflux blood flow, V: blood velocity, τ: wall shear stress, and ρ: blood density.

Imposing as well the law of momentum conservation (Newton's law) one obtains:

$$\sum F_x = m\, a_x$$

$$\big(P - (P + dP)\big)A - \tau 2\pi R dx = m\, a_x$$

$$\big(P - (P + dP)\big)A - \tau 2\pi R dx = \rho A dx \frac{dV}{dt}$$

$$-\frac{dP}{dx}A - \tau 2\pi R = \rho A \frac{dV}{dt}$$

Equation 5

Assuming now wall shear stress (friction) to be negligible, and assuming A to be constant along dx (compared to V) Equation 5 becomes:

$$-\frac{dP}{dx}A = \rho \frac{dAV}{dt}$$

$$-\frac{dP}{dx}A = \rho \frac{dQ}{dt}$$

$$\frac{dQ}{dt} = -\frac{A}{\rho}\frac{dP}{dx}$$

Equation 6

We define now arterial compliance to be $C_A = \frac{dA}{dP}$. Recalling the mass conservation expression of Equation 4, and assuming C_A to be constant in time, one obtains:

$$\frac{dA}{dt} + \frac{dQ}{dx} = 0$$

$$\frac{dA}{dP}\frac{dP}{dt} + \frac{dQ}{dx} = 0$$

$$C_A \frac{dP}{dt} + \frac{dQ}{dx} = 0$$

$$C_A \frac{\partial^2 P}{\partial t^2} + \frac{\partial^2 Q}{\partial x \partial t} = 0$$

Equation 7

We rewrite now the momentum conservation expression of Equation 6 in order to contain the $\frac{\partial^2 Q}{\partial x \partial t}$ term as well, assuming A to be a constant arterial section:

$$\frac{\partial^2 Q}{\partial x \partial t} = -\frac{A}{\rho}\frac{\partial^2 P}{\partial x^2}$$

Equation 8

Finally including the modified momentum expression of Equation 8 into the modified mass expression of Equation 7, one obtains the following wave equation:

$$\frac{\partial^2 P}{\partial t^2} = \frac{A}{\rho C_A}\frac{\partial^2 P}{\partial x^2}$$

Equation 9

Therefore, according to the proposed model, a pressure wave $P(x,t)$ travels along an arterial segment obeying a wave equation, *i.e.*

$$\frac{\partial^2 P}{\partial t^2} = c^2 \frac{\partial^2 P}{\partial x^2}$$

Equation 10

with a propagation speed determined by:

$$c = \sqrt{\frac{A}{\rho C_A}}$$

Equation 11

The propagation speed of a pressure pulse travelling along an artery is thus expected to be inversely related to the arterial compliance, *i.e.* the more compliant the artery the slower the pulse will propagate. Equation 11 is known as Bramwell-Hill equation [35].

Developing further the definition of arterial compliance one obtains:

$$C_A = \frac{dA}{dP} = \frac{d(\pi R^2)}{dP} = 2\pi R \frac{dR}{dP}$$

Equation 12

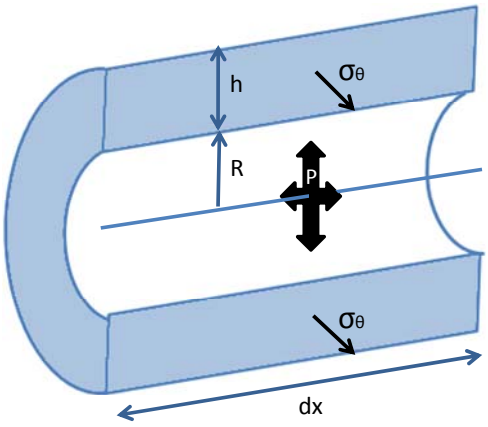

Figure 2.16: Biomechanical model of the arterial wall. R: internal arterial radius, h: thickness, dx: segment length, σ_θ: wall circumferential stress, and P: arterial pressure.

And by inserting Equation 12 into the Equation 11 a modified Bramwell-Hill equation is obtained:

$$c = \sqrt{\frac{R}{2\rho}\frac{dP}{dR}}$$

Equation 13

Unfortunately, both the Bramwell-Hill equation and its modified version are unable to predict the propagation speed of pressure pulses along an artery from the stiffness of its wall. In the following we aim at expressing the term $\frac{dP}{dR}$ appearing in the modified Bramwell-Hill equation as a function of the wall Young's modulus.

Based on the arterial wall biomechanical model proposed by Figure 2.16, we start by applying the momentum conservation law to all tangential components:

$$\sum F_\theta = 0$$

$$P2R\mathrm{dx} - 2\sigma_\theta h\mathrm{dx} = 0$$

$$\sigma_\theta = \frac{PR}{h}$$

Equation 14

obtaining the so-called Laplace law. By differentiating Equation 14 one obtains:

$$d\sigma_\theta = \frac{RdP}{h} + \frac{PdR}{h} - \frac{PRdh}{h^2}$$

Equation 15

Assuming the arterial wall to be incompressible and thin, *i.e.* $h \ll R$,

$$\pi(R+h)^2 - \pi R^2 = \gamma$$

$$h(2R+h) = \gamma'$$

$$hR = \gamma''$$

$$dr\ h = -r\ dh$$

Equation 16

one obtains a differenced Laplace law in the form:

$$d\sigma_\theta = \frac{RdP}{h} + 2\frac{PdR}{h}$$

Equation 17

At this point, we recall the concept of Young's elastic modulus and we aim at introducing it into Equation 17. The Young's elastic modulus describes the measured arterial wall stress (σ_θ) when a given strain (ε) is applied to it, *i.e.*:

$$E_{inc} = \frac{d\sigma_\theta}{d\varepsilon} = \frac{d\sigma_\theta}{dR/_R}$$

Equation 18

Merging now the geometrical description of the arterial wall (Equation 17) together with the introduced biomechanical variable of Equation 18, one obtains:

$$E_{inc} = \frac{R^2 dP}{hdR} + 2\frac{PR}{h}$$

$$E_{inc} = \frac{R^2 dP}{hdR} + 2\sigma_\theta$$

Equation 19

Assuming now the σ_θ term to be negligible, one obtains the searched relationship between $\frac{dP}{dR}$ and Young's modulus of the arterial wall:

$$E_{inc} = \frac{R^2}{h}\frac{dP}{dR}$$

Equation 20

Finally introducing the Young's modulus expression of Equation 20 into the modified Bramwell-Hill expression of Equation 13, one obtains the so-called Moens-Korteweg equation:

$$c = \mathrm{PWV} = \sqrt{\frac{hE_{inc}}{2\rho R}}$$

Equation 21

Accordingly, the speed of propagation of a pressure pulse along the arterial wall depends on:

- the biomechanics properties of the wall: and in particular its stiffness E_{inc} or Young's modulus,
- the geometry of the wall, and in particular its thickness *h* and radius R,
- and the density of blood.

Even though the derivation of the Moens-Korteweg model relies on several (and severe) simplifications, it provides an intuitive insight on the propagation phenomenon in arteries predicting that the stiffer the artery (increased E_{inc}) the faster a pressure pulse will propagate along it. Therefore, for large elastic arteries such the aorta where the thickness to radius ratio is almost invariable, PWV is expected to carry relevant information related to arterial stiffness.

2.6.3. Clinical aspects of Pulse Wave Velocity

Recall that the present thesis aims at exploiting PWV as a technique to non-invasively and non-occlusively measure blood pressure. Nevertheless, it is of capital importance to understand the clinical context in which PWV techniques have been historically developed. Therefore this section reviews the clinical aspects and implications of PWV measurements, and in particular, in relation to the assessment of arterial stiffness.

Cardiovascular disease is the leading cause of morbidity and mortality in western countries and is associated with changes in the arterial structure and function. It is today generally accepted that arterial stiffening has a central role in the development of such diseases. Aortic PWV is considered the gold standard for the assessment of arterial stiffness and is one of the most robust parameters for the prediction of cardiovascular events [36]. Because the structure of the arterial wall differs between the central (elastic) and the peripheral (muscular) arteries, several PWV values are encountered along the arterial tree, with increasing stiffness when moving to the periphery. Because carotid-to-femoral PWV is considered as the standard measurement of aortic arterial stiffness, we will refer to it as simply PWV.

In the following we review the most important factors determining PWV of elastic arteries, we analyse the pathophysiological consequences of increased arterial stiffness and, we highlight the clinical relevance of PWV as an independent marker of cardiovascular risk.

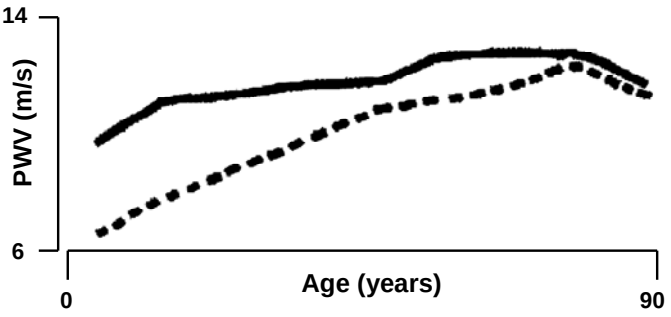

Figure 2.17: The dependency of PWV with age for central elastic arteries (dashed line) and peripheral muscular arteries (continuous line). Adapted from [37].

Major determinants of Pulse Wave Velocity

Before elucidating the role that PWV plays in the generation and diagnosis of pathological situations, it is necessary to understand which are its determinant factors under normal conditions. It is currently accepted that the four major determinants of PWV are age, blood pressure, gender and heart rate.

Age affects the wall propreties of central elastic arteries (aorta, carotid, iliac) in a different manner than in muscular arteries (brachial, radial, femoral, popliteal). With increasing age the pulsatile strain breaks the elastic fibers, which are replaced by collagen [38]. These changes in the arterial structure lead to increased arterial stiffness, and consequently to increased central PWV (Figure 2.17). On the other hand, there is only little alteration of distensibility of the muscular, *i.e.* distal, arteries with age [37, 39]. This fact supports the use of generalized transfer functions to calculate the central aortic pressure wave from the radial pressure wave in adults of all ages, as will be described in 2.6.4.

Arterial blood pressure is also a major determinant of PWV. Increased blood pressure is associated with increased arterial stiffness and vice versa. Ejection of blood into the aorta generates a pressure wave that travels along the whole arterial vascular tree. A reflected wave that travels backwards to the ascending aorta is principally generated in the small peripheral resistance arterioles. With increasing arterial stiffness both the forward and the reflected waves propagate more rapidly along the vessels. Consequently, instead of reaching back the aorta during the diastole, the reflected pulse wave reaches it during the systole. This results in an increase of aortic pressure during systole and reduced pressure during diastole, thus leading to an increase of the so-called Pulsatile Pulse (PP) parameter (Figure 2.18). Asmar studied large untreated populations of normotensive and hypertensive subjects and found that the two major determinants of PWV were age and systolic blood pressure in both groups [36]. This result confirms the close interdependence between systolic blood pressure and arterial stiffness.

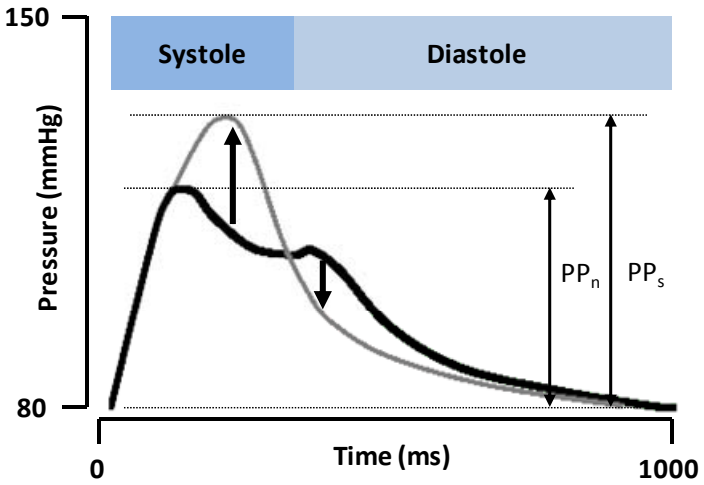

Figure 2.18: Consequences of increased arterial stiffness on central blood pressure: increase of systolic and decrease of diastolic central pressures. Pulsatile Pressure is defined as the difference of both pressure amplitudes. PP_n stands for PP under normal conditions and PP_s stands for PP understiff conditions.

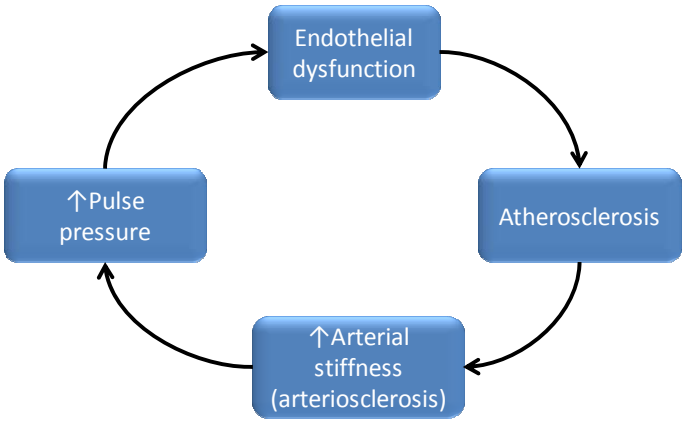

Figure 2.19: Vicious circle of events resulting from endothelial dysfunction and augmented arterial stiffness.

Concerning gender, studies in children revealed no gender difference in PWV, whereas in young and middle age, healthy adult men displayed higher PWV values compared to women [40, 41]. Indeed premenopausal women show lower carotid-radial PWV values than age-matched men, but carotid-femoral PWV is found to be similar. Once women become postmenopausal, PWV values become similar to those of age-matched men [40].

Heart rate is related to PWV through two independent mechanisms. Firstly, heart rate influences PWV because of the frequency-dependant viscoelasticity of the arterial wall: if heart rate increases, the time allowed to the vessels to distend is reduced, resulting in an increased rigidity of the arterial wall. Hence, increasing rate is associated with increasing arterial stiffness. In a recent study [42], it was showed that particularly in hypertensive patients increased heart rate was one of the major determinants of accelerated progression of arterial stiffness. Secondly, heart rate is related to PWV through the influence of the sympathetic nervous system: sympathetic activation is associated with increased stiffness of

the arteries [43] due to an increase in heart rate, blood pressure and smooth muscle cells tonus.

Pathophysiology of increased arterial stiffness

Up to this point we simply outlined that increased arterial stiffness appears to be normally associated to factors such as aging and blood pressure, among others. As natural as it seems, one might then wonder, why do we need to keep arterial stiffness under controlled (low) values? We will answer this question backwards: what would happen if we did not do so? In other words, we are interested in understanding the pathophysiological consequences of increased arterial stiffness.

Firstly we describe the role of arterial stiffness in the development of endothelial dysfunction. Endothelial dysfunction is the first step in the development of atherosclerosis and plays a central role in the clinical emergence and progression of atherosclerotic vascular disease (Figure 2.19). The endothelium plays not only an important role in atherogenesis but also in the functional regulation of arterial compliance since endothelial cells release a number of vasoactive mediators such as the vasodilatator nitric oxide (NO) and the vasoconstrictor endothelin. The complex interplay between endothelial function and arterial stiffness leads to a vicious cycle of events [44], as illustrated in Figure 2.19.

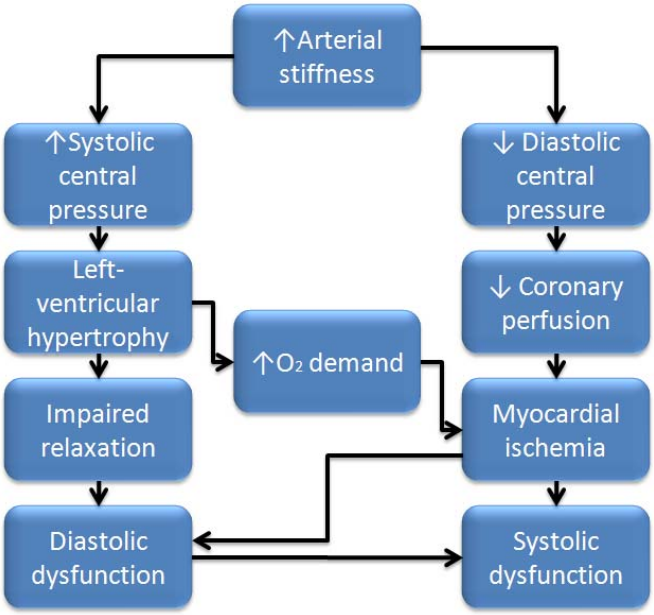

Figure 2.20: Effects of increased arterial stiffness on the myocardium and its function.

Increased arterial stiffness is also an important determinant of myocardium and coronary perfusions. In Figure 2.18 we already described the mechanism through which increasing arterial stiffness leads to augmented central PP, *i.e.* the difference between systolic and diastolic aortic pressures. The increase in central systolic pressure is thus associated with an increased afterload, which if persistent, promotes the development of left ventricular (LV) hypertrophy, an independent cardiovascular risk factor [45, 46]. Conversely, the decrease in central diastolic pressure compromises myocardial blood supply, particularly in patients with coronary artery stenosis. However, the increased LV-mass induced by the augmented afterload will require an increased oxygen supply. Therefore, a mismatch between oxygen

demand and supply may occur, leading to myocardial ischemia, LV diastolic and later systolic dysfunction. The full mechanism is illustrated in Figure 2.20.

Finally, the widening of central PP induced by increasing arterial stiffness may affect the vascular bed of several end-organs, particularly of brain and kidney. Because both organs are continually and passively perfused at high-volume flow throughout systole and diastole, and because their vascular resistance is very low, pulsations of pressure and flow are directly transmitted to the relatively unprotected vascular bed. By contrast, other organs if exposed to increased PP may protect themselves by vasoconstriction [47]. This unique situation predisposes the brain and kidney to earlier micro- and macrovascular injuries [48-50].

Relevance of Pulse Wave Velocity in clinical conditions

We already described the factors that modify arterial stiffness in normal conditions. We also reviewed the consequences of an increase of arterial stiffness to endothelial function, coronary perfusion and possible damages to heart muscle, brain and kidneys. We are interested in reviewing now the broad uses of PWV as an independent cardiovascular risk factor and its interaction with the others classical risk factors such as arterial hypertension, diabetes mellitus, and dyslipidemia. The independent predictive value of PWV for cardiovascular and all-cause mortality is finally underlined.

Structural arterial abnormalities are already observed at an early stage of hypertension. Changes in the structure of the arterial wall, particularly of the matrix and the three-dimensional organization of the smooth muscle cells, have an important impact in determining arterial stiffness. Studies of white-coat hypertension [51] and borderline hypertension [52] showed higher values of PWV compared to controls. Moreover, for a similar blood pressure, PWV was higher in patients than in controls, suggesting that the increased PWV was not only due to the elevated blood pressure but also to some structural changes of the arterial wall. As already mentioned, increased arterial stiffness leads to increased central systolic blood pressure, augmented afterload and ultimately left ventricular hypertrophy (Figure 2.20) which is itself a major cardiovascular risk factor [45, 53]. Arterial stiffness and its associated augmented PWV is now recognized as an independent marker of cardiovascular risk [54, 55] especially in hypertensive patients [56].

Diabetes mellitus is one of the major cardiovascular risk factors and has been associated with premature atherosclerosis. There are numerous studies showing that both patients suffering from type 1 diabetes [57] and type 2 diabetes [58, 59] have an increased arterial stiffness compared to controls. The increase in arterial stiffening in patients with type 1 and type 2 diabetes mellitus is evident even before clinical micro- and macrovascular complications occur [60, 61], being already present at the stage of impaired glucose tolerance [62]. Moreover, as in hypertensive patients, increased aortic PWV is identified as an independent predictor of mortality in diabetics [58].

Beyond its predictive value of morbidity, aortic stiffness appears to be relevant because of its independent predictive value for all-cause and cardiovascular mortality, in patients with arterial hypertension [55], older age [63-65] and even in the general population [54]. As an

example, Figure 2.21 demonstrates PWV to be a BP-independent cardiovascular risk factor for patients with end-stage renal disease.

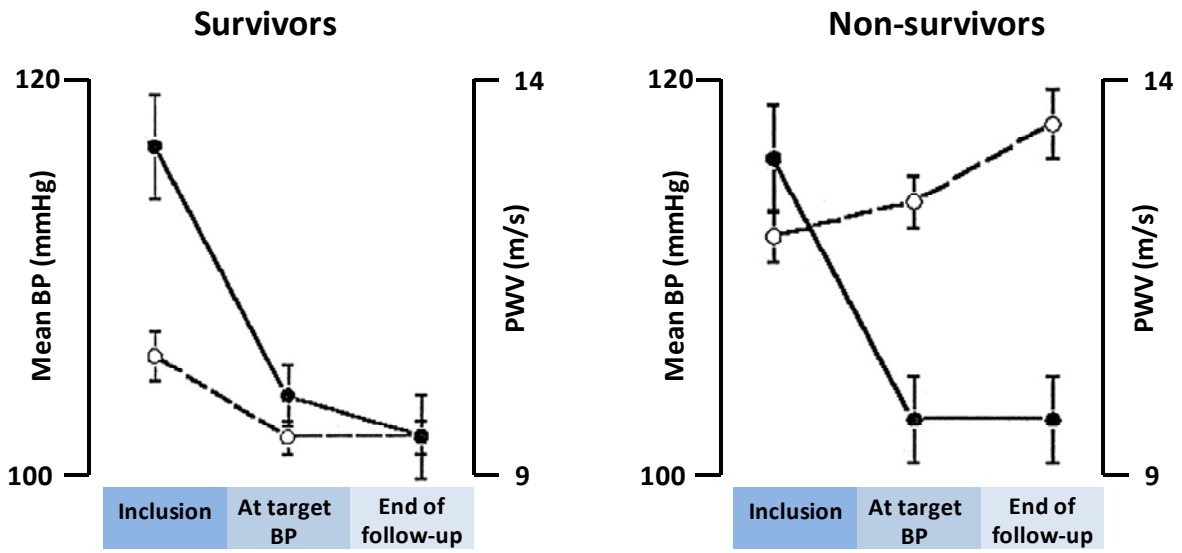

Figure 2.21: Changes in mean BP (solid circles) and aortic PWV (open circles) of patients with end-stage renal disease for survivors and non-survivors: despite achievement of target BP non-survivors showed no improvement or even an increase in PWV, demonstrating on the one hand the presence of a pressure-independent component of PWV, and on the other hand, the relevance of PWV as an independent predictor for mortality. Adapted from [66].

The association between lipids and arterial stiffness has been studied since the seventies, but the results are so far controversial. In patients suffering from coronary artery disease (CAD), an association between increased arterial stiffness and higher LDL has been proved [67]. On the other hand, in the general population the results regarding the relationship between LDL and arterial stiffness are controversial and some studies have reported a lack of association between total cholesterol and arterial stiffness [68].

Acute smoking is associated with increased arterial stiffness in healthy individuals and several patients subgroups, including normotensive, hypertensive and CAD. Studies on the chronic effects of smoking demonstrated contradictory results. However, the largest studies showed that chronic cigarette smoking was associated with increased PWV both in normotensive and hypertensive subjects [69, 70].

Arterial hypertension and arterial stiffness induce the same end-organ damages such as coronary artery disease (CAD), cerebrovascular disease (CVD), peripheral artery disease (PAD) and chronic kidney disease (CKD) [56]. Many studies showed an association between increased PWV and the severity of CAD [71, 72], CVD [48, 49, 63], PAD [73] and CKD [40, 74].

2.6.4. Non-invasive measurement of central Pulse Wave Velocity

In the preceding sections we pointed out the need of including a vascular-related parameter into ambulatory monitoring, and we highlighted the clinical relevance of PWV as a surrogate measurement of arterial stiffness. In this section we analyse the strategies and devices that have been so far developed to measure PWV *in vivo*. Although in some cases these

techniques rely on rather simplistic physiologic and anatomic approximations, their commercialization has triggered the interest in the diagnostic and prognostic uses of PWV. For the sake of clearness, Table 2.7 summarizes the different approaches described in this section.

In general, given an arterial segment of length D, we define its PWV as:

$$\mathrm{PWV} = \frac{\mathrm{D}}{\mathrm{PTT}}$$

Equation 22

where PTT is the so-called Pulse Transit Time, *i.e.* the time that a pressure pulse will require to travel through the whole segment. Formally PTT is defined as:

$$\mathrm{PTT} = \mathrm{PAT_d} - \mathrm{PAT_p}$$

Equation 23

where $\mathrm{PAT_p}$ corresponds to the arrival time of the pressure pulse at the proximal (closer to the heart) extremity of the artery, and $\mathrm{PAT_d}$ corresponds to the arrival time of the pressure pulse at its distal (distant to the heart) extremity.

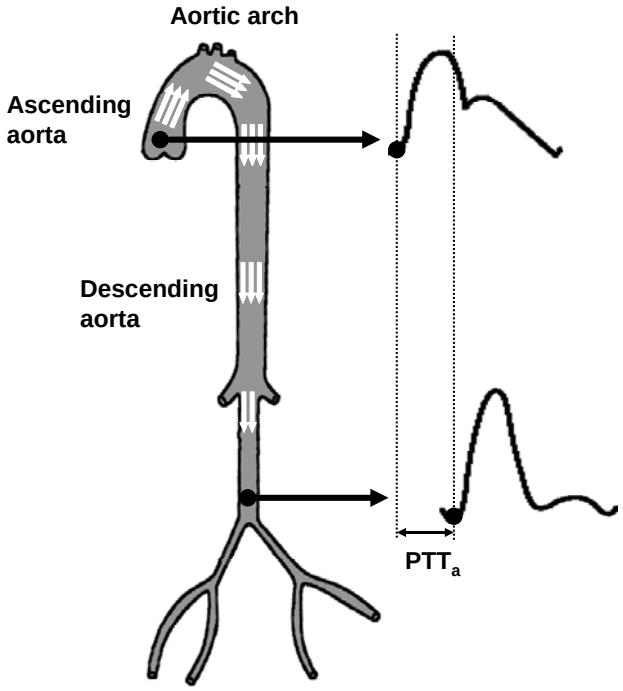

Figure 2.22: Aortic PWV is defined as the average velocity of a pressure pulse when travelling from the aortic valve, through the aortic arc until it reaches the iliac bifurcation.

In particular, concerning the aorta, we define PWV as the average velocity of a systolic pressure pulse travelling from the aortic valve (proximal point) to the iliac bifurcation (distal point), as Figure 2.22 illustrates. Note that this definition concerns the propagation of the pulse through anatomically rather different aortic segments, namely the ascending aorta, the aortic arch and the descending aorta. Accordingly, we re-define aortic PWV as:

$$\mathrm{PWV} = \frac{\mathrm{D_{asc}} + \mathrm{D_{arch}} + \mathrm{D_{desc}}}{\mathrm{PTT_a}}$$

Equation 24

Hence, the *in vivo* determination of aortic PWV is a two-step problem: first one needs to detect the arrival times of a pressure pulse at both the ascending aorta and the iliac bifurcation, and secondly one needs to precisely measure the distance travelled by the pulses.

A first group of aortic PWV measurement methods corresponds to those approaches that measure transit times in the aorta in a straight-forward fashion, that is, without relying on any model-based consideration. Because the aorta is not easily accessible by neither optical nor mechanical means, the strategy is to detect the arrival of a pressure pulse at two substitute arterial sites, remaining as close as possible to the aorta [75]. Starting from the aorta and moving to the periphery, the first arteries that are accessible are the common carotid arteries (at each side of the neck) and the common femoral arteries (at the upper part of both thighs, near the pelvis). This family of devices assumes thus the carotid-to-femoral transit time to be the best surrogate of the aortic transit time. Currently three commercial automatic devices based on this assumption are available: the Complior (Artech Medical, Paris, France), the SphygmoCor (AtCor Medical, New South Wales, Australia) illustrated in Figure 2.11, and the PulsePen (DiaTecne, Milano, Italy). While Complior simultaneously records the arrival of a pressure pulse at the carotid and femoral arteries by means of two pressure sensors (Figure 2.23), Sphygmocor and PulsePen require performing the two measurements sequentially by means of a single hand-held tonometer. A simultaneously recorded ECG supports the post-processing of the data obtained from both measurements (Figure 2.24). It has been suggested that because measurements are not performed on the same systolic pressure pulses, the SphygmoCor might introduce artifactual PTT variability [76]. Unfortunately, there is so far no consensus on whether the transit times obtained by Complior and SphygmoCor display significant differences [76, 77]. Concerning the estimation of the travelled distance D, each manufacturer provides different and inconsistent recommendations on how to derive D from superficial morphological measurements with a tape [76]. Regrettably Complior, SphygmoCor and PulsePen require the constant presence of a skilled operator who manually localizes the carotid and femoral arteries and holds the pressure sensors during the examination.

A second group of devices estimate aortic transit time based on wave reflection theory. It is generally accepted [35] that any discontinuity on the arterial tree encountered by a pressure pulse traveling from the heart to the periphery (downstream) will create a reflected wave on the opposite direction (upstream). Main reflection sites in humans are

high-resistance arterioles and major arterial branching points. In particular, the iliac bifurcation at the distal extremity of the descending aorta has empirically been shown to be a main source of pulse reflections [78].

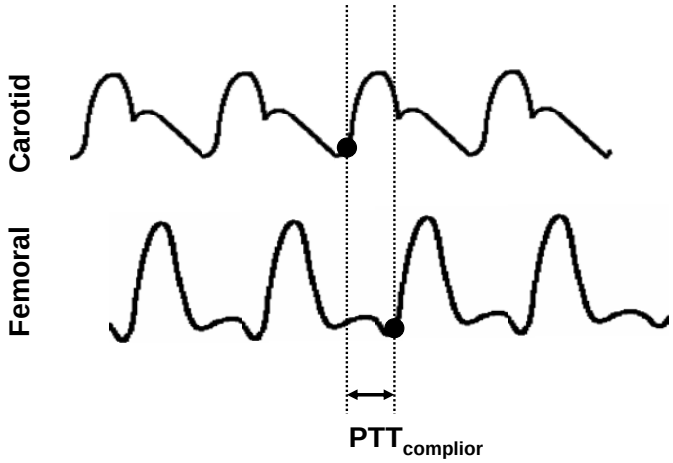

Figure 2.23: Pulse transit time (PTT) as measured by Complior. The arrival time of a pressure pulse is simultaneously detected on the carotid and femoral artery. Complior implements as well a correlation-based PTT estimation.

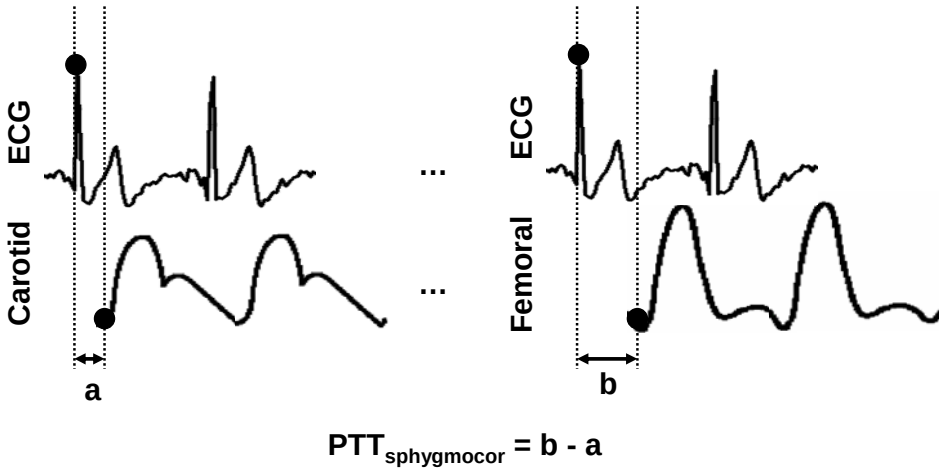

Figure 2.24: Pulse transit time (PTT) as measured by SphysgmoCor. The delay between the R-Wave on the ECG and the arrival time of a pressure pulse is sequentially measured on the carotid and the femoral arteries. Both measurements are further combined to obtain a single PTT value.

Consequently, a pulse pressure generated at the aortic valve is expected to propagate downstream through the aorta, to reflect at the iliac bifurcation and to propagate upstream towards the heart, reaching its initial point after Tr seconds (Figure 2.25). Commonly depicted as Time to Reflection, Tr is related to the aortic length (D) and the aortic pulse wave velocity as:

$$\mathrm{Tr} = \frac{2\mathrm{D}}{\mathrm{PWV}}$$

Equation 25

Even though the concept of a unique and discrete reflection point in the arterial tree is not widely accepted and is currently the source of fervent discussions [79], PWV values derived from the time to reflection method have been shown to be at least positively correlated to PWV measured by Complior, r=0.69 [80] and r=0.36 [76].

Obviously a main issue is how to record aortic pressure pulses non-invasively. Two approaches have been proposed so far. A first device, Arteriograph (TensioMed, Budapest, Hungary), records a sequence of pressure pulses at the upper arm by inflating a brachial cuff above systolic pressure, typically 35 mmHg. The brachial pressure waveform is then simply assumed to be a surrogate of the aortic one. Regardless of its manifest lack of methodological formalism, Arteriograph is so far the unique fully automatic and unsupervised commercial available device. Similarly, some recent studies aim at analyzing pressure pulses recorded at the finger to obtain similar results [81]. A second device, SphygmoCor (AtCor Medical, New South Wales, Australia), records pressure pulses at the radial artery by a hand-held tonometer and then estimates an associated aortic pressure pulse by applying a generalized transfer function. In brief, the generalized transfer function

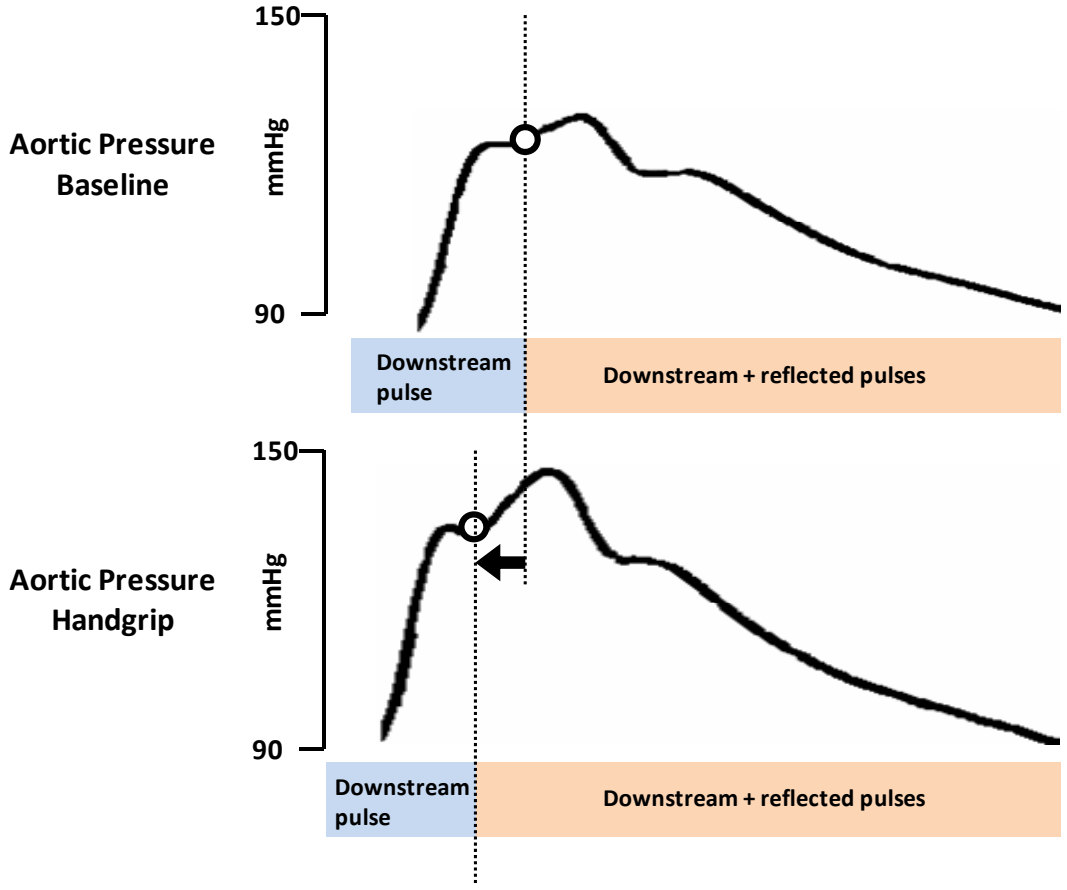

Figure 2.25: Time to reflection (Tr) is defined as the arrival time of a pressure pulse that has been reflected in the arterial tree and travels back towards the heart. This example illustrates an important shortening of Tr for a male adult when performing a handgrip effort. During the sustained handgrip, mean arterial pressure is augmented, increasing the stiffness of the aorta and thus aortic PWV. Consequently, the reflected pulse reaches the aortic valve prematurely: Tr is shifted to the left in the bottom pressure pulse.

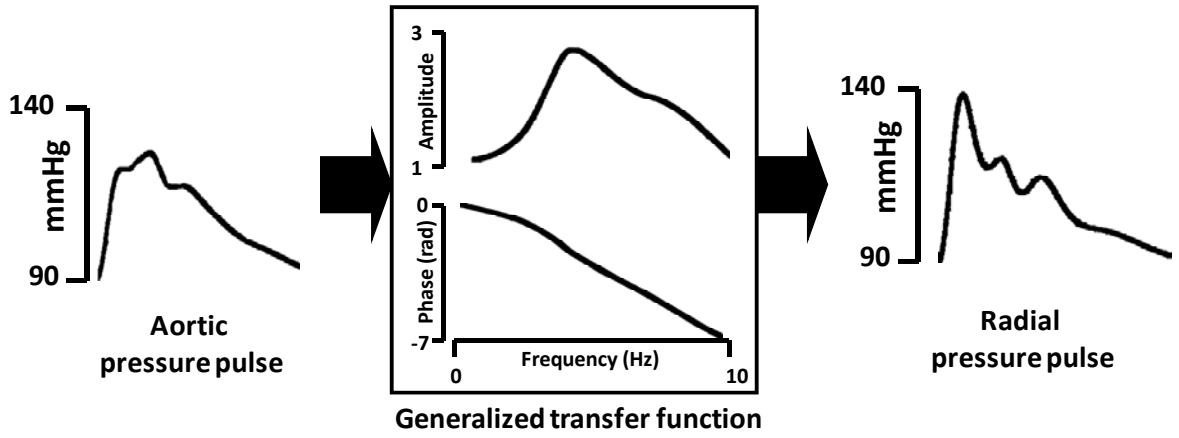

Figure 2.26: Example of aortic pressure pulse, radial pressure pulse and the generalized transfer function that relates them. Adapted from [82].

approach relies on a series of empirical studies conducted during the 90s in which it was proven that the relationship between aortic and radial pressure pulses is consistent among subjects and unaffected even by aging and drug action [83]. Consequently, transfer functions provide a method for universally estimating aortic pressure pulses from radial artery measurements in a non-invasive fashion. Figure 2.26 illustrates the modulus and phase of the widely accepted aortic-to-radial general transfer function [82]. Large population studies [84] and numerical models of the arterial tree [85] have shown that the generalized transfer function is indeed consistently unchanged for frequencies below 5 Hz.

A third group of approaches comprises those developments based on the R-wave-gated pulse transit time. In brief, this technique exploits the strength of the ECG signal on the human body, and assumes its R-wave to trigger the genesis of pressure pulses in the aorta, at time $T_{R\text{-}wave}$. Then, by detecting the arrival time of a pressure pulse on a distal location (PAT_d) one calculates:

$$\mathrm{PTT_{R\text{-}Wave}} = \mathrm{PAT_d} - \mathrm{T_{R\text{-}Wave}}$$

Equation 26

Unfortunately the physiological hypothesis relating $PTT_{R\text{-}wave}$ to PWV neglects the effects of cardiac isovolumetric contraction: indeed, after the onset of the ventricle depolarization (R-Wave in the ECG) left ventricles start contracting while the aortic valve remains closed. It

is only when the left ventricle pressure exceeds the aortic one, that the aortic valve opens and generates the aortic pressure pulse. The introduced delay is commonly known as Pre-Ejection Period (PEP) and depends on physiological variables such as cardiac preload, central arterial pressure, and cardiac contractibility [86]. Hence, $PTT_{R\text{-}wave}$ is to be corrected for the delay introduced by PEP as proposed in [87]:

$$\mathrm{PTT'_{R\text{-}Wave}} = \mathrm{PAT_d} - (\mathrm{T_{R\text{-}Wave}} + \mathrm{PEP})$$

Equation 27

Several strategies to assess PEP non-invasively are nowadays available, mainly based on the joint analysis of the ECG [88] and either an impedance cardiogram or a phono-cardiogram (see Section 2.7). Nevertheless, even obviating the PEP correction, $PTT_{R\text{-}wave}$ has been shown to be weakly correlated with PWV (r=0.37) [89] and systolic blood pressure (r=0.64). Concerning the distal detection of the pressure pulse arrival time (PAT_d), different approaches have been proposed so far. We describe here the most relevant ones. Novacor (Cedex, France) commercializes an ambulatory method to monitor PWV based on a fully automatic auscultatory approach: the so-called Qkd index. Qkd is defined as the time interval between the R-Wave on the ECG and the second Korotkoff sound detected on an inflated brachial cuff. The device is currently being used to evaluate long-term evolution of systemic sclerosis in large population studies [90]. A different technology, photo-plethysmography, is probably the approach that has given rise to the largest number of research developments and studies in the field (see Section 2.7.2 for a detailed description). Being non-obtrusive and cheap, this technology consists in illuminating a human perfused tissue with an infra-red light source and to analyse the changes in absorption due to arterial pulsatility. Each time a pressure pulse reaches the illuminated region, the absorption of light is increased due to a redistribution of volumes in the arterial and capillary beds. The analysis of temporal series of light absorption then allows the detection of the arrival of the pressure pulse. Regrettably, to obtain reliable photo-plethysmographic signals is not a simple task and, so far, only those body locations displaying very rich capillary beds have been exploited: namely the finger tips or phalanxes [91-94], the toes and the ear lobe.

Finally, an emerging non-invasive technique remains to be cited, although its implantation in ambulatory monitoring seems nowadays unfeasible: the phase-contrast MR imaging (PCMRI) [95]. PCMRI opens the possibility to perform local measurements of PWV for any given segment of the aorta, by simply defining two regions of interest on the image: a proximal and a distal region. By analysing the evolution of the regional blood flow velocity in each region, one determines the arrival times (PTT_p and PTT_d) of the pressure pulse. Because the distance between both aortic regions (D) can now be precisely measured, this approach is expected to provide highly accurate regional aortic PWV measurements. PCMRI was already introduced in the 90s [96], but the recent advances in MRI capturing rates seem to be encouraging the apparition of new studies [97-99]. Fitting in the same category, some studies have been published on the assessment of PAT_d by means of ultrasound Doppler probes [100].

Note that we have intentionally skipped from our analysis some works that have been performed on the tracking of pressure pulses artificially induced to the arterial wall by mechanical oscillators [101]. Similarly, we have excluded those works based on the analysis of pressure-diameter and flow-diameter measurements [35]. Both techniques have been

discarded because of the fact that they require respectively inducing mechanical excitations to the CVS, or performing compliance measurements of given arterial segments. Such approaches are considered out of scope of the current thesis.

Table 2.7: Summary of state-of-the-art approaches to measure central PWV. Detailed descriptions are available on the text. PTT stands for Pulse Transit Time, *D* for distance, and AMB for ambulatory compatibility.

Segments of the arterial tree	Method	Measurements of PTT and *D*	AMB	Commercial device
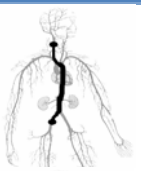	Carotid to Femoral PTT (simultaneous)	PTT is measured by two pressure sensors placed over the carotid and femoral arteries. *D* is estimated from superficial morphologic measurements.	No	Complior
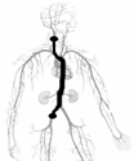	Carotid to Femoral PTT (sequential)	PTT is measured by a single pressure sensor placed sequentially over the carotid and femoral arteries. ECG is used for synchronization purposes. *D* is estimated from superficial morphologic measurements.	No	SphygmoCor Pulse Pen
	Time to reflection, from brachial pressure pulse	PTT is measured by extracting Tr from the brachial pressure pulse waveform recorded by a brachial obtrusive cuff. *D* is estimated from superficial morphologic measurements.	Yes	Arteriograph
	Time to reflection, from radial pressure pulse (generalized transfer function)	The aortic pressure pulse is estimated by applying a generalized transfer function to a radial pressure pulse waveform recorded by a handheld tonometer. PTT is measured as Tr. D is estimated from superficial morphologic measurements.	No	SphygmoCor
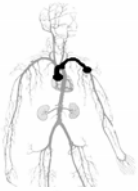	ECG to brachial pulse transfer time	PTT is approximated as the delay between the R-Wave at the ECG, and the arrival of the pressure pulse at the brachial artery, recorded by a brachial obtrusive cuff. *D* is estimated from superficial morphologic measurements	Yes	NovaCor
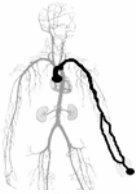	ECG to radial pulse transfer time	PTT is approximated as the delay between the R-Wave at the ECG, and the arrival of the pressure pulse at the digital artery, recorded by photo-plethysmography. *D* is estimated from superficial morphologic measurements	Yes	-
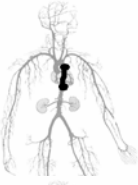	MR Imaging of aortic blood flow	PTT is measured by detecting the arrival of the pressure pulse at two or more different aortic sites, associated to different regions of interest in the PCMR images. *D* is accurately determined from the images.	No	-
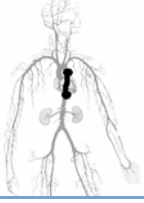	Sequential Doppler measurements of aortic blood flow	PTT is measured by detecting the arrival of the pressure pulse at two or more different aortic sites, by performing ECG-gated Doppler measurements. *D* is estimated from superficial morphologic measurements	No	-

2.6.5. Blood pressure measurement by pulse wave velocity techniques

During the last 20 years a lot has been written on the use of PWV as a surrogate of arterial blood pressure (BP). The current lack of non-occlusive devices for measuring BP (see Section 2.2) has probably awakened the interest on this particular use of the PWV parameter. Yet, no commercial device based on the PWV principle has so far been released on the market. This section provides an overview of two generations of PWV-based techniques to measure BP (an illustrated synopsis is given by Figure 2.27). In summary:

- Generation #1a corresponds to the state of the art in BP monitoring, and relies on the measurement of PWV at peripheral arterial sites (finger, ear, ...), and on intermittent calibration phases to be performed via an inflation brachial cuff.
- Generation #1b is a modified version of this first generation of techniques. This approach has been first suggested during the current thesis works. Although it relies as well on the measurement of PWV at peripheral arterial sites, it replaces brachial cuff inflations by a non-occlusive strategy to compensate for vasomotion effects.
- Generation #2 is the core technology covered by this thesis. This technique aims at measuring PWV at very central elastic sites, typically at the aorta, and avoids the need of any subsequent recalibration or compensation of vasomotion phenomena.

In the following, a detailed description of the different generations is provided.

First generation of PWV-based techniques: generation #1a

Historically, the dependency of PWV with respect to blood pressure was already observed in 1905 by Frank, although the underlying mechanism was not fully understood until half a century later [101]. We already described that PWV depends on arterial stiffness, and we introduced a mathematical model for this relationship: the Moens-Korteweg equation (Equation 21). Accordingly, the greater the stiffness of an artery (E_{inc}), the faster a pressure pulse will propagate through it. Assume now that we increase the transmural pressure of the arterial wall, for instance by increasing systemic blood pressure. Because of the elastic properties of the wall, the artery will increase in diameter and decrease in thickness, while becoming stiffer. Additionally, at a certain point the recruitment of collagen fibers will start and will enhance the stiffness in a highly non-linear way [101]. Hence, the stiffness of the arterial wall will depict a strong dependence to its transmural pressure [102].

Putting now the two puzzle pieces together, we conclude that an increase of blood pressure will raise arterial stiffness and thus, increase PWV. This is particularly true for those arteries fulfilling the hypothesis underlying the Moens-Korteweg model, *i.e.* elastic central arteries such as the aorta. Unfortunately, for non-elastic arteries (muscular arteries such as the brachial, radial, or any peripheral arterial segment) the relationship blood pressure - arterial stiffness - PWV is not unique because of the effects of vasomotion (see Figure 2.28).

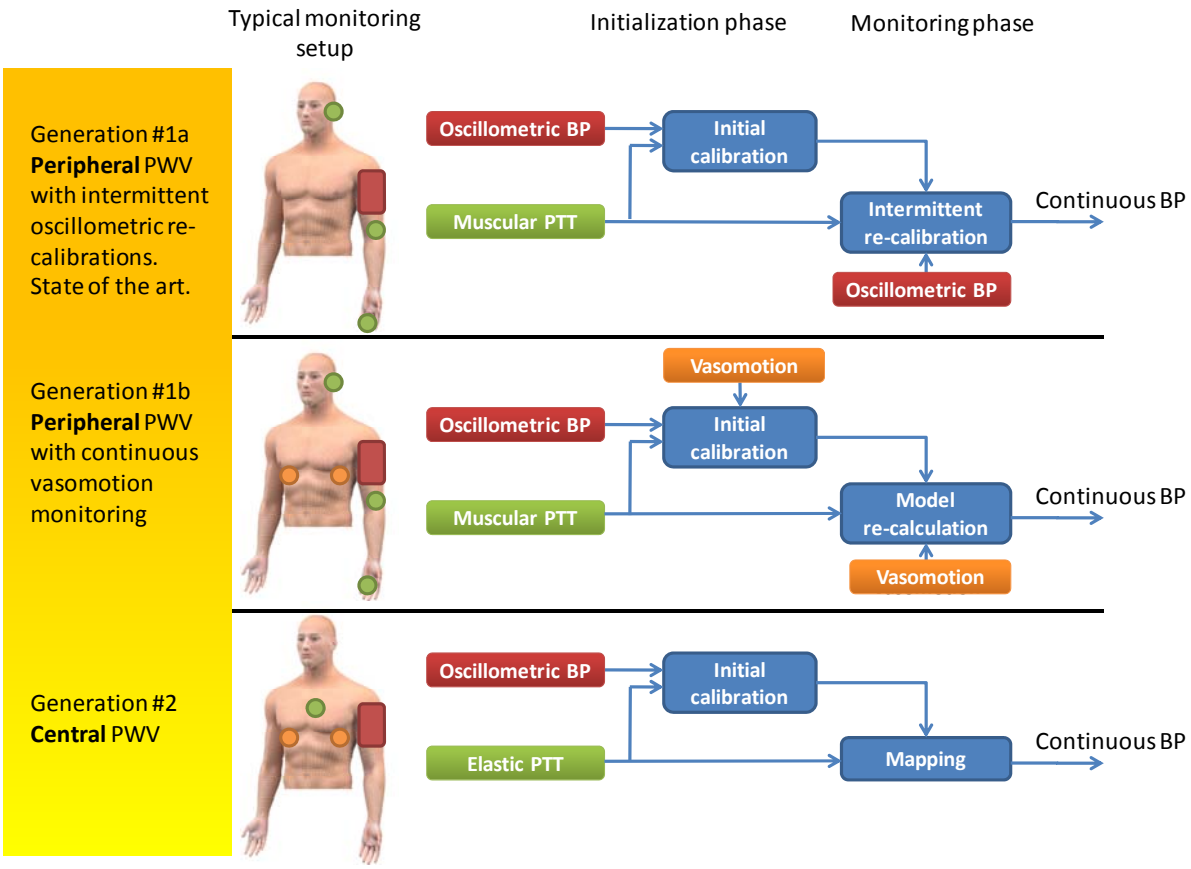

Figure 2.27: Overview of two generations of PWV-based BP monitors. The state of the art relies on family #1a: the measurement of peripheral PWV (or muscular PTT), and the subsequent intermittent recalibrations performed by inflating brachial cuff. This thesis suggests a modified version (family #1b) that replaces intermittent cuff measurements by the continuous non-occlusive surveillance of vasomotion. The main body of this thesis proposes and studies then two implementations of a second generation (family #2) based on the measurement of central PWV (or elastic PTT), and that requires no additional re-calibration means.

A prominent study published in 2006 analyzed the dependency of PTT measured at muscular arteries with respect to blood pressure for 12 subjects to whom vasoactive drugs were administered [87]. The goal of the experiment was to quantify how the predictive capacities of PTT were degraded by drug alterations of arterial stiffness. PTT was measured as the transit time between the opening of the aortic valve and the arrival of the pressure pulse at the fingertip, including thus several muscular arterial segments. All subjects and all drug conditions confounded, Payne still found that PTT was correlated with Diastolic Blood Pressure (DBP) with r=0.64. However, when “speaking in mmHg” this correlation appeared to be insufficient. Assuming that one would generate a calibration slope for each subject in order to use PTT measurements to predict DBP, one would obtain a BP measurement device classed as “grade D”, according to the British Society of Hypertension (see Section 2.2), the cumulative percentage of readings falling within 5 mmHg, 10 mmHg and 15 mmH of actual

DBP values being 44%, 66% and 73% respectively. Consequently, following the BSH directives, a finger PTT-based blood pressure monitor should not be recommended.

Nevertheless, the dependency of PWV versus blood pressure has still been shown to be sufficiently dominant to be statistically exploitable under standard conditions (no major vasomotion activity): in [103] a finger-based PWV estimation of BP was found to reach the AAMI requirements over 85 subjects, and in [104] a very good correlation was found between systolic BP and PTT over 31 subjects (r=0.91). In this sense, and especially because of the expected clinical and commercial impact of a non-obtrusive BP monitor, promising research works and developments have been released in the past years. We now review the most relevant ones.

A good illustrative development of the state of the art is that of [105]: assuming that the factors that may interfere with the relationship BP-PWV have slow time dynamics, *i.e.* slower than actual blood pressure changes, Chen investigated the use of a hybrid BP monitor: while a brachial oscillometric cuff regularly inflated to perform reference BP measurements, continuous PTT measurements were performed through a non-obtrusive ECG-fingertip approach. Chen then proposed to use the PTT series to interpolate the BP intermittent readings, beat-by-beat. Such a setup still demanded the use of brachial cuffs, but was a first step towards the non-obtrusive beat-to-beat BP monitoring. With this setup, Chen analyzed 42 hours of data on 20 subjects and obtained BSH cumulative percentages of 38.8%, 97.8% and 99.4%. Note that Chen did not account for PEP changes in his measurements, and that therefore, his results might have been improved.

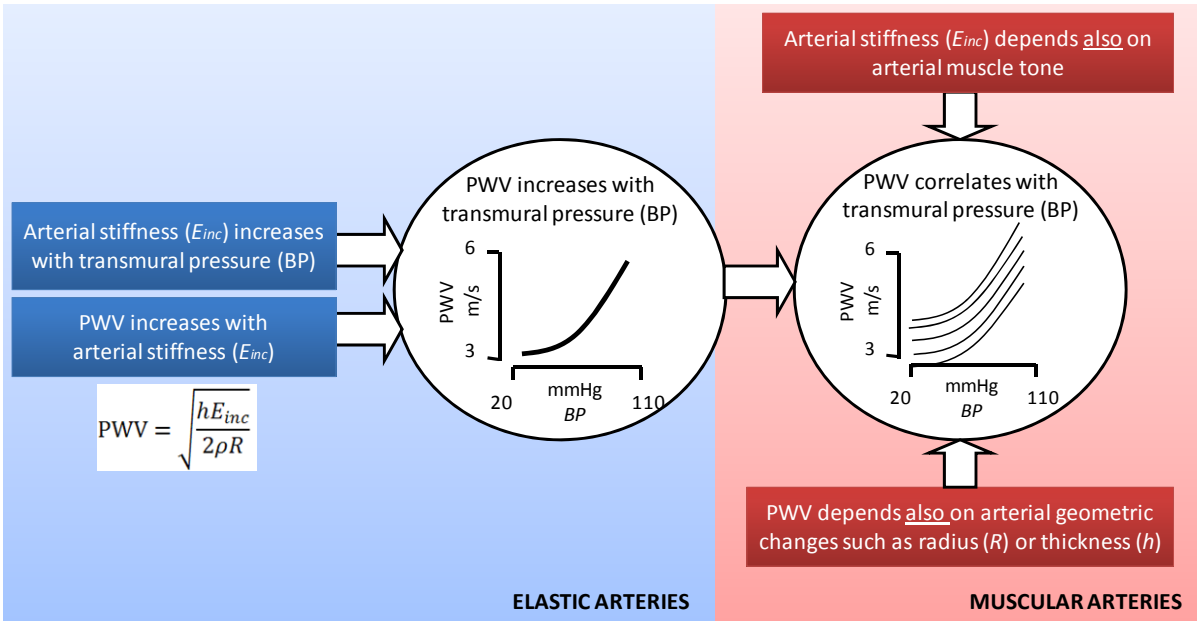

Figure 2.28: In elastic arteries, increasing transmural pressure (BP) augments stiffness (Einc). According to the Moens-Korteweg model, this results in an increased velocity of propagation of pressure pulses (PWV). Therefore, under controlled conditions it is possible to establish a relationship BP-PWV. Unfortunately, in muscular arteries, vasomotion phenomena blur the PWV-BP relationship.

Hence, PWV-based methods rely nowadays on the mapping of measured PTT values (in ms) to estimated BP values (in mmHg) through some initial or intermittent calibrations performed by oscillometric brachial cuffs [106]. Several different calibration strategies and techniques have been described so far, mainly based on the use of neural networks [107], linear regressions [108-110], model-based functions [111, 112], or hydrostatic-induced changes [113].

Modified first generation of PWV-based techniques: generation #1b

Initial research works of the current thesis aimed at developing an improved version of the first generation PWV-based techniques that reduces the required frequency of occlusive cuff recalibrations by adding to the system an estimate of vasomotion phenomenon. Accordingly, the theoretical principles of such a novel technique were suggested in a publication [114], and a patent [115]. However, since no extensive experimental works were further performed in the pointed direction, this material is provided in Annex 1 as an indication of future works to be performed.

Second generation of PWV-based techniques: generation #2

As depicted above, the use of PWV as a surrogate for blood pressure is justified under controlled conditions, that is, when the effects of vasomotion can be neglected. Unfortunately, the ambulatory monitoring of PWV currently passes through the detection of pressure pulses at distal sites such as the radial artery, or the fingertip. Because such measurement setups involve the propagation of pressure pulses through conduit arteries, the effects of vasomotion are, at best, unfavorable. The ideal solution would pass through the monitoring of PWV of central elastic arteries only. However, as we demonstrated (see Table 2.7), there is currently no available technology capable of providing ambulatory very-proximal (*i.e.* aortic) PWV measures.

The main target of the present thesis is thus to explore new techniques to assess aortic PWV non-invasively. In particular, two new technologies have been developed, implemented, and experimentally evaluated:

- The measurement of central PWV via a chest sensor performing electro-cardiographic, impedance-cardiographic, phono-cardiographic, and photo-plethysmographic measurements (Section 0).
- The measurement of aortic PWV via a chest sensor performing electrical impedance tomographic measurements (Section 4).

Before describing both novel PWV technologies, Section 2.7 provides a comprehensive overview of the principles and implementation issues of the measurement technologies involved in these research works.

2.7. Available non-invasive measurement technologies

A theoretical and applicative background on the technologies used to non-invasively assess cardiovascular parameters implemented during this thesis are provided in this section. The presented material is meant to facilitate the understanding of the research works, as well as to provide a comprehensive summary of the acquired knowledge. Technologies covered by this section are electrocardiography (ECG), photo-plethysmography (PPG), phono-cardiography (PCG), impedance-cardiography (ICG), and electrical impedance tomography (EIT).

2.7.1. Electro-cardiography (ECG)

Electro-cardiography (ECG) is a non-invasive bioelectrical technique that aims at characterizing the electrical activity of the heart. Relying on the placement of a set of electrodes over the skin surface, ECG allows identifying the source and nature of some cardiac pathologies by observing the evolution of electrical dipoles generated by cardiac cells during a full cardiac cycle. In the context of the current thesis, ECG techniques are implemented to obtain timing indexes of left-ventricular contraction.

This section starts reviewing the genesis of ECG signals from a simplified electrophysiological perspective. After describing those leads (projections of cardiac electrical dipoles into different coordinate systems) commonly used in clinical practice, the background on ECG-technology issues is provided. Finally, some remarks on the processing of ECG time series are given.

Genesis of ECG signals

In order to understand how ECG signals are generated, basic concepts of cell electrophysiology are required. In summary, it is important to retain that along the cardiac cycle, the mechanical contraction of heart cells (myocytes) is triggered by a depolarization-repolarization sequence. At its basal state, from an electrical perspective, a myocyte is a negatively-charged cell. In a very specific phase of the cardiac cycle each myocite is commanded to depolarize: by receiving an influx of Na+ ions it will become positively charged. This phenomenon will trigger the beginning of the cell contraction. Later on the cardiac cycle, the myocyte will be requested to repolarize, by releasing K+ ions and becoming negatively charged again. Before the next depolarization-repolarization sequence occurs, the ionic balance of the myocyte membrane will be reestablished by displacing Na+ and K+ ions back to their original locations. More detailed information on the electrophysiology of myocyte contraction is given in [116].

Thus, the contraction of a group of myocytes is associated to its electrical depolarization-repolarization cycle. As a consequence of this flux of ions, changes at the extracellular fluids will occur as well (see Figure 2.29). When myocytes at the right side of the figure start depolarizing (panel 2), the influx of sodium ions will generate a negative polarization of the extracellular fluid. Temporary, and while myocytes at the left side keep polarized, this will induce an electrical dipole at the extracellular level, pointing to the left. After all myocytes will have depolarized (panel 3) such local electrical dipole will vanish. At the onset of repolarization of the right myocytes (panel 4), calcium ions will be released into the

extracellular space generating a positive polarization of the extracellular fluid, and thus, an electrical dipole pointing towards the right. A final ionic rebalance process (simultaneous outflow of sodium ions and inflow of potassium ions) will lead to the initial polarized state of panel 1.

The depolarization-repolarization cycle of myocytes as illustrated in Figure 2.29 propagates through all the cardiac tissues: a cell-to-cell activation mechanism is then responsible for creating a wavefront of electrical depolarization-repolarization processes. The propagation of such electrical wavefront is not randomly executed, but supported by a set of conductive fibers, *i.e.* bundles, that coordinate the timing of contraction of different heart structures, assuring an optimal pumping function of the heart. A map of heart bundles is provided by Figure 2.30. The cardiac cycle is initiated by the depolarization of the sinus node (located at the upper region of the right atrium). Instantaneously an electrical activation wave propagates towards and through all surrounding myocytes, inducing the contraction of both atria. When reaching the boundary between the atria and ventricles this activation wave is stopped: non-conductive fibrous tissue is located at this region. At this point, the bundle conduction system takes over the propagation of the electrical activation, transmitting and delivering it towards the apex (lower part) of both ventricles. The capturing gate of the conduction system is called A-V node, and the transmission and delivering fibers are respectively the bundle of His and the Purkinje fibers (see Figure 2.30). Ventricle myocytes start finally contracting from the apex, moving upwards.

It was shown by Figure 2.29 that each depolarization-repolarization process induces a local electrical dipole. Together with the knowledge on the heart bundle system as provided above, it is now possible to predict the electrical dipoles that will be generated by the heart at different phases of the cardiac cycle. Figure 2.32 illustrates a sequence of atria-ventricle depolarization and repolarization (yellow arrows). The projection of the induced electrical dipole into Einthoven ECG leads is provided as well.

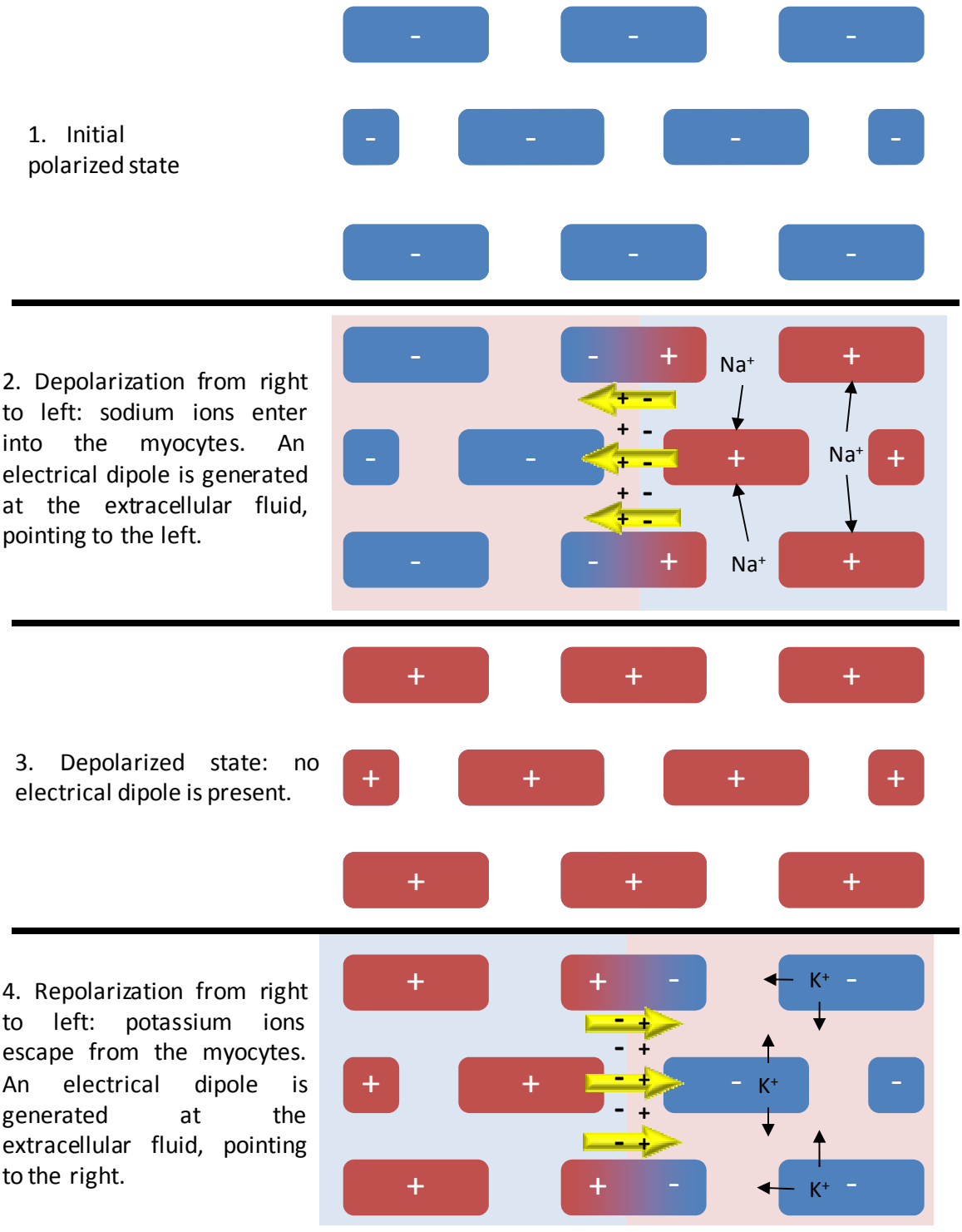

Figure 2.29: The depolarization-repolarization cycle of heart cells. The induced flux of ions generates a polarization of the extracellular fluids as well, and temporary, an extracellular electrical dipole (yellow arrows).

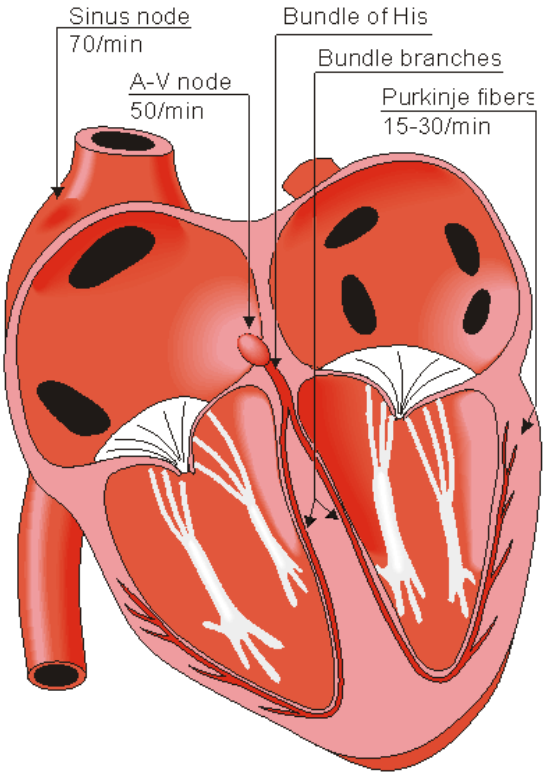

Figure 2.30: Electrical conduction system of the heart. From [116].

The Einthoven ECG leads

In clinical practice the goal of ECG analysis is to non-invasively obtain an image of the electrical behavior of the heart. In particular, it aims at assessing the movement of the heart's electrical dipole along a complete cardiac cycle. The rationale behind the technique is that since any cardiomyopathy is expected to modify the way heart tissues depolarize and repolarize, the analysis of dipole movements (including rotation and amplitude analysis) will depict information on the location and nature of the problem. ECG technology relies thus on measuring the heart's electrical dipole from the skin surface, assuming that it propagates through body without considerable distortions.

The pioneering works of W. Einthoven back in 1908 allowed standardizing the methodology to measure such electrical dipole [1]. In particular, and since an estimate of the dipole vector in a 3D space was difficult to be obtained, he proposed instead to measure the projection of such vector in three electrical leads, *i.e.* seen from different angles (see Figure 2.31):

- Lead I: projection of the dipole into a horizontal axis, measured as the voltage difference between the left arm and the right arm.
- Lead II: projection of the dipole into an oblique axis, measured as the voltage difference between the right arm and the left foot.
- Lead III: projection of the dipole into a vertical axis, measured as the voltage difference between the left arm and the left foot.

The analysis of time series of said projections of heart's electrical dipole into Einthoven leads has become a standard tool of clinical routine. A more sophisticated lead configuration, allowing better discrimination between different cardiac events, consists on augmenting the density of projections planes around the heart region by placing a set of pre-cordial leads at the thorax. A total number of 12 ECG leads, *i.e.* projections of the dipole, are then derived. The projection of the heart's electrical dipoles along the cardiac cycle into the three standard Einthoven leads is depicted in Figure 2.32.

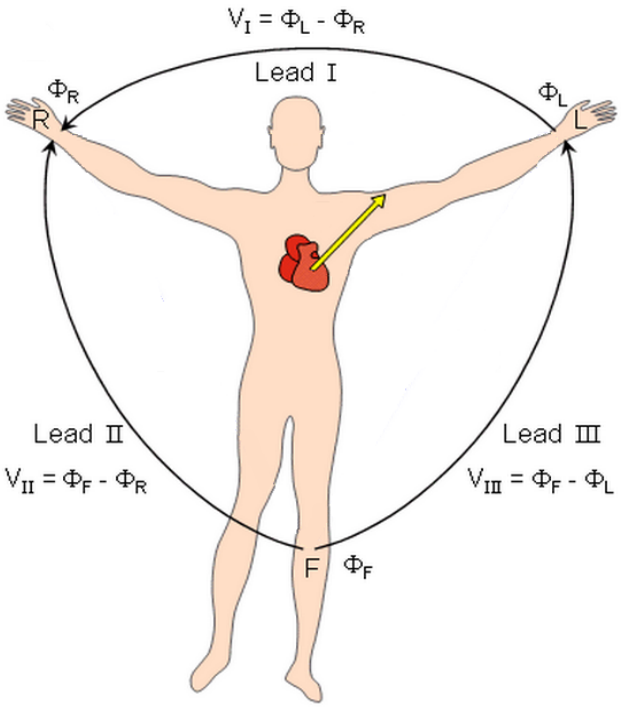

Figure 2.31: Definition of Einthoven ECG leads. Adapted from [116].

Measurement of ECG signals

Electrical dipoles generated by the heart during the different phases of a cardiac cycle induce ionic currents that propagates through the whole body, with Na^+, Ca^+ and Cl^- ions being responsible for this propagation [117]. ECG technology is meant to detect such ionic current from the skin surface. A classic ECG electrode is thus a sensor that transduces the ionic current reaching the skin into an electrical current in a metallic wire.

The standard ECG electrode (typically an Ag/Ag^+Cl^- electrode) is a sensor formed by a metallic part (typically Ag) in contact with an electrolyte (typically water with Ag^+Cl^- ions). The sensor part saturated with electrolyte is in contact with the skin. When an ionic current reaches the skin surface, a re-equilibration of charges occurs in the electrolyte giving off an electron to the metallic part. Conducted via a metallic wire, this electron is the source of an electrical current that can be detected via an ECG electronic front-end. The so-called Nerst equation describes the depicted electrochemical process. Because electrolytes in Ag/AgCl electrodes are typically disposed in a gel-like surface, this electrode technology is commonly depicted as wet electrodes. For a description of equivalent circuits for skin-electrode interfaces see [118].

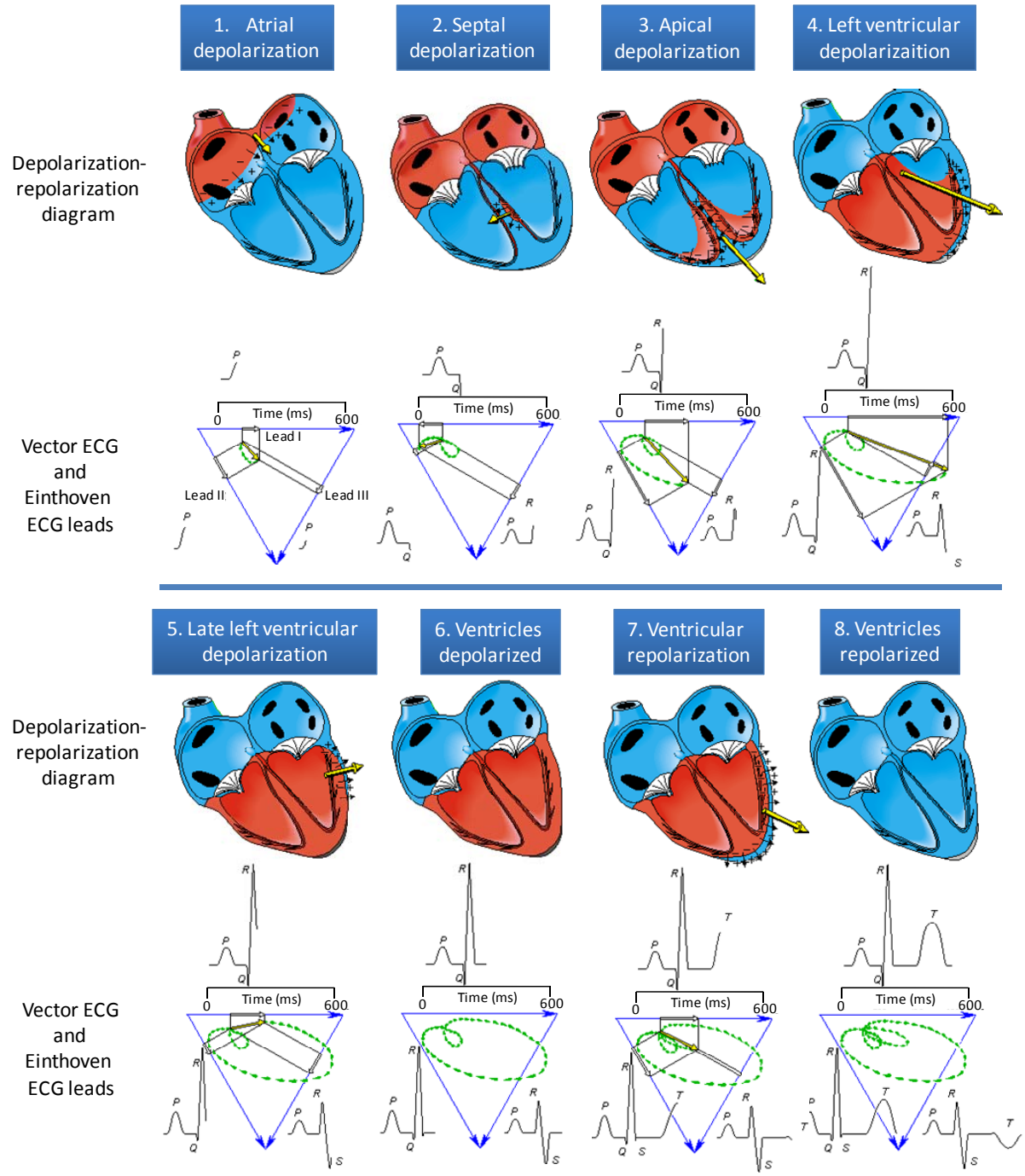

Figure 2.32: Genesis of ECG signals along a full cardiac cycle: depolarizated structures appear in red in the depolarization-repolarization diagrams. Local generated electrical dipoles are indicated as yellow arrows. The projection of heart dipoles into Einthoven ECG leads is provided as well. Adapted from [116].

Although wet electrodes provide best achievable ECG signals, their use in continuous ambulatory monitoring is problematic: first because of the long-term degradation of the electrolyte composition, second because they are not reusable, and third because of the

discomfort that wet electrode gels create to patients. In order to overcome these limitations, a large amount of research and development works have been performed in the last years on the development of electrodes technologies that are gel-free. Of particular interest are dry electrodes [117] and textile electrodes [118]. Both new technologies allow integrating ECG monitoring in re-usable and comfortable ambulatory setups such as t-shirts [119-121] and chest belts [122].

Finally, an ECG measuring system consists on an analog front-end in charge of digitalizing the electrical current transported through the metallic wire. Details on the requirements of the analog-to-digital conversion are provided in the International Standard - IEC 60601-2-47 [123].

Processing of ECG signals

Recall that the final goal of ECG is to provide a non-invasive estimate on heart function. The analysis of ECG time series must thus target at identifying patterns and signal structures related to different pathologies. Historically, clinicians have been taught to visually perform such analysis. Since the 60s unsupervised signal processing strategies have been developed and tested to perform such analysis automatically: the so-called computerized electrocardiography. An exhaustive description of ECG pathological patterns and their interpretation has been documented by the American College of Cardiology [124-128].

In the context of the current thesis, ECG technology is required to obtain estimates on the onset timing of left-ventricular contractions. As it was already illustrated in Figure 2.32 this cardiac event is represented in standard ECG leads as a prominent positive peak, so-called R-Wave. An example of automated robust technique to identify R-Waves in ECG time series is provided in [129].

2.7.2. Photo-plethysmography (PPG)

Photo-plethysmography is an optical non-invasive technology allowing the assessment of information related to subcutaneous blood circulation. By illuminating a living tissue with an infrared light source, PPG obtains estimates on both arterial pulsatility and arterial blood content. In particular, PPG techniques are implemented in the current thesis to assess the arrival time of arterial pressure pulses at specific body locations.

This chapter describes the principle of work of PPG by providing a model of light-tissue interaction, provides some indications on the actual implementation of PPG measurement setups, and reviews its most relevant clinical applications.

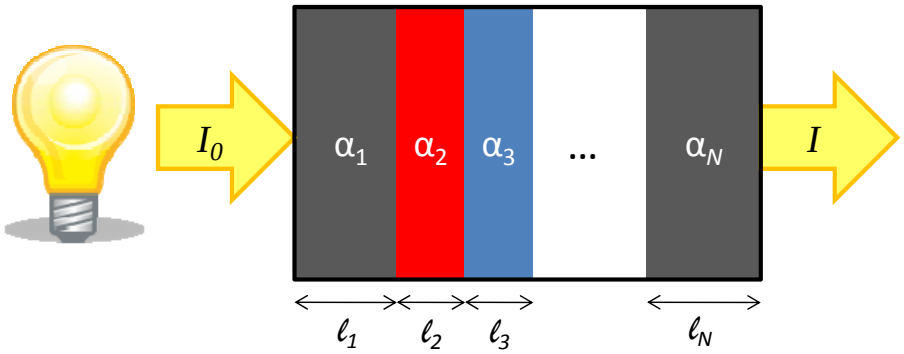

Figure 2.33: Beer-Lambert model describing the genesis of PPG signals.

The principle of photo-plethysmography

From an etymological perspective, photo-plethysmography relates to the measurement (*-graphy*) of volume changes (*-plethysmo-*) by optical means (*photo-*). In general, PPG techniques rely on [130]:

1. illuminating a living tissue with a light beam,
2. capturing a portion of the light that has propagated through the tissue,
3. and analyzing said captured light, depicting functional or structural information on the tissue.

In particular, PPG techniques have spread in clinical practice because of their ability to measure blood-related changes of volume. The principle of work of PPG is easily understood via the Beer-Lambert law [131]: a simple model of PPG measurement consists on considering a living tissue as the series concatenation of N absorbing optical segments, each one being characterized by a length l_n and an light absorption coefficient α_n. Accordingly, and assuming the intensity of an injected light beam being I_0, one expects the intensity of the transmitted light through the tissue to be (Figure 2.33):

$$I = I_0 e^{-\sum_N \alpha_n l_n}$$

Equation 28

Assume now that at least one of the optical segments being illuminated is an arterial, *i.e.* pulsatile, segment. Each time a pressure pulse will reach the illuminated region, an increase of the local blood volume will occur, augmenting the local absorption *i.e.* locally increasing l_n. For an observer placed out of the tissue and observing the evolution of the transmitted light I, this phenomenon will be characterized by a decrease of light intensity.

Therefore, the intensity of transmitted light through a living tissue can be rewritten as:

$$I = I_0 e^{-\sum_{N-1} \alpha_n l_n} \, e^{-\alpha_b l_a} = \mathrm{DC} \; e^{-\alpha_b l_a}$$

Equation 29

where DC is a constant value determined by the optical and geometrical properties of all non-pulsatile tissues and the intensity of the injected light, α_b is determined by the optical properties of the arterial blood, and l_a is the length of the segment of the arterial involved in the measurement. According to the depicted model, and assuming that during the

systolic phase of a cardiac cycle the diameter of an artery involved in the measurement increases from l_a to $l_a + \Delta_{\text{sys}}$, one observes a change on transmitted light characterized by:

$$I_{\text{sys}} = I_{\text{dia}} \; e^{-\alpha_b \Delta_{\text{sys}}}$$

Equation 30

where I_{dia} is the intensity of light received in a diastolic phase, and I_{sys} is the intensity of light received in a systolic phase. Equation 30 is thus a theoretical proof of the feasibility of using PPG technology to measure blood volume changes, and in particular, demonstrates that PPG provides information on cardiac-related blood volume changes.

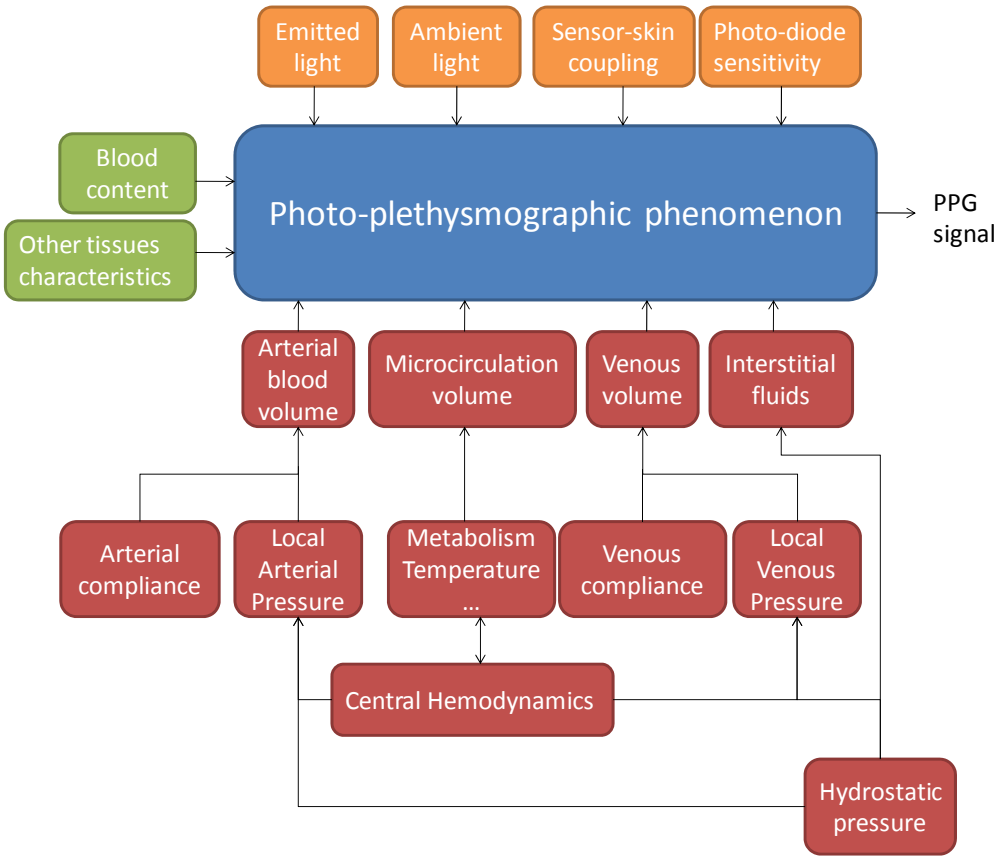

Figure 2.34: Cardiovascular (red boxes), biological (green boxes) and sensing (yellow boxes) factors involved in the measurement of PPG signals. Adapted from [132].

Unfortunately the Beer-Lambert of arterial pulsatility depicted by Equation 30 provides an incomplete description of reality: some of its limitations are here reviewed (see Figure 2.34). In addition to cardiogenic changes on blood volume, several additional volume changes might occur within a living tissue. Actually, the DC factor is not constant, but influenced by several physiological, biological and sensing factors: the genesis of PPG signals is therefore only partly related to cardiogenic oscillations at the arterial tree. In particular, changes in venous volume induced by cardiac pulsatility has been reported to be a major confounding factor of PPG assessment of arterial pulsatility [131]. Artifacts generated by changes on skin-sensor contact are a main source of confounding signal patterns as well [130]. Note that the

link between local arterial blood pressure and local arterial blood volume depends on the compliance of the artery involved in the PPG measurement. Therefore, in general, there is no straight-forward relationship between the amplitude of PPG arterial pulsation and the underlying amplitude of blood pressure pulsation [133]. Several compliance-controlled techniques to measure BP from PPG signals have been described in previous sections [25, 132]. Finally, it is important to note that the depicted model of light propagation through biological tissues based on the Beer-Lambert law copes only with absorption phenomena. Unfortunately, the interaction between light and tissues is much more complex, and involves additional mechanisms such as scattering. The effects of light propagation via scattering mechanisms in PPG measurements has been deeply studied by theoretical [134] and numerical models [135, 136].

Performing PPG measurements

As depicted above, the measurement of PPG signals requires the use of at least one light emitting means and one light receiving means. Common light emitting means used in PPG measurements are Light Emitting Diodes (LED) or Laser sources [130]. The actual choice of light wavelength depends on the targeted application, but typically ranges from 600 to 1300nm [137], *i.e.* in the red-infrared window. The raison for using light sources in the infrared window relies on the fact that while longer wavelengths are strongly absorbed by water (main tissue constituent), shorter wavelengths are strongly absorbed by melanin (a major skin component).

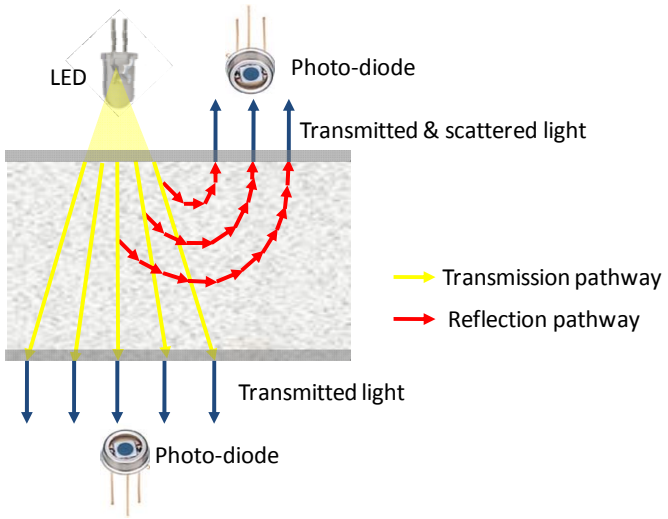

Figure 2.35: Transmission versus reflectance PPG: the roles of absorption and scattering mechanisms.

Therefore, infrared lights depict an optimal trade-off between both absorption phenomena, and ensure a maximum penetration of photons into deeper skin layers [130]. In particular, typical wavelengths used in pulse oximetry (a major application of PPG technology, described in further sections) are 660nm and 910nm. The gathering of light having travelled through a tissue is finally performed by a photodiode or a phototransistor sensitive to infrared window wavelengths. The principle of work of the PPG technology as described by Figure 2.33 assumes an operational configuration called transmission PPG technique: a

tissue is illuminated at one side, and the light transmitted through it is gathered at the other side. Unfortunately not all body locations are prone to be monitored via transmission PPG measurements. When aiming at performing PPG analysis at body locations such as the forehead, the sternum or the ankle, infrared light is fully absorbed before reaching the opposite body side. For this purpose, an alternative operational configuration is required: the so-called reflectance PPG technique [138]. In reflection PPG, light sources and light receiving means are placed onto the skin surface at the same side of the body location. While in transmission PPG the predominant light-tissue interaction mechanism was absorption (Equation 28), in reflectance PPG the predominant interaction is that of scattering, *i.e.* photons penetrate the skin surface and are successively scattered while travelling into the tissue, until reaching again the skin (backscattering phenomenon) [136]. Figure 2.35 illustrates the backscattering process.

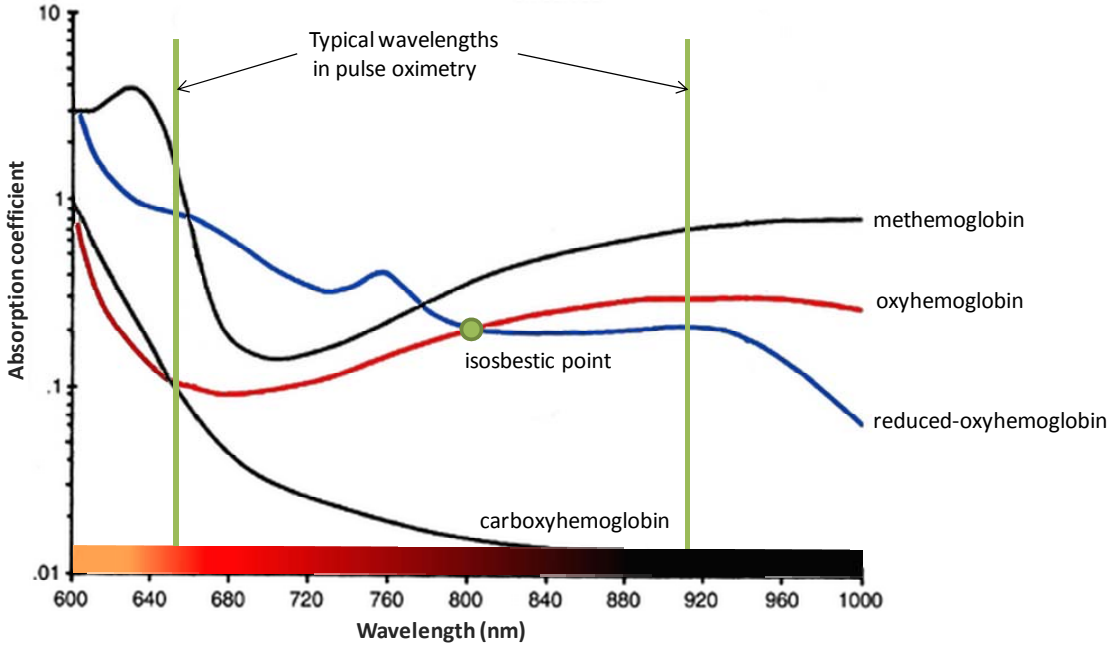

Figure 2.36: Absorption coefficients of main blood absorbents at infrared window wavelengths. Typical wavelengths used in pulse oximetry and isosbestic point for oxyhemoglobin and reduced-hemoglobin are shown as well. Adapted from [131].

Optimal distances between light emitters and receivers is to be chosen as a trade-off between the desired depths of tissue penetration (larger distance will depict deeper penetration of photons through the scattering process), and the achievable light intensity to be injected into the skin (smaller distance will require smaller light intensities to achieve a reasonable amount of photons reaching the photo-diode). Empirical studies have shown that optimal separation distances are on the range of 6 to 10mm [138]. Numerical studies have shown that reflectance PPG measurements should be avoided in regions where large arteries induce pulsatility of all surrounding tissues [136]. In some body locations, reflectance PPG relying on light absorption (instead of scattering) can be achieved as well. In such operational configuration a bone surface is used to reflect part of the injected photons back to the skin surface [139].

Clinical uses of PPG

The introduction of PPG in clinical routine has been undeniably triggered by the commercialization of first pulse oximeters around the 80s. Pulse oximetry is a non-invasive spectrometric technique that provides estimates on arterial blood gas content. Based on the propagation of two light beams through the skin (typically at 660nm and 910nm), pulse oximeters analyze the pulsatility that arterial pressure pulses create on light absorption. Because main blood absorbents at these two wavelengths are reduced-hemoglobin and oxy-hemoglobin (Figure 2.36), one is then able to determine the relative concentration of oxy-hemoglobin and obtain thus an index of blood oxygenation [131]. Based on the particular pulsatile nature of such a spectrometric analysis, the obtained value is commonly referred to as SpO2 (in contrast with the invasive assessment of arterial blood oxygenation, or SaO2).

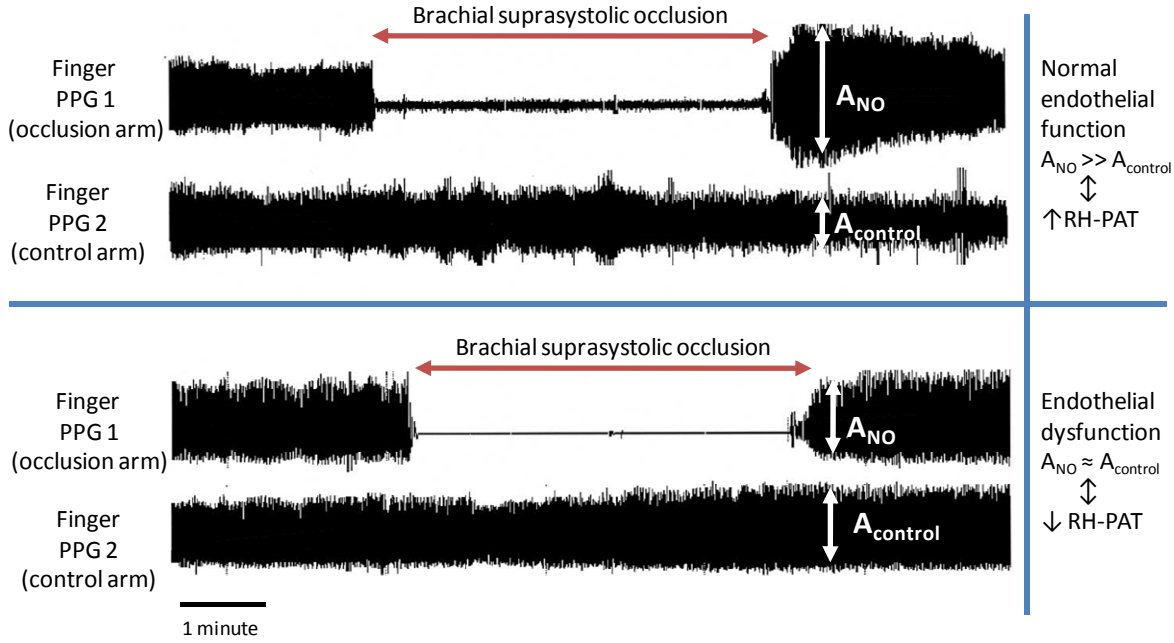

Figure 2.37: Detection of endothelial dysfunction by Reactive Hyperemia Peripheral Arterial Tonometry (RH-PAT). Adapted from [140].

Unfortunately, at the infrared wavelength window additional light absorbents are present in blood, biasing classical two-wavelength pulse oximetry readings (see Figure 2.36). Answering to such a problem, multiple wavelength pulse oximeters have been recently released [141].

An additional application of PPG in cardiovascular research and physiology studies is the beat-to-beat measurement of blood pressure. In particular the use of PPG techniques for the occlusive measurement of finger arterial pressure via the so-called volume-clamp method has already been described in Section 2.5.2.

In the past months, a new device exploiting PPG signals from standard pulse oximetry devices to derive fluid responsiveness indexes [142] has been commercialized. The goal of assessing fluid responsiveness in acute environments, *e.g.* at intensive care units, is to

determine whether administrating additional fluid will improve patient condition or not [143]. State-of-the-art indexes of fluid responsiveness are based on the quantification of the amount of interaction between respiratory activity and variations in beat-to-beat stroke volumes. Depending on the strategy implemented to quantify such variations different indexes have been developed, namely stroke volume variations and pulse pressure variations [144]. Unfortunately, both approaches require the use of either arterial femoral catheters or ultra-sound probes mounted in direct contact with the aorta. The novel PPG-based technique relies on the analysis of fluctuations of an arterial signal along the respiratory cycle as well. The fluctuations of finger PPG arterial amplitudes are now analyzed to derive a so-called Pleth Variation Index (PVI) [145]. Although representing a major break-through for the non-invasive assessment of fluid responsiveness, the accuracy of such a technique remains, at least, controversial [146].

A new revolutionary method exploiting PPG technology for the early prediction of adverse cardiovascular events has spread since 2004 [147]. Depicted as Reactive Hyperemia Peripheral Arterial Tonometry (RH-PAT), this technique is a measure of endothelial function. Endothelial function is the capacity of the endothelium (layer of cells present at the whole arterial system being in charge of the interface between blood and tissues) to actively participate in vascular responses. In particular for healthy individuals, the endothelium is expected to facilitate flow-induced vasodilations. Endothelium cells continuously sense the shear stress created by blood flow. When an increase of flow is detected, *i.e.* by increased shear, the endothelium cells react by releasing vasoactive agents (nitric oxide: NO). NO will automatically have an effect on the adjacent vascular smooth cells by locally dilating the vessel, and thus facilitating the transportation of the increased blood flow [1]. RH-PAT assesses endothelial function at arm vessels by measuring the amplitude of arterial PPG pulsatility at the finger. A brachial cuff is then inflated on one arm at suprasystolic pressures during five minutes. At the release of such brachial pressure, the sudden raise of flow at the occluded arm will induce a massive local release of NO. The RH-PAT index is then calculated by comparing the PPG amplitude at the manipulated arm against the PPG amplitude at the control arm. Accordingly, endothelial dysfunction will be associated to low RH-PAT indexes [140]. A typical example of NO-induced blood flow increase during a RH-PAT experiment is provided by Figure 2.37.

Obviously, RH-PAT provides a measure of endothelial function of the arteries of one finger. The interest of performing such experiments in clinical routine relies on the fact that endothelial dysfunctioning is a generalized phenomena (not constrained to a single segment of the arterial tree), and therefore, detecting dysfunctioning of the endothelial cell at the finger appears to be a very good predictor of endothelial dysfunctioning of coronary vessels [140]. A commercial device (Endo-PAT) performing automatic unsupervised RH-PAT measurements has been released by Itamar Medical, Caeserea, Israel.

Finally, although not introduced yet in clinical practice, the use of PPG technology for the measurement of Pulse Arrival Times at different body locations has been suggested by several authors [130, 148, 149].

2.7.3. Phono-cardiography (PCG)

Phonocardiography (PCG) is an electric-acoustic technology that allows the measurement and analysis of heart sounds. Heart sounds were already known by Hippocrates, who described a succession of splash when he applied his ear directly on patient's chest [150]. PCG aims at improving this simple technique by providing more quantitative and repeatable measurement of heart sounds and murmurs [151].

In the context of the presented thesis, PCG is a key technology to provide estimates on the time of opening of the aortic valve, and has been particularly applied in Section 5. The current section provides a summary on the phenomenon underlying the genesis of heart sounds, describes the technology required to record PCG tracings, and reports the state of the art in the digital processing of PCG time series.

Heart sounds genesis

The genesis of heart sounds is related to the propagation of vibrations originated by heart mechanical activity towards the chest surface. In particular, the closing of heart valves is considered the main source of heart sounds [152]: the simultaneous vibration of the valve, neighboring heart structures and surrounding blood occurring during the closing event rapidly propagates through the thorax as an acoustic, *i.e.* vibration, wave (cardiohemic theory). Traditionally two heart sounds have been documented: the so-called S1 and S2 heart sounds (see Figure 2.38). Because of their high intensity these heart sounds can be identified by simple auscultation of the chest. The actual cardiac mechanical events generating the S1 and S2 heart sounds are here described:

- The S1 heart sound is originated during ventricular contraction, and is the composite of four events [153]. First, the acceleration of blood from the ventricles towards the atria. Second, the closing of the atrioventricular valves and its subsequent recoiling of blood back to the ventricle. Third, oscillations generated at the aorta and pulmonary artery caused during the opening of the aortic and pulmonary valves. And fourth, the fast turbulent ejection of blood into the aorta.
- The S2 heart sound is originated at the end of cardiac systole, and is the composite of two events: the closing of the aortic valve and the closing of the pulmonary valve, the time delay between these two events varying during the respiratory cycle [152].

A description on heart sounds, murmurs and mathematical models is provided in [152].

Acquisition of phono-cardiographic signals

Medical examination of heart activity is still nowadays performed with a stethoscope: a pure mechanical sensor transducing vibrations at the chest surface into acoustic waves that can be heard by a human expert. It consists thus of a surface in contact with the body (transducer), and of a tube that propagates acoustic waves towards an earpiece. Unfortunately, stethoscopes require a non-negligible amount of expertise and training, and have the disadvantage of distorting the original heart sound while it propagates from the surface in contact with the body towards the earpieces, *e.g.* via a device-dependent transfer

function). Note that the first acoustic stethoscope was already introduced in 1816 by Laennec [151]

Phono-cardiography (PCG) aims at overcoming the limitations of auscultation methods by measuring heart sounds directly at the chest surface, and by converting them into electrical signals. Two technologies have been proposed to acquire heart sounds, namely piezzo-electric accelerometers and microphones. Parameters such as frequency response and resonance frequency determine the characteristics of each sensor. The digitalization of electrical signals generated by the so-called phono-cardiographs is finally done via standard signal acquisition electronic modules [152].

.

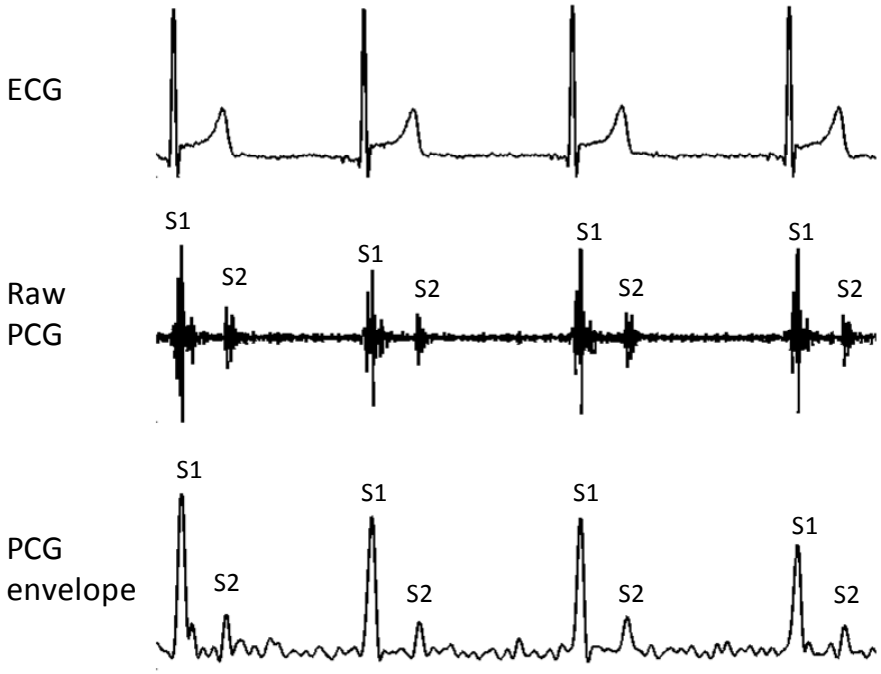

Figure 2.38: Example of synchronously recorded ECG and PCG tracings on a male subject. Phono-cardiography tracings were acquired via a microphone-based electronic stethoscope (TSD108, BIOPAC Systems Inc, CA, US) placed at the cardiac apex. Calculation of PCG envelope tracing has been described in the text.

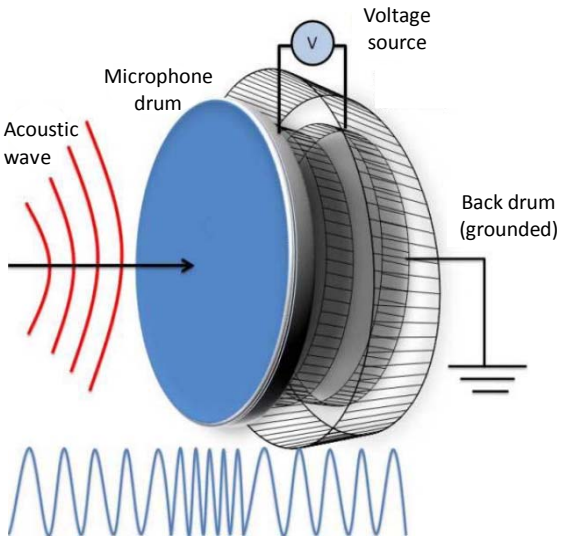

Figure 2.39: Measurement principle of a phono-cardiograph: transduction of chest-wall vibrations into electrical signals. Extracted from [151].

Processing of phono-cardiographic time series

Two families of techniques to process PCG time series have been proposed in the state of the art: on the one hand those techniques aiming at localizing the time occurrences of heart sounds, and on the other hand those techniques aiming at identifying heart sounds characteristics and classifying them according to different heart pathologies. A comprehensive description of both techniques is provided in [152]. For the current thesis, the interest of analyzing PCG time series focuses on the first family of techniques, and in particular, on the identification (time localization) of S1 (see Section 0).

A generic description of a S1 detection algorithm is provided in Figure 2.40. Initially, the raw PCG time series is pre-processed. Typical pre-processing routines consist on band-pass filtering the raw data in order to retain only the S1-related frequency band, *i.e.* on the 10 to 140 Hz frequency range.

Figure 2.41 illustrates a typical frequency distribution of heart sounds as recorded by phonocardiography. Wavelet denoising of the raw PCG has been investigated as well [154]. On a second step, the pre-processed series is analyzed in order to extract S1-related features. In the literature different feature extraction techniques have been proposed, ranging from a simple energy calculation [155], a PCG envelope estimation via a Hilbert transform [152] or a Shannon envelogram [156], a correlation analysis of the filtered time series with a pre-computed ensemble-average template of S1 [157], or a wavelet decomposition [151, 158]. Finally, from heart sounds transformed into a feature-based domain are detected according to thresholding methods [155], or more sophisticated statistical models such as hidden Markov models [159] or neural networks [151].

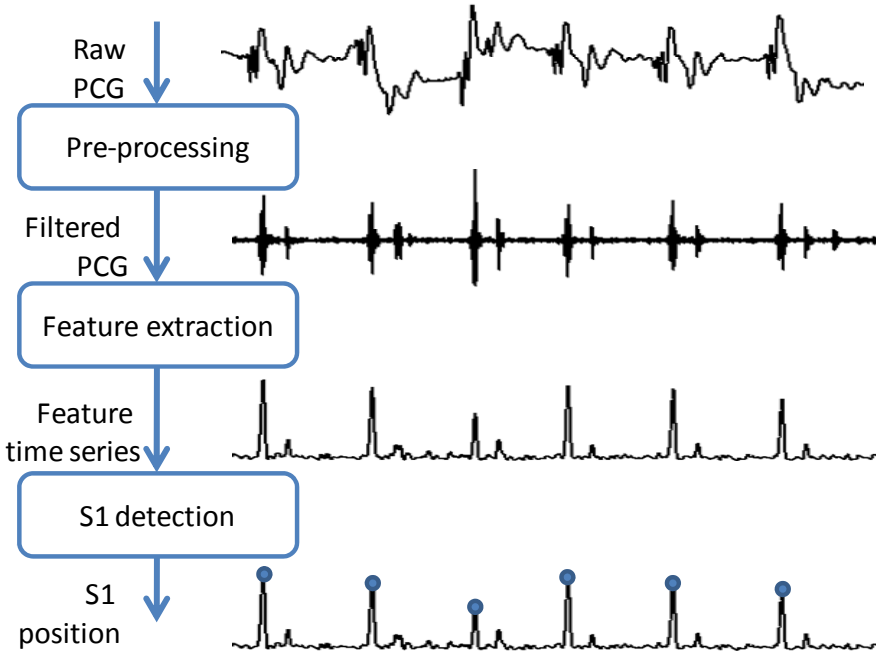

Figure 2.40: Generic S1 detection algorithm after the pre-processing of the raw PCG signals, a feature-based time series is generated. In the feature-transformed domain the exact localization of S1 is performed.

2.7.4. Impedance-cardiography (ICG)

Impedance-cardiography (ICG) is a non-invasive bio-electrical technique aiming at monitoring cardio-related displacements of blood within the thorax [160]. ICG was already introduced in 1966 by Kubicek [161] answering to a NASA demand to non-invasively assess cardiac output. In contrast with the already-described ECG technology, ICG actively senses cardiovascular activity by injecting electrical currents within the thoracic cavity and further measuring changes in the voltages generated by such electrical currents. At each cardiac cycle, right after the opening of the aortic valve, a volume of fresh blood is spread through the different thoracic organs and anatomical structures, locally decreasing their impedance value. The interest of the ICG technology is thus to [162]:

1. Estimate the amount of fresh blood being released at each cardiac cycle, *i.e.* the stroke volume value, by analyzing the amplitude of the cardio-related changes of bio-impedance occurring at the thorax.
2. Estimate the timing of several systolic events, *e.g.* pre-ejection period and left-ventricular ejection time, by analyzing time features of the cardio-related changes of bio-impedance occurring at the thorax.

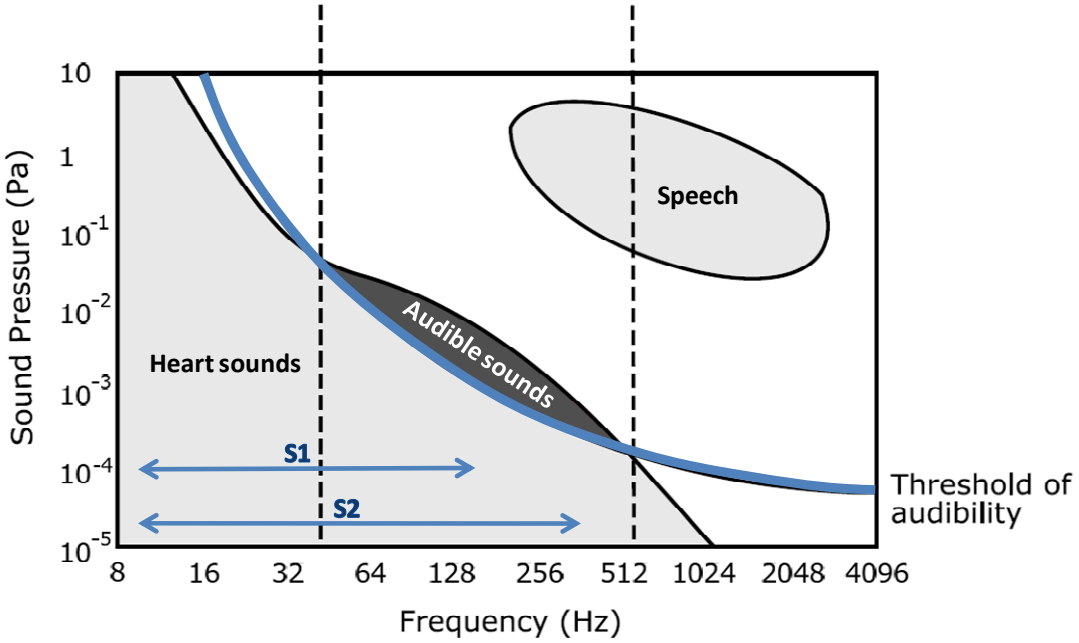

Figure 2.41: Frequency description of heart sounds, compared to speech. S1 heart sound is mainly located in the range of 10 to 140 Hz, and S2 heart sound is located in the range of 10 to 400 Hz. Adapted from [152]

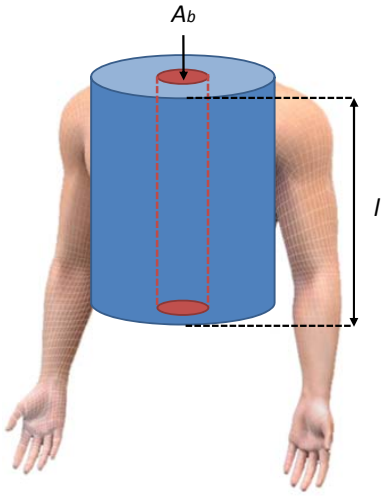

Figure 2.42: Kubicek's model of the thorax to describe the genesis of ICG phenomena. A cylinder containing blood perfused tissues (area A_b and length l) is surrounded by a cylinder of non-perfused tissues [161].

In this section a review on the state of the art of the ICG technology is provided concerning the genesis of ICG phenomena, the placement bio-impedance electrodes, the processing of ICG signals and the applications in the clinical domain. Issues related to thoracic tissue resistivity and patient safety are covered in Section 2.7.5.

Understanding the genesis of ICG phenomenon

The historical developments by Kubicek [161] assumed the thorax to be modeled by two concentrical cylinders: a cylinder containing blood perfused tissues and organs, and a surrounding cylinder containing the remaining tissues. Given the geometry of the model (blood conductive area A_b and length l as illustrated in Figure 2.42), and assuming the blood perfused cylinder to be a homogeneous conductive volume with a constant resistive component given by the conductive properties of blood ρ_b, the electrical impedance associated to perfused cylinder in the vertical axis Z_b is determined by:

$$Z_b = \rho_b \frac{l}{A_b}$$

Equation 31

Accordingly to the model geometry, and assuming the electrical impedance associated to the surrounding cylinder to be Z_s, the overall electrical impedance of the thorax (Z_o) is determined by:

$$Z_o = \frac{Z_b Z_s}{Z_b + Z_s}$$

Equation 32

After the opening of the aortic valve, the amount of fresh blood in the thoracic perfused tissues and organs will increase, decreasing the value of Z_b. Note that according to the geometry of the model, the total amount of blood volume v_b in the thorax is defined by the quantity:

$$v_b = A_b l$$

Equation 33

Differentiating Equation 31 with respect to v_b, one obtains that a given decrease of $Z_b$will be associated to an underlying increase of blood volume as it follows:

$$\frac{dZ_b}{dv_b} = -Z_b^2 \frac{1}{\rho_b l^2}$$

Equation 34

Similarly, one encounters that a change in Z_b will induce a change in the overall impedance of the thorax (Z_o) as it follows (derived from Equation 32):

$$\frac{dZ_o}{dZ_b} = \frac{Z_o^2}{Z_b^2}$$

Equation 35

Merging now Equation 34 and Equation 35, Kubick's model predicts a change in thoracic perfused blood volume to induce an overall change of thoracic electrical impedance of:

$$\frac{dZ_o}{dv_b} = -\frac{Z_o^2}{\rho_b l^2}$$

Equation 36

A first conclusion of such an expression is that there is a linear relationship between:

- A change of bio-electrical impedance measured through the thorax, or dZ_o
- And the amount of fresh blood being injected by the heart into the thorax at each cardiac cycle, or dv_b.

In consequence, Kubicek's model shows the analysis of time series of ICG signals to be a non-invasive surrogate of the cardiac blood injection patterns. In other words, systolic time events as measured by an arterial lines (*e.g.* pre-ejection period, left-ventricular ejection time), can be measured as well by ICG techniques [162-167]. These results have been exploited in the present thesis, being a key element of the research work presented in Section 0. An example of measurement of pre-ejection period and left-ventricular ejection time values in an adult male is provided by Figure 2.43. The identification of characteristic points in ICG tracings is further described in this section (see Processing of ICG signals). Note that the ICG tracing is defined as the first time derivative of the $Z_o(t)$ time series.

Moreover, the ICG model as described by Equation 36 was further exploited by Kubicek in order to predict the absolute amount of blood volume being injected by the heart, opening the door to a first non-invasive monitor of stroke volume [161].

Rewriting Equation 36 in order to isolate the v_b quantity, and replacing v_b by Stroke Volume SV one obtains:

$$\mathrm{SV} = \frac{\rho_b l^2}{Z_o^2}\Delta Z_o$$

Equation 37

According to Equation 37, SV can be calculated by ICG techniques by:

- measuring the amount of overall impedance change within the thorax during the cardiac cycle (ΔZ_o)
- measuring the total thoracic electrical impedance (Z_o)
- measuring a blood conductivity characteristics (ρ_b)
- and by estimating an model-equivalent cylindrical length of the thorax (*l*)

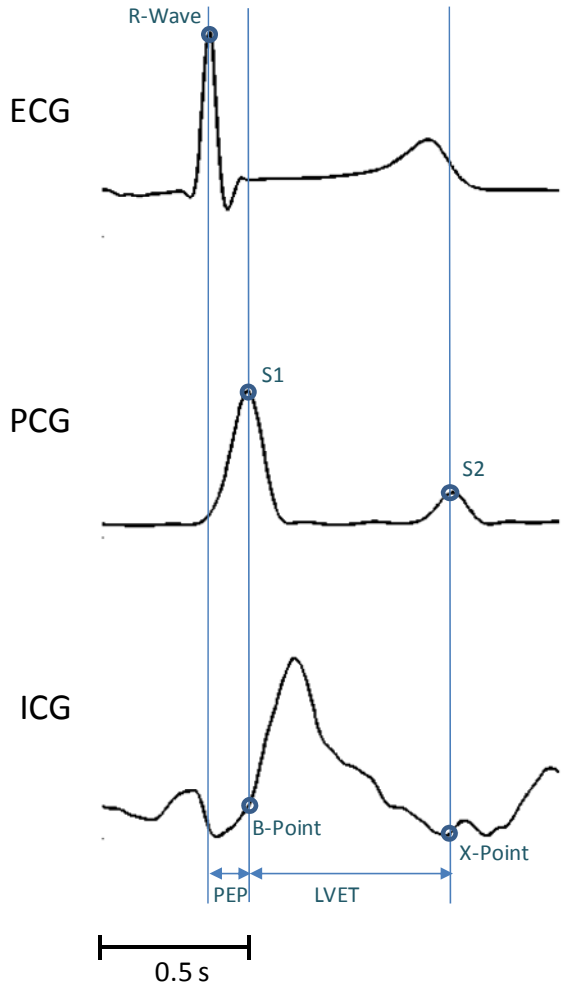

Figure 2.43: Simultaneous recording of Electro-Cardiogram (ECG), Phono-Cardiogram (PCG) and Impedance-Cardiograpm (ICG) tracings on a male adult. After the beginning of ventricular polarization (R-Wave), the opening of the aortic valve is observed in both the PCG (S1 sound) and the ICG (B-Point). The closing of the aortic valve is observed in the PCG (S2 sound) and the ICG (X-Point). Pre-Ejection Period (PEP) and Left-Ventricular Ejection Time (LVET) values are defined as well.

Unfortunately, a main limitation of the model is that it assumes that during systole the thorax continuously fills with blood. In reality this is not the case, and as soon as blood is released by the left ventricle a large amount of the SV is spread through the body, escaping thus the thoracic cavity [116]. Consequently, the total amount of overall impedance change ΔZ_o is not a realistic representation of the total amount of released blood. Some add-hoc solutions to this limitation have been proposed in the literature [161, 168]. The classical approach by Kubicek relies on the analysis of a time series of successively measured Z_o values during a full cardiac cycle, named $Z_o(t)$. The algorithm consists then on determining the value of the maximum change of $Z_o(t)$ occurring during the cardiac cycle $\left[\frac{dZ_o(t)}{dt}\right]_{\max}$, and assumes that this would be an accurate estimate of ΔZ_o if no blood was escaping from

the thorax. By multiplying said quantity by the duration of the systole (or ejection time, E_t), an hypothetic estimate of the total ΔZ_o is obtained. Accordingly, the Kubicek's approach to estimate SV is summarized by Equation 38:

$$\mathrm{SV} = \frac{\rho_b l^2}{Z_o^2} E_t \left[\frac{dZ_o(t)}{dt}\right]_{\max}$$

Equation 38

Although the simplistic model of Kubicek (Figure 2.42) allowed deriving an easy strategy to estimate systolic time intervals and stroke volume values, it relies on important methodological limitations. In particular, the origin of the ICG signal is not well defined, and the interpretation of the $Z_o(t)$ time series is no straight forward. While each thoracic organ and structure receives a burst of fresh blood during the cardiac cycle, the arrival times of these bursts are not homogeneous. Even more, the contribution of each organ perfusion to the overall change of thoracic impedance is not homogeneous either. Therefore $Z_o(t)$ is to be interpreted as a weighted-mixture of delayed contributions from different sources. Several authors have thus suggested that the use of ICG to measure absolute values of SV is methodologically limited *per se* [169-171]. More sophisticated models [172] and several empirical studies [173] have investigated these phenomena and have proposed detailed models of the actual genesis of the ICG signal.

Notwithstanding, ICG technology offers a valuable resource for the non-invasive assessment of cardiac events, and has been selected in the present thesis as a support for the assessment of systolic time intervals.

Placement of ICG bio-impedance electrodes

The original research works by Kubicek [161] recommended the use of four band electrodes for the measurement ICG: while two of the electrodes inject the electrical currents, the remaining two sense the generated voltages through the thorax (Figure 2.44, panel a).

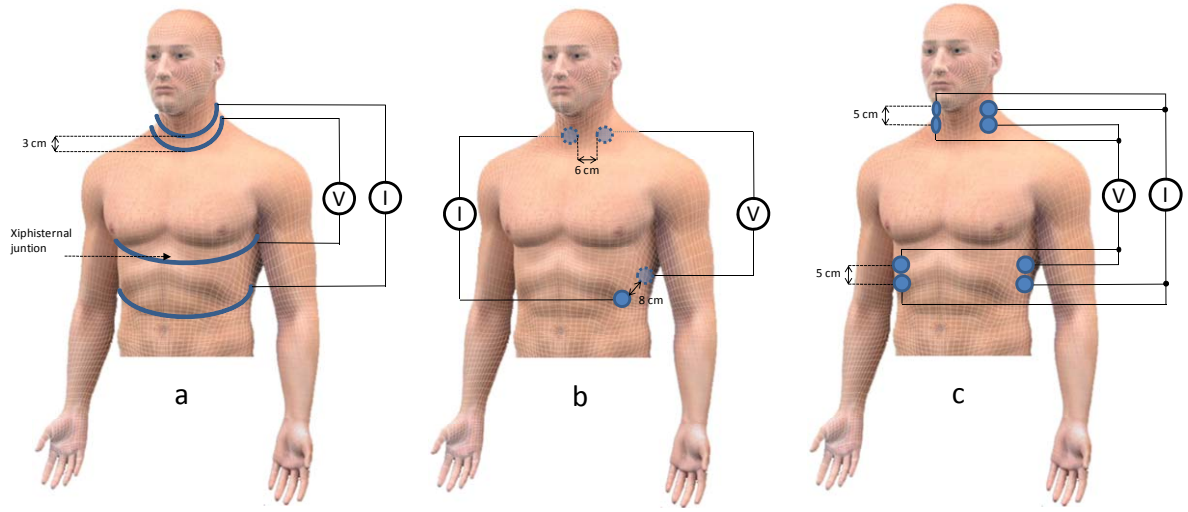

Figure 2.44: Different ICG electrode configurations. Panel a) corresponds to a tetrapolar band electrode configuration, panel b) corresponds to a 4 spot electrodes configuration, and panel c) corresponds to a 8 spot electrode configuration.

Typical implementations of this setup consist on using four adhesive strip bands of about 2.5 cm covered by electrode gel [162]. The four bands are placed circumferentially around the body: two at the neck (separated by about 3 cm) and two at the thorax (one at the level of the xiphisternal joint, and one far below it), as illustrated by Figure 2.44, panel a.

However, because of the bulky effect of the band-electrode setup, already in 1985 Penney suggested using spot electrodes instead [173], *i.e.* standard disposable ECG electrodes. Figure 2.44 (panel b) illustrates Penney's electrode configuration. The proposed setup consists on injecting the electrical currents between a spot electrode placed at the base of the neck, near the prominence of C-7, and an electrode placed below the heart at end of the ninth intercostal space. Voltage measurements are then performed by a spot electrode located at the base of the neck, separated by 6 cm from the injecting electrode, and an electrode located at the tenth intercostal space, separated 8 cm from the injecting electrode. Experimental work by Penney demonstrated that the four-spot-electrode configuration provided similar ICG tracings to those simultaneously measured by a Kubicek's four-band-electrode configuration [173]. Other four-electrode configurations have been proposed in the literature as well [162].

Finally, currently available ICG systems recommend the use of an alternative eight-electrode configuration [162]. This measurement setup uses pairs of four electrodes, miming the original band-electrode configuration (Figure 2.44, panel c): one pair of current electrodes is first placed at the base of the neck, and the second pair of electrodes at the mid-axilliary line. One pair of voltage electrodes is then placed at the base of the neck 5 cm below the current electrodes, and the remaining pair at the thoracic level 5 cm above the current electrodes.

Several studies have assessed and compared the performances of band versus spot electrode configurations. Of particular interest is the work performed by McGrat *et al.* [174]. Said study compared Cardiac Output (CO) and systolic time interval measurements on 30 subjects in several conditions recording almost-simultaneously ICG tracings using a band and a spot electrode system. They reported that while systolic time intervals correlate very highly between both approaches (LVET depicted correlation scores greater than 0.91 for all subjects and conditions together, and PEP greater than 0.82), CO measurements were only slightly correlated (correlation score of 0.61 all subjects and conditions together). Such a difference is justified by the already-reported fact that spot electrodes systematically provide smaller Z_0 values than band electrodes, influencing thus the estimation of CO (see Equation 38). Finally, it is important to highlight that there is currently no systematic comparison between the performances of the 4- and the 8-spot electrodes configuration.

Therefore, and according to the reviewed studies, for the measurement of systolic time intervals the use of spot electrodes is recommended: while producing PEP estimates that are highly correlated with those provided by band electrodes, they increase patient comfort by diminishing the bulkiness of ICG. Additionally, simulation works done by Sakamoto [175] demonstrated that the use of spot electrodes, and in particular the optimal positioning of those, is capable of providing much useful information by allowing to monitor blood circulation in particular thoracic organs and structures.

Processing of ICG signals

It has been described in previous sections that ICG technology is capable of providing both timing information on the cardiac cycle, and estimates on stroke volume. In the context of the current thesis ICG techniques have been primarily implemented to non-invasively estimate the so-called Pre-Ejection period of living human beings. An overview of the signal processing strategies to obtain such estimates is now provided.

A pioneering work on the interpretation of ICG time series to determine cardiac cycle timing information was done in 1971 by Lababidi *et al* [166]. The systematic analysis of ICG tracings obtained from 91 subjects, and simultaneously recorded with an electro-cardiogram and phono-cardiogram, provided a first empirical base to interpret ICG signals. Lababidi found that relevant timing information was not coded on the ICG time series itself, but on its first time derivative. Accordingly, all along this thesis, when discussing about the localization of characteristic points in ICG time series we will, indeed, refer to the localization of said points on the first time derivative of the $Z_0(t)$, and we define:

$$\mathrm{ICG} = \frac{dZ_0(t)}{dt}$$

Equation 39

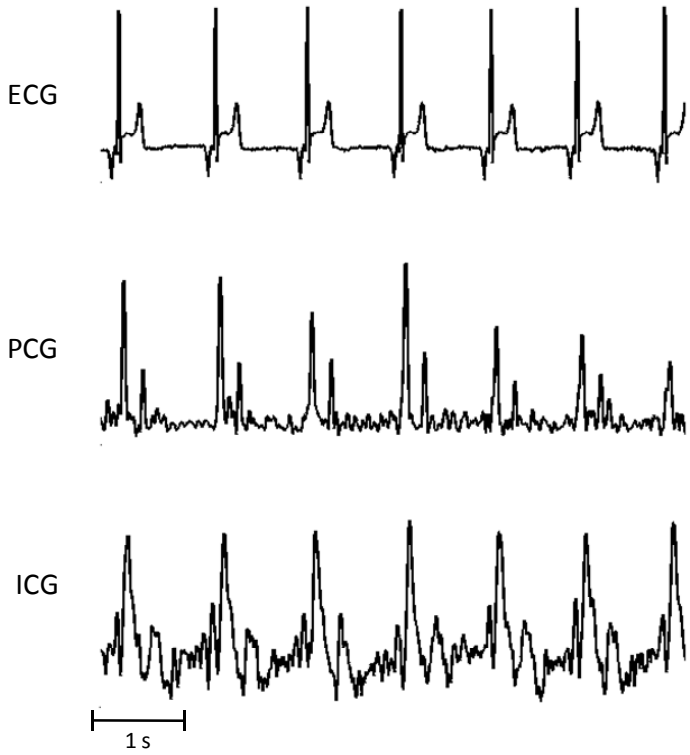

Figure 2.45: Simultaneous recording of Electro-Cardiogram (ECG), Phono-Cardiogram (PCG) and Impedance-Cardiograpm (ICG) time series on a male adult. Time series correspond to raw recorded data.

From the results obtained by Lababidi two main characteristic points of the ICG' time series are to be highlighted (see Figure 2.43):

- B-Point: deflection point occurring simultaneously with the first cardiac sound (S1). Empirical studies performed after Lababidi experiments, recording simultaneously ICG and echo-cardiograms, confirmed that such characteristic point is temporally associated with the onset of left-ventricular ejection [162, 166]. Several signal processing strategies have been proposed to identify a B-point on ICG' tracings. On one hand DeMarzo defined the B-Point as the first inflection point of the ICG' time series when travelling from maximum ICG' amplitude value towards the past [176]. On the other hand Doornen proposed in [162] to use the maximum of the third derivative ICG, *i.e.* ICG''', to identify B-Points even in the absence of inflection points in ICG'. A comprehensive comparison on the features and reliability of these two approaches is provided in [177].
- X-Point: deflection point occurring simultaneously with the second cardiac sound (S2), and being associated with the closing of the aortic valve at the end of left-ventricular ejection [162]. The X-Point is commonly identifiable as a sharp minimum notch of ICG' time series at the end of each cardiac cycle. In particular cases where two notches are observed (10% of subjects), a simultaneous PCG recordings can be used to support the identification.

Unfortunately, ICG data recorded *in-vivo* hardly resembles the tracings illustrated by Figure 2.43: respiratory and movement artifacts, as well as electronic noise render ICG monitoring a real signal processing challenge. Figure 2.45 illustrates the raw time series of three simultaneously recorded ECG, PCG and ICG, obtained from the same experiment described in Figure 2.43. One observes that the identification of characteristic points, as described above, is not straight forward. In order to cope with the noisy nature of *in-vivo* ICG signals, several strategies have been proposed in the literature.

Ensemble averaging: Hurwitz first introduced this technique in the field of ICG in 1990 [178]. The approach relies on the assumption that ICG signals can be modeled by the concatenation of a basic ICG pattern, repeated in time with a periodicity determined by the heart rate, and to whom a zero-mean noise has been added, *i.e.*:

$$\mathrm{ICG(t)} = \sum_i p(t - T_i) + u(t)$$

Equation 40

Where $p(t)$ is a basic ICG pattern, T_i is a time value depicting the time at which the i^{th} heart beat occurs, and $u(t)$ is a zero-mean noise. By requiring an *a-priori* estimate of $T(i)$ the ensemble averaging provides a single estimate of $p(t)$ given a set of N heart beats by operating:

$$\hat{p}\mathrm{(t)} = \frac{1}{N}\sum_n \mathrm{ICG}(t - T_n) w\,(t - T_n)$$

Equation 41

where $w(t)$ is a time window of finite length centered around $t = 0$, and typically of a length close to the heart beat period. Developing Equation 41 further together with Equation 40 one obtains:

$$\hat{p}(\mathrm{t}) = \frac{1}{N}\sum_{n} \mathrm{p(t)}w\,(t) + \frac{1}{N}\sum_{n} \mathrm{u(t} - T_n)w\,(t - T_n)$$

Equation 42

Applying now the initial hypothesis on zero-mean for the noise $u(t)$, one finally obtains:

$$\hat{p}(\mathrm{t}) = \mathrm{p(t)w(t)}$$

Equation 43

Since the shape of the window $w(t)$ is known, $\hat{p}(\mathrm{t})$ is thus an accurate estimate of $p(\mathrm{t})$. Typical implementations of the ensemble averaging technique use the ECG as the information source providing estimates on T_n. In particular, the common approach is to assume the position of the R-Wave at the ECG to be the ensemble average trigger. An example of ECG-triggered ICG ensemble averaging is illustrated by Figure 2.46.

The interest of applying ensemble averaging techniques is better justified from a frequency domain perspective. Accordingly, Annex 2 provides the theoretical background justifying the ensemble averaging technique to be a particular case of a very narrow band-pass comb filter capable of coping with heart rate variability phenomena.

PCG-supported ICG processing: the use of ICG technology for the estimation of systolic time intervals relies on the identification of characteristic points in the first derivative of the ICG, for instance the so-called B- and X-points. Even though some signal processing strategies on how to perform such identification in *in-vivo* ICG tracings have already been mentioned, in realistic scenarios of ICG monitoring these are not robust enough. For instance, the identification of the maximum of the third derivative ICG as proposed in [162] is not straight forwards in noisy ICG time series, where several maxima are likely to correspond to the selection criterion. In order to overcome such limitations, several authors have recently proposed to support the analysis of ICG time series by adding a synchronously recorded Phono-Cardiograph (PCG) as an additional independent information source [179, 180]. Assuming that PCG time series allow robustly identifying the so-called S1 and S2 heart sounds (see Section 2.7.3 for further details), the time position of these events provides initial guesses on the most likely time positions of both the B- and X-points. An implementation of this strategy has been deeply described in Section 0.

Other ICG processing strategies have been proposed in the literature. Of particular interest are the match-filter approach proposed in [181], and the wavelet decomposition approach proposed in [182].

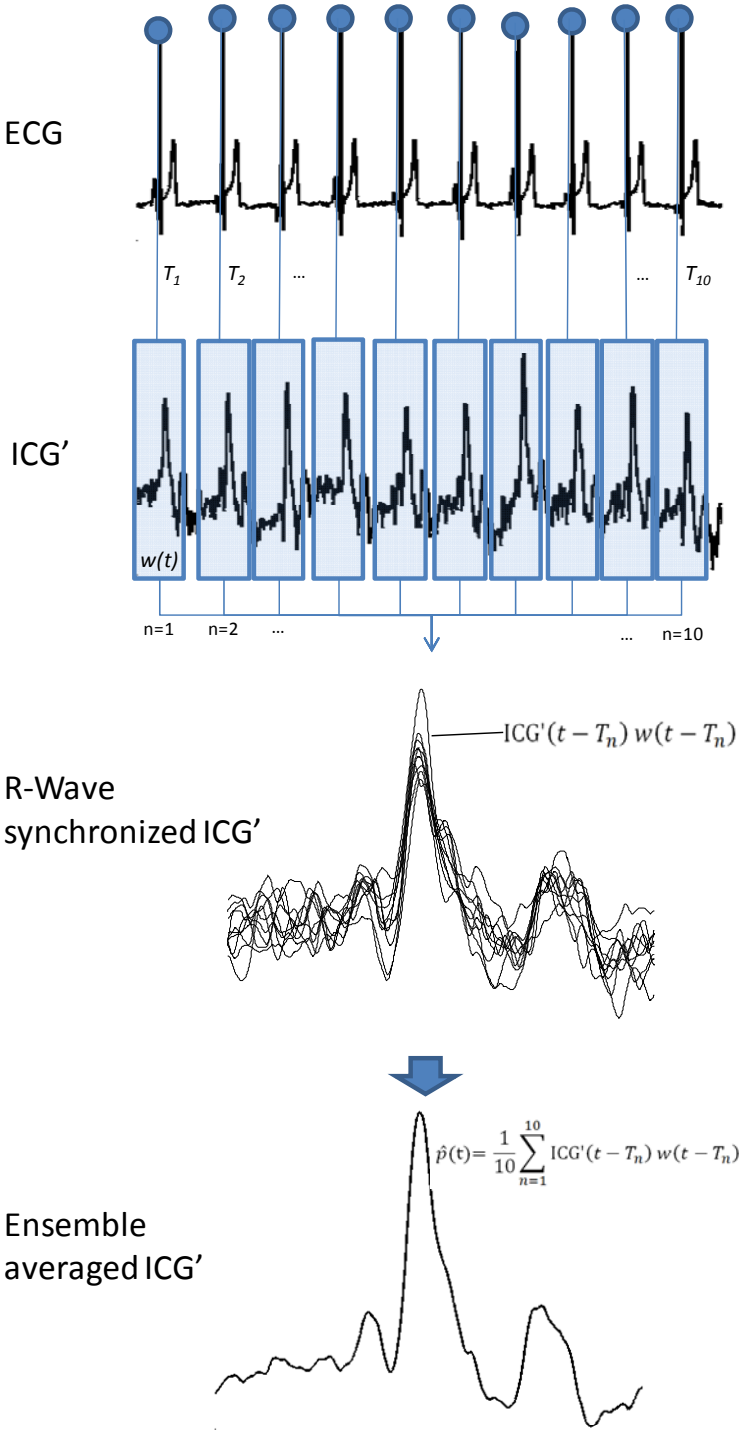

Figure 2.46: Example of ECG-triggered ensemble averaging of an ICG' time series. Position of R-Waves at the ECG (blue spots) defines the location of ten $w(t)$ windows. Windowed segments of ICG' are then synchronously overlapped in time. The ensemble averaged ICG' is finally obtained by calculating the mean of the R-wave-synchronized ICG' tracings. Under the assumption of zero-mean additive noise, $\hat{p}(t)$ is an optimal estimate of the underlying ICG' phenomenon.

Summarizing, in the context of the present thesis the goal of using ICG technology is to obtain *in-vivo* non-invasive estimates of two particular systolic time intervals [86] (see Figure 2.43):

- Pre-Ejection Period (PEP): defined as the time delay between the onset of ventricular depolarization (R-Wave at the ECG), and the onset of left-ventricular ejection (B-Point at the ICG'). In some fields, PEP is also referred as isovolumetric contraction period.
- Left-Ventricular Ejection Time (LVET): defined as the time delay between the onset of left-ventricular ejection (B-Point at the ICG'), and the closing of the aortic valve (X-Point at the ICG').

Table 2.8: Commercial ICG systems.

Commercial ICG devices	
BioZ DX Diagnostic system Electrode configuration: 8 spot electrodes Measured parameters: • Cardiac Output • Systolic Time Intervals: PEP, LVET. • Thoracic Fluid Content • Systemic Vascular resistance FDA-cleared Producer: Sonosite, US	
Niccomo monitor Electrode configuration: 8 spot electrodes Electrical injection frequency: 1.5mA at 85kHz Measured parameters: • Cardiac Output • Systolic Time Intervals: PEP, LVET. • Thoracic Fluid Content • Systemic Vascular resistance Class IIa Medical Device Directive Standard Producer: Medis Medizinische Messtechnik, DE	
LIFEGARD II Multi-Parameter Patient Monitor Electrode configuration: 8 spot electrodes Measured parameters: • Cardiac Output • Systemic Vascular resistance FDA-cleared Producer: CAS Medical Systems Inc., US	

Commercialized ICG systems

Although ICG technology was introduced already 50 years ago, the amount of commercial ICG devices has been rather limited: the fact that there is no unanimous agreement on the sources of ICG signals (see sections above) has compromised the community confidence on ICG-related measurements of Stroke Volume. Yet, the increasing interest in some research fields on assessing systolic time intervals non-invasively has justified the commercialization of some of these devices. A list of commercial ICG systems is provided in Table 2.8.

2.7.5. Electrical impedance tomography (EIT)

Impedance Tomography (EIT) is a non-invasive imaging technology that generalizes the principle of tissue impedance monitoring, as described in Section 2.7.4. By performing several simultaneous impedance measurements around the thorax, EIT generates bi-dimensional representations of tissue impedance distribution. In the context of the current thesis, EIT technology has been implemented to non-invasively assess pulsatility properties of the descending aorta (Section 4).

The state of the art on the use of EIT technology for the non-invasive monitoring of cardio-respiratory events is initially reviewed in this section. After presenting the principles of the EIT technology, basic concepts of thoracic bioimpedance science are illustrated. Analog hardware and regulatory issues are then reported before defining the concept of stimulation-measurement patterns. Finally absolute and functional EIT imaging techniques are presented and the mathematical background of EIT reconstruction techniques is described. This section ends with some examples of functional cardio-respiratory EIT imaging and with a listing of currently-available EIT recording systems.

The principles of EIT

Electrical Impedance Tomography (EIT) is an experimental non-invasive monitoring technology based on the analysis of bio-impedance signals [183]. From an electrical perspective, the thoracic cavity is composed of distributed impedance volumes. While the lungs (filled with air) form high impedance volumes, the heart and blood vessels (filled with blood) form low impedance volumes. As input signals, EIT requires a set of impedance measurements performed around the chest. Basic *a-priori* knowledge about chest anatomy allows reconstruction algorithms to estimate the most likely distribution of regional impedances. Hence, EIT provides tomographic reconstructions of the distribution of impedance volumes within the thorax at high sampling rates.

Because it requires a relatively simple measurement setup (electrodes placed around the thorax), EIT is a candidate technology for the non-invasive assessment of cardio-respiratory phenomena within the chest in ambulatory. In this section the working principles of EIT technology as well as some proposed cardiovascular applications are described. Figure 2.47 provides an overview of the use of EIT to non-invasively monitor cardiovascular parameters.

Performing impedance measurements

EIT image generation relies thus on the fact that different thoracic organs and structures create different resistances to the flow of electrical currents. For instance, air-filled organs such as the lungs are known to depict higher tissue impedance values than blood-filled structures like the heart, arteries and veins. Even more, at different phases of the cardiac and respiratory cycles, one expects such impedance values to vary according to the amounts of blood/air being displaced. Unfortunately, no consensus on the orders of magnitude of tissue impedance values for these biological tissues has been reached to date. In the last decades, several studies have been published assessing impedance properties of biological tissues, but published values are, at least, controversial [184]. A main limitation of currently available data is the lack of homogeneity in the measurement setups: published studies are related to different electrode configurations, frequency ranges, tissue temperatures, and are performed both *in vivo* and *in vitro*, and on human and animal tissues. In order to obtain a homogenized view on the orders of magnitude of tissue resistivities present within the thoracic cavity, systematic measurements of different biological tissues were performed during this thesis. Annex 3 provides such experimental data.

A critical issue in EIT (and in general, in any bioimpedance measurement system) is the actual choice of the frequency of injected electrical currents. Common applied frequencies are on the range of 10 to 200 kHz. While inner-thoracic tissues depict similar impedance characteristics at these frequencies (see Table 9.1), the optimal frequency choice relies on a trade-off between:

- Skin-electrode impedance dependency on frequency: skin impedance is reduced by at least a 10-fold factor when increasing current frequencies from 1KHz (10kΩ) to 100kHz (<1 kΩ) [185]. Increasing current frequencies allows thus reducing the influence of skin in EIT imaging.
- Maximum allowed electrical current to be applied at a given frequency: medical electrical safety regulations limit leakage currents to 0.1mA at 1KHz, and up to 10mA at 100kHz. Therefore, while increasing frequency one is allowed to increase leakage currents, improving thus signal-to-noise ratio.
- Increasing complexity of electronic design with frequency: increasing current frequencies requires more complex analog frontends, increases amplifier errors and the augments amount of cross talk between analog channels [186].

Figure 2.48 illustrates the elements participating on the optimization of the electrical current frequency choice for EIT systems.

As depicted above, the amount of electrical leakage current to be injected in human body is limited by medical safety regulations. In particular, electrical currents for impedance measurements are described by the international standard IEC 60601 [187]. Accordingly, bioimpedance devices fall into a “Type BF applied part” class, *i.e.* devices that have conductive contact with the patient, and are therefore limited to a maximum patient leakage current of 0.1mA in DC. Because human body, and in particular heart tissue, depict a low-pass filter behavior, leakage currents being injected at higher frequencies will be better tolerated. Accordingly, IEC 60601 allows augmenting the total amount of leakage

current to the body when increasing frequency. Table 2.9 and Figure 2.49 provide indication on the maximum allowed leakage currents for type BF impedance devices.

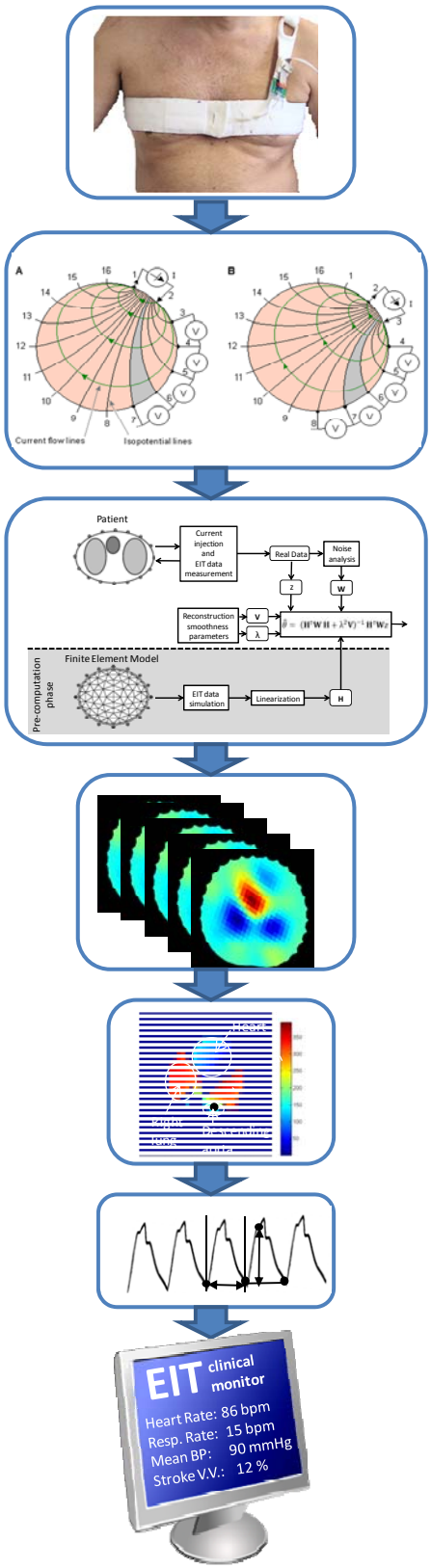

1.- An electrode belt is placed around the thorax. The belt contains 32 impedance contact points with the skin.

2.- Impedance measurements are performed by injecting currents through a pair of electrodes, and reading the generated voltages at two different electrodes. Several stimulation-measurement patterns are possible.

3.- From the measured impedance values, a tomographic image is generated estimating the most likely distribution of impedance volumes within the thorax that generated such measurements. A modified Newton-Raphson algorithm is commonly used.

4.- By repeating steps 2-3 at fast velocities, sequences of 50 tomographic images per second are generated. Impedance changes induced by respiratory events, and by the propagation arterial pressure pulses through the thorax, are represented within said sequences.

5.- From the sequences of EIT images, those pixels depicting functional information related to organs such as the heart and lungs, or anatomical structures such as the aorta, are identified.

6.- Time series representing impedance changes at the identified organs and anatomical structures are generated, containing information related to blood volume changes at such locations. Clinical parameters are calculated from such volume tracings, as if a virtual catheter had been invasively placed.

7.- Calculated parameters from the virtual catheter are finally displayed to clinicians, providing new insights to cardiovascular regulation and stability… non-invasively.

Figure 2.47: Virtual catheter approach: use of the Electrical Impedance Tomography (EIT) for the non-invasive monitor of cardiovascular parameters.

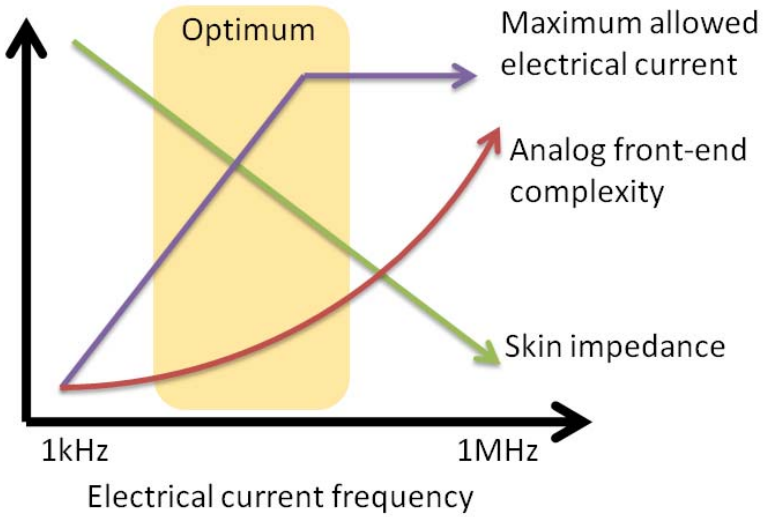

Figure 2.48: Choice of the optimal EIT electrical current frequency as a trade-off between medical electrical safety regulations, analog front-end complexity and skin impedance.

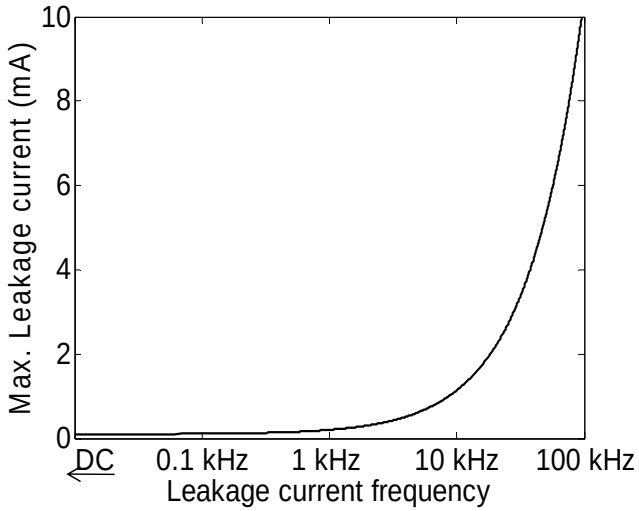

Figure 2.49: Maximum allowed leakage current to human body depending on leakage current frequency for type BF medical devices, as described by IEC 60601 [187].

Table 2.9: Maximum allowed leakage current to human body depending on leakage current frequency for type BF medical devices, as described by IEC 60601 [187].

Leakage current frequency	Maximum leakage current
DC	0.1 mA
1 kHz	0.2 mA
10 kHz	1.1 mA
100 kHz	10 mA

From *N* electrodes placed around the thorax, several strategies can be applied to scan the actual distribution of impedance volumes. Under the name of stimulation-measurement patterns, these strategies assign measurement roles to each electrode: either injecting/receiving an electrical current (stimulation), or measuring a voltage value (measurement) [116]. The choice of a pattern for an EIT system relies on a trade-off between technological complexity and expected performance. Classical current patterns, so-called pair-driven patterns, perform voltage measurements between two electrodes while a current is injected between two other sites [188]. While being relatively easy to implement, adjacent patterns have been shown to provide rather poor scanning performances, *i.e.* providing impedance data from which it is not possible to distinguish small changes in thoracic impedance distribution [189]. Unfortunately, the majority of existing EIT systems relies on pair-driven stimulation-measurement patterns. Alternative approaches based on simultaneous injection of homogeneous electrical currents through pairs of electrodes have been proposed. Referred to as optimal patterns these strategies provide improved distinguishability performance [189]. The classical implementation of optimal patterns is the so-called trigonometric pattern [190]. Arbitrary optimized patterns have been recently explored as well [191, 192]. Unfortunately optimal patterns require the use of rather sophisticated current sources: electrical currents at each electrode are set and controlled to achieve an optimal distribution of current patterns through the thorax. Table 2.10 shows most implemented stimulation-measurement patterns in EIT: three strategies of pair-driven patterns (adjacent, cross and opposite) and one strategy of optimal pattern (trigonometric).

The use of EIT in biomedical applications is more interested on assessing cardio-pulmonary changes of impedance occurring within the thorax than in measuring absolute thoracic impedance values. A clear difference is thus to be made between absolute and functional EIT imaging. While absolute imaging requires deep knowledge on the measurement setup in order to provide absolute impedance values par pixel (body shape, electrode position and system dimensions are to be clearly stated) [193] [194], functional imaging simply determines how the impedance value of a pixel has changed compared to a reference measurement, *i.e.* baseline, of such impedance. If a thoracic reference image is taken at the end of expiration, the respiration cycle will be represented by a sequence of EIT images for which lung pixels will increase their impedance values during inspiration (filling of the lungs with air), and *vice versa*. If a thoracic reference image is taken at the end of systole, the cardiac cycle will be represented by a sequence of EIT images for which heart pixels will decrease their impedance values during diastole (filling of the heart with conductive blood), and *vice versa*.

Therefore, functional EIT imaging measurement procedure consists of:

1. Measuring a set of reference bioimpedance values (z_0) around the thorax.
2. For all subsequent sets of bioimpedance values (z') generating EIT tomographic reconstructions of cardio-respiratory cycles using as input information the corrected impedance sets: $z = z' - z_0$.

Table 2.10: Definition of common stimulation-measurement patterns in EIT. Number of measurements (#), sequences and illustrations correspond to a 16 electrodes system setup. S1-2 depicts 'Stimulate current between electrodes 1 and 2', M3-4 depicts 'Measure voltage between electrodes 3 and 4'. Illustrations adapted from [116].

Definition	Example (16 electrodes)
Adjacent current pattern *Type: pair-driven pattern* # measurements: 16*13= 208 # independent measurements: 104 Stimulation-measurement sequence: S1-2 M3-4, M4-5,..., M15-16 S2-3 M4-5, M5-6,..., M1-2 ...	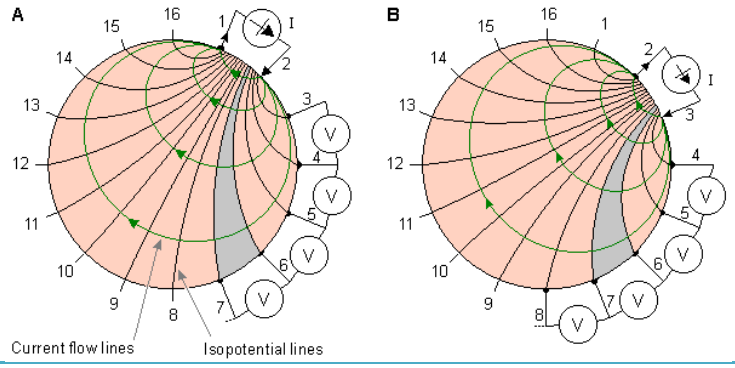
Cross current pattern *Type: pair-driven pattern* # measurements: 2*7*13= 182 # independent measurements: 104 Stimulation-measurement sequence: S16-2 M1-3,M1-4,..., M1-15 S16-4 M1-2,M1-3,..., M1-15 ... S3-5 M2-4,M2-6,..., M2,1 ...	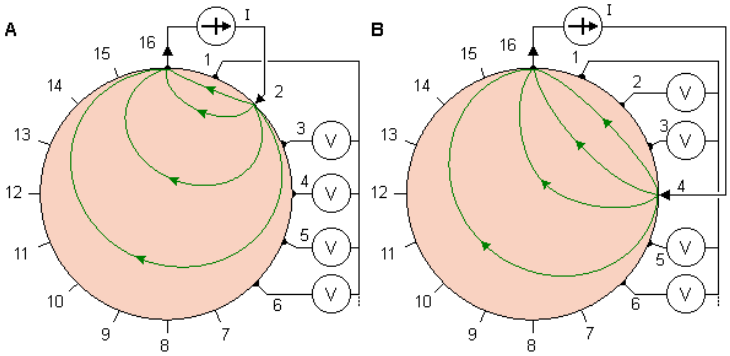
Opposite current pattern *Type: pair-driven pattern* # measurements: 8*13= 104 # independent measurements: 104 Stimulation-measurement sequence: S16-8 M1-2, M1-3, ..., M1-15 S1-9 M2-3, M2-4, ..., M2-16	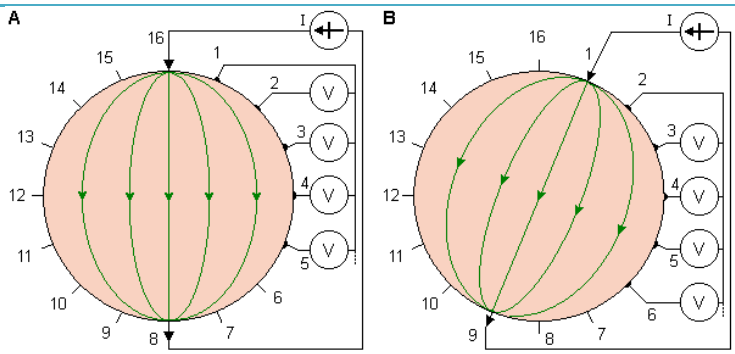
Trigonometric current pattern *Type: optimal pattern* # measurements: 8*15= 120 # independent measurements: 120 Stimulation-measurement sequence: S1-15, S2-14,..., S7-9 M16-1, M16-2, ..., M16,15 S16-14, S1-13, ..., S6-8 M15-16, M15-1, ..., M15-14 ...	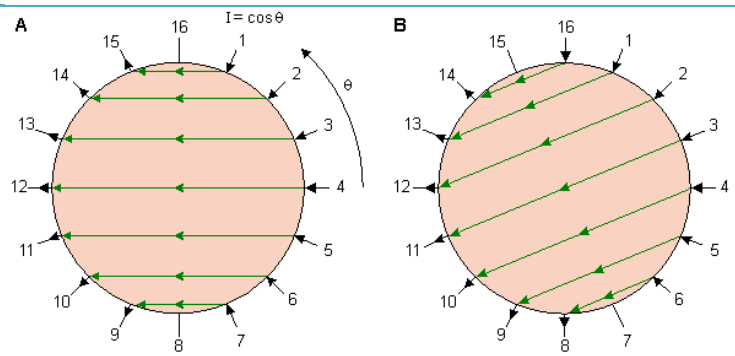

Several strategies to determine the optimal z_0 set have been described in the state of the art [186]. Most common implementations define z_0 to be the average of the first *N* EIT bioimpedance measurement sets (*N* normally corresponding to some seconds of EIT recordings), or define z_0 to be a particular cardio-respiratory event (end of expiratory respiration cycle, or end of systolic cardiac cycle) as detected by an external sensor.

EIT Tomographic reconstructions

After having summarized the state of the art on hardware and metrological issues for the acquisition of sequences of impedance values around the thorax, this section describes the generation of EIT images from the acquired data. The starting point of this description will thus be a set of n bioimpedance values (z) collected in-vivo around the chest. In particular, z will be assumed to be a functional bioimpedance value as described in previous section:

$$z = z' - z_0.$$

Equation 44

Recall that the goal of EIT is to estimate the most likely distribution ($\hat{\theta}$) of internal impedances within the thorax given z. Based on a modified Newton-Raphson algorithm [195], the classical approach (Figure 2.50) consists on recursively updating the distribution of impedance values of a finite element model of the thorax (θ), until the impedance measurements simulated by θ best represent the measured z values. In other words, EIT searches a $\hat{\theta}$ that satisfies:

$$\hat{\theta} = \mathrm{argmin}_{\theta}\ \phi(f(\theta), z)$$

$$\phi(f(\theta), z) = \|f(\theta) - z\|_{\mathbf{W}}^{a}$$

$$f(\theta) : D\ \subset\ \mathbb{R}^m \rightarrow \mathbb{R}^n$$

Equation 45

where:

- $\phi(f(\theta), z)$ depicts the error function between the measurements ($z \in \mathbb{R}^n$) and the simulated bioimpedance values $f(\theta)$. The error function is defined by its norm a, and weighting matrix $\mathbf{W}$.
- $f(\theta)$ is a function generating n bioimpedance values for an hypothesized finite element model of the thorax θ.

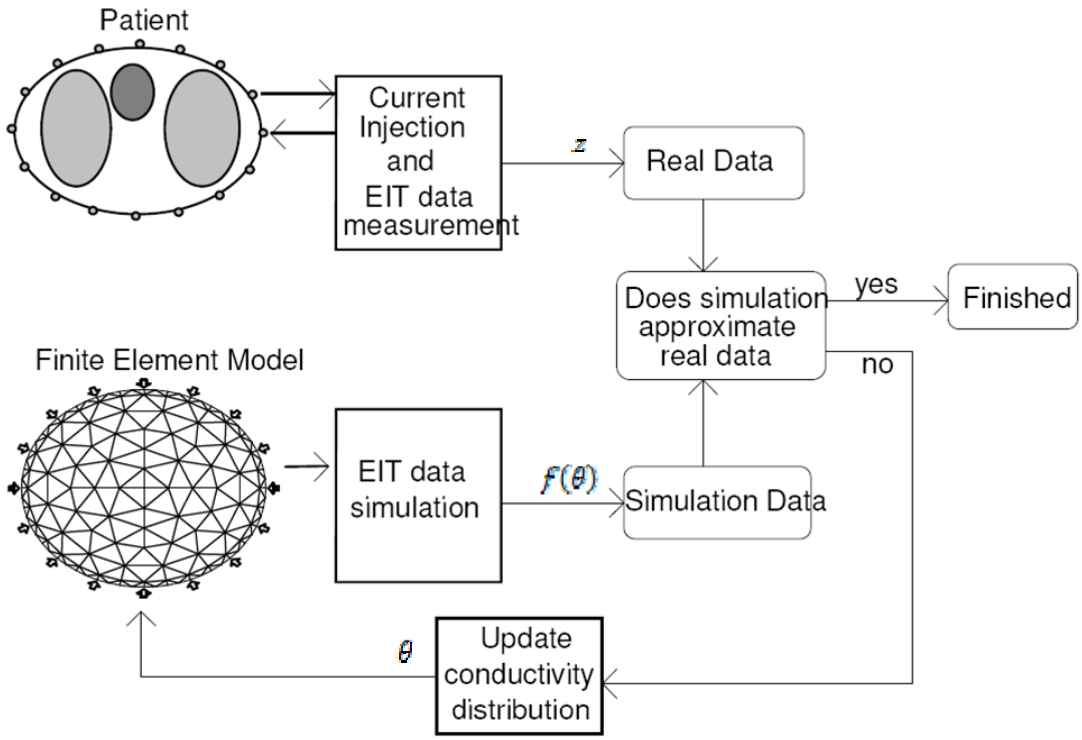

Figure 2.50: EIT reconstruction algorithm as a modified Newton-Raphson algorithm. The parameters of a finite element model of the thorax (θ) are recursively updated until the simulated measurements created by the model ($f(\theta)$) best match the *in-vivo* bioimpedance measurements z. Adapted from [195].

In EIT, $f(\theta)$ is commonly referred as the forward problem, and it consists on projecting an hypothetic distribution of impedances ($\theta \subset D \in \mathbb{R}^m$) into the measurement space $\in \mathbb{R}^n$, *i.e.* on simulating what bioimpedance values one would measure on the skin surface given a certain thoracic model. In principle, given a non-homogeneous impedance medium (e.g. a biological tissue), $f(\theta)$ can be determined by solving for instance Kirchhoff equations. Obviously, the morphology of a real human thorax makes such analytical solutions unrealistic. The common way of approaching the problem is the numerical solution of a set of differential equations supported by a finite element model of the thorax [196]. In synthesis, the method consists on creating a model of the thorax cross-section formed by a set of m elements, each of them depicting a constant impedance value σ_m and on solving the simplified version of the Maxwell equations with different boundary conditions for the potential variable v [197]:

$$\text{Given } \theta\text{: } \nabla \cdot \sigma_m \nabla v = 0 \; \forall m$$

Equation 46

An open-source tool for FEM meshing and tomographic reconstruction is available by the EIT community under the umbrella of the open-source EIDORS project [198]. Obviously, the similarity of the FEM mesh to the real morphology of the thorax will be of paramount importance in the accuracy of the solution [199]. Examples of MRI-based meshing can be

found in [200] and [201]. Note that the number of elements (m) of the FEM corresponds to the dimensionality of the parameter vector θ to be estimated in Equation 45.

Although the different biological tissues within the thorax depict a very large range of impedance values, cardio-respiratory activity induce only small modifications. Accordingly, , $f(\theta)$ can be linearized around a working point θ_0:

$$f(\theta) \simeq \mathbf{F}(\theta_0) + \mathbf{H}(\theta - \theta_0)$$

Equation 47

where **F** is in general a non-linear function according to Equation 45, and **H** is a $n \cdot m$ matrix projecting small changes of θ into the induced changes in z. **H** is commonly referred as sensitivity matrix. A first advantage of performing differential EIT image reconstructions is now introduced. Since the working point θ_0 of differential imaging is a null model, *i.e.* we assume $\mathrm{E}[\theta] = 0$, the forward model becomes a purely linear model:

$$f(\theta) \simeq \mathbf{H}\theta$$

Equation 48

In practical terms, both assumptions (1- linearized $f(\theta)$ and 2- differential EIT imaging) allow the forward model to be replaced by a simple matrix multiplication. The sensitivity matrix **H** is then to be computed only once, given the FEM of a thorax and the location of the EIT electrodes.

The inverse problem in EIT consists on solving the posed minimization problem $\hat{\theta} = \mathrm{argmin}_\theta \ \phi(f(\theta), z)$. The nature of such a problem depends on the actual definition of the error function $\phi(f(\theta), z)$. On the one hand, the computation of 1-norm distances ($a = 1$) has been demonstrated to provide optimal reconstruction contrast [202]. Unfortunately, such a strategy leads to a non-linear problem, and the resolution of Equation 45 requires iterative numerical solutions [195]. Since the introduction of EIT to monitor cardiovascular phenomena demands to acquire tomographic images at high imaging rates (*e.g.* 50 images per second), such numerically complexity is not desired. On the other hand, the computation of 2-norm distances ($a = 2$) leads to a quadratic problem. Because of the interesting properties of quadratic problems, this is the most implemented version of the EIT inverse problem. In the following, we develop Equation 45 under the assumption of a quadratic error definition. In particular, we are looking for a $\hat{\theta}$ that satisfies:

$$\hat{\theta} = \mathrm{argmin}_\theta \ \|f(\theta) - z\|_{\mathbf{W}}^2$$

Equation 49

Unfortunately, the large amount of parameters to be estimated in Equation 49 turns EIT to be an ill-posed problem, and may lead the instabilities producing unrealistic θ estimates. The introduction of a Tikhonov regularization term controls such instabilities by avoiding θ diverging towards infinite, *i.e.*:

$$\hat{\theta} = \mathrm{argmin}_\theta \ \|f(\theta) - z\|_{\mathbf{W}}^2 + \lambda^2 \ \|\theta - \theta_0\|_{\mathbf{V}}^2$$

Equation 50

Where:

- λ controls the strength of the regularization (penalty strength, or hyper-parameter)
- θ_0 depicts a reference numerical model of the thorax
- $\mathbf{V}$ defines a regularization weighting matrix.

The second advantage of performing differential EIT reconstructions (versus absolute EIT reconstructions) appears at this stage of the inverse problem. Assuming now θ_0 to be a null vector, and assuming the forward model to be well represented by the sensitivity matrix **H**, Equation 50 becomes:

$$\hat{\theta} = \text{argmin}_{\theta} \ \|\mathbf{H}\theta - z\|_{\boldsymbol{W}}^2 + \lambda^2 \ \|\theta\|_{\mathbf{V}}^2$$

Equation 51

Differentiating and solving for θ creates a closed-form solution as it follows:

$$\hat{\theta} = \ (\mathbf{H}^t\mathbf{W}\,\mathbf{H} + \lambda^2\mathbf{V})^{-1}\,\mathbf{H}^t\mathbf{W}z$$

Equation 52

Therefore, under the assumptions of linearity and differential imaging, the EIT inverse problem is simplified to (Figure 2.51):

1. Calculating once the sensitivity matrix **H**, given a FEM of the thorax and the position of the EIT electrodes.
2. For each set of differential impedance measurements z, obtaining the quadratic-optimal EIT reconstruction by performing the matrix operation depicted in Equation 52.

The solution to the inverse problem is thus controlled by three parameters:

- **V** is a matrix controlling the behavior of the regularization process, regularization matrix in Equation 51. In particular, **V** is commonly used to determine the amount of sharpness of the model θ, *i.e.* **V** is a smoothing matrix encouraging smooth θ solutions and penalizing sharp and abrupt solutions. See [198] for a description of actual **V** matrix implementation.
- λ is a positive scalar value controlling the strength of the smoothing penalty term. In particular, high λ values will produce smooth EIT images, and low λ values will produce sharp and discontinuous EIT images.
- **W** is a matrix controlling the weight given to each element of z in the computation of the errors. In particular, **W** is used to penalize those measurements that are assumed to be noisy or unreliable, and to increase the influence of those measurements identified as reliable. See [203, 204] for a description of actual **W** matrix implementations.

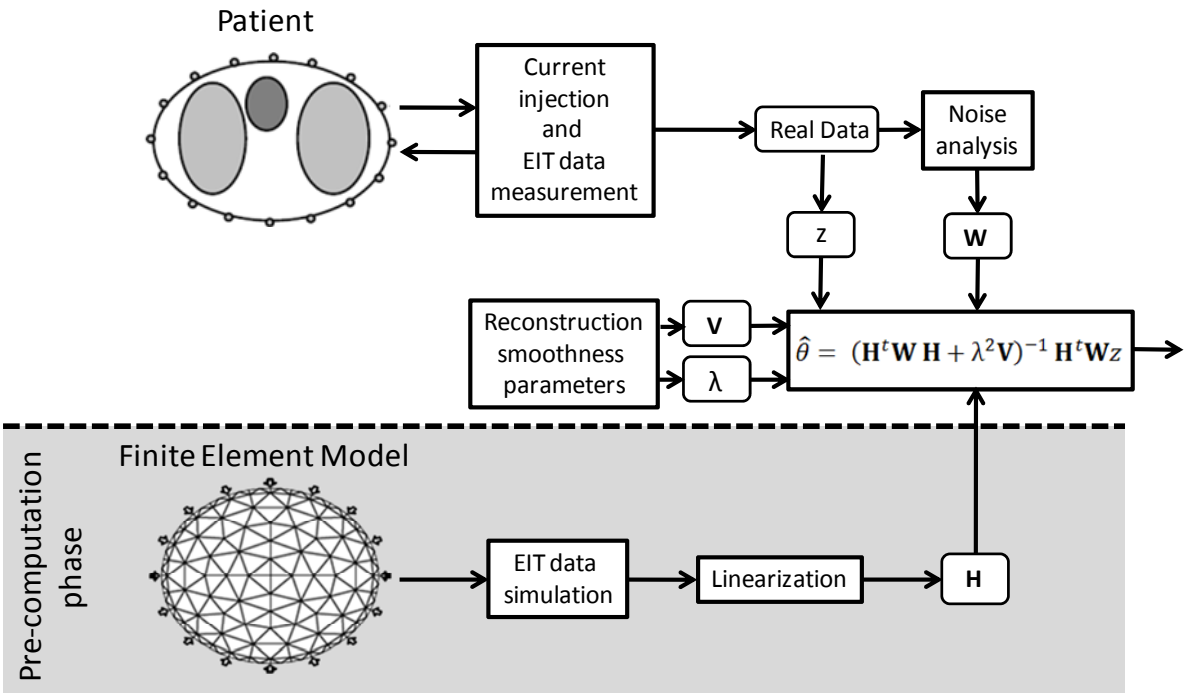

Figure 2.51: Linearized EIT reconstruction algorithm. After the pre-computation of the sensitive matrix $\mathbf{H}$, the estimation of the most-likely distribution of thoracic impedances requires only a matrix calculation involving the measured impedance data z, a noise-penalty matrix $\mathbf{W}$, and the smoothness parameter λ and smoothness matrix $\mathbf{V}$.

Novel strategies for the resolution of the EIT problem given a quadratic minimization problem such as Equation 52 have been proposed relying on the Bayesian philosophy [197]. Within this probabilistic framework the challenge is to estimate the thoracic impedance distribution (θ) that maximizes a likelihood function $p(\theta|z)$, given the measurements z. Then, applying Baye's theorem, the so-called maximum *a-posteriori* (MAP) estimate of θ is:

$$\begin{aligned}\hat{\theta}_{\mathrm{MAP}} &= \mathrm{argmax}_{\theta}\, p(\theta|z) \\ &= \mathrm{argmax}_{\theta}\, p(z|\theta)\, p(\theta)\end{aligned}$$

Equation 53

Finally, assuming the likelihood function p to be Gaussian, it can be shown [186] that the θ fulfilling the MAP criterions is:

$$\hat{\theta}_{\mathrm{MAP}} = \mathrm{argmin}_{\theta}\, \frac{1}{2}\big(z - f(\theta)\big)^T\, \mathbf{C}_z^{-1}\big(z - f(\theta)\big) + \frac{1}{2}(\theta - m_\theta)^T\, \mathbf{C}_\theta^{-1}(\theta - m_\theta)$$

Equation 54

which is a particular case of the Tikhonov-regularized estimator of Equation 50, with $\boldsymbol{C}_z^{-1} = \mathbf{W}$, $\mathbf{C}_\theta^{-1} = \mathbf{V}$, and $m_\theta = \theta_0$. Note that according to such a Bayesian framework, the regularization matrix $\mathbf{V}$ is now interpreted as the prior information of probability distribution of the model θ.

Notwithstanding, the Bayesian view of the EIT problem provides much more than a simple probabilistic understanding of a deterministic problem. An innovative technique for EIT has been introduced by Vauhkonen to resolve the EIT inverse problem [197]: rather than considering a punctual optimal estimate of θ, the proposed dynamic approach takes into account the temporal evolution of θ, *i.e.* estimating the optimal sequence of $\theta(t)$ [205]. Because, in general, physical and physiological constraints determine the dynamics of $\theta(t)$ this is expected to guide the solution of the inverse problem. The method by Vauhkonen is based on the particular hypothesis that the temporal dynamics of $\theta(t)$ can be modeled by a state-space representation and particularly by an Auto-Regressive model (AR), i.e:

$$\begin{aligned} \theta_{t+1} &= \mathbf{A}_t\theta_t + \omega_t \\ f(\theta_t) &= \mathbf{H}_t\,\theta_t \end{aligned}$$

Equation 55

where $\mathbf{A}_\mathrm{t}$ and ω_t are respectively the state transition matrix of the AR model and the state transition process noise, and $\mathbf{H}_t$ is the linearized forward model as described in Equation 48. Now, given a set of bioimpedance measurements $z(t)$: $t = 0 \ldots T$, the goal is to determine the most likely set of underlying thoracic model states θ_t: $t = 0 \ldots T$ that generated such measurements. Under the exposed constraints, such a classical linear system identification problem can be dynamically solved, in a MMSE optimal sense, by the so-called Kalman Filter. Implementations of this dynamic estimate have been already proposed [206, 207].

Functional analysis of electrical impedance tomography

As depicted by Figure 2.47, from a sequence of EIT images acquired at high sampling frequencies (*e.g.* 50 images/second) those pixels depicting functional information related to the heart, lungs and other anatomical structures such as the aorta are to be identified.

Functional analysis of electrical impedance tomography images relies thus on the identification of specific pixels according to functional behavior. In particular, functional analysis comprises the steps of:

1. Generating for each pixel a time series depicting functional changes of impedance at the underlying anatomical structure due to either respiratory or cardiac activities.
2. Analyzing said time series to extract a set of features characterizing the functional behavior of the corresponding pixel. Pixel-dependent features might include information on the amount of respiratory activity at the pixel, the amount of cardio-related activity (*i.e.* perfusion of the underlying structure), shape of a pressure pulse arriving at the pixel, arrival time of such pressure pulse, …
3. Grouping together those pixels depicting similar functional behavior and/or being located at specific regions of interest

Functional information from the identified pixels is then processed as if a virtual catheter was placed into the target organs and structures (see Figure 2.46). An example functional analysis of sequences of electrical impedance tomography for the detection of pixels depicting relevant information on the heart and lungs is provided in [199]. A novel functional analysis approach to identify aorta-related pixels is described in in Section 4.

Commercialized EIT systems

In order to conclude this section, a list of commercial EIT systems is provided in Table 2.11. Note that the most of the listed devices are research-oriented, and have been produced in very small quantities. To date, none of these systems has been introduced in clinical routine.

Table 2.11: Commercial EIT systems.

Commercial and research EIT devices	
Sheffield Mk 3.5 Number of electrodes: 8 Electrical Injection Frequency: 2 kHz - 1.6 MHz Image rate: 25 images/second Producer: Maltron International Ltd, UK	
Dräger EIT-guided ventilator Number of electrodes: 16 Electrical Injection Frequency: not available Image rate: 30 images/second Producer : Dräger Medical AG & Co, Germany	
Göttingen GoeMF II EIT tomograph Number of electrodes: 16 Electrical Injection Frequency: n.a. Image rate: 44 images/second Producer : CareFusion, CA, US	
Enlight Number of electrodes: 32 Electrical Injection Frequency: 125 kHz Image rate: 50 images/second Producer : Timpel SA, BR	
Swisstom Number of electrodes: 32 Electrical Injection Frequency: 125 kHz Image rate: 50 images/second Producer : Swisstom AG, CH	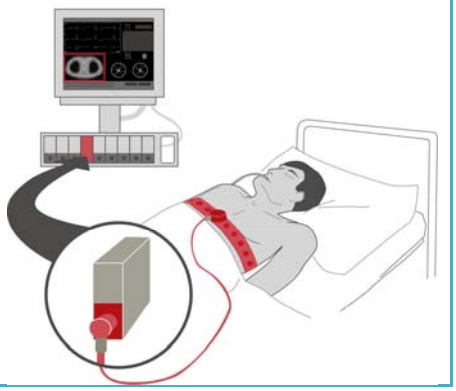

References

[1] J. R. Levick, *An introduction to Cardiovascular Physiology*, Fourth ed. New York: Arnold Publishers, 2003.

[2] A. C. Guyton and J. E. Hall, *Textbook of Medical Physiology*: Saunders, 2000.

[3] K. Hirata*, et al.*, "Pulse wave analysis and pulse wave velocity: a review of blood pressure interpretation 100 years after Korotkov," *Circ J,* vol. 70, pp. 1231-9, Oct 2006.

[4] G. Mancia*, et al.*, "[ESH/ESC 2007 Guidelines for the management of arterial hypertension]," *Rev Esp Cardiol,* vol. 60, pp. 968 e1-94, Sep 2007.

[5] P. M. Kearney*, et al.*, "Global burden of hypertension: analysis of worldwide data," *Lancet,* vol. 365, pp. 217-23, Jan 15-21 2005.

[6] P. K. Whelton*, et al.*, "Prevalence, awareness, treatment and control of hypertension in North America, North Africa and Asia," *J Hum Hypertens,* vol. 18, pp. 545-51, Aug 2004.

[7] G. Mancia*, et al.*, "2007 Guidelines for the management of arterial hypertension: The Task Force for the Management of Arterial Hypertension of the European Society of Hypertension (ESH) and of the European Society of Cardiology (ESC)," *Eur Heart J,* vol. 28, pp. 1462-536, Jun 2007.

[8] E. O'Brien*, et al.*, "Use and interpretation of ambulatory blood pressure monitoring: recommendations of the British hypertension society," *BMJ,* vol. 320, pp. 1128-34, Apr 22 2000.

[9] L. A. Geddes, *Handbook of Blood Pressure Measurement*: Humana Press, 1991.

[10] E. O'Brien*, et al.*, "Blood pressure measuring devices: recommendations of the European Society of Hypertension," *BMJ,* vol. 322, pp. 531-6, Mar 3 2001.

[11] E. O'Brien. (2011). *A short history of blood pressure measurement*. Available: http://www.bloodpressurehistory.com/history.html

[12] Y. L. Shevchenko and J. E. Tsitlik, "90th Anniversary of the development by Nikolai S. Korotkoff of the auscultatory method of measuring blood pressure," *Circulation,* vol. 94, pp. 116-8, Jul 15 1996.

[13] T. G. Pickering*, et al.*, "Recommendations for blood pressure measurement in humans and experimental animals: Part 1: blood pressure measurement in humans: a statement for professionals from the Subcommittee of Professional and Public Education of the American Heart Association Council on High Blood Pressure Research," *Hypertension,* vol. 45, pp. 142-61, Jan 2005.

[14] M. Nitzan*, et al.*, "Automatic noninvasive measurement of systolic blood pressure using photoplethysmography," *Biomed Eng Online,* vol. 8, p. 28, 2009.

[15] M. Ramsey, 3rd, "Blood pressure monitoring: automated oscillometric devices," *J Clin Monit,* vol. 7, pp. 56-67, Jan 1991.

[16] M. Marey, "Lectures on the Graphic Method the Experimental Sciences, and on its Special Application to Medicine," *Br Med J,* vol. 1, pp. 65-6, Jan 15 1876.

[17] J. S. Floras, "Ambulatory blood pressure: facilitating individualized assessment of cardiovascular risk," *J Hypertens,* vol. 25, pp. 1565-8, Aug 2007.

[18] J. A. Staessen*, et al.*, "Task Force II: blood pressure measurement and cardiovascular outcome," *Blood Press Monit,* vol. 6, pp. 355-70, Dec 2001.

[19] G. M. Drzewiecki*, et al.*, "Arterial tonometry: review and analysis," *J Biomech,* vol. 16, pp. 141-52, 1983.
[20] K. Matthys and P. Verdonck, "Development and modelling of arterial applanation tonometry: a review," *Technol Health Care,* vol. 10, pp. 65-76, 2002.
[21] G. K. Archibald*, et al.*, "Wrist mounted blood pressure sensor," US Patent, 1997.
[22] K. Belani*, et al.*, "A new noninvasive method to measure blood pressure: results of a multicenter trial," *Anesthesiology,* vol. 91, pp. 686-92, Sep 1999.
[23] C. L. Cua*, et al.*, "A comparison of the Vasotrac with invasive arterial blood pressure monitoring in children after pediatric cardiac surgery," *Anesth Analg,* vol. 100, pp. 1289-94, table of contents, May 2005.
[24] S. Skinner, "A clinical guide to pulse wave analysis," A. Medical, Ed., ed, 2009.
[25] J. Penaz, "Photoelectric measurement of blood pressure, volume and flow in the finger," presented at the International Conference in Medicine and Biological Engineering, 1973.
[26] FMS, "Finger pressure reference guide," FMS, Finapres Medical Systems BV2005.
[27] B. P. Imholz*, et al.*, "Continuous finger arterial pressure: utility in the cardiovascular laboratory," *Clin Auton Res,* vol. 1, pp. 43-53, Mar 1991.
[28] A. Lindqvist, "Beat-to-beat agreement of non-invasive finger artery and invasive radial artery blood pressure in hypertensive patients taking cardiovascular medication," *Clin Physiol,* vol. 15, pp. 219-29, May 1995.
[29] A. A. Birch and S. L. Morris, "Do the Finapres and Colin radial artery tonometer measure the same blood pressure changes following deflation of thigh cuffs?," *Physiol Meas,* vol. 24, pp. 653-60, Aug 2003.
[30] H. L. Ristuccia*, et al.*, "Incremental bias in Finapres estimation of baseline blood pressure levels over time," *Hypertension,* vol. 29, pp. 1039-43, Apr 1997.
[31] B. P. Imholz*, et al.*, "Fifteen years experience with finger arterial pressure monitoring: assessment of the technology," *Cardiovasc Res,* vol. 38, pp. 605-16, Jun 1998.
[32] L. W. Bogert and J. J. van Lieshout, "Non-invasive pulsatile arterial pressure and stroke volume changes from the human finger," *Exp Physiol,* vol. 90, pp. 437-46, Jul 2005.
[33] S. Laurent and J. Cockroft, *Central aortic blood pressure*: Elsevier, 2008.
[34] E. King*, et al.*, "The reliable measurement of radial pulse characteristics," *Acupunct Med,* vol. 20, pp. 150-9, Dec 2002.
[35] N. Westerhof*, et al.*, *Snapshots of Hemodynamics*: Springer, 2005.
[36] R. Asmar, *Arterial Stiffness and Pulse Wave Velocity. Clinical Applications*: ELSEVIER, 1999.
[37] A. P. Avolio*, et al.*, "Effects of aging on arterial distensibility in populations with high and low prevalence of hypertension: comparison between urban and rural communities in China," *Circulation,* vol. 71, pp. 202-10, Feb 1985.
[38] M. Faber and G. Oller-Hou, "The human aorta. V. Collagen and elastin in the normal and hypertensive aorta," *Acta Pathol Microbiol Scand,* vol. 31, pp. 377-82, 1952.
[39] A. P. Avolio*, et al.*, "Effects of aging on changing arterial compliance and left ventricular load in a northern Chinese urban community," *Circulation,* vol. 68, pp. 50-8, Jul 1983.
[40] G. M. London*, et al.*, "Influence of sex on arterial hemodynamics and blood pressure. Role of body height," *Hypertension,* vol. 26, pp. 514-9, Sep 1995.

[41] B. Sonesson*, et al.*, "Compliance and diameter in the human abdominal aorta--the influence of age and sex," *Eur J Vasc Surg,* vol. 7, pp. 690-7, Nov 1993.

[42] A. Benetos*, et al.*, "Determinants of accelerated progression of arterial stiffness in normotensive subjects and in treated hypertensive subjects over a 6-year period," *Circulation,* vol. 105, pp. 1202-7, Mar 12 2002.

[43] P. Boutouyrie*, et al.*, "Sympathetic activation decreases medium-sized arterial compliance in humans," *Am J Physiol,* vol. 267, pp. H1368-76, Oct 1994.

[44] A. M. Dart and B. A. Kingwell, "Pulse pressure--a review of mechanisms and clinical relevance," *J Am Coll Cardiol,* vol. 37, pp. 975-84, Mar 15 2001.

[45] J. D. Bouthier*, et al.*, "Cardiac hypertrophy and arterial distensibility in essential hypertension," *Am Heart J,* vol. 109, pp. 1345-52, Jun 1985.

[46] A. Toprak*, et al.*, "Relation of pulse pressure and arterial stiffness to concentric left ventricular hypertrophy in young men (from the Bogalusa Heart Study)," *Am J Cardiol,* vol. 103, pp. 978-84, Apr 1 2009.

[47] M. F. O'Rourke and M. E. Safar, "Relationship between aortic stiffening and microvascular disease in brain and kidney: cause and logic of therapy," *Hypertension,* vol. 46, pp. 200-4, Jul 2005.

[48] S. Laurent*, et al.*, "Aortic stiffness is an independent predictor of fatal stroke in essential hypertension," *Stroke,* vol. 34, pp. 1203-6, May 2003.

[49] L. H. Henskens*, et al.*, "Increased aortic pulse wave velocity is associated with silent cerebral small-vessel disease in hypertensive patients," *Hypertension,* vol. 52, pp. 1120-6, Dec 2008.

[50] P. Fesler*, et al.*, "Pulse pressure is an independent determinant of renal function decline during treatment of essential hypertension," *J Hypertens,* vol. 25, pp. 1915-20, Sep 2007.

[51] S. K. Glen*, et al.*, "White-coat hypertension as a cause of cardiovascular dysfunction," *Lancet,* vol. 348, pp. 654-7, Sep 7 1996.

[52] X. Girerd*, et al.*, "Early arterial modifications in young patients with borderline hypertension," *J Hypertens Suppl,* vol. 7, pp. S45-7, Feb 1989.

[53] B. H. Lorell and B. A. Carabello, "Left ventricular hypertrophy: pathogenesis, detection, and prognosis," *Circulation,* vol. 102, pp. 470-9, Jul 25 2000.

[54] T. Willum-Hansen*, et al.*, "Prognostic value of aortic pulse wave velocity as index of arterial stiffness in the general population," *Circulation,* vol. 113, pp. 664-70, Feb 7 2006.

[55] S. Laurent*, et al.*, "Aortic stiffness is an independent predictor of all-cause and cardiovascular mortality in hypertensive patients," *Hypertension,* vol. 37, pp. 1236-41, May 2001.

[56] G. Mancia*, et al.*, "2007 Guidelines for the Management of Arterial Hypertension: The Task Force for the Management of Arterial Hypertension of the European Society of Hypertension (ESH) and of the European Society of Cardiology (ESC)," *J Hypertens,* vol. 25, pp. 1105-87, Jun 2007.

[57] F. J. van Ittersum*, et al.*, "Autonomic nervous function, arterial stiffness and blood pressure in patients with Type I diabetes mellitus and normal urinary albumin excretion," *J Hum Hypertens,* vol. 18, pp. 761-8, Nov 2004.

[58] K. Cruickshank*, et al.*, "Aortic pulse-wave velocity and its relationship to mortality in diabetes and glucose intolerance: an integrated index of vascular function?," *Circulation,* vol. 106, pp. 2085-90, Oct 15 2002.

[59] M. T. Schram, *et al.*, "Increased central artery stiffness in impaired glucose metabolism and type 2 diabetes: the Hoorn Study," *Hypertension,* vol. 43, pp. 176-81, Feb 2004.

[60] C. Giannattasio, *et al.*, "Early impairment of large artery structure and function in type I diabetes mellitus," *Diabetologia,* vol. 42, pp. 987-94, Aug 1999.

[61] R. Ravikumar, *et al.*, "Comparison of carotid intima-media thickness, arterial stiffness, and brachial artery flow mediated dilatation in diabetic and nondiabetic subjects (The Chennai Urban Population Study [CUPS-9])," *Am J Cardiol,* vol. 90, pp. 702-7, Oct 1 2002.

[62] R. M. Henry, *et al.*, "Arterial stiffness increases with deteriorating glucose tolerance status: the Hoorn Study," *Circulation,* vol. 107, pp. 2089-95, Apr 29 2003.

[63] F. U. Mattace-Raso, *et al.*, "Arterial stiffness and risk of coronary heart disease and stroke: the Rotterdam Study," *Circulation,* vol. 113, pp. 657-63, Feb 7 2006.

[64] S. Meaume, *et al.*, "Aortic pulse wave velocity predicts cardiovascular mortality in subjects >70 years of age," *Arterioscler Thromb Vasc Biol,* vol. 21, pp. 2046-50, Dec 2001.

[65] K. Sutton-Tyrrell, *et al.*, "Elevated aortic pulse wave velocity, a marker of arterial stiffness, predicts cardiovascular events in well-functioning older adults," *Circulation,* vol. 111, pp. 3384-90, Jun 28 2005.

[66] A. P. Guerin, *et al.*, "Impact of aortic stiffness attenuation on survival of patients in end-stage renal failure," *Circulation,* vol. 103, pp. 987-92, Feb 20 2001.

[67] J. D. Cameron, *et al.*, "The relationship between arterial compliance, age, blood pressure and serum lipid levels," *J Hypertens,* vol. 13, pp. 1718-23, Dec 1995.

[68] A. M. Dart, *et al.*, "Large artery stiffness is not related to plasma cholesterol in older subjects with hypertension," *Arterioscler Thromb Vasc Biol,* vol. 24, pp. 962-8, May 2004.

[69] Y. L. Liang, *et al.*, "Effects of Blood Pressure, Smoking, and Their Interaction on Carotid Artery Structure and Function," *Hypertension,* vol. 37, pp. 6-11, Jan 2001.

[70] N. A. Jatoi, *et al.*, "Impact of smoking and smoking cessation on arterial stiffness and aortic wave reflection in hypertension," *Hypertension,* vol. 49, pp. 981-5, May 2007.

[71] T. Hirai, *et al.*, "Stiffness of systemic arteries in patients with myocardial infarction. A noninvasive method to predict severity of coronary atherosclerosis," *Circulation,* vol. 80, pp. 78-86, Jul 1989.

[72] C. Giannattasio, *et al.*, "Relationship between arterial distensibility and coronary atherosclerosis in angina patients," *J Hypertens,* vol. 25, pp. 593-8, Mar 2007.

[73] N. M. van Popele, *et al.*, "Association between arterial stiffness and atherosclerosis: the Rotterdam Study," *Stroke,* vol. 32, pp. 454-60, Feb 2001.

[74] K. Shinohara, *et al.*, "Arterial stiffness in predialysis patients with uremia," *Kidney Int,* vol. 65, pp. 936-43, Mar 2004.

[75] R. Asmar, *et al.*, "Assessment of arterial distensibility by automatic pulse wave velocity measurement. Validation and clinical application studies," *Hypertension,* vol. 26, pp. 485-90, Sep 1995.

[76] M. W. Rajzer, *et al.*, "Comparison of aortic pulse wave velocity measured by three techniques: Complior, SphygmoCor and Arteriograph," *J Hypertens,* vol. 26, pp. 2001-7, Oct 2008.

[77] S. C. Millasseau, *et al.*, "Evaluation of carotid-femoral pulse wave velocity: influence of timing algorithm and heart rate," *Hypertension,* vol. 45, pp. 222-6, Feb 2005.

[78] R. D. Latham*, et al.*, "Regional wave travel and reflections along the human aorta: a study with six simultaneous micromanometric pressures," *Circulation,* vol. 72, pp. 1257-69, Dec 1985.

[79] W. W. Nichols and M. F. O'Rourke, "Aortic pulse wave velocity, reflection site distance, and augmentation index," *Hypertension,* vol. 53, p. e9; author reply e10, Jan 2009.

[80] J. Baulmann*, et al.*, "A new oscillometric method for assessment of arterial stiffness: comparison with tonometric and piezo-electronic methods," *J Hypertens,* vol. 26, pp. 523-8, Mar 2008.

[81] S. C. Millasseau*, et al.*, "Contour analysis of the photoplethysmographic pulse measured at the finger," *J Hypertens,* vol. 24, pp. 1449-56, Aug 2006.

[82] C. H. Chen*, et al.*, "Estimation of central aortic pressure waveform by mathematical transformation of radial tonometry pressure. Validation of generalized transfer function," *Circulation,* vol. 95, pp. 1827-36, Apr 1 1997.

[83] M. F. O'Rourke, "Time domain analysis of the arterial pulse in clinical medicine," *Med Biol Eng Comput,* vol. 47, pp. 119-29, Feb 2009.

[84] D. Gallagher*, et al.*, "Validation of the transfer function technique for generating central from peripheral upper limb pressure waveform," *Am J Hypertens,* vol. 17, pp. 1059-67, Nov 2004.

[85] M. Karamanoglu*, et al.*, "Pressure wave propagation in a multibranched model of the human upper limb," *Am J Physiol,* vol. 269, pp. H1363-9, Oct 1995.

[86] Q. Li and G. G. Belz, "Systolic time intervals in clinical pharmacology," *Eur J Clin Pharmacol,* vol. 44, pp. 415-21, 1993.

[87] R. A. Payne*, et al.*, "Pulse transit time measured from the ECG: an unreliable marker of beat-to-beat blood pressure," *J Appl Physiol,* vol. 100, pp. 136-41, Jan 2006.

[88] G. G. Berntson*, et al.*, "Where to Q in PEP," *Psychophysiology,* vol. 41, pp. 333-7, Mar 2004.

[89] P. Abassade and Y. Baudouy, "Relationship between arterial distensibility and left ventricular function in the timing of Korotkoff sounds (QkD internal). An ambulatory pressure monitoring and echocardiographic study.," *American Journal of Hypertension,* vol. 15, p. 67A, 2002.

[90] J. Constans*, et al.*, "Arterial stiffness predicts severe progression in systemic sclerosis: the ERAMS study," *J Hypertens,* vol. 25, pp. 1900-6, Sep 2007.

[91] R. P. Smith*, et al.*, "Pulse transit time: an appraisal of potential clinical applications," *Thorax,* vol. 54, pp. 452-7, May 1999.

[92] P. Fung*, et al.*, "Continuous noninvasive blood pressure measurement by pulse transit time," *Conf Proc IEEE Eng Med Biol Soc,* vol. 1, pp. 738-41, 2004.

[93] D. J. Schwartz, "The pulse transit time arousal index in obstructive sleep apnea before and after CPAP," *Sleep Med,* vol. 6, pp. 199-203, May 2005.

[94] J. Muehlsteff*, et al.*, "Cuffless estimation of systolic blood pressure for short effort bicycle tests: the prominent role of the pre-ejection period," *Conf Proc IEEE Eng Med Biol Soc,* vol. 1, pp. 5088-92, 2006.

[95] J. Lotz*, et al.*, "Cardiovascular flow measurement with phase-contrast MR imaging: basic facts and implementation," *Radiographics,* vol. 22, pp. 651-71, May-Jun 2002.

[96] R. H. Mohiaddin and D. B. Longmore, "MRI studies of atherosclerotic vascular disease: structural evaluation and physiological measurements," *Br Med Bull,* vol. 45, pp. 968-90, Oct 1989.

[97] G. Gang, *et al.*, "Measurement of pulse wave velocity using magnetic resonance imaging," *Conf Proc IEEE Eng Med Biol Soc,* vol. 5, pp. 3684-7, 2004.
[98] S. S. Giri, *et al.*, "Automated and accurate measurement of aortic pulse wave velocity using magnetic resonance imaging," *Computers in Cardiology,* pp. 661 - 664 2007.
[99] M. Butlin, *et al.*, "Determining pulse wave velocity using MRI: a comparison and repeatability of results using seven transit time algorithms," *Artery research,* vol. 2, 2008.
[100] J. P. Baguet, *et al.*, "Analysis of the regional pulse wave velocity by Doppler: methodology and reproducibility," *J Hum Hypertens,* vol. 17, pp. 407-12, Jun 2003.
[101] W. W. Nichols and M. F. O'Rourke, *McDonald's Blood Flow in Arteries*. Oxford: Oxford University Press, 2005.
[102] D. H. Bergel, "The static elastic properties of the arterial wall," *J Physiol,* vol. 156, pp. 445-57, May 1961.
[103] C. C. Poon and Y. T. Zhang, "Cuff-less and noninvasive measurements of arterial blood pressure by pulse transit time," *Conf Proc IEEE Eng Med Biol Soc,* vol. 6, pp. 5877-80, 2005.
[104] J. Y. Foo, *et al.*, "Evaluation of blood pressure changes using vascular transit time," *Physiol Meas,* vol. 27, pp. 685-94, Aug 2006.
[105] W. Chen, *et al.*, "Continuous estimation of systolic blood pressure using the pulse arrival time and intermittent calibration," *Med Biol Eng Comput,* vol. 38, pp. 569-74, Sep 2000.
[106] A. Steptoe, *et al.*, "Pulse wave velocity and blood pressure change: calibration and applications," *Psychophysiology,* vol. 13, pp. 488-93, Sep 1976.
[107] D. Barschdorff, *et al.*, "Noninvasive continuous blood pressure determination," presented at the XVI IMEKO World Congress, Wien, 2000.
[108] E. Park, *et al.*, "Continuous measurement of systolic blood pressure using the PTT and other parameters," *Conf Proc IEEE Eng Med Biol Soc,* vol. 4, pp. 3555-8, 2005.
[109] J. S. Kim, *et al.*, "Two unconstrained methods for blood pressure monitoring in a ubiquitous home healthcare," presented at the Fifth International Conference Biomedical Engineering, Innsbruck, 2007.
[110] C. Y. Poon and Y. T. Zhang, "The Beat-toBeat Relationship between Pulse Transit time and Systolic Blood Pressure," presented at the International Conference on Information Technology and Application in Biomedicine, Shenzen, 2008.
[111] Y. Chen, *et al.*, "Continuous non-invasive blood pressure monitoring method and apparatus," US Patent, 2003.
[112] Y. S. Yan and Y. T. Zhang, "A Novel Calibration Method for Noninvasive Blood Pressure Measurement Using Pulse Transit Time," presented at the IEEE-EMBS International Summer School and Symposium on Medical Devices and Biosensors, Cambridge, 2007.
[113] D. B. McCombie, *et al.*, "Adaptive hydrostatic blood pressure calibration: development of a wearable, autonomous pulse wave velocity blood pressure monitor," *Conf Proc IEEE Eng Med Biol Soc,* vol. 2007, pp. 370-3, 2007.
[114] J. Sola, *et al.*, "Continuous monitoring of coordinated cardiovascular responses," *Conf Proc IEEE Eng Med Biol Soc,* vol. 2008, pp. 1423-6, 2008.
[115] J. Solà and H.-A. Loeliger, "Method and apparatus for a continuous non-invasive and non-occlusive monitoring of blood pressure," 2009.

[116] J. Malmivuo and R. Plonsey, *Bioelectromagnetism - Principles and Applications of Bioelectric and Biomagnetic Fields*. New York: Oxford University Press, 1995.

[117] A. Gruetzmann*, et al.*, "Novel dry electrodes for ECG monitoring," *Physiol Meas,* vol. 28, pp. 1375-90, Nov 2007.

[118] P. J. Xu*, et al.*, "Textile-structured electrodes for electrocardiogram," *Textil progress,* vol. 40, pp. 183-213, 2008.

[119] J. Luprano*, et al.*, "Heartcycle sensors and parameter extraction," in *pHealth 2010*, 2010.

[120] M. Pacelli*, et al.*, "Sensing Fabrics for Monitoring Physiological and Biomechanical Variables: E-textile solutions," presented at the International Summer School and Symposium on Medical Devices and Biosensors, MIT, Boston, 2006.

[121] R. Paradiso and D. De Rossi, "Advances in textile technologies for unobtrusive monitoring of vital parameters and movements," *Conf Proc IEEE Eng Med Biol Soc,* vol. 1, pp. 392-5, 2006.

[122] O. Chételat*, et al.*, " Continuous multi-parameter health monitoring system," presented at the World Congress on Medical Physics and Biomedical Engineering, Seoul, 2006.

[123] IEC, "Medical electrical equipment," in *Particular requirements for the safety, including essential performance, of ambulatory electrocardiographic systems* vol. IEC 60601-2-47:2001(E), ed, 2001.

[124] P. Kligfield*, et al.*, "Recommendations for the standardization and interpretation of the electrocardiogram. Part I: The electrocardiogram and its technology. A scientific statement from the American Heart Association Electrocardiography and Arrhythmias Committee, Council on Clinical Cardiology; the American College of Cardiology Foundation; and the Heart Rhythm Society," *Heart Rhythm,* vol. 4, pp. 394-412, Mar 2007.

[125] J. W. Mason*, et al.*, "Recommendations for the standardization and interpretation of the electrocardiogram: part II: electrocardiography diagnostic statement list a scientific statement from the American Heart Association Electrocardiography and Arrhythmias Committee, Council on Clinical Cardiology; the American College of Cardiology Foundation; and the Heart Rhythm Society Endorsed by the International Society for Computerized Electrocardiology," *J Am Coll Cardiol,* vol. 49, pp. 1128-35, Mar 13 2007.

[126] B. Surawicz*, et al.*, "AHA/ACCF/HRS recommendations for the standardization and interpretation of the electrocardiogram: part III: intraventricular conduction disturbances: a scientific statement from the American Heart Association Electrocardiography and Arrhythmias Committee, Council on Clinical Cardiology; the American College of Cardiology Foundation; and the Heart Rhythm Society: endorsed by the International Society for Computerized Electrocardiology," *Circulation,* vol. 119, pp. e235-40, Mar 17 2009.

[127] P. M. Rautaharju*, et al.*, "AHA/ACCF/HRS recommendations for the standardization and interpretation of the electrocardiogram: part IV: the ST segment, T and U waves, and the QT interval: a scientific statement from the American Heart Association Electrocardiography and Arrhythmias Committee, Council on Clinical Cardiology; the American College of Cardiology Foundation; and the Heart Rhythm Society: endorsed by the International Society for Computerized Electrocardiology," *Circulation,* vol. 119, pp. e241-50, Mar 17 2009.

[128] G. S. Wagner*, et al.*, "AHA/ACCF/HRS recommendations for the standardization and interpretation of the electrocardiogram: part VI: acute ischemia/infarction: a scientific statement from the American Heart Association Electrocardiography and Arrhythmias Committee, Council on Clinical Cardiology; the American College of Cardiology Foundation; and the Heart Rhythm Society. Endorsed by the International Society for Computerized Electrocardiology," *J Am Coll Cardiol,* vol. 53, pp. 1003-11, Mar 17 2009.

[129] J. Pan and W. J. Tompkins, "A real-time QRS detection algorithm," *IEEE Trans Biomed Eng,* vol. 32, pp. 230-6, Mar 1985.

[130] J. Allen, "Photoplethysmography and its application in clinical physiological measurement," *Physiol Meas,* vol. 28, pp. R1-39, Mar 2007.

[131] J. G. Webster, *Design of Pulse Oximeters*. Bristol: Institute of Physics Publishing, 1997.

[132] A. Reisner*, et al.*, "Utility of the photoplethysmogram in circulatory monitoring," *Anesthesiology,* vol. 108, pp. 950-8, May 2008.

[133] P. Shaltis*, et al.*, "Calibration of the photoplethysmogram to arterial blood pressure: capabilities and limitations for continuous pressure monitoring," *Conf Proc IEEE Eng Med Biol Soc,* vol. 4, pp. 3970-3, 2005.

[134] I. Fine and A. Weinreb, "Multiple scattering effect in transmission pulse oximetry," *Med Biol Eng Comput,* vol. 33, pp. 709-12, Sep 1995.

[135] P. D. Mannheimer, "The light-tissue interaction of pulse oximetry," *Anesth Analg,* vol. 105, pp. S10-7, Dec 2007.

[136] J. L. Reuss, "Arterial Pulsatility and the Modeling of Reflectance Pulse Oximetry," presented at the 25th Annual International Conference of the IEEE EMBS, Cancun, Mexico, 2003.

[137] J. T. Moyle, *Pulse Oximetry*, Second ed. Loondon: BMJ Books, 2002.

[138] Y. Mendelson and B. D. Ochs, "Noninvasive pulse oximetry utilizing skin reflectance photoplethysmography," *IEEE Trans Biomed Eng,* vol. 35, pp. 798-805, Oct 1988.

[139] P. Hua*, et al.*, "Iterative reconstruction methods using regularization and optimal current patterns in electrical impedance tomography," *IEEE Trans Med Imaging,* vol. 10, pp. 621-8, 1991.

[140] P. O. Bonetti*, et al.*, "Noninvasive identification of patients with early coronary atherosclerosis by assessment of digital reactive hyperemia," *J Am Coll Cardiol,* vol. 44, pp. 2137-41, Dec 7 2004.

[141] S. J. Barker and J. J. Badal, "The measurement of dyshemoglobins and total hemoglobin by pulse oximetry," *Curr Opin Anaesthesiol,* vol. 21, pp. 805-10, Dec 2008.

[142] F. Michard and J. L. Teboul, "Using heart-lung interactions to assess fluid responsiveness during mechanical ventilation," *Crit Care,* vol. 4, pp. 282-9, 2000.

[143] S. Maisch*, et al.*, "Heart-Lung Interactions Measured by Electrical Impedance Tomography," *Critical Care Medicine,* 2011.

[144] C. K. Hofer*, et al.*, "Stroke volume and pulse pressure variation for prediction of fluid responsiveness in patients undergoing off-pump coronary artery bypass grafting," *Chest,* vol. 128, pp. 848-54, Aug 2005.

[145] T. Loupec*, et al.*, "Pleth variability index predicts fluid responsiveness in critically ill patients," *Crit Care Med,* vol. 39, pp. 294-9, Feb 2011.

[146] O. Broch*, et al.*, "Accuracy of the pleth variability index to predict fluid responsiveness depends on the perfusion index," *Acta Anaesthesiol Scand,* Apr 11 2011.
[147] R. Rubinshtein*, et al.*, "Assessment of endothelial function by non-invasive peripheral arterial tonometry predicts late cardiovascular adverse events," *Eur Heart J,* vol. 31, pp. 1142-8, May 2010.
[148] J. E. Naschitz*, et al.*, "Pulse transit time by R-wave-gated infrared photoplethysmography: review of the literature and personal experience," *J Clin Monit Comput,* vol. 18, pp. 333-42, Dec 2004.
[149] S. Loukogeorgakis*, et al.*, "Validation of a device to measure arterial pulse wave velocity by a photoplethysmographic method," *Physiol Meas,* vol. 23, pp. 581-96, Aug 2002.
[150] I. R. Hanna and M. E. Silverman, "A history of cardiac auscultation and some of its contributors," *Am J Cardiol,* vol. 90, pp. 259-67, Aug 1 2002.
[151] A. K. Abbas and R. Bassam, *Phonocardiography Signal Processing*: Morgan & ClayPool Publishers, 2009.
[152] C. Ahlström, "Nonlinear Phonocardiographic Signal Processing," Department of Biomedical Engineering, Linköping University, Linköping, 2008.
[153] R. F. Rushmer, *Cardiovascular dynamics*. London: Saunders, 1976.
[154] S. R. Messer*, et al.*, "Optimal wavelet denoising for phonocardiograms," *Microelectronics Journal,* vol. 32, pp. 931-941, 2001.
[155] J. Martinez-Alajarin and R. Ruiz-Merino, "Efficient method for events detection in phonocardiographic signals," presented at the Bioengineered and bioinspired systems, Seveille, Spain, 2005.
[156] J. Singh and R. S. Anand, "Computer aided analysis of phonocardiogram," *J Med Eng Technol,* vol. 31, pp. 319-23, Sep-Oct 2007.
[157] C. Ahlstrom*, et al.*, "A method for accurate localization of the first heart sound and possible applications," *Physiol Meas,* vol. 29, pp. 417-28, Mar 2008.
[158] S. M. Debbal and F. Bereksi-Reguig, "Computerized heart sound analysis," *Computers in Biology and Medicine,* vol. 38, pp. 263-280, 2008.
[159] P. Wang*, et al.*, "Phonocardiographic signal analysis method using a modified hidden Markov model," *Ann Biomed Eng,* vol. 35, pp. 367-74, Mar 2007.
[160] M. J. Parry and J. McFetridge-Durdle, "Ambulatory impedance cardiography: a systematic review," *Nurs Res,* vol. 55, pp. 283-91, Jul-Aug 2006.
[161] W. G. Kubicek*, et al.*, "Development and evaluation of an impedance cardiac output system," *Aerosp Med,* vol. 37, pp. 1208-12, Dec 1966.
[162] A. Sherwood*, et al.*, "Methodological guidelines for impedance cardiography," *Psychophysiology,* vol. 27, pp. 1-23, Jan 1990.
[163] B. J. van der Meer*, et al.*, "Non-invasive evaluation of left ventricular function by means of impedance cardiography," *Acta Anaesthesiol Scand,* vol. 43, pp. 130-4, Feb 1999.
[164] T. Ono*, et al.*, "Beat-to-beat evaluation of systolic time intervals during bicycle exercise using impedance cardiography," *Tohoku J Exp Med,* vol. 203, pp. 17-29, May 2004.
[165] N. M. Albert, "Bioimpedance cardiography measurements of cardiac output and other cardiovascular parameters," *Crit Care Nurs Clin North Am,* vol. 18, pp. 195-202, x, Jun 2006.

[166] Z. Lababidi, *et al.*, "The first derivative thoracic impedance cardiogram," *Circulation,* vol. 41, pp. 651-8, Apr 1970.
[167] G. H. Willemsen, *et al.*, "Ambulatory monitoring of the impedance cardiogram," *Psychophysiology,* vol. 33, pp. 184-93, Mar 1996.
[168] D. P. Bernstein, "A new stroke volume equation for thoracic electrical bioimpedance: theory and rationale," *Crit Care Med,* vol. 14, pp. 904-9, Oct 1986.
[169] J. Wtorek, "Relations between components of impedance cardiogram analyzed by means of finite element model and sensitivity theorem," *Ann Biomed Eng,* vol. 28, pp. 1352-61, Nov-Dec 2000.
[170] I. Milsom, *et al.*, "Measurement of stroke volume with impedance cardiography," *Clin Physiol,* vol. 2, pp. 409-17, Oct 1982.
[171] A. D. Goedhart, *et al.*, "Temporal stability of ambulatory stroke volume and cardiac output measured by impedance cardiography," *Biol Psychol,* vol. 72, pp. 110-7, Apr 2006.
[172] A. Trakic, *et al.*, "Computational modelling of blood-flow-induced changes in blood electrical conductivity and its contribution to the impedance cardiogram," *Physiol Meas,* vol. 31, pp. 13-33, Jan 2010.
[173] B. C. Penney, "Theory and cardiac applications of electrical impedance measurements," *Crit Rev Biomed Eng,* vol. 13, pp. 227-81, 1986.
[174] J. J. McGrath, *et al.*, "Comparability of Spot Versus Band Electrodes for Impedance Cardiography," *Journal of Psychophysiology,* vol. 19, pp. 195-203, 2005.
[175] K. Sakamoto, *et al.*, "Problems of impedance cardiography," *Med Biol Eng Comput,* vol. 17, pp. 697-709, Nov 1979.
[176] A. P. DeMarzo and R. M. Lang, "A new algorithm for improved detection of aortic valve opening by impedance cardiography," *Computers in Cardiology,* pp. 373-376, 1996.
[177] T. T. Debski, *et al.*, "Stability of cardiac impedance measures: aortic opening (B-point) detection and scoring," *Biol Psychol,* vol. 36, pp. 63-74, Aug 1993.
[178] B. E. Hurwitz, *et al.*, "Coherent ensemble averaging techniques for impedance cardiography," in *Third annual IEEE Symposium on Computer-Based Medical Systems*, University of North Carolina at Chapel Hill. Los Alamitos, Calif. , 1990, pp. 228-235.
[179] V. K. Pandey and P. C. Pandey, "Improved detectoin of ventricular ejection time for impedance cardiography," presented at the Indian Conference on Medical Informatics & Telemedicine (ICMIT 2005),, 2005.
[180] D. Bartnik and B. Reynolds, "Impedance Cardiography system," 2009.
[181] J. H. Nagel, *et al.*, "New signal processing techniques for improved precision of noninvasive impedance cardiography," *Ann Biomed Eng,* vol. 17, pp. 517-34, 1989.
[182] L. Y. Shyu, *et al.*, "The detection of impedance cardiogram characteristic points using wavelet transform," *Comput Biol Med,* vol. 34, pp. 165-75, Mar 2004.
[183] D. S. Holder, *Electrical Impedance Tomography: Methods, History And Applications*: Institute of Physics Publishing, 2004.
[184] T. J. Faes, *et al.*, "The electric resistivity of human tissues (100 Hz-10 MHz): a meta-analysis of review studies," *Physiol Meas,* vol. 20, pp. R1-10, Nov 1999.
[185] J. Rosell, *et al.*, "Skin impedance from 1 Hz to 1 MHz," *IEEE Trans Biomed Eng,* vol. 35, pp. 649-51, Aug 1988.
[186] D. S. Holder, *Electrical Impedance Tomography: Methods, History and Applications*: Institute of Physics Publishing), 2005.

[187] I. E. C. (IEC), "Medical Electrical Equipement," in *General requirements for safety - Collateral standard: Safety requirements for medical electrical systems* vol. IEC 60601-1-1:2000(E), ed: IEC, 2000, p. 1.

[188] L. Zhang and H. Wang, "Single source current drive patterns for electrical impedance tomography," presented at the Instrumentation and Measurement Technology Conference (I2MTC), Austin, TX 2010.

[189] A. Adler and Y. Maimaitijiang, "Adjacent Stimulation and Measurement Patterns Considered Harmful " *Physiol. Meas.,* 2011.

[190] D. Isaacson, "Distinguishability of conductivities by electric current computed tomography," *IEEE Trans Med Imaging,* vol. 5, pp. 91-5, 1986.

[191] E. Demidenko*, et al.*, "On optimal current patterns for electrical impedance tomography," *IEEE Trans Biomed Eng,* vol. 52, pp. 238-48, Feb 2005.

[192] W. R. Lionheart*, et al.*, "Generalized optimal current patterns and electrical safety in EIT," *Physiol Meas,* vol. 22, pp. 85-90, Feb 2001.

[193] M. A. Denai*, et al.*, "Absolute electrical impedance tomography (aEIT) guided ventilation therapy in critical care patients: simulations and future trends," *IEEE Trans Inf Technol Biomed,* vol. 14, pp. 641-9, May 2010.

[194] A. Adler, "Electrical Impedance Tomography: Image Algorithms and Applications," Carleton2008.

[195] A. Adler, "Measurement of pulmonary function with electrical impedance tomography," Institut de Génie Biomédical, École Polytechnique de Montréal, Montréal, 1995.

[196] R. H. Bayford, "Bioimpedance tomography (electrical impedance tomography)," *Annu Rev Biomed Eng,* vol. 8, pp. 63-91, 2006.

[197] M. Vauhkonen, "Electrical impedance tomography and prior information," University of Kuopio, Kuopio, 1997.

[198] A. Adler and W. R. Lionheart, "Uses and abuses of EIDORS: an extensible software base for EIT," *Physiol Meas,* vol. 27, pp. S25-42, May 2006.

[199] D. Ferrario*, et al.*, "Unsupervised localization of heart and lung regions in EIT images: a validation study," in *12th International Conference in Electrical Impedance Tomography*, Bath (UK), 2011.

[200] A. Vonk-Noordegraaf, 2nd*, et al.*, "Determination of stroke volume by means of electrical impedance tomography," *Physiol Meas,* vol. 21, pp. 285-93, May 2000.

[201] J. Zhang and R. P. Patterson, "Analysis on the influence of tissues/organs' movements in EIT images of lung ventilation using finite difference thorax models," *Conf Proc IEEE Eng Med Biol Soc,* vol. 2, pp. 1557-60, 2004.

[202] A. Borsic*, et al.*, "In vivo impedance imaging with total variation regularization," *IEEE Trans Med Imaging,* vol. 29, pp. 44-54, Jan 2010.

[203] A. E. Hartinger*, et al.*, "Real-time management of faulty electrodes in electrical impedance tomography," *IEEE Trans Biomed Eng,* vol. 56, pp. 369-77, Feb 2009.

[204] A. Adler, "Accounting for erroneous electrode data in electrical impedance tomography," *Physiol Meas,* vol. 25, pp. 227-38, Feb 2004.

[205] M. Vauhkonen*, et al.*, "A Kalman filter approach to track fast impedance changes in electrical impedance tomography," *IEEE Trans Biomed Eng,* vol. 45, pp. 486-93, Apr 1998.

[206] B. S. Kim*, et al.*, "Dynamic electrical impedance imaging of a chest phantom using the Kalman filter," *Physiol Meas,* vol. 27, pp. S81-91, May 2006.

[207] F. C. Trigo*, et al.*, "Electrical impedance tomography using the extended Kalman filter," *IEEE Trans Biomed Eng,* vol. 51, pp. 72-81, Jan 2004.

Chapter 3

Parametric estimation of pulse arrival times

Adapted from postprint version of:

Parametric estimation of pulse arrival time: a robust approach to pulse wave velocity

Josep Solà[1], Rolf Vetter[1], Philippe Renevey[1], Olivier Chételat[1], Claudio Sartori[2] and Stefano F. Rimoldi[3]

[1]CSEM – Centre Suisse d'Electronique et de Microtechnique, Neuchâtel, Switzerland

[2]CHUV – Internal Medicine, University Hospital, Lausanne, Switzerland

[3]Swiss Cardiovascular Center Bern, University Hospital Bern, Bern, Switzerland

Published in:

Physiological Measurement

Physiol. Meas. 30 (2009) 603-615

DOI: 10.1088/0967-3334/30/7/006

Publisher version: http://iopscience.iop.org/0967-3334/30/7/006

3. Parametric estimation of pulse arrival times

3.1. Rationale

Assessing the velocity of propagation of pulse waves through the arterial tree has attracted the attention of physicians and physiologists for two centuries now: already in 1808, Young stated the relationship between pulse wave velocity (PWV) and artery stiffness. Since then, PWV has been claimed to be associated with the most relevant cardiovascular risk factors, such as hypertension, and to be an independent predictor of cardiovascular events [1]. Nevertheless, it is the use of PWV as a surrogate for beat-to-beat changes of mean arterial pressure that has stimulated the greatest interest in recent years [2]. In particular, when combined with other non-invasive monitoring technologies [3], PWV is an appealing technique for the continuous assessment of cardiovascular homeostasis and regulation [4].

The common clinical approach to assess PWV *in vivo* relies on the tracking of pressure pulses created by systolic ejection, *i.e.* the pressure waves created at the onset of left-ventricular ejection. While traveling toward the periphery, the arrival times of a pressure pulse at two different sites of the arterial tree are detected. The delay between the two times provides a measurement of the propagation time or pulse transit time. One finally calculates the PWV parameter as the ratio between the distance between the two measurement sites and the pulse transit time [1].

The recent expansion of PWV has been driven by technological progresses in the performance of external skin transducers that allow the easy recording of pressure pulses. Among them, photo-plethysmography (PPG), a non-invasive non-obtrusive technique based on the analysis of temporal patterns of light absorption in living tissues, is of particular interest [5]. Despite the wide clinical popularity and use of PPG-based vital parameters, *e.g.* SpO2, its clinical exploitation for PAT and PWV assessment has been relatively limited due to the specific morphologic shape of PPG signals. Indeed, traditionally PAT estimations are performed directly on pressure signals obtained from cardiac catheterization through the extraction of several characteristics points.

Examples of state-of-the-art characteristic points are provided in Figure 3.1. In particular, the literature describes [2, 4, 6-9]:

- The maximum (MAX) of the pressure pulse is defined as the location at which the pulse reaches its maximum amplitude.
- The foot (FOOT) of the pressure pulse is defined as the last minimum of the pulse before the beginning of its upstroke. Iterative threshold-and-slope techniques to robustly detect FOOT have been proposed in the literature.
- The partial amplitude on the rising edge of the pressure pulse (PARE) is defined as the location at which the pulse reaches a certain percentage of its foot-to-peak amplitude.
- The maximum of the first derivative of the pressure pulse (D1) is defined as the location of the steepest rise of the pulse. First derivative are commonly computed using the central difference algorithm in order to reduce noise influences [10].

- The maximum of the second derivative of the pressure pulse (D2) is defined as the location of the maximum inflection point of the pulse during its anacrotic phase.
- The intersecting tangent of the pressure pulse (TAN) is defined as the point of intersection of a tangent line to the steepest segment of the upstroke with a tangent line to the foot of the pulse.

Unfortunately, the straightforward application of these characteristic points to the noisy and corrupted PPG signals yields often unlikely and unreliable results with erratic behavior and compromises the repeatability of associated clinical PAT measurements [8]. Thus, the design of robust extraction techniques, capable of estimating the arrival time of a pressure pulse in a measurement setup such as PPG, remains an open problem.

This research targets the definition of a new family of PAT estimators that improve the robustness to artifact and measurement noises based on a parametric modeling of pressure pulse waveforms. Agreement with state-of-the-art characteristic points is evaluated on the basis of 200 h of intensive care unit PPG signals extracted from the public available MIMIC database. Repeatability in the presence of noise is evaluated using Monte Carlo simulations and *in vivo* fingertip PPG recordings.

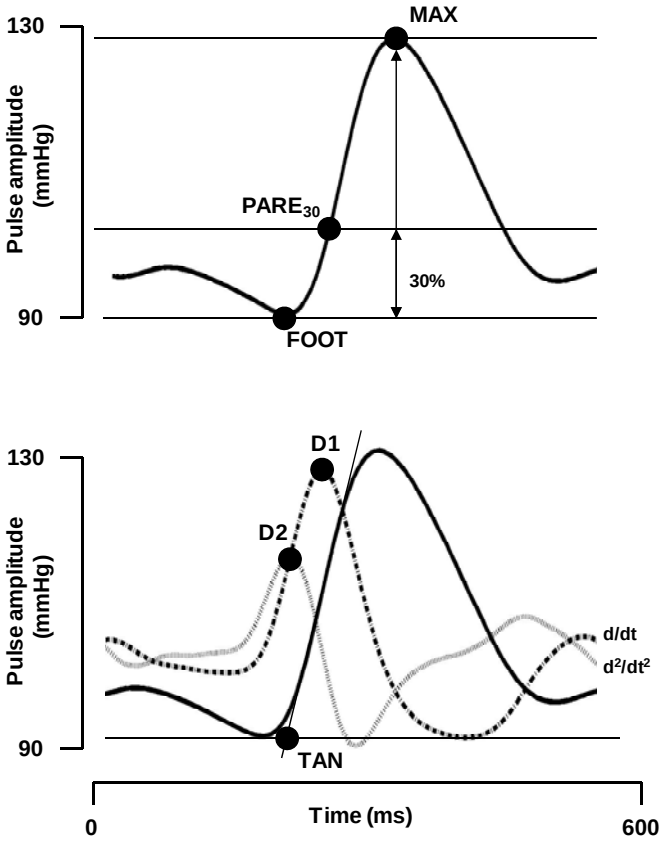

Figure 3.1: Determination of PAT on a pressure pulse (bold line) according to the state of the art: characteristic points of the pulse waveform are identified in the time domain via empirically-determined rules. Characteristic point definition is provided in the text. Time zero corresponds to the R-Wave of a simultaneously recorded ECG.

3.2. Parametric modeling of pressure pulses

We propose a novel PAT estimation method that, instead of detecting a characteristic point of the pressure pulse, takes into account the whole pressure pulse waveform through a specific parametric model. In particular, given a pressure pulse waveform p(t), we search for an estimator of its arrival time that satisfies:

$$\mathrm{PAT} = \psi \operatorname{argmin} \mathrm{E}\left[\left(p(t) - m_{\Omega}(t)\right)^2\right]$$

Equation 56

where $m_{\Omega}(t)$ is a parametric model of the pressure pulse waveform determined by the set of parameters Ω, E[·] depicts mathematical expectation over one pressure pulse and ψ is a transformation from the parameters space to the time domain, *i.e.* $\psi : \Omega \rightarrow t$. In other words, we estimate the pulse arrival time of a given pulse waveform p(t) by first finding the parametric model $m_{\Omega}(t)$ that *best fits* to $p(t)$, and by then transforming the parametric description of $m_{\Omega}(t)$ into time domain values of PAT (Figure 3.2). Note that through the averaging by the E[·] operator, in a model-based parametric approach we have overcome the need of identifying characteristic points in $p(t)$ and we rely on its overall waveform. In this study, the computation of the optimal set of parameters Ω that minimizes the quadratic error defined in Equation 56 is done by an implementation of the steepest descent algorithm [11] and the localization of the pressure pulse waveforms $p(t)$ is supported by the detection of ECG R-Waves [2].

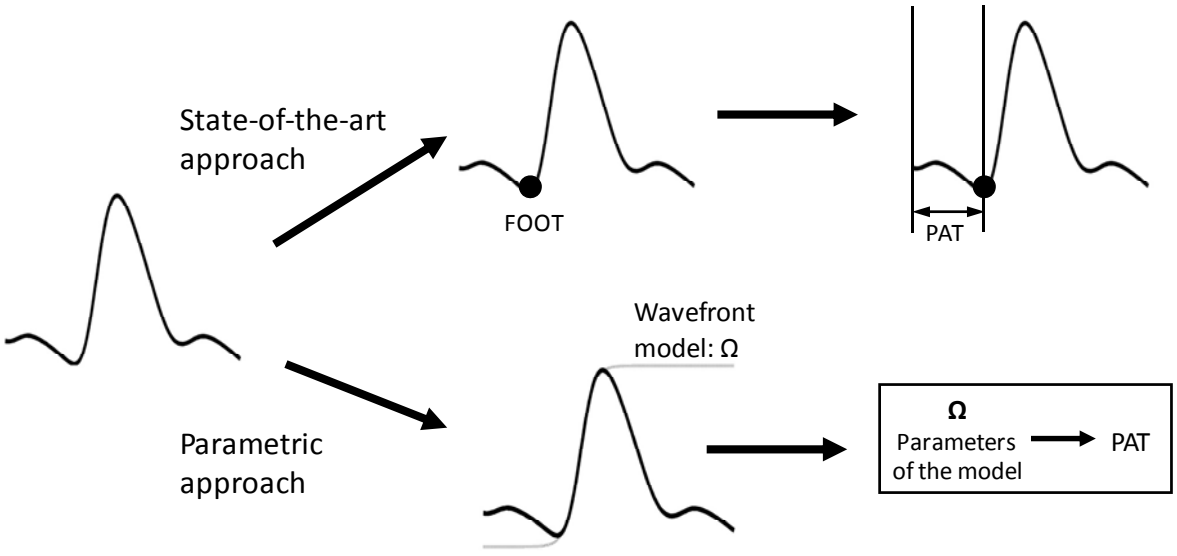

Figure 3.2: State-of-the-art estimation of PAT consists of detecting a characteristic point within the PPG waveform. Parametric estimation of PAT consists of first fitting a parametric model to the original PPG waveform, and then processing the parameters of the model in order to obtain PAT equivalent values.

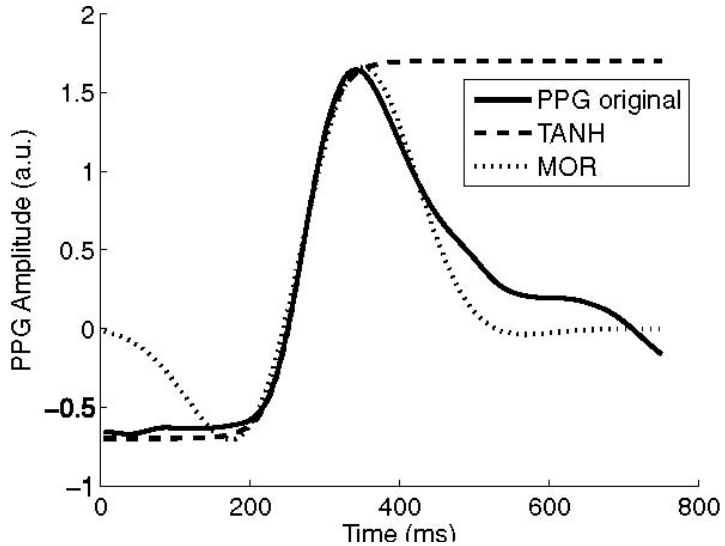

Figure 3.3: Example of PPG pressure pulse waveform recorded at the fingertip. t = 0 corresponds to the onset of ventricular ejection (*i.e.* R-wave on the ECG). Dashed lines illustrate two examples of parametric waveform model fitting.

The remaining question is how to design a parametric model of PPG pulse waveform, such that the pulses $m_\Omega(t)$ corresponding to the space spanned by Ω cover the whole range of physiologically possible pressure pulse morphologies. Unfortunately, PPG waveforms present a large range of possible morphologies and thus, to design a general description model is practically unrealistic: see for instance [12]. Such waveform variability arises from the frequency-dependent distortions that pulse waves undergo while they propagate through the arterial tree. Therefore, variables such as measurement site [13], vasomotricity [5], age [13], structure of the arterial wall and different sensor configurations will modify the morphology of p(t). At this point, a simplification of the design problem needs to be introduced: indeed we are not interested in describing the whole morphology of p(t), but solely its upstroke, or wavefront. The justification is straightforward: although information on pulse arrival is present in the whole waveform, only the anacrotic phase is free of reflection phenomena [14].

3.2.1. MOR parametric estimation

In this section, a first parametric description of the anacrotic phase of a pressure pulse waveform $p(t)$ is suggested. We propose to model the wavefront of $p(t)$ as the rising edge of a sinusoidal function. Even more, because the rising edge of pressure pulses is limited in time, one must combine the sinusoidal function together with a localization function. Assuming a Gaussian-like localization function, we proceed by defining $m_\Omega(t)$ according to a Morlet wavelet design [15]:

$$m_\Omega(t) = A \sin\left(\frac{2\pi t}{T} + \phi\right) \exp\left\{\frac{(t-\mu)^2}{\sigma^2}\right\}$$

Equation 57

We define the set of parameters that fully characterizes $m_\Omega(t)$ as $\Omega = [A, T, \phi, \mu, \sigma]$. Note that while μ and σ support the temporal localization of $m_\Omega(t)$, the actual information on the rising edge is embedded on the subset of parameters $[T, \phi]$. In particular, we define the arrival time of the sinusoidal rising edge, as the position of a positive-slope zero crossing, that is:

$$\mathrm{PAT} = 2\pi - \frac{\phi}{2\pi}T \pm kT$$

Equation 58

where the kT term ($k \in \mathbb{N}$) corrects for jumps on the PAT value by multiples of the fundamental period T. The PAT computation in Equation 58 corresponds to the transformation function $\psi : \Omega \to t$ depicted in Equation 56. The fitting of a MOR parametric model to a PPG pressure pulse recorded at the fingertip is illustrated in Figure 3.3.

3.2.2. TANH parametric estimation

It might be argued that the proposed MOR parametric estimation is prone to be influenced by portions of the catacrotic phase of $p(t)$. This argument and the agreement analysis results presented in Section 3.4.1 justify the definition of an alternative parametric model which focuses exclusively on the characterization of the wavefront of $p(t)$, *i.e.* on its rising edge.

Among all the possible models of a wavefront, we seek a representation that copes with both the arrival time and the curvature of the wavefront near the uprising segment, as in a sigmoidal function. Additionally, assuming a Windkessel model of the arterial tree [12], the rising edge is expected to obey an exponential law. Hence, a hyperbolic tangent function is proposed as the parametric exponential-like sigmoidal model $m_\Omega(t)$ of a pressure pulse waveform:

$$m_\Omega(t) = A \tanh\left(\frac{t-\mu}{\sigma}\right) + C$$

Equation 59

where A stands for the amplitude of the modeled wavefront, μ and σ control respectively the position of the inflection point and the slope of the wavefront, and C defines a constant offset. Figure 3.3 illustrates the fitting of a hyperbolic tangent function to a pressure pulse waveform recorded at the fingertip.

A model of pressure pulse waveform is now determined by a set of three parameters, *i.e.* $\Omega = [A, \mu, \sigma]$. Note that PAT is solely determined by the position of the inflection point of the parametric model $m_\Omega(t)$, namely, μ. A single issue remains to be solved: because the hyperbolic tangent of Equation 59 is not a finite energy signal, we need to limit the computation of the quadratic error to a certain segment of t. In particular, we are only interested on the behavior of the parametric model $m_\Omega(t)$ near its inflection point. Hence, we propose to weigh the quadratic error in Equation 56 by a symmetric window centered

around μ. The results presented in this study are based on the use of a hamming window [16], centered at μ, and that extends from $\mu - 3\sigma$ to $\mu + 3\sigma$. The choice of a 6σ window length relies on a trade-off between the robustness and the applicability of the TANH parametric model, *i.e.* while shorter window lengths would tend to fit $m_\Omega(t)$ to subsegments of $p(t)$, longer window lengths would demand $m_\Omega(t)$ to model not only the wavefront of $p(t)$ but its pre-anacrotic and catacrotic phases.

3.3. Materials and methods

3.3.1. Agreement analysis

The first proposed analysis aims at assessing the agreement between state-of-the-art and novel PAT estimation techniques. The added value of introducing parametric estimations of PAT in physiology and clinical research will be demonstrated if it can be proven that they are in agreement with currently known characteristic points.

The analysis is performed on a subset of the publicly available MIMIC database [17]. The original database is part of the Physionet platform and contains data from over 72 intensive care unit patients at the Boston Beth Israel Hospital [18]. From the currently available recordings, we select those that simultaneously include arterial blood pressure, ECG and PPG signals. Because several PPG recordings present temporal intervals where PPG signals are lost, we only include in our analysis the recordings with a sufficient stability, resulting in 21 recordings. Thus, the agreement analysis database includes a total number of 950 000 heartbeats, corresponding to more than 200 h of data (mean heart rate 88.0 ± 21.0 bpm, mean systolic blood pressure 103.0 ± 19.0 mmHg and mean PAT (24.05 ± 5.0 ms). Initially, raw ECG and PPG signals are extracted from the MIMIC database and re-sampled to 200 samples s−1. R-wave detection is performed on the ECG signal based on a fixed threshold detection and a localization of the maximum value. The position of R-waves is used to detect and synchronize the presence of pressure pulses in the PPG signal. Initially, raw PPG signals are forward and reverse low-pass filtered at 15 Hz in order to avoid phase distortions [8]. Then, singular pressure pulse waveforms p(t) are detected by R-wave synchronization and post-processed by an ensemble averaging technique [19]. In the current experiments, the ensemble averaging is performed on the basis of eight consecutive heartbeats.

The agreement definition proposed by Bland and Altman is adopted: given two measurement methods of the same quantity, one obtains an estimation of their agreement by computing the standard deviation of their differences [20]. The choice of such an agreement metrics is justified by the fact that different PAT estimation techniques do consistently depict different estimation biases, *e.g.*, the MAX characteristic point provides larger PAT values than FOOT does because of the intrinsic definition of both characteristic points. The proposed strategy is thus to first compute the differences between the measurements provided by the two methods, and then to compute their dispersion. Two methods will present good agreement if this dispersion is minimized [6].

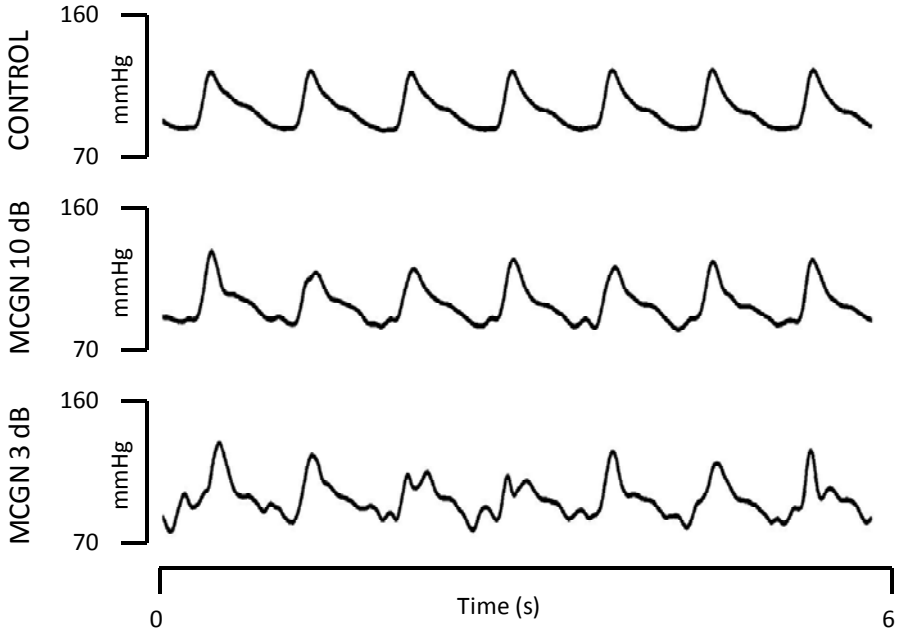

Figure 3.4: Six seconds of simulated corrupted signals. CONTROL corresponds to the original PPG clean signal and MCGN corresponds to signals corrupted with multiplicative colored Gaussian noise in different SNR scenarios (SNR = 10 dB and SNR = 3dB).

Therefore, given a set of *M* methods, we define the elements of an agreement matrix (AM) as:

$$\mathrm{AM}_{i,j} = 2\ \mathrm{std}\left[\mathrm{PAT}_i - \mathrm{PAT}_j\right], \qquad i,j \in [1,\mathrm{M}]$$

Equation 60

That is, the $\mathrm{AM}_{i,j}$ element depicts the limits within which 95.4% of the PAT estimations by methods *i* and j differ. For instance, $\mathrm{AM}_{\mathrm{D1,D2}}$ = 4.5 ms indicates that when comparing the agreement of D1 and D2, 95.4 % of the measurement are expected to be within ±4.5ms. Note that, by definition, AM has a null diagonal and it is symmetric. For the sake of completeness, Pearson's correlation coefficients are provided as well.

3.3.2. Repeatability analysis on Monte Carlo simulations

The goal of this analysis is to provide first figures on the robustness (*i.e.* repeatability) of the different PAT estimation methods in the presence of noise.

Because no gold-standard measurement of PAT is available in *in vivo* experiments, repeatability is in a first instance tested with Monte Carlo simulations. The simulation strategy is the following. Initially, a prototype of pressure pulse waveform p(t) is extracted from an *in vivo* PPG recorded signal. This prototype is replicated in time, generating a series

of PPG pulses with constant, *i.e.* deterministic, PAT. The series of PPG pulses is then corrupted with noise and the distribution of PAT estimations is computed on the corrupted data. The interest of the described simulation approach is the generation of noisy perturbations that match particular spectral characteristics, such as micro-movement artifacts. Specifically we are interested in colored noises with energy distributed between 1 and 7 Hz. Our simulations involve perturbations caused by multiplicative colored Gaussian noise [21] in different SNR scenarios (Figure 3.4).

Repeatability is assessed as the spread of PAT estimations when calculated on synthetic replicated measurements [20]: good performances are thus associated with low spread values. Assuming Gaussian distribution, repeatability is computed as the standard deviation of the series of consecutive PAT estimations.

3.3.3. Repeatability analysis on in-vivo data

The repeatability analysis performed on the basis of Monte Carlo simulations can be argued to be biased by the actual choice of the replicated prototype of the pressure pulse waveform. In order to overcome this limitation, an additional experiment is proposed based on the analysis of noisy *in vivo* PPG recordings.

The analysis relies on a database consisting of 140 min of PPG data recorded at the fingertip of seven young healthy subjects (mean age 31.3 ± 3.5 years, mean body mass index 22.6 ± 1.2, mean heart rate 61.6 ± 9.1 bpm and mean systolic blood pressure 120.8 ± 21.0 mmHg). The protocol included 10 min of artifact-free recordings and 10 min of free hand movements while the subjects remained in a sitting position. Subjects were asked not to drink caffeine, eat or smoke and to refrain from performing unusual physical activity on the recording day. After a 10 min cardiovascular stabilization phase, subjects were asked to remain still while the recording was performed: cardiovascular variability was thus minimized during the experiment. ECG and PPG were simultaneously recorded by a BIOPAC (BIOPAC Systems 2009) platform (sampling rate 200 Hz, PPG100C high pass filter set to 0.05 Hz, input signal range set to 200 mV). Heart rate and mean arterial pressure were assessed by a Portapres (FMS 2009) platform.

Similarly to Section 3.3.2 a methodological problem appears: in principle repeatability is impossible to assess because of the fact that no gold-standard measurement of ECG-fingertip PAT is available. Nevertheless, a statistical inspection of PAT series can resolve this dilemma under the assumption of statistical independence. Indeed, the variance of a series of PAT measurement by a given method (σ^2_{PAT}) is assumed to be contributed by two independent random variables: the intrinsic variability in PAT due to cardiovascular regulation (σ^2_{CV}) and the variability in PAT due to measurement inaccuracy (σ^2_{MEAS}). Hence,

$$\sigma^2_{\mathrm{PAT}} = \sigma^2_{\mathrm{CV}} + \sigma^2_{\mathrm{MEAS}}$$

Equation 61

Repeatability analysis is thus possible because of the fact that for a given experiment (σ^2_{CV}) is identical for every PAT estimation method. Hence, when comparing (σ^2_{PAT}) across methods one is indeed comparing the underlying methods (σ^2_{MEAS}). In other words,

independently of the hidden intrinsic PAT variability, (σ^2_{PAT}) provides information on the relative repeatability performances of each PAT estimator.

Table 3.1: Agreement matrix values for the different PAT estimation methods computed over 950 000 heartbeats in the MIMIC database. Values depict 2 SD of the dispersion between two methods in ms. Bold values depict good agreement pairs of methods. The underlined value corresponds to the best encountered agreement pair of methods.

(ms)	MAX	FOOT	PARE	D1	TAN	D2	MOR
FOOT	17.4						
PARE	16.9	11.5					
D1	15.0	9.6	7.3				
TAN	17.0	6.9	6.8	**5.6**			
D2	18.1	9.6	9.3	**4.5**	**5.2**		
MOR	14.7	10.2	9.0	9.2	9.2	11.2	
TANH	14.4	8.9	6.0	**2.4**	**5.4**	5.6	8.7

Table 3.2: Pearson's correlation coefficients for the different PAT estimation methods computed over 950 000 heartbeats in the MIMIC database. All values correspond to $p<0.001$. Bold values depict good agreement pairs of methods. The underlined value corresponds to the best encountered agreement pair of methods.

[.]	MAX	FOOT	PARE	D1	TAN	D2	MOR
FOOT	0.73						
PARE	0.76	0.88					
D1	0.79	0.89	0.93				
TAN	0.71	0.94	0.93	0.95			
D2	0.68	0.86	0.89	**0.96**	**0.94**		
MOR	0.82	0.87	0.92	0.90	0.87	0.81	
TANH	0.80	0.91	0.94	**0.99**	**0.96**	0.94	0.91

3.4. Results

3.4.1. Agreement analysis

For the MIMIC database, the values of the agreement analysis and the Pearson's correlation analysis are presented in tables 1 and 2. In general, both analyses consistently highlight the relevant agreements between the pairs of methods TAN & D1, D2 & D1, D2 & TAN, TANH & D1 and TANH & TAN. The agreement is considered to be good when two methods provide AM < 6 ms (25% of PAT dynamical range in the database) and CC > 0.95.

The good agreement of TAN and D2 was already highlighted by [8] and [6]: it is assumed that they both robustly detect the foot of the waveform. Similarly, the good agreement between TAN and D1 had been already pointed out by [8]. Additionally, our analysis highlights good agreement indexes between D1 and D2. It is relevant to note as well that the characteristic points D1 and FOOT, used, respectively, by the commercial devices

Complior, and SpygmoCor do not present substantial agreement as already pointed by [9]. Remarkably, the new proposed TANH depicts excellent agreement and correlation with the Complior characteristic point D1.

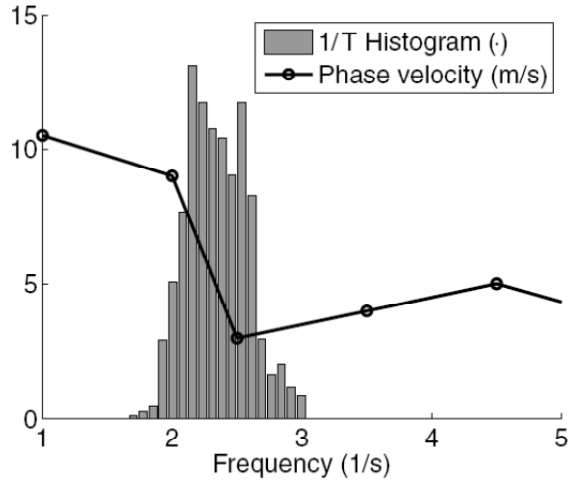

Figure 3.5: Histogram of estimated MOR fundamental frequencies $\left(\frac{1}{T}\right)$ for one subject in the MIMIC database. Solid line: measured phase velocities of pressure pulse waves in dog ascending aorta (adapted from [22]). Note that most-encountered MOR fundamental frequencies lay on the region of maximum phase velocity variations.

We are in particular interested in examining the poor performances of the new proposed MOR method. Although very promising in terms of repeatability (see Sections 3.4.2 and 3.4.3), its performance in the agreement analysis is not as good as expected. Indeed we observed that the temporal evolution of MOR estimations presented recurrent slow deviations from that of TANH. We propose two hypotheses to justify this method failure. A first physiological hypothesis is based on the fact that MOR attempts to fit a sinusoidal function to the pressure pulse waveform in terms of its period, phase and amplitude. Therefore, given a period T (or its equivalent frequency $\frac{1}{T}$), MOR estimates the phase shift of a single harmonic component of the pressure pulse traveling from the left ventricle to the measurement location. It is known [22] that phase velocities of pressure pulses traveling through the arterial tree are strongly dependent on frequency. As displayed in Figure 3.5, these phase velocity variations are particularly important for pressure pulses whose frequencies range from 1 to 3 Hz in dogs, and in humans [12]. To illustrate the incidence of this phenomenon on our analysis, Figure 3.5 displays the histogram of frequencies $\frac{1}{T}$ determined by the MOR method when computed over one subject in the MIMIC database. Statistics correspond to 67 000 heartbeats and number of bins is set according to Sturges' formula [23]. One can observe that the MOR method converges to $\frac{1}{T}$ values distributed from 1.8 to 3 Hz. Hence, our hypothesis is that in order to minimize the quadratic error in Equation 56, MOR estimates the phase shift of harmonic components of different frequencies. The fundamental frequency will vary according to the actual morphology of the pressure pulse waveform. Then, because phase velocity in the arterial tree is frequency

dependent, the pulse arrival time estimated by MOR will continuously fluctuate. A second hypothesis for the poor agreement performances of MOR is based on the fact that, because of its definition (Equation 57), the position of a positive-slope zero crossing is influenced by both a sinusoidal and a localization function. Hence the search space will present multiple minima depending on the interactions between the subsets of parameters [T,ϕ] and [μ,σ]. Such a non-uniform search space configuration is prone to guide the error minimization algorithms toward sub-optimal solutions of Ω. Note that in TANH a single subset of parameters determines the solution and thus, this problem is avoided.

3.4.2. Repeatability analysis on Monte Carlo simulations

The repeatability of PAT measurements in the presence of multiplicative colored Gaussian noise (MCGN) is illustrated in Figure 3.6. Each simulation result involves statistics on 5000 corrupted heartbeats. The depicted SNR values represent typical recording scenarios: 20 dB corresponds to very clean PPG signals as one would encounter in ICU recordings, 10 dB corresponds to mildly corrupted signals as in sleep laboratories environments, 3 dB corresponds to signals in ambulatory artifact-free recordings and 0 dB approaches the scenario encountered in typical ambulatory PPG recordings.

In the best scenario, all methods depict very low PAT spreads (converging to 0 ms because of the synthetic nature of the data). When the SNR is decreased to 10 dB, TAN and PARE performances are considerably affected. Because TAN estimation requires the preliminary determination of FOOT and D1, uncertainties on both characteristic points are propagated and combined into TAN. Following the analysis, when the SNR is decreased to 3 dB only FOOT, D1, D2, MOR and TANH are able to contain the dispersion of PAT values. Yet, MOR and TANH reduce the dispersion of D1 by 30% and 60%, respectively. In the worst scenario, when approaching very low SNRs, MOR and TANH control the raise of PAT repeatabilities reducing the dispersion of D1 by respectively 25% and 36%.

Accordingly, the introduction of parametric estimation methods that include information of a segment of the PPG pressure pulse, rather than considering a single characteristic point, considerably reduces the effects of noise corruption. The presented simulation results indicate that parametric estimation methods reduce the spread of PAT estimation by at least 25% when the SNR is below 10 dB.

3.4.3. Repeatability analysis on in vivo data

The repeatability results for the *in vivo* experiments are illustrated in Figure 3.7 and Figure 3.8. Varying-length ensemble averaging [19] has been used to alter the influence of noise on PAT estimation methods, *i.e.* prior to extracting a PAT value, several consecutive PPG waveforms (*i.e.* 2, 4, 8 and 16) are averaged by means of an ECG synchronization algorithm [24]. Therefore, one might interpret the averaging length in Figure 3.7 and Figure 3.8 as a surrogate for the SNR scenarios presented in Figure 3.6: that is, longer ensemble averaging values correspond to higher SNR values. Note that in contrast with Monte Carlo analysis, *in vivo* repeatability does not converge to 0 when ensemble averaging length is increased. The convergence limit depicts now the experimental variability associated with cardiovascular regulation. Although, in general, the increase of the averaging length leads to an

undesirable smoothing of the PPG waveform, this effect is limited in our study where cardiovascular variability has been minimized during the recordings.

Under motionless conditions (Figure 3.7) all methods converge to similar repeatability values for averaging lengths greater than eight heartbeats. Similarly to the Monte Carlo analysis, one observes a fast degradation of TAN. When no ensemble averaging is performed, that is when averaging length equals 0, parametric estimators reduce estimation spread of characteristic points by 50%. Under motion conditions (Figure 3.8) one observes that only D1, D2, MOR and TANH contain the explosion of spreads as the ensemble averaging length is reduced. Note the remarkable repeatability results of the D2 characteristic point, approaching those of the parametric method MOR. Finally, one notes that TANH reduces by 55% the spread of the Complior characteristic point D1.

In order to illustrate the relevance of the presented repeatability analysis, a practical example is provided. Assume that one aims at monitoring the PAT variability of a subject during an ambulatory experiment (for the motion experiments in Figure 3.7 the underlying cardiovascular variability would be of σ_{CV}: 10 ms). Because cardiovascular regulation might undesirably smooth ensemble-averaged PPG waveforms in ambulatory scenarios, we decide to avoid the ensemble averaging approach. Alternatively, one chooses to first perform single PAT measurements and then to average a series of n consecutive PAT measurements. Assuming that the spread of the data collection will decrease according to a $\frac{1}{\sqrt{n}}$ law [25], cardiovascular variability (σ_{CV}: 10 ms) will be measurable after n = 5 heartbeats when TANH is used, and only after n = 25 heartbeats when the Complior characteristic point D1 is used. Hence, the achievable temporal resolution is reduced by a five-fold factor when one decides to use parametric PAT estimators instead of single point characteristic points.

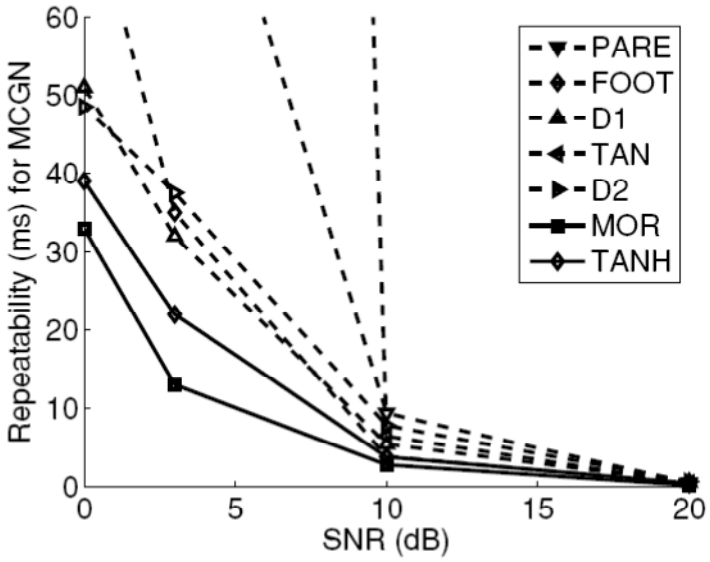

Figure 3.6: Repeatability indexes for simulated PPG data under the presence of multiplicative colored Gaussian noise when SNR degrades from 20 dB to 0 dB.

Repeatability is defined as the spread of PAT estimations for a given method when calculated on replicated measurements, *i.e.* a low spread depicts good repeatability performance.

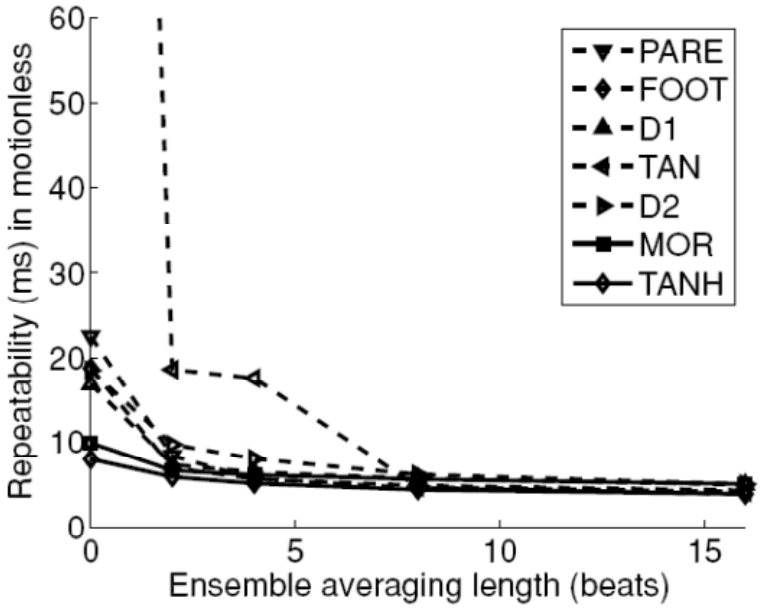

Figure 3.7: Repeatability indexes for 20 min of motionless PPG recordings, when the ensemble averaging length is reduced from 15 to 1 heartbeats. Repeatability is defined as the spread of PAT estimations for a given method, *i.e.* a low spread depicts good repeatability performance.

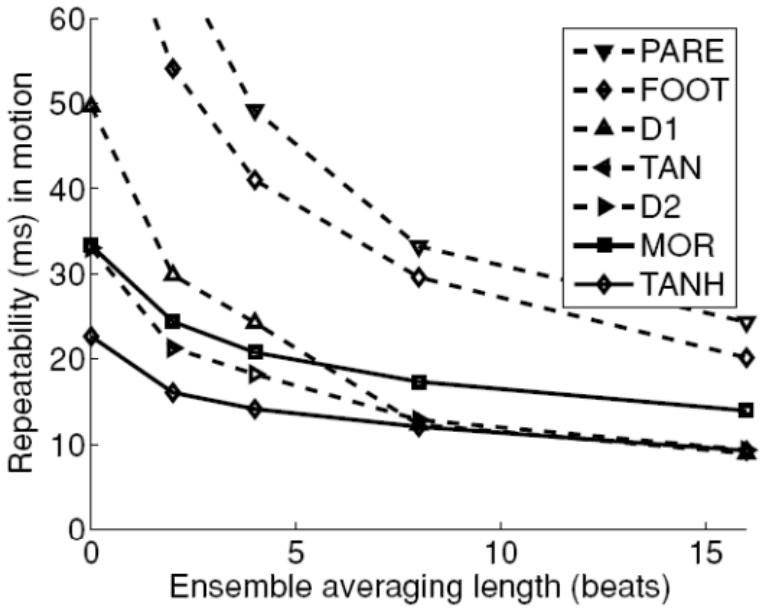

Figure 3.8: Repeatability indexes for 20 min of motion-corrupted PPG recordings, when the ensemble averaging length is reduced from 15 to 1 heartbeats. Repeatability is defined as the spread of PAT estimations for a given method, *i.e.* a low spread depicts good repeatability performance.

3.5. Discussion

The unsupervised extraction of characteristic points in pressure pulses in view of determining pulse arrival times still lacks general consensus. In this study we demonstrated that while state-of-the-art techniques present good repeatability when applied to very clean photo plethysmographic signals, they fail when applied to mild-to-severely noisy signals, *i.e.* $\mathrm{SNR} \leq 10\,\mathrm{dB}$. Indeed, all clinical studies published so-far required subjects to be in the supine position, while noisy corrupted pulses were systematically discarded. Even thought these experimental conditions can be reproduced in intensive care units, it seems unrealistic to expect them to be met in clinical continuous monitoring, or even worse, in portable monitoring. Consequently, we found that the hyperbolic tangent parametric estimator (TANH) provided pulse arrival time values in agreement with state-of-the-art techniques (*e.g.* Complior characteristic point) under very low noise conditions and that outperformed them in the presence of noise. This novel method extracts information from the whole anacrotic phase of a pressure pulse and avoids thus, the dependence on particular characteristics of the waveform itself. Obviously, the computational complexity of the extraction procedure has been increased, but we suggest a recursive implementation that could be used in real-time applications. In conclusion, the proposed TANH method is a good candidate for the real-time continuous monitoring of pulse arrival time and its potential applications in stiffness and/or blood pressure assessment. This may provide a new possibility to more precisely assess cardiovascular risk and the effects of therapeutic interventions.

References

[1] R. Asmar, *Arterial Stiffness and Pulse Wave Velocity. Clinical Applications*: ELSEVIER, 1999.

[2] R. A. Payne*, et al.*, "Pulse transit time measured from the ECG: an unreliable marker of beat-to-beat blood pressure," *J Appl Physiol,* vol. 100, pp. 136-41, Jan 2006.

[3] Y. Chen*, et al.*, "Continuous non-invasive blood pressure monitoring method and apparaturs," 2003.

[4] J. Muehlsteff*, et al.*, "Continuous cuff-less blood pressure monitoring based on the pulse arrival time approach: the impact of posture," *Conf Proc IEEE Eng Med Biol Soc,* vol. 2008, pp. 1691-4, 2008.

[5] J. Allen, "Photoplethysmography and its application in clinical physiological measurement," *Physiol Meas,* vol. 28, pp. R1-39, Mar 2007.

[6] G. Ning*, et al.*, "Comparison of Pulse Wave Velocity Computed by Different Characteristic Points," *Proceeding Biomedical Engineering* vol. 458, 2005.

[7] D.-k. Jung*, et al.*, "Changes of Pulse Wave Velocity in Arm According to Characteristic Points of Pulse Wave," *Proc International Conference on Convergence Information Technology (ICCIT 2007),* pp. 821-826, 2007.

[8] Y. C. Chiu*, et al.*, "Determination of pulse wave velocities with computerized algorithms," *Am Heart J,* vol. 121, pp. 1460-70, May 1991.

[9] M. W. Rajzer*, et al.*, "Comparison of aortic pulse wave velocity measured by three techniques: Complior, SphygmoCor and Arteriograph," *J Hypertens,* vol. 26, pp. 2001-7, Oct 2008.

[10] K. D. F. J. H. Mathews, *Numerical Methods Using MATLAB*: Prentice-Hall, 1998.

[11] D. G. Manolakis*, et al.*, *Statistical and Adaptive Signal Processing*. New York: McGraw-Hill, 2000.

[12] W. W. Nichols and M. F. O'Rourke, *McDonald's Blood Flow in Arteries*. Oxford: Oxford University Press, 2005.

[13] J. Allen and A. Murray, "Comparison of regional variability in multi-site photoplethysmographic pulse wave characteristics," presented at the First International Conference on Advances in Medical Signal and Information Processing, 2000. (IEE Conf. Publ. No. 476) 2000.

[14] A. B. Hertzman and C. R. Spealman, "Observations on the finger volume pulse recorded photo-electrically," *Am. J. Physiol.,* vol. 119, pp. 334-335, 1937.

[15] S. Mallat, *A Wavelet Tour of Signal Processing*, Second ed. New York: Academic Press, 1998.

[16] R. W. S. Alan V. Oppenheim, John R. Buck, *Discrete-time Signal Processing*, Second ed.: Prentice Hall, 1999.

[17] G. B. Moody and R. G. Mark, "A database to support development and evaluation of intelligent intensive care monitoring," *Computers in Cardiology,* pp. 657-660, 1996.

[18] A. L. Goldberger*, et al.*, "PhysioBank, PhysioToolkit, and PhysioNet: components of a new research resource for complex physiologic signals," *Circulation,* vol. 101, pp. E215-20, Jun 13 2000.

[19] B. E. Hurwitz*, et al.*, "Coherent ensemble averaging techniques for impedance cardiography," in *Third annual IEEE Symposium on Computer-Based Medical Systems*, University of North Carolina at Chapel Hill. Los Alamitos, Calif. , 1990, pp. 228-235.

[20] J. M. Bland and D. G. Altman, "Measuring agreement in method comparison studies," *Stat Methods Med Res,* vol. 8, pp. 135-60, Jun 1999.

[21] M. J. Hayes and P. R. Smith, "Artifact reduction in photoplethysmography," *Appl Opt,* vol. 37, pp. 7437-46, Nov 1 1998.

[22] D. A. McDonald, "Regional pulse-wave velocity in the arterial tree," *J Appl Physiol,* vol. 24, pp. 73-8, Jan 1968.

[23] H. A. Sturges, "The choice of a class interval," *J. Am. Stat. Assoc.,* vol. 21, pp. 65-66, 1926.

[24] J. G. Webster, *Design of Pulse Oximeters*. Bristol: Institute of Physics Publishing, 1997.

[25] R. H. Riffenburg, *Statistics in Medicine*. Burlington, MA: ELSEVIER Academic Press, 1999.

Chapter 4

Aortic blood pressure measured by electrical impedance tomography

Adapted from postprint version of:

Non-invasive monitoring of central blood pressure by Electrical Impedance Tomography (EIT): first experimental evidence

Josep Solà[1], Andy Adler[2], Arnoldo Santos[3], Gerardo Tusman[4], Fernando Suárez Sipmann[3] and Stephan H. Bohm[1]

[1]CSEM – Centre Suisse d'Electronique et de Microtechnique, Neuchâtel, Switzerland

[2]Systems and Computer Engineering, Carleton University, Ottawa, Canada

[3]Department of Critical Care, Fundación Jiménez Díaz-UTE, IIS-FJD, CIBERES, Madrid, Spain

[4]Department of Anesthesiology, Hospital privado de Comunidad, Mar del Plata, Argentina

Published in:

Medical & Biological Engineering & Computing

Med Biol Eng Comput, Vol 49, Num 4, 409-415, 15 March 2011

DOI: 10.1007/s11517-011-0753-z

Publisher version: http://www.springerlink.com/content/w17w284714422u82/

4. Aortic blood pressure measured by electrical impedance tomography

4.1. Rationale

There is an increasing demand for devices monitoring human cardiovascular function continuously non-invasively and non-obtrusively under clinical and ambulatory conditions: the goal is to reduce the need for long hospitalizations and costs, while improving patient comfort and safety. In recent years, electrocardiograms, intermittent Blood Pressure (BP) monitors and pulse oximeters have been successfully released into the market paving the way towards the monitoring of cardiac and vascular parameters in hospitals and out-patients [1]. Unfortunately, these parameters still provide an incomplete picture of a patient´s health status and do not fully meet clinical demand. In particular, discontinuous intermittent measurements of BP as provided by inflation of brachial cuffs are unsuitable for monitoring short-term BP regulation mechanisms, for which ideally beat-by-beat BP measurements should be performed. In addition, they may not yield representative BP during sleep as these repeated inflations induce arousal reactions, which may interfere with the measurement and lead to non-representative overestimated values [2]. Thus, the development of new techniques to monitor BP continuously with less frequent or even no inflations of pneumatic cuffs is justified.

Pulse Wave Velocity (PWV) is the velocity at which pressure pulses propagate along the arterial tree. In addition to being considered the gold standard methodology for assessing arterial wall stiffness [3], PWV has been shown to strongly depend on arterial BP. In particular, in central segments of the arterial tree where arterial walls are mainly elastic, PWV values depend exclusively on the subject-dependent arterial wall stiffness and the mean BP [4]. Therefore, and since changes in arterial stiffness occur only over long-term periods of time, PWV has been proposed as an adequate surrogate measure of short-term BP variability. Combined with intermittent cuff-based BP calibration procedures, several PWV-derived methods to provide continuous absolute BP measurements have been recently proposed: see [5] for a review. To date continuous PWV monitors have been limited to the monitoring of distal superficial large or cutaneous small arteries. Due to their autoregulation, wave reflections and differences in stiffness these peripheral arteries do not match the requirement of an ideal central point of measurement.

Electrical Impedance Tomography (EIT) is a non-invasive monitoring technology based on the analysis of bioimpedance signals [6]. From an electrical perspective, the thoracic cavity is composed of distributed impedance volumes. While the lungs (filled with air) form high impedance volumes, the heart and blood vessels (filled with blood) form low impedance volumes. EIT creates tomographic reconstructions of the distribution of these impedance volumes within the thorax at high sampling rates. As input signals, EIT requires a set of impedance measurements performed around the chest (see Figure 4.1). Basic a-priori knowledge about chest anatomy allows then reconstruction algorithms to estimate the most likely distribution of regional impedances.

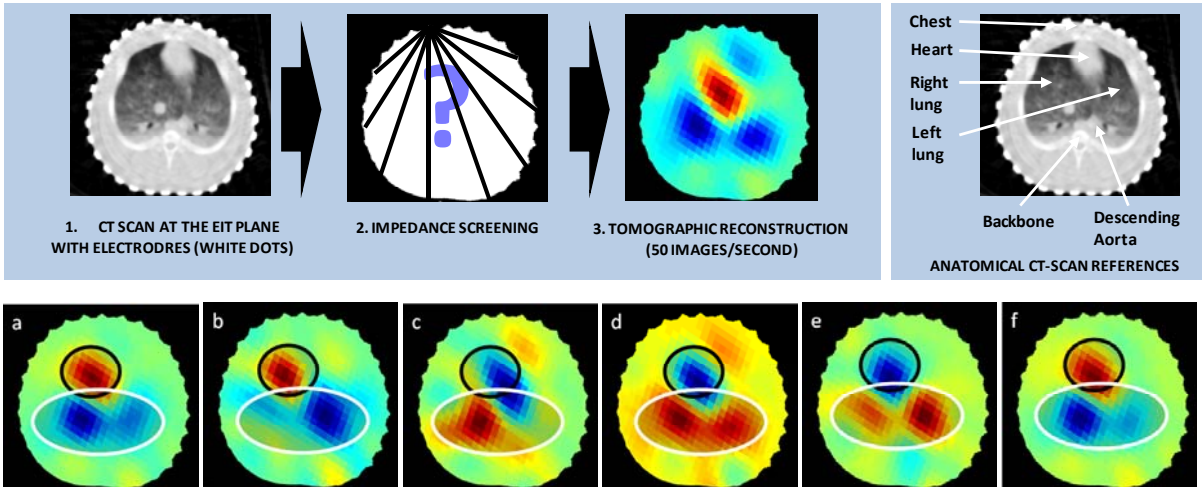

Figure 4.1 Tracking the propagation of arterial pressure pulses by EIT: After placing several electrodes around the chest (1), impedance measurements are performed for each electrode pair (2) and used to construct a tomographic impedance image (3). A CT-scan of pig chest is provided as anatomical reference. Lower panel shows an example of pulse propagation during an entire cardiac cycle: in a) and b) the filling of the heart is observed (red pixels). In c) the heart empties while the right lung (here on the left hand side) is starting to be perfused with conductive blood. In d) and e) both lungs are perfused. Finally, in f) the pulmonary blood returns to the left heart (blue lung pixels) and the cardiac cycle starts again.

During each cardiac cycle vascularized structures within the thorax receive bursts of electrically conductive blood, which decrease local impedance. Hence, when looking at a sequence of EIT images local pulsations of the impedance signal (impedance pulse) are observed which are associated with the underlying pulsation of the blood (pressure pulse). One example of an EIT-based visualization of a pressure pulse propagating from the heart to the lungs of an anesthetized pig is illustrated in Figure 4.1).

The aim of this pilot study was to experimentally test whether EIT could be used to measure central blood pressure continuously and non-invasively by providing unsupervised estimations of aortic pulse transit time.

4.2. Materials

4.2.1. Animal preparation

This pilot study was approved by the Animal Ethics Committee of the Instituto de Investigación Sanitaria, Fundación Jiménez Díaz, Madrid, Spain. Electrical Impedance Tomography (EIT) and respective reference data were gathered in an anesthetized domestic piglet, weighing approximately 25 kg. After fasting over night with free access to water, anesthesia was induced with intramuscular Ketamine (10 mg kg-1), Xylacine (10 mg kg-1)

and Atropine (1 mg). Anesthesia was maintained with Remifentanyl (0.05 to 0.10 µg kg-1 min-1) and Propofol (0.05 to 0.15 mg kg-1 min-1) once tracheal access by a cuffed 7 mm ID orotracheal tube (Mallinckrodt, Athlone, Ireland) was secured. No muscle relaxation was administered. The healthy lungs were normoventilated in the supine position at 5 cmH_2O PEEP in a volume controlled mode using a Servo i ventilator (Maquet Critical Care, Solna, Sweden). The animal was monitored by standard ECG and pulse oximeter via an MP50 device (Philips Medical, Böblingen, Germany). Ringer's lactate was administered to maintain fluid balance.

4.2.2. Data acquisition

Cardiac output and other hemodynamic parameters were measured in one femoral artery using the $PiCCO_2$ system (Pulsion Medical Systems, Munich, Germany). A catheter for continuous monitoring of aortic pressures and for determining the aortic valve opening was inserted into the ascending aorta via the other femoral artery under radiographic guidance and contrast agent injections. A central venous catheter was advanced through the introducer until it reached the right ventricle and the correct location was confirmed by X-ray.

The skin was shaved, electrode gel applied and the 32 electrodes of the EIT device Enlight® (Timpel SA, Sao Paulo, Brazil) placed equidistantly around the circumference of the thorax just below the level of the axilla. This system produces 50 real time images per second. Small electrical currents (<10 mA; 125 kHz; meeting the electrical safety requirements of standard IEC 60601) were administered in a rotating sequence through pairs of electrodes, with three non-injecting electrode interposed between them. The resulting potentials were measured by the non-injecting electrodes, amplified, measured and fed into an image reconstruction algorithm. Note that although electrical currents propagate three-dimensionally within the thorax, the EIT reconstruction algorithm creates projections of impedance changes in thoracic volumes in the form of a 2-D tomographic image located within the electrode plane.

4.3. Methods

4.3.1. Detection of aortic region of interest by saline bolus injections

An initial estimate of Regions of Interest (ROI) comprising EIT pixels with information on heart, lungs and aorta was obtained by injecting boluses of 20% hypertonic saline at two anatomical locations: the right ventricle and the ascending aorta. Similar to the approach described in [7] the hypertonic saline solution was used as contrast agent: by locally increasing the electrical conductivity of blood by approximately four-fold, the passage of the bolus was identified by a circumscribed local transient decrease in impedance. After injecting the contrast agent into the ascending aorta its downstream propagation was tracked, and the descending aorta ROI was identified by the arrival of the contrast at the dorsal EIT electrode plane.

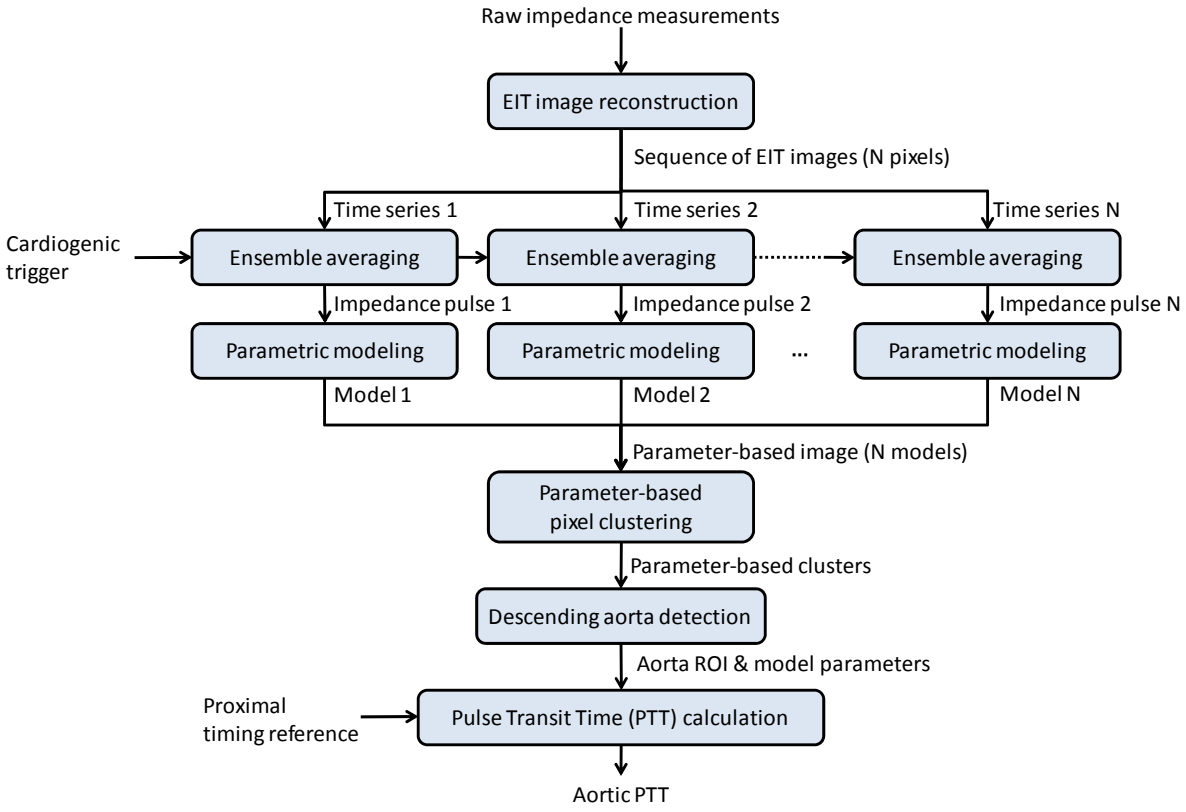

Figure 4.2 Estimation of an aortic Pulse Transit Time (PTT) value from a sequence of EIT images. Initially, an ensemble-averaged impedance pulse [8] for each of the N pixels in the sequence of EIT images is calculated. A parametric model [9] is then fitted to each impedance pulse. A PAT-based image is generated by assigning a parameter of the fitted model to each pixel. Those pixels containing information on the descending aorta are identified by an unsupervised clustering technique. From the identified pixels, a single impedance pulse representing the pulsatility information of the descending aorta is obtained. A non-invasive aortic PTT value is finally calculated by incorporating a proximal timing reference for the opening of the aortic valve.

4.3.2. Unsupervised detection of aortic region of interest

The exact location of the descending aorta ROI within a series of EIT images was determined by a novel unsupervised method based on the estimation of pixel-specific Pulse Arrival Times (PAT), as illustrated by Figure 4.2.

After leaving the ventricles, pressure pulses propagate along the systemic and pulmonary arterial trees and induce increases of the local volume of conductive blood, thereby decreasing the local electrical impedance (Figure 4.1). This phenomenon generates impedance pulses. Although the amplitude information contained within these impedance pulses (in Ohms) cannot necessarily be associated with the actual amplitude of the pressure pulses (in mmHg), its coded timing information, however, is identical. In particular, the onset of a pressure pulse at a given anatomical location instantaneously induces the onset

of its associated impedance pulse. The PAT value depicts thus the time at which this arrival event occurs. From a sequence of EIT images containing at least one cardiac cycle, one is then able to calculate a PAT-based image where the numerical value of each pixel corresponds to the arrival time of the pressure pulse at its underlying anatomical region.

For this pilot study, the generation of PAT-based EIT images was performed as follows: ensemble averaging [8] of impedance pulses at each EIT pixel (N=1024) was performed during ventilation pauses using the onset of the pressure pulse in the aortic catheter as a trigger (cardiogenic trigger). The arrival time of each averaged impedance pulse was then calculated via a robust parametric detection algorithm [9]. A numerical model $m_\Omega(t)$ of pressure pulse was fitted to each of the 1024 impedance pulses, depicting information of its arrival time (μ) and morphology, *i.e.* amplitude (A), slope (σ) and offset (C):

$$m_\Omega(t) = A\ \tanh\left(\frac{t-\mu}{\sigma}\right) + C$$

Equation 62

The fitting of the model $m_\Omega(t)$ to each impedance pulse $p(t)$ was performed by finding the set of parameters $\Omega = \{A, \mu, \sigma, C\}$ that minimized the quadratic error between $m_\Omega(t)$ and $p(t)$, via a multi-parametric steepest descent search [9]. A PAT-based image was finally generated by assigning to each EIT pixel its associated μ value. Those pixels for which the fitted parametric model was either unreliable or the fitting algorithm did not converge, were excluded (parameter-based clustering).

The novel unsupervised aorta detection method relied thus on the analysis of the above mentioned PAT-based EIT images. In particular the method was able to identify the descending aorta ROI based on the fact that after the opening of the aortic valve the first segment of the arterial tree within the EIT plane to receive the arriving pressure pulse is the descending aorta. Hence, for this pilot study the aortic ROI was identified as those pixels located centrally behind the lungs for which the PAT values were lowest.

4.3.3. EIT aortic pulse transit time as a surrogate for aortic blood pressure

Impedance pulses of pixels belonging to the aortic ROI were hypothesized to represent the underlying aortic pressure pulse phenomenon. Their arrival times, estimated as the μ parameter of the numerical model, were assumed to be non-invasive surrogates of the aortic Pulse Transit Time (PTT). Accordingly, EIT-derived aortic PTT values were compared to aortic BP values for several hemodynamic conditions. The goal of this analysis was to test if EIT-derived aortic PTT values could be used as surrogate measurements of BP, by testing if both measurements were negatively correlated, *i.e.* increased aortic pressure should result in shorter pulse transit time from the aortic valve to the descending aorta, and *vice versa*. Different hemodynamic conditions were generated aiming at mean arterial pressures values within the wide range between 60 and 150 mmHg. Pressure values were actively adjusted and stabilized at each level for several minutes using infusions of either nitroglycerine or noradrenaline. Data from all devices were recorded simultaneously during ventilation pauses of 30 seconds on each pressure level immediately after stabilization, and PAT-based EIT images calculated for each condition.

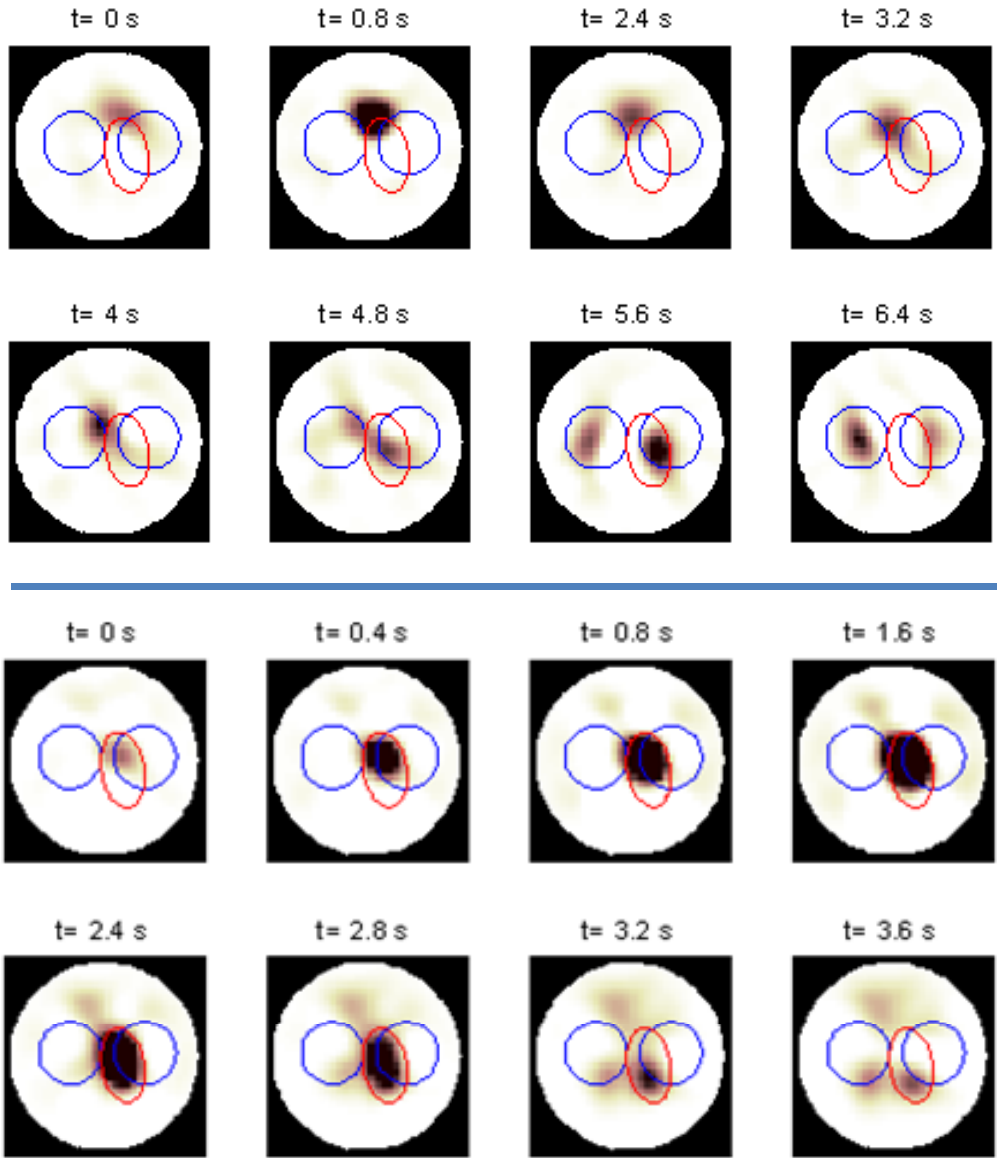

Figure 4.3 Upper Panel: Downstream propagation of a hypertonic saline bolus injected into the right ventricle. Lower Panel: Downstream propagation of a hypertonic saline bolus injected into the ascending aorta. Blue circles identify lung ROIs and red ellipse the aortic ROI.

4.4. Results

4.4.1. Detection of aortic region of interest by saline bolus injections

The upper panel of Figure 4.3 illustrates the identification of the ROIs corresponding to both lungs when a 10 ml bolus of hypertonic saline solution was injected into the right ventricle: after an initial accumulation of saline within the ventricle for about 2 seconds (t=2.4s), the bolus propagated towards the pulmonary artery (t=4.8s) before reaching the left and right lungs (t=6.4s, blue ROIs).

The lower panel of Figure 4.3 illustrates the identification of the aortic ROI when a similar bolus was injected in the ascending aorta, right downstream of the aortic valve. During the injection of EIT contrast agent (t=0.0s, upper region of red ROI) the bolus rapidly spread into the aortic arch (t=0.8s). At the end of injection (t=2.8s) only little saline remained within the aortic arch and the upper thoracic aorta, but finally appeared in the descending aorta (t=3.6s, lower region of red ROI). The descending aorta was thus localized at the medial-dorsal outline of the left lung.

Note that although the ascending aorta, the aortic arch and the descending aorta belong to different transverse planes along the cranio-caudal axis, they were all projected into one single EIT plane (red ROI).

4.4.2. Unsupervised detection of aortic region of interest

Figure 4.4 shows the PAT-based image, averaged for all hemodynamic conditions. A PAT value was assigned to each pixel, corresponding to the μ parameter estimated from the impedance pulses at that pixel. A set of 7 pixels was identified as having aorta-like behavior (*i.e.* lowest PAT values being located centrally behind the lungs) and clustered into a single aortic ROI. Note that the location of the aortic pixels identified by the proposed unsupervised algorithm matched with the aortic ROI as identified by the hypertonic saline bolus.

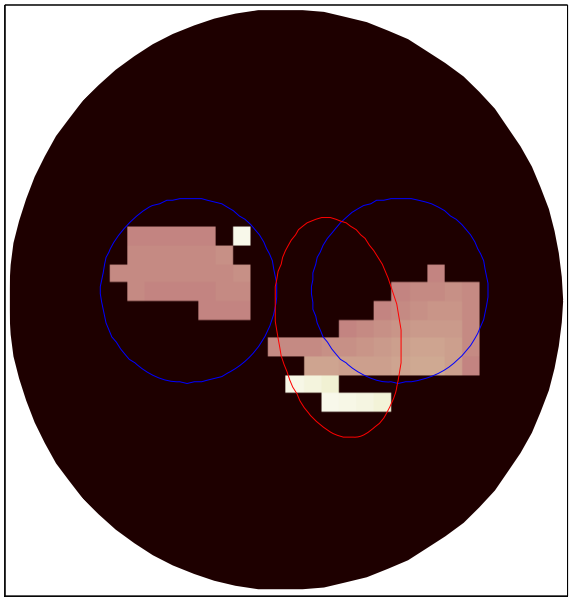

Figure 4.4 Averaged PAT-based EIT image for the 11 hemodynamic conditions. Bright pixels depict an early arrival of pressure pulses (aortic pixels), and dark pixels depict a late arrival (lung pixels). Black pixels correspond to pixels for which the parametric modelling did not provide reliable estimations. Blue circles and red ellipse correspond to lungs and aorta, as identified by hypertonic saline bolus injections (see figure 3). Yellow ellipse marks the pixels for which best negative correlations were found between EIT-PTT and mean aortic BP.

Table 4.1 Correlation coefficients when comparing EIT aortic PTT values with mean aortic blood pressure values for each of the 7 pixels within the aortic ROI

Pixel	Correlation
(17,21)	-0.867 ($p<10^{-3}$)
(18,21)	-0.864 ($p<10^{-3}$)
(19,21)	-0.829 ($p<10^{-2}$)
(19,22)	-0.885 ($p<10^{-3}$)
(20,22)	-0.931 ($p<10^{-4}$)
(21,22)	-0.967 ($p<10^{-5}$)
(22,22)	-0.967 ($p<10^{-5}$)

4.4.3. EIT aortic pulse transit time as a surrogate for aortic blood pressure

Table 4.1 shows jointly for all hemodynamic condition the correlation scores between aortic PTT values as calculated for the aortic EIT pixels and the invasively-measured mean BP. Very strong negative correlations were encountered, suggesting that EIT-derived aortic PTT is a potential surrogate of aortic BP. Pixels {21,22) and {22,22) provided the best correlation scores: r=-0.967, p<0.00001. For illustrative purposes these two pixels have been highlighted in Figure 4.4 (yellow circle). Figure 4.5 provides a correlation plot comparing EIT-PTT to aortic BP for pixel {21,22}. Note that EIT-PTT values are expressed as [%], depicting the μ value of the fitted parametric model [9] divided by the maximum μ search range.

4.5. Discussion

We provided first experimental evidence for the feasibility of using EIT to measure pulsatility within the descending aorta in a non-invasive way. Given a sequence of EIT images of several cardiac cycles, we presented a novel method to identify an aortic Region of Interest (ROI) in an unsupervised manner. The correct location of the aortic ROI was confirmed by hypertonic saline bolus injections directly into the aorta. Since the aortic EIT-PTT obtained by the unsupervised EIT method correlated inversely and strongly with the corresponding invasive aortic BP, we suggest that EIT-PTT is a candidate-technology for the continuous non-invasive and non-occlusive monitoring of central BP. If robust, the EIT-PTT technique offers significant advantages over other unsupervised PTT based schemes; specifically, EIT-PTT analyzes blood-pressure-related impedance pulses in the aorta, while state-of-the-art ambulatory PTT schemes require measurement of pulses in peripheral arteries. Since pulsatility of peripheral arteries is affected by autoregulation, wave reflections and local wall stiffness EIT-PTT has the advantage of providing unique central hemodynamic measurements: EIT-PTT may be understood as placing a “virtual catheter” into the central vessel, being thus free of peripheral interferences.

For this study, the invasively-obtained arterial pressure curve was used as both, a cardiogenic trigger for performing ensemble averaging, and as a timing reference for the opening of the aortic valve. The ECG, or signals from other EIT-regions such as the heart ROI, should be explored in the future as alternative non-invasive proximal timing references. Both alternatives were discarded from the presented study since the goal was to show EIT to be a valid technology to detect the arrival time of impedance pulses at the descending

aorta. For this purpose, a ground-truth proximal timing reference was required directly at the aortic valve.

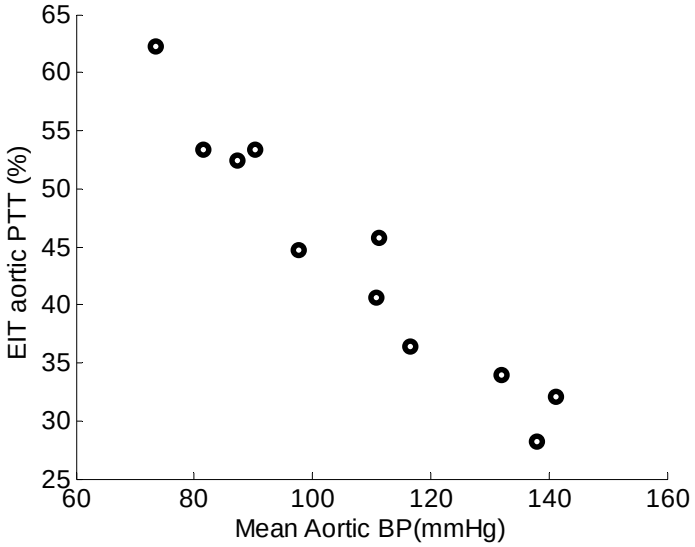

Figure 4.5 Correlation plot comparing EIT-derived aortic PTT values with mean aortic BP values for pixel {21,22) (marked in yellow in figure 4). Hypotensive and hypertensive conditions were generated by noradrenalin and nitroglycerine administration. PTT: Pulse Transit Time, BP: Blood Pressure.

Although a wide range of mean BP values (from 60 to 150 mmHg) were obtained in this single pig, the low amount of intra-individual experimental data (N=11) is a main limitation of this study, impeding any reproducibility analysis. Even more, the one-animal nature of this pilot study limits the extrapolation of the obtained conclusions to other pigs, other species or even humans. However, these initial encouraging results warrant the prospective systematic evaluation of the proposed method in a sufficiently large number of animals.

Future studies should compare EIT-PTT not only with BP but also directly with PTT measured by two catheters within the aorta, one located at the aortic valve, the other one exactly within the EIT plane.

Further development work needs to be done to be able to measure aortic EIT-PTT values at even higher and lower blood pressures and also during mechanical ventilation and spontaneous breathing. Future studies including additional cardiovascular maneuvers such as NO administration and cold stress need to be performed in order to assess the sensitivity of the proposed EIT-PTT parameter to vasomotion phenomena [10].

The use of dedicated EIT reconstruction algorithms and the reduction of the number of EIT electrodes are to be studied as well. Even more, although for this study a standard EIT electrode configuration with electrodes equally-spaced around the thorax was used, better resolution in particular regions of interest such as the aorta may be achieved in the future by designing dedicated electrode placements. Finally the feasibility of performing EIT-PTT measurements at lower imaging rates (<50 frames per second) is to be evaluated.

In conclusion, the presented data provide first experimental evidence that EIT is a candidate technology for the assessment of arterial pulsatility at the descending aorta, suggesting a way towards a new family of non-invasive continuous monitors of central blood pressure.

References

[1] G. Parati*, et al.*, "European Society of Hypertension guidelines for blood pressure monitoring at home: a summary report of the Second International Consensus Conference on Home Blood Pressure Monitoring," *J Hypertens,* vol. 26, pp. 1505-26, Aug 2008.

[2] R. J. Davies*, et al.*, "Effect of measuring ambulatory blood pressure on sleep and on blood pressure during sleep," *BMJ,* vol. 208, pp. 820-823, 1994.

[3] S. Laurent*, et al.*, "Expert consensus document on arterial stiffness: methodological issues and clinical applications," *Eur Heart J,* vol. 27, pp. 2588-605, Nov 2006.

[4] W. W. Nichols and M. F. O'Rourke, *McDonald's Blood Flow in Arteries*. Oxford: Oxford University Press, 2005.

[5] J. Solà*, et al.*, "Ambulatory monitoring of the cardiovascular system: the role of Pulse Wave Velocity," in *New Developments in Biomedical Engineering*, D. Campolo, Ed., ed Vienna:: I-Tech Education and Publishing, 2010.

[6] D. S. Holder, *Electrical Impedance Tomography: Methods, History and Applications*: Institute of Physics Publishing), 2005.

[7] I. Frerichs*, et al.*, "Regional lung perfusion as determined by electrical impedance tomography in comparison with electron beam CT imaging," *IEEE Trans Med Imaging,* vol. 21, pp. 646-52, Jun 2002.

[8] B. E. Hurwitz*, et al.*, "Coherent ensemble averaging techniques for impedance cardiography," in *Third annual IEEE Symposium on Computer-Based Medical Systems*, University of North Carolina at Chapel Hill. Los Alamitos, Calif. , 1990, pp. 228-235.

[9] J. Sola*, et al.*, "Parametric estimation of pulse arrival time: a robust approach to pulse wave velocity," *Physiol Meas,* vol. 30, pp. 603-15, Jul 2009.

[10] M. F. O'Rourke, "Time domain analysis of the arterial pulse in clinical medicine," *Med Biol Eng Comput,* vol. 47, pp. 119-29, Feb 2009.

Chapter 5

Central pulse wave velocity measured by impedance- and photo-plethysmography

Partly adapted from postprint version of:

Chest Pulse Wave Velocity: a Novel Approach to Assess Arterial Stiffness

Josep Solà[1], Olivier Chételat[1], Claudio Sartori[2], Yves Allemann[3] and Stefano F. Rimoldi[2,3]

[1]CSEM – Centre Suisse d'Electronique et de Microtechnique, Neuchâtel, Switzerland

[2]Department of Internal Medicine, CHUV University Hospital, Lausanne, Switzerland

[3]Swiss Cardiovascular Center Bern, University Hospital Bern, Bern, Switzerland

Published in:

IEEE Transactions on Biomedical Engineering

IEEE Trans. Biomed. Eng., Vol 58, Num 1, 215-223, January 2011

DOI: 10.1109/TBME.2010.2071385

5. Central pulse wave velocity measured by impedance- and photo-plethysmography

5.1. Rationale

Pulse Wave Velocity (PWV) represents the velocity at which pressure pulses propagate through the arterial tree. PWV is considered as the gold standard measurement to assess arterial stiffness (in particular, carotid to femoral PWV), and has been identified as an independent predictor of cardiovascular morbidity and mortality [1]. In line with this data, in 2007 the European Society of Hypertension has introduced PWV as a recommended test to assess cardiovascular risk in its guidelines for the diagnosis and management of hypertension [2].

Nowadays techniques that allow non-invasive assessment of PWV fall into two main categories. On the one hand, Complior (Alam Medical, France), SphygmoCor (AtCor Medical, Australia), Vicorder (Skidmore Medical, UK) and PulsePen (Diatecne, Italy) rely on the placement of two pressure transducers onto two superficial arteries. These devices detect the arrival time of a pressure pulse that propagates through the arterial tree, and calculate the delay in pulse arrival time between the proximal and distal sensors [3]. By approximately measuring the distance through which the pulse wave has propagated, one estimates then a pulse propagation velocity value. Large clinical studies support the reliability and clinical validity of this technique [1].

On the other hand, Arteriograph (TensioMed, Hungary) estimates aortic PWV by applying pulse wave analysis techniques [4] to a pressure pulse recorded by an inflated brachial cuff. The major interest of this approach is that PWV measurements can be performed automatically, reducing the need of trained medical staff. The measurement is based on the fact that during systole, the blood volume having been ejected into the aorta generates a pressure pulse (early systolic peak). This pulse runs down and reflects from the bifurcation of the aorta, creating a second pulse (late systolic peak). The return time (RT S35) is the difference between the first and the second systolic pulse waves, and is claimed to be a surrogate of aortic PWV. Unfortunately, clinical [5] and numerical [6] studies currently question the reliability and working principles of the RT S35 technique.

A broader review on the technical and physiological background of the described techniques is provided in [7], highlighting the demand for new implemented techniques that reduce the amount of supervision currently required to perform PWV measurements.

This paper provides evidence for a novel technique that assesses pulse transit times along a vascular tree including both central elastic and peripheral non-elastic arteries, and that is prone to be integrated in a chest belt sensor. Comparison with Complior PWV measurements is provided.

The paper is organized as it follows: Section 5.2 describes the underlying physiological principles of the measurement technique and proposes a method to measure pulse transit times at the chest. Section 5.3 discusses methodological issues, Section 5.4 further specifies

the proposed method up to an algorithmic level with parameters obtained from a development cohort, and Section 5.5 presents the results of a prospective validation study. Finally, Section 5.6 suggests a method to obtain Chest PWV values, and Section 5.7 concludes the paper.

5.2. Measureming central Pulse Transit Times at the chest

Arterial pressure pulses are generated at the onset of left-ventricular ejection: after an initial period of isovolumetric contraction, the ventricular pressure exceeds arterial pressure and forces the aortic valve to open. The sudden rise of aortic pressure distends the elastic walls of the ascending aorta, thus creating a pressure pulse that propagates through the walls of the entire arterial tree [8]. Of particular interest in the context of this paper is the pressure pulse traveling from the aortic valve (proximal site) to the sternum subcutaneous vascular bed (distal site). The transit time between said proximal and distal sites is refereed as Chest PTT.

5.2.1. Anatomy of the thoracic arterial tree

Figure 5.1 provides an overview of the arterial segments propagating a pressure pulse before reaching the sternum. After leaving the left ventricle, the pressure pulse propagates through the aorta and moves forward to the brachiocephalic trunk. Up to this point, the propagation is performed through elastic arteries only and at relatively low velocities. From the brachiocephalic trunk the pressure pulse accelerates while propagating through the internal thoracic artery (a large muscular artery, similar to the radial artery [9]) before reaching the heterogeneous subcutaneous vascular bed covering the sternum manubrium.

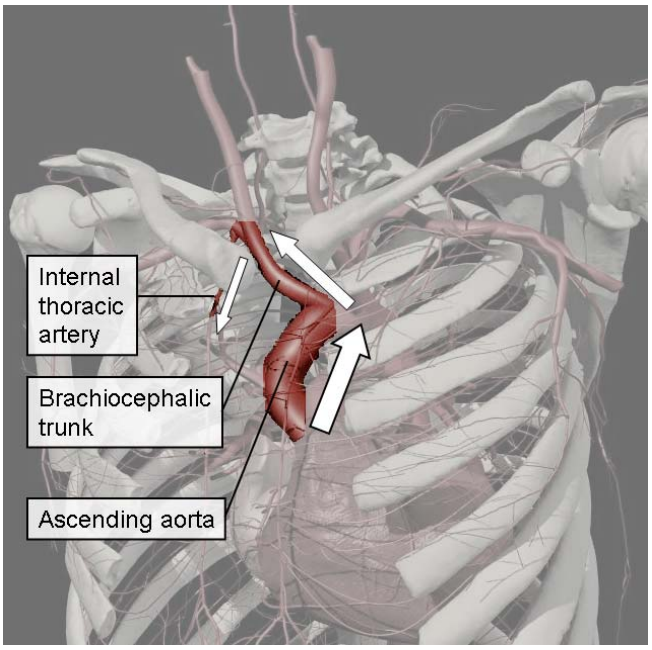

Figure 5.1 Overview of the arterial segments involved in the propagation of a pressure pulse from the left ventricle to the vascular bed at the upper region of the sternum. 3D model courtesy and copyright from Primal Pictures, Ltd.

Table 5.1: Propagation delays for the different arterial segments involved in the measurement of pulse transit times from the aortic valve to the vascular bed covering the sternum manubrium, *i.e.* the Chest PTT.

Segment of the arterial tree	Typical PWV	Typical length	Expected delay	Expected incidence
Ascending aorta and aortic arch	4.8 m/s	7 cm	15 ms	37%
Brachiocephalic truck	5.1 m/s	10 cm	20 ms	49%
Internal thoracic artery (mammary artery)	8.5 m/s	5 cm	6 ms	15%
Overall Chest PTT	5.3 m/s	22 cm	41 ms	100%

For illustrative purposes, Table 5.1 details the arterial segments through which a pulse pressure propagates before reaching the sternum, together with the expected delays introduced at each segment. Typical PWV values have been obtained from [10] and [9]. According to the model, the timing information contained into the Chest PTT parameter is expected to be 85% related to large vessels (aortic and carotid) and only 15% related to conduit arteries (internal thoracic artery). In other words, the arrival time of a pressure pulse at the sternum is mainly expected to be determined by the propagation through large vessels, and only minimally affected by other secondary arteries. Additionally, note that because pressure pulse propagation at the sternum vascular bed is performed at high velocities (Moens-Koprteweg equation [11] applied to arterioles geometry), the influence of arteriolar autoregulation to the total transit time can be neglected.

5.2.2. Chest sensor concept

Opening of the aortic valve: phonocardiogram-guided impedance-plethysmography

Impedance Cardiography (ICG) is a well established technique [12] to non-invasively assess cardiac events and other hemodynamic variables such as Pre-Ejection Period (PEP), and cardiac output—see for instance the recently FDA-cleared device BioZ DX (Sonosite, USA). ICG relies on the analysis of voltage signals resulting from currents injected through the thorax. A typical ICG setup requires placing four electrodes around the thorax: two current injection electrodes and two voltage measurement electrodes. When detectable, the onset of the rapidly increasing slope of the first derivative of the ICG signal is considered to be a good estimate of the opening of the aortic valve, and is referred to as B-point [13]. However, the wide range of physiological variability of ICG patterns through different subjects and hemodynamic status turns the apparently straightforward identification of B-point to be a critical task [14]. In [15] an improved method based on the analysis of the third derivative of the ICG was proposed. This method allows locating B-points even when no inflections are present in the ICG signals. Unfortunately, the third derivative of ICG contains several misleading local maxima, and this approach is hard to be implemented in an unsupervised manner [16].

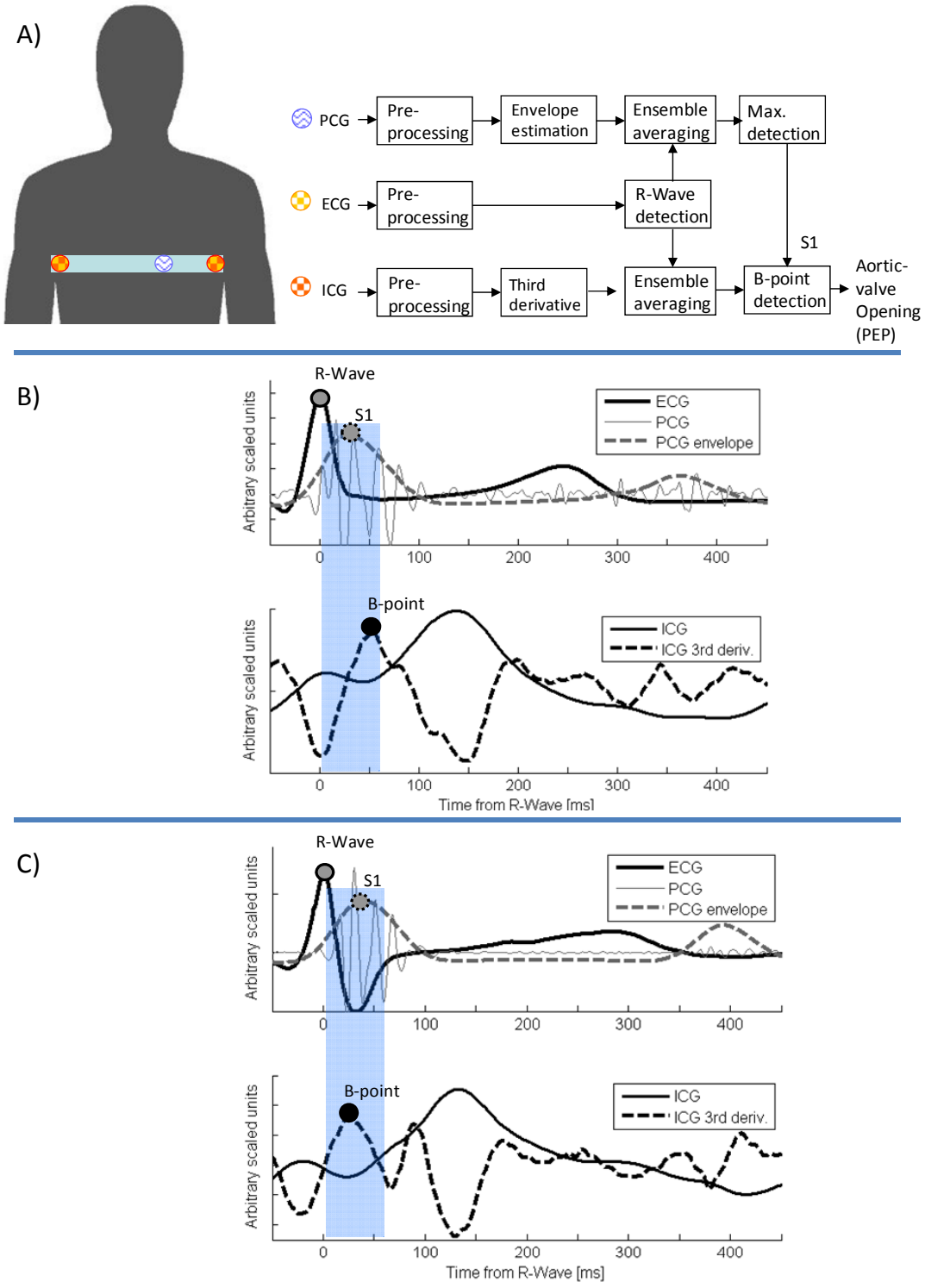

Figure 5.2: Panel A: the novel method to determine the opening of the aortic valve (or Pre-Ejection Period, PEP). Panel B: example of data where a single maximum of the ICG third derivative is present. Panel C: example of data where two local maxima of the ICG third derivative exist. In this case, the *a-priori* window defined by the PCG guides the B-point detection, constraining the ICG analysis to a unique solution.

Phono Cardiography (PCG) is a computerized approach to the traditional auscultation of heart sounds. When placing an electronic stethoscope on the chest, one obtains a series of electrical signals containing representative patterns of the first and second heart sounds. In particular the first heart sound of the PCG (S1) is associated to the closure of the tricuspid and mitral valves, preceding the opening of the aortic valve [17]. Although the accurate determination of S1 requires complex signal processing techniques, the maximum of the PCG envelope has been shown to be already a rough estimate of S1 [18].

For the chest sensor, the joint analysis [19] of PCG and ICG is proposed for the detection of the aortic valve opening (see Figure 5.2). The present approach exploits the robustness of PCG-based techniques and the precision of ICG third-derivative-based techniques. Initially, the R-Wave at the ECG triggers the onset of left-ventricular depolarization. Then, a maximum of the PCG envelope is detected (S1), roughly indicating the onset of left-ventricular ejection. Local maxima of the third derivative of the ICG are then identified, and the closest maximum to the previously-determined S1 point is finally selected as the opening of the aortic valve (B-point). Thus, the proposed approach introduces S1 as an *a-priori* estimate of the opening of aortic valve, guiding the identification of the B-point at the ICG. Two examples of PCG-guided ICG analysis are illustrated in Figure 5.2.

Distal pulse arrival: multichannel reflective photo-plethysmography

The arrival of a pressure pulse at the sternum manubrium is characterized by a fast and heterogeneous spread of the pulsatile energy through its subcutaneous vessels. Reflective Photo Plethysmography (PPG) is a non-invasive technique [20] that allows detecting the arrival of these pressure pulses. When illuminating the chest region with infrared light, the sternum reflects part of the injected photons. A photodiode in contact with the skin receives then a portion of the reflected energy, containing information on the pulsatility of the illuminated tissues. Unfortunately, chest PPG is severely affected by the heterogeneous distribution of the underlying vascular bed, and the probability that a single PPG sensor illuminates a low-irrigated portion of tissue is non-negligible [21]. Moreover, the low perfusion encountered at the chest implies PPG signals with low signal-to-noise ratios. In this study a multi-dimensional parametric estimation of Pulse Arrival Times (PAT) is proposed to cope with these difficulties.

Perfusion heterogeneity is managed by introducing spatial diversity (multi-dimensional PAT estimation), and low perfusion by applying noise-robust PAT estimation techniques. In [22] a parametric approach to estimate PAT in low SNR conditions is described. Instead of identifying a characteristic point in a PPG pressure pulse this approach fits a parametric model onto the entire pulse. A PAT-equivalent value is finally extracted from the parameters of the model.

Thus, the proposed PAT estimation technique combines the parametric information extracted from a set of M simultaneously-recorded PPG channels, and provides a single robust estimation of PAT.

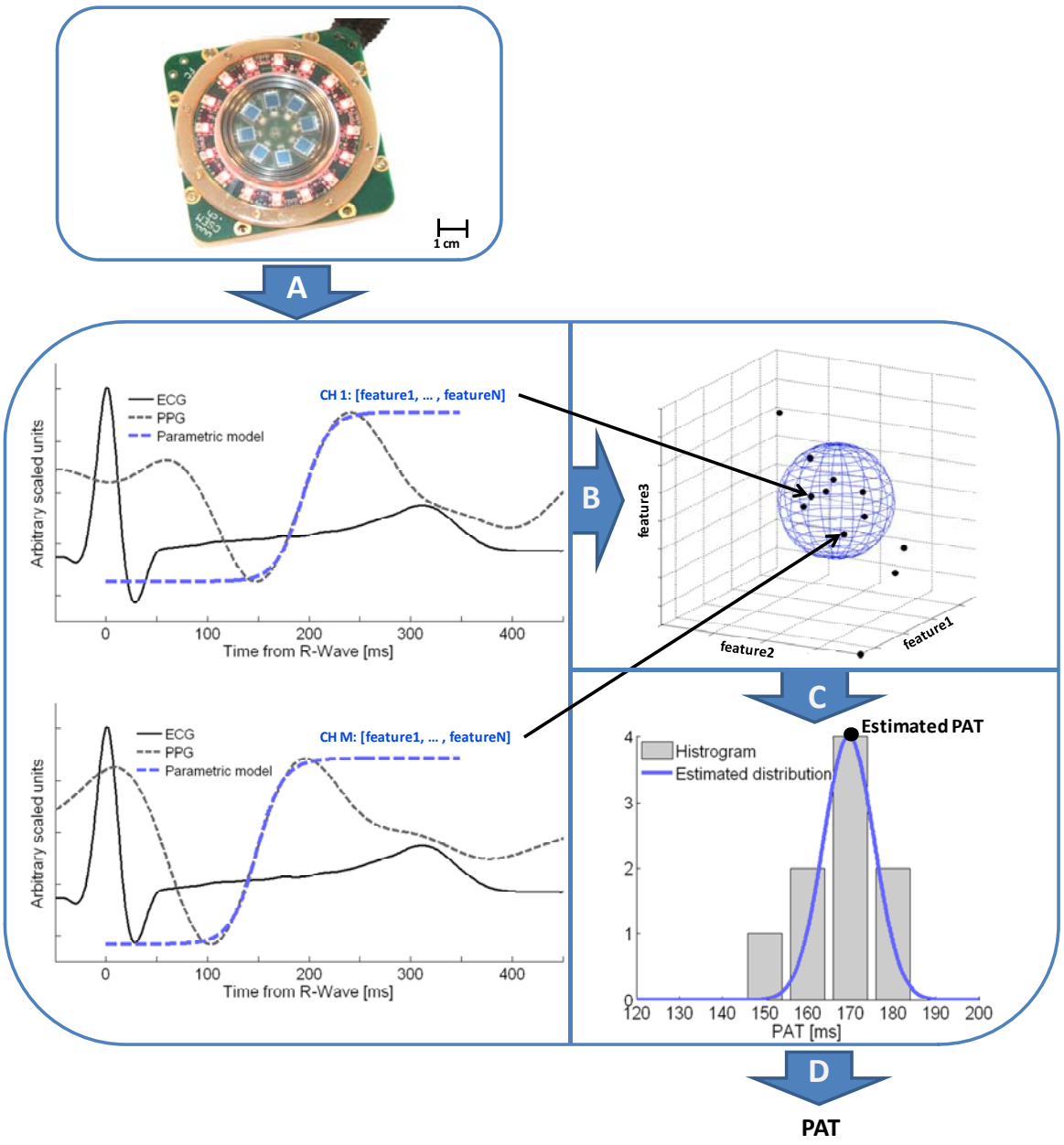

Figure 5.3: Multi-dimensional parametric estimation of Pulse Arrival Time (PAT). A) For each of the *M* channels simultaneously recorded at the chest a parametric model of the local pressure pulse is estimated. B) Each parametric description is mapped onto an *N*-dimensional feature space where a clustering procedure excludes unreliable channels. C) A single PAT value is estimated by post-processing the parametric descriptions of the selected channels.

The technique is developed in three steps, as illustrated by Figure 5.3. First, a parametric model [22] is estimated for each of the *M* PPG channels. The shape and arrival time of the pressure pulse *seen* by each channel is described by *N* parameters, which correspond to a point in an *N*-dimensional feature space. Secondly, the distribution of the *M* points in this feature space is considered: outliers are removed by an unsupervised clustering procedure [23] in order to estimate the most likely model of pressure pulse. The clustering procedure

aims at excluding non-representative (probably low-perfused) channels from the analysis. The procedure relies on the assumption that whereas those PPG channels located over a locally rich vascular bed generate similar parametric descriptions, those PPG channels located over low-perfused regions generate spread points in the feature space. Thus, non-representative channels are defined as points that lay beyond the borders of a hypersphere in a Mahalanobis-transformed feature space. Thirdly, the parametric descriptions of the remaining representative channels are processed through a histogram analysis to provide a single chest PAT value.

Because phase velocity information of pressure pulses is mainly contained in high frequencies harmonics [10], PPG channels can be initially high-pass filtered without any loss of relevant information. In addition to increase the signal-to-noise ratio, high-pass filtering limits non-relevant channel-dependent patterns that might latter influence the parametric model fitting.

From Pulse Arrival Times to Pulse Transit Times

As described above, the joint analysis of the ECG, PCG, ICG and PPG data recorded at the chest provides information on the opening of the aortic valve (PEP), and the arrival time of the pressure pulse at the chest (PAT). Then, a Pulse Transit Time value (PTT) from the aortic valve to the chest is obtained as the difference: PTT = PAT – PEP. Accordingly, a full overview of the chest sensor setup is provided by Figure 5.4.

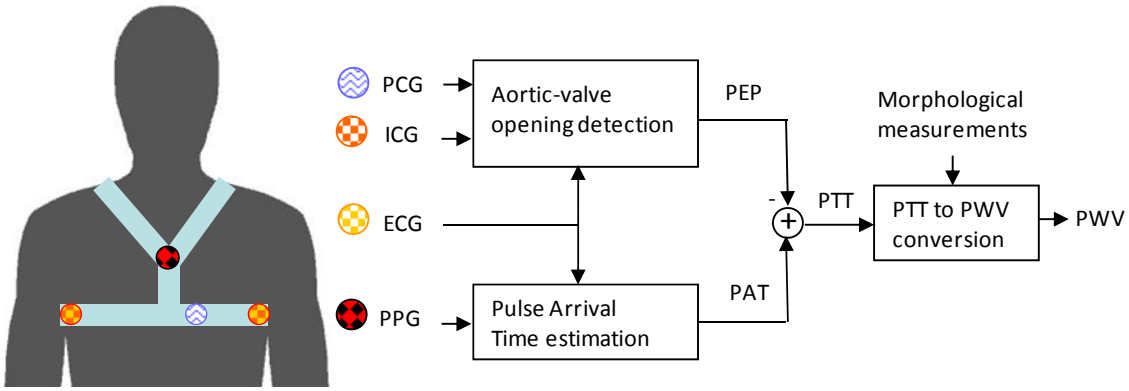

Figure 5.4: The complete chest sensor approach to estimate PWV. A Phono Cardiogram (PCG) and Impedance Cardiogram (ICG) are combined to detect the opening of the aortic valve, producing a Pre-Ejection Period (PEP) value. A multi-channel Photo Plethysmograph (PPG) provides an estimation of the arrival time of the pressure pulse at the capillary bed at the sternum (PAT). The Pulse Transit Time (PTT) from the aortic valve to the chest is computed by subtracting PEP from PAT. Pulse Wave Velocity (PWV) is finally estimated by converting PTT values (in ms) to PWV values (in m/s).

Methodological approach

After having described the method to obtain PTT measurements at the chest, one needs to determine the optimal parameters of the algorithm implementing it. Finding the parameters that maximize the accuracy of an algorithm is actually an optimization process which requires *in-vivo* data, a reference, and an objective function. In our study, the *in-vivo* data were gathered from 9 subjects (development cohort). The output of the developed algorithm being a PTT value, a suitable PTT reference was needed. Unfortunately, no chest PTT reference exists so far, and the closest reference that we could acquire was the PTT value as measured by a COMPLIOR device. Therefore, we defined the objective function for the optimization of the algorithm to be the correlation between the output of the Chest PTT algorithm, and the COMPLIOR PTT for all subjects within the development cohort. Section 5.4 describes the parameters of the optimized algorithm.

After having defined and fixed the parameters of the algorithm, we evaluated how the Chest PTT estimations correlated with COMPLIOR Carotid to Femoral (CF) and Carotid to Radial (CR) PWV measurements in a prospective study involving 31 normo- and hypertensive subjects (Section 5.5).

For this study, the experimental protocol was approved by the institutional review boards on human investigation of the University of Lausanne, Switzerland. All participants provided written informed consent.

5.3. Development study: materials

The development cohort involved 9 subjects (age: 26…74 years, BMI: 19…23 kg/m^2, height: 173…194 cm, COMPLIOR CF PWV 7.2…15.4 m/s, and COMPLIOR CR PWV 8…12.3 m/s).

The experimental protocol consisted on the simultaneous recording of both COMPLIOR PWV and Chest PTT values at rest. After enrollment, subjects laid in supine position while two operators started the instrumentation phase. Chest PTT measurements were performed by means of a multichannel chest reflective PPG sensor (CSEM's proprietary integrated chest electrode prototype with 7 infrared concentric PPG channels [24], 32 Samples/s; and 2 spot gel ECG electrodes, 1 kSample/s) and a BIOPAC (BIOPAC Systems, US) platform (4 spot gel electrodes connected to an EBI100C electrical bio-impedance amplifier, 50 kHz, 1 kSample/s; and 2 spot wet electrodes connected to an ECG100C electrocardiogram amplifier, 1 kSample/s). The placement of the sensor on the sternum naturally set the measurement surface at a constant temperature, reducing temperature-induced skin vasocontraction phenomena. Chest PTT data was continuously recorded in an unsupervised manner during the whole experiment. COMPLIOR PWV measurements were performed according to standard COMPLIOR uses, *i.e.* after measuring external carotid to femoral and carotid to radial distances, three pressure transducers were placed over the carotid, femoral and radial arteries. An experienced operator visualized the quality of the data in real time and decided when a measurement could be performed. Carotid to Femoral (CF) and Carotid to Radial (CR) PWV values were thus obtained. Consecutive COMPLIOR measurements were performed until a set of at least three similar COMPLIOR PWV values were available. Brachial oscillometric blood pressure was measured, as well as height and thoracic circumference. Data sets were stored for off-line data analysis.

5.4. Development study: methods

From the raw ECG, PCG, ICG and PPG signals, the chest sensor is expected to provide estimates of the transit time of a pressure pulse travelling from the aortic valve to the chest subcutaneous vascular bed, *i.e.* Chest PTT= PAP−PEP (see Figure 5.4). Unfortunately, no reference of actual values of Chest PTT is available. As a first approach, we adopted values of COMPLIOR CR PTT as a set of typical examples to which Chest PTT should correlate. In particular, the correlation score between these two variables was adopted as the objective function to be optimized during the development of the signal processing routines. COMPLIOR PTT values were calculated by dividing COMPLIOR distances over COMPLIOR PWV values. In the following, we describe the obtained optimal parameterization.

5.4.1. Optimized signal processing routines

ICG data was initially band-pass filtered by a 4^{th} order Butterworth filter with cut-off frequencies of 0.8 and 15 Hz. Third derivatives were computed by applying successive seven-point stencils [25]. PCG envelopes were computed by initially band-pass filtering the raw PCG data by a 4^{th} order Butterworth filter with cut-off frequencies of 50 and 140 Hz, and by post filtering the absolute value of the band-pass filtered series with a 4^{th} order Butterworth low-pass filter with cut-off frequency of 10 Hz. Finally, two-minute signals of ICG and PCG were ensemble averaged [26] using the R-Wave of the simultaneously-recorded ECG as synchronization trigger. The most likely maximum of the ensemble averaged third derivatives was manually identified by finding the local maximum closer to the maximum of the ensemble averaged PCG envelope (PCG-guided B-point identification). PEP was defined as the delay between the R-Wave and the identified B-point.

Each infrared PPG channel was initially band-pass filtered by an 8^{th} order Butterworth filter with cut-off frequencies between 5 and 11 Hz before being oversampled to 1 kSample/s. After performing a two-minute R-Wave-triggered ensemble averaging, a parametric model of the pressure pulse was fitted according to the TANH method described in [22]. The parameters of the model were then considered in a 3-dimensional feature space, where unsupervised outlier rejection was performed. For each channel, the Mahalanobis distance of the associated point to the median of all available points was computed [23]. Those channels with greater distances than the standard deviation of all the distances were rejected. From the remaining representative channels, the mean of individuals PATs was assumed to be the most likely PAT at the chest.

5.5. Development study: results

The parameterization described above defines the optimal algorithm that extracts PTT values from the chest sensor, and that maximizes the correlation score (objective function) between Chest PTT and COMPLIOR CR PTT. Figure 5.5 illustrates the correlations obtained for the development cohort.

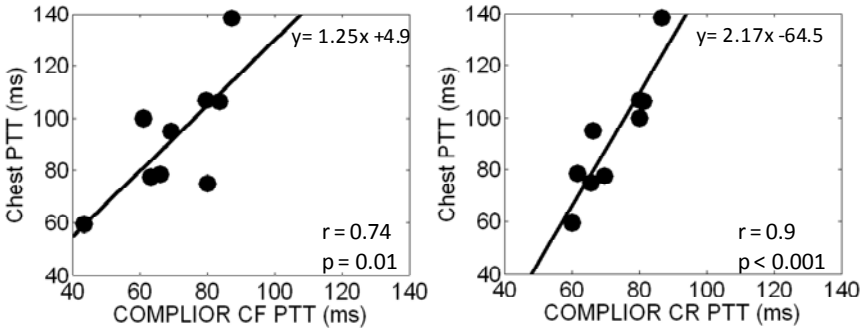

Figure 5.5: Achieved correlation scores during the development of the chest PTT algorithm for the 9 subjects of the development cohort. Chest PTT was compared to COMPLIOR CF PTT and COMPLIOR CR PTT.

5.6. Development study: discussion

The data recorded from the 9 subjects of the development cohort supported the optimization of the chest sensor signal processing algorithms. Although the correlation of Chest PTT with COMPLIOR PTT measurements was good, this result is to be treated with caution. On the one hand because the algorithm was optimized on the same database (self-fitting), and on the other hand, because the population size was small and with limited PWV range of values, *i.e.* only one subject depicted COMPLIOR CF PWV greater than 12 m/s. Note that correlation with COMPLIOR CR PTT values was better than the correlation with COMPLIOR CF PTT, since the first one was the objective function for the algorithmic optimization.

An independent validation cohort with larger population size and depicting a wider range of PWV values was therefore needed.

5.7. Validation study: materials

The goal of the validation study was to assess the performances of the chest sensor, prospectively, and in a new cohort of normo- and hypertensive male subjects (n=31 subjects, age: 26… 72 years, BMI: 19… 40 kg/m^2, height: 163… 195 cm, COMPLIOR CF PWV: 6.2 … 17.5 m/s, COMPLIOR CR PWV: 8.3… 16.8 m/s). Note that the enrolled population depicted a wider range of arterial stiffness conditions than the population enrolled in the development study. The same experimental protocol as for the preliminary training study was per formed.

5.8. Validation study: methods

The study consisted in comparing Chest PTT values to COMPLIOR CF PWV values, *i.e.* the only PWV value of clinical interest. Yet, since PTT values and PWV values are not linearly related (PWV is proportional to 1 / PTT, and not to PTT), correlation analysis was here performed by comparing COMPLIOR PWV to 1 / Chest PTT. The parameterization of the signal processing algorithm corresponded to the one optimized for the development cohort. Data analysis was performed offline.

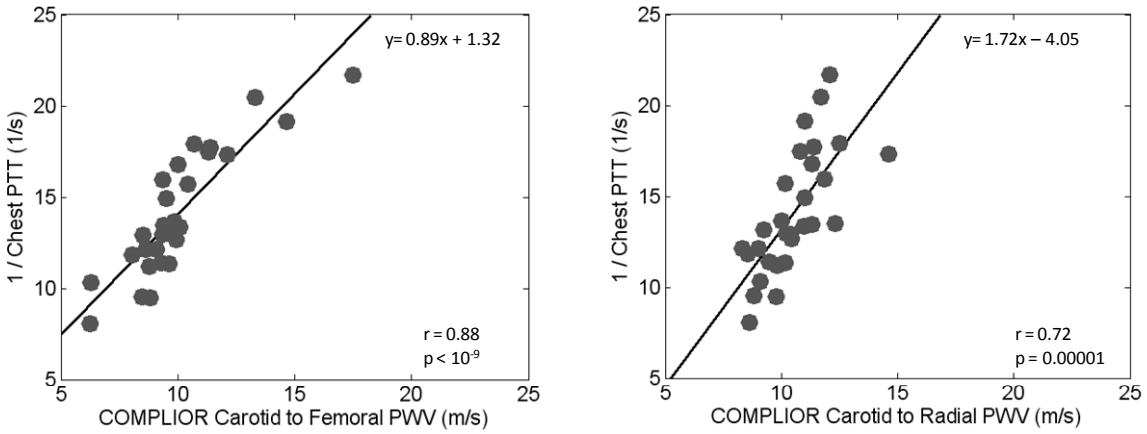

Figure 5.6: Linear correlation analysis when comparing 1 / Chest PTT to COMPLIOR CF PWV and COMPLIOR CR PWV for the 29 subjects in the prospective validation study.

5.9. Validation study: results

From the 31 subjects enrolled, two were excluded from the study because the COMPLIOR device was unable to detect carotid pressure pulses. Figure 5.6 illustrates the correlation analysis when comparing 1 / Chest PTT values to simultaneously recorded COMPLIOR PWV measurements.

1 / Chest PTT correlated very well with COMPLIOR CF PWV ($r=0.88$, $p<10^{-9}$), and well with COMPLIOR CR PWV ($r= 0.72$, $p= 0.00001$). Linear regression lines and regression equations for these datasets are displayed as well.

5.10. Validation study: discussion

For the 29 subjects of the validation cohort, 1 / Chest PTT correlated very well with COMPLIOR CF PWV. Since CF PWV is the only parameter depicting predictive value of cardiovascular morbidity and mortality [29] this is a very encouraging result. Note that 1 / Chest PTT correlated very well with the COMPLIOR CF PWV for its whole range of values, going from 6.7 m/s up to 17.5 m/s.

The correlation score of 1 / Chest PTT when compared to COMPLIOR CR PWV was good, but a wide homogeneous spread of the data points around the fitted linear regression was observed. These findings suggest that Chest PTT is not a pure measurement of muscular arterial stiffness, as compared to a CR PWV measurement. Note that in accordance with clinical evidence [27], the range of CR PWV values for the studied population was smaller than the range of CF PWV values.

5.11. Measuring Pulse Wave Velocity at the chest

5.11.1. Rationale

Since the clinical interest of pressure pulse propagation is on the assessment of propagation velocities and not on propagation times, PTT values (ms) are to be converted into Chest PWV values (m/s) by measuring an associated arterial path length *d* (m). One calculates Chest PWV = *d* / PTT. Yet, a main limitation of the present study is the impossibility of measuring the arterial path lengths associated to Chest PTT. Accordingly, in this last section we propose and test an empirical method to derive COMPLIOR-adjusted values of PWV from Chest PTT measurements. In future studies, arterial path lengths within the chest should be accurately measured, *e.g.* by imaging techniques.

5.11.2. Surrogates of arterial path lengths within the chest

The state of the art suggests approximating arterial path lengths by measuring surface distances between well defined anatomical points [1]. Unfortunately, no large population study has been conducted so far investigating chest arterial path lengths, and thus the current knowledge on typical distributions of arterial segments and arterial tortuousness within the chest remains limited.

Following an empirical methodology, we explored the use of different morphological measurements as surrogate values of arterial path length *d*, under the hypothesis that morphology would normalize Chest PTT values for large body size variations. Table 5.2 depicts correlation coefficients of Chest PWV values with COMPLIOR PWV values, when different arterial path length surrogates are introduced for all the subjects in the development and validation datasets.

Apart from thoracic circumference, the different tested surrogates did not generate large variations of the correlation scores, not even when a constant path length was set for all subjects. Accordingly, and in order to reduce the amount of variables involved in analysis, we adopted a constant and arbitrary chest arterial path length for all subjects, *i.e.* we compared COMPLIOR PWV values to 1 / Chest PTT values. Note that the results derived from this analysis are only representative of the population enrolled in our study, and that different study groups such as children may require body-size normalization means.

Table 5.2: Correlation coefficients with Chest PWV for different arterial path length surrogates (n=38 subjects)

	COMPLIOR CF PWV	COMPLIOR CR PWV
Height	$r = 0.82, p < 10^{-7}$	$r = 0.76, p < 10^{-5}$
Thoracic circumference	$r = 0.75, p < 10^{-4}$	$r = 0.60, p = 0.004$
CF distance	$r = 0.82, p < 10^{-7}$	$r = 0.69, p < 10^{-5}$
CR distance	$r = 0.82, p < 10^{-7}$	$r = 0.79, p < 10^{-6}$
½ (CF + CR)	$r = 0.82, p < 10^{-7}$	$r = 0.75, p < 10^{-5}$
Constant value (1)	$r = 0.84, p < 10^{-7}$	$r = 0.72, p < 10^{-4}$

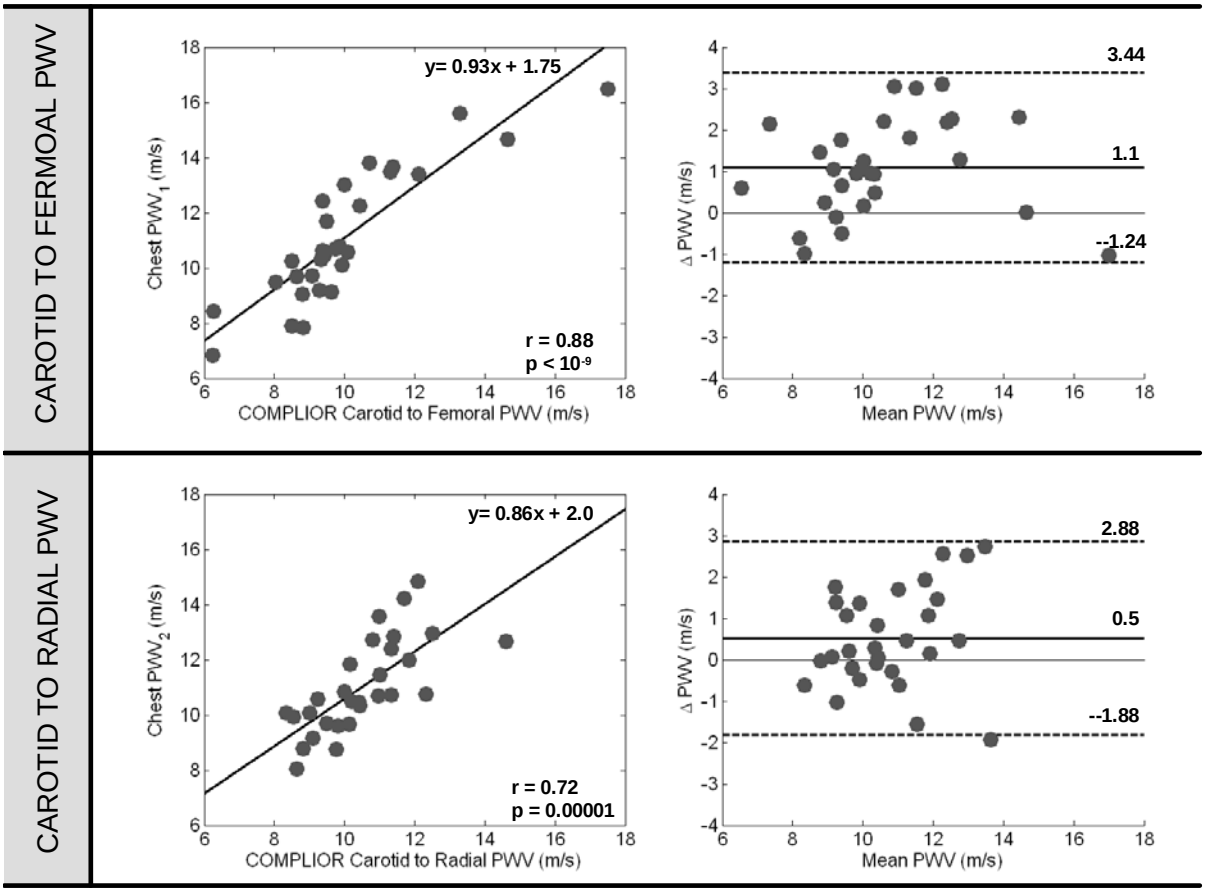

Figure 5.7: First row illustrates correlation analysis and Bland-Altman plot when comparing Chest PWV_1 values to COMPLIOR CF PWV values for the validation study (n=29 subjects). Second row illustrates correlation analysis and Bland-Altman plot when comparing Chest PWV_2 values to COMPLIOR CR PWV values for the validation study (n=29 subjects). Chest PWV_1 is the mapping of 1 / Chest PTT to COMPLIOR CF PWV, and Chest PWV_2 is the mapping of 1 / Chest PTT to COMPLIOR CR PWV, both mappings being optimized on the development cohort (n=9 subjects).

5.11.3. Mapping of 1 / Chest PTT to absolute PWV values

Although we demonstrated that 1 / Chest PTT correlate with COMPLIOR PWV, no estimation of the actual propagation distance was introduced, and 1 / Chest PTT remains a scaled value of the actual underlying Chest PWV value. In other words, the comparison of 1 / Chest PTT with COMPLIOR PWV is not possible in terms of absolute velocity numbers (m/s).

Going back to the development cohort, we proceeded by identifying with a linear regression, the best affine mapping that minimized the squared error between COMPLIOR PWV and a Chest PWV value, defined as a / Chest PTT + b. Therefore, the chest sensor algorithm was further extended by this equation, optimized on the development cohort (9 subjects). Note that affine operators do not modify linear correlations, and therefore, the scores obtained between 1 / Chest PTT and COMPLIOR PWV remain untouched.

5.11.4. Results and discussion

The algorithm defined above was applied on the validation cohort (29 subjects) and the obtained results are discussed through the correlations and Bland-Altman plots illustrated by Figure 5.7. Actually, two algorithms Chest PWV_1 and Chest PWV_2 with *a* and *b* optimized for COMPLIOR CF and CR, respectively, were compared. The results for Chest PWV_1 are Mean bias = 1.1 m/s, Mean Square Error (RMSE) = 1.17 m/s, and for Chest PWV_2, Mean Bias = 0.5 m/s, RMSE = 1.19 m/s.

Chest PWV values as provided by the proposed affine mapping algorithm are close to the ones measured by COMPLIOR for the population of the validation study. Yet, when targeting at providing actual measurements of Chest PWV, the assessment of the involved arterial path lengths remains a main limitation of the chest sensor.

5.12. Conclusions

A novel chest sensor providing estimates of the transit time of pressure pulse waves to propagate from the aortic valve to the sternum vascular bed has been presented. In the validation study, Chest PTT was demonstrated to strongly correlate with carotid to femoral PWV measurements.

Due to its ease of use, which is operator-independent, this novel technique of PTT measurement is very appealing. However, before routine usage can be recommended, the present results should be independently confirmed, and its prognostic significance be determined in large prospective clinical trials.

Annex 4 provides first experimental evidence on the feasibility of using this novel technique to measure not only basal central PTT values, but to monitor continuous changes of PTT and BP in a subject during different cardiovascular maneuvers.

References

[1] S. Laurent, *et al.*, "Expert consensus document on arterial stiffness: methodological issues and clinical applications," *Eur Heart J,* vol. 27, pp. 2588-605, Nov 2006.

[2] G. Mancia, *et al.*, "2007 Guidelines for the management of arterial hypertension: The Task Force for the Management of Arterial Hypertension of the European Society of Hypertension (ESH) and of the European Society of Cardiology (ESC)," *Eur Heart J,* vol. 28, pp. 1462-536, Jun 2007.

[3] R. Asmar, *et al.*, "Assessment of arterial distensibility by automatic pulse wave velocity measurement. Validation and clinical application studies," *Hypertension,* vol. 26, pp. 485-90, Sep 1995.

[4] P. Segers, *et al.*, "Limitations and pitfalls of non-invasive measurement of arterial pressure wave reflections and pulse wave velocity," *Artery Research,* vol. 3, pp. 79-88, 2009.

[5] M. W. Rajzer, *et al.*, "Comparison of aortic pulse wave velocity measured by three techniques: Complior, SphygmoCor and Arteriograph," *J Hypertens,* vol. 26, pp. 2001-7, Oct 2008.

[6] B. Trachet, *et al.*, "Numerical validation of a new method to assess aortic pulse wave velocity from a single recording of a brachial artery waveform with an occluding cuff," *Ann Biomed Eng,* vol. 38, pp. 876-88, Mar 2010.

[7] J. Solà, *et al.*, "Ambulatory monitoring of the cardiovascular system: the role of Pulse Wave Velocity," in *New Developments in Biomedical Engineering*, D. Campolo, Ed., ed Vienna:: I-Tech Education and Publishing, 2010.

[8] S. Laurent and J. Cockroft, *Central aortic blood pressure*: Elsevier, 2008.

[9] C. Acar, *et al.*, "Comparative anatomy and histology of the radial artery and the internal thoracic artery. Implication for coronary artery bypass," *Surg Radiol Anat,* vol. 13, pp. 283-8, 1991.

[10] W. W. Nichols and M. F. O'Rourke, *McDonald's Blood Flow in Arteries*. Oxford: Oxford University Press, 2005.

[11] N. Westerhof, *et al.*, *Snapshots of Hemodynamics*: Springer, 2005.

[12] B. C. Penney, "Theory and cardiac applications of electrical impedance measurements," *Crit Rev Biomed Eng,* vol. 13, pp. 227-81, 1986.

[13] A. Sherwood, *et al.*, "Methodological guidelines for impedance cardiography," *Psychophysiology,* vol. 27, pp. 1-23, Jan 1990.

[14] J. H. Nagel, *et al.*, "New signal processing techniques for improved precision of noninvasive impedance cardiography," *Ann Biomed Eng,* vol. 17, pp. 517-34, 1989.

[15] T. T. Debski, *et al.*, "Stability of cardiac impedance measures: aortic opening (B-point) detection and scoring," *Biol Psychol,* vol. 36, pp. 63-74, Aug 1993.

[16] D. L. Lozano, *et al.*, "Where to B in dZ/dt," *Psychophysiology,* vol. 44, pp. 113-9, Jan 2007.

[17] J. R. Levick, *An introduction to Cardiovascular Physiology*, Fourth ed. New York: Arnold Publishers, 2003.

[18] C. Ahlström, "Nonlinear Phonocardiographic Signal Processing," Department of Biomedical Engineering, Linköping University, Linköping, 2008.

[19] D. Bartnik and B. Reynolds, "Impedance Cardiography system," 2009.

[20] Y. Mendelson and B. D. Ochs, "Noninvasive pulse oximetry utilizing skin reflectance photoplethysmography," *IEEE Trans Biomed Eng,* vol. 35, pp. 798-805, Oct 1988.

[21] E. Kaniusas*, et al.*, "Optical tissue absorption sensor on the thorax: Possiblities and restrictions," *Int. J. App. Electromagnetics and Mechanics,* vol. 25, pp. 649-654, 2007.

[22] J. Sola*, et al.*, "Parametric estimation of pulse arrival time: a robust approach to pulse wave velocity," *Physiol Meas,* vol. 30, pp. 603-15, Jul 2009.

[23] V. J. Hodge and J. Austin, "A Survey of Outlier Detection Methodologies," *Artificial Intelligence Review,* 2004.

[24] R. Vetter*, et al.*, "Frequency domain SpO2 estimation based on a multichannel photoplethysmographic measurments at the sternum," presented at the Frequency domain SpO2 estimation based on a multichannel photoplethysmographic measurments at the sternum, Munich, 2009.

[25] K. D. F. J. H. Mathews, *Numerical Methods Using MATLAB*: Prentice-Hall, 1998.

[26] B. E. Hurwitz*, et al.*, "Coherent ensemble averaging techniques for impedance cardiography," in *Third annual IEEE Symposium on Computer-Based Medical Systems*, University of North Carolina at Chapel Hill. Los Alamitos, Calif. , 1990, pp. 228-235.

[27] A. P. Avolio*, et al.*, "Effects of aging on arterial distensibility in populations with high and low prevalence of hypertension: comparison between urban and rural communities in China," *Circulation,* vol. 71, pp. 202-10, Feb 1985.

Chapter 6

Synthesis

6. Synthesis

6.1. Thesis contributions

The continuous and non-occlusive measurement of arterial Blood Pressure (BP) is a major challenge of the medical monitoring field. In particular, there is a high demand from clinicians and patients on new technologies allowing measuring BP in ambulatory. Compared to currently commercialized techniques, new developed solutions should remain accurate, reduce the degree of occlusiveness, and increase the frequency of BP readings.

The present PhD thesis identified Pulse Wave Velocity (PWV) -based techniques to be a candidate approach to respond to this demand. In particular, the measurement of the velocity at which pressure pulses propagate along central arteries was highlighted as a reliable solution for the continuous non-occlusive monitoring of central BP (thesis aim #2). The fact that central arteries depict high elastic properties, *i.e.* being unaffected by vasomotion phenomena, supports this statement. Hence, the research question addressed by the current thesis is whether there exists an ambulatory-prone non-occlusive technique capable of providing continuous measurements of central PWV, and thus reliable surrogates of BP.

The first main contribution of this thesis was the prove that PWV can be measured at central locations of the arterial tree in a continuous, non-invasive, non-occlusive and unsupervised way via two different monitoring techniques that are prone to be implemented in ambulatory (thesis aims #4 and #5).

On the one side the Electrical Impedance Tomography (EIT) technology was explored in Chapter 4. By providing very fast imaging capabilities of changes of impedances within the thoracic cavity, EIT was evaluated as a means to track the propagation of arterial pressure pulses from the left ventricle towards the descending aorta. Experimental results showed that EIT is capable of performing such a tracking task, and that aortic Pulse Transit Time (PTT) values obtained by the post-processing of sequences of EIT images highly correlate with BP values. This scientific contribution, together with the fact the EIT measurements can be performed by simply placing an electrode chest belt around the thorax, suggest that this novel technique has the potential to fulfill the requirements of a continuous and non-occlusive ambulatory BP monitoring technique.

On the other side the use of a chest belt integrating a set of non-occlusive sensors was explored in Chapter 5. Simultaneously performing electro-cardiographic, impedance-cardiographic, phono-cardiographic and photo-plethysmographic measurements, the ability of the chest belt approach to estimate the propagation time of pressure pulses from the aortic valve towards the subcutaneous vasculature of the sternum was evaluated. *In-vivo* measurements performed on 31 normo- and hypertensive-subjects showed that central PTT values obtained by the multi-parametrical analysis of the signals provided by the chest belt sensor positively correlate with central PTT values provided by clinical gold-standard measurement techniques. Because of the fact that the chest belt technology is relatively cheap and already mature, this technique is a short-term candidate for the continuous and non-occlusive monitoring of BP in ambulatory.

A second main contribution of this thesis was the introduction of a novel family of signal processing techniques that improve the robustness of the estimation of Pulse Arrival Time (PAT) of pressure pulses in the presence of noise (thesis aim #3). Although state-of-the-art approaches to measure PAT were shown to be reliable in controlled clinical conditions, they fail when pressure pulse time series are corrupted by measurement and/or motion noises. Chapter 3 demonstrated that the estimation of PAT values via a parametric modeling of arterial pressure pulses outperforms gold-standard PAT estimation techniques in terms of noise robustness, while it provides equivalent results. This scientific contribution opens a new perspective in the field of non-invasive cardiovascular monitoring, offering new tools for the processing of arterial pressure time series. In particular, it paves the way towards the ambulatory measurement of PWV of central, *i.e.* not superficial, arteries by means of sensing technologies that although promising, to date could not be considered because of their noisy nature; photo-plethysmography and EIT being two practical examples.

A third and final contribution of this thesis resided on the generation and publication of a multi-disciplinary understanding of the gap currently separating clinical needs in BP monitoring and state-of-the-art technological capabilities (thesis aim #1). In particular, this thesis revisited and analyzed the “ambulatory BP monitoring dilemma” from four different perspectives: cardiovascular physiology, clinical applicability, system integration, and signal/information processing. Chapter 2 provided a genuine multidisciplinary tour to the unsolved problem of ambulatory BP monitoring.

6.2. Limitations and future work

Recall that the main research question to be answered by the current thesis was whether there exists an ambulatory-prone non-occlusive technique capable of providing continuous BP measurements. The thesis research path consisted on an initial theoretical exploration of the field, followed by the identification of potential solutions and their experimental implementation. Along this path, several crossroads were encountered for which decision and trade-offs were taken. In the following, the limitations of the performed research work are provided together with suggestions on possible tracks to be followed in the future.

On the choice of PWV as a surrogate BP measurement

The identification of available and/or potential technologies for the ambulatory monitoring of BP was described in Section 2. After a detailed analysis of the capabilities of each technique, PWV-based technology was selected as the optimal solution because of its strictly non-occlusive nature, and because of the existence of a theoretical model supporting its validity. Therefore, from this decision point the entire thesis research work was tailored towards the development and improvement of PWV-based technologies, discarding other approaches. Alternative techniques based on indirect observations of the cardiovascular system were not further explored. In the future, of particular interest would be to explore those techniques based on the prediction of BP by the multi-parametric processing of cardiovascular variables [1], or those based on the influence of BP on alternative observable parameters such as the timing information coded within heart sounds [2]. In this direction, numerical models of the cardiovascular system might be a useful tool supporting the validation of hypotheses: see for instance the models proposed in [3] and [4]. Annex 1 provides an example of a model-based multi-parametric processing.

The choice of PWV as a BP surrogate carries an additional intrinsic limitation. As defined in Section 2.6.5 (see Figure 2.27), the PWB-BP relationship relies on the fact that an increase on transmural pressure increases the stiffness of the arterial wall, and that such a stiffness increase induces then higher pulse propagation velocities. In a living cardiovascular system the arterial transmural pressure is continuously modified along the cardiac cycle, being low during diastole, and high during systole. A fundamental question arises then: are PWV-based techniques expected to carry information on the diastolic, systolic or mean BP? No clear answer has been published so far, since PWV appears to correlate with all of them [5]. In any case, from a formal perspective, PWV must only be exploited to track changes of one of the three. Because Pulse Arrival Times (PAT) are commonly computed by detecting the foot of a pressure pulse, *i.e.* at the transition of diastole to systole, the conditions through which the pulse has propagated along the arterial tree are best expected to correspond to diastolic BP conditions, or alternatively, to mean BP conditions. Even if some attempts have been published on using the peak of the pulse to estimate a "systolic PAT", and derive then a surrogate of systolic BP value, this approach cannot be justified. On the one side because peak-PAT values are biased by the superposition of anacrotic and catacrotic signal signatures (see Section 3), and on the other side because the characteristic point "pressure pulse peak" is propagated along the arterial tree at infra-systolic BP values (the systolic BP value is actually established at the vessel wall when the peak has already passed along a given measurement point). Hence, while current clinical practice relies on the monitoring of both systolic and diastolic BP, a major limitation of the PWV-based technique is that it is restricted to provide only one of the diastolic or the mean BP values. However, the fact that this new technology allows performing first-ever non-occlusive beat-by-beat monitoring of one of the BP values is a clear advantage. Further research is here required to develop strategies to combine periodic, *i.e.* intermittent, cuff-based measurements of systolic and diastolic BP with beat-by-beat BP measurements via PWV.

On the strategy to measure PWV

Concerning the actual measurement principle of PWV, this thesis only considered the family of approaches relying on the detection of a pressure pulse at two different locations of the arterial tree, *i.e.* at a proximal and at a distal point. These approaches rely then on measuring/estimating the distance between these two points, and calculating a PWV value as the ratio of distance over propagation time (see Section 2.6.4). This strategic choice relies on the fact that Pulse Arrival Time (PAT) values can be assessed by means of available ambulatory-prone technology. A main limitation though is that one assumes the propagation of the pressure pulse to happen in a homogeneous arterial segment: a segment of the arterial tree with constant propagation characteristics. This is obviously not the case in actual measurement setups (heterogeneous arterial tree segment), and irrevocably leads to estimation inaccuracies (see Table 5.1). An alternative approach to this limitation would be the measurement of local PWV, in contrast with the implemented "global PWV" approach: based on the modified Bramwell-Hill expression (Equation 13) one could estimate the velocity of a pressure pulse at a given arterial location by measuring pressure/volume ratio changes observed during the passage of a pulse. Unfortunately, currently available technologies to assess pressure and volumes require high-velocity and high-resolution imaging techniques that are too bulky and too motion-sensitive to be used in ambulatory.

Yet, new technology capabilities might in the future facilitate the implementation of such techniques.

On calibration issues

Yet another limitation of the PWV-based approach to assess BP is that it requires a calibration maneuver to identify a subject-dependent mapping of the measured PWV values towards the underlying BP values. While several strategies to perform such maneuvers have been described in the state of the art (see Section 2.6.5), the current thesis did not investigate in this direction. In particular, it will be of particular interest to further study the need of performing re-calibration maneuvers: aspects such re-calibration periodicity, and calibration inaccuracy trends remain unsolved. In this thesis two novel approaches to measure PWV in central elastic arteries were introduced in Section 4 and Section 5. Although these approaches are expected to minimize the need of performing regular re-calibration maneuvers (reduced vasomotion phenomenon), experimental proof of the principle is lacking yet. Further animal and human experimental investigations, involving longer term measuring campaigns, are here required.

On the use of EIT technology to measure BP

The feasibility of tracking the propagation of pressure pulses along the aorta using the non-occlusive Electrical Impedance Tomography (EIT) technology was assessed in Section 4. Large BP fluctuations were induced in an anesthetized pig (by administrating vaso-active drugs) while aortic Pulse Transit Times (PTT) were assessed via EIT. Very high correlation scores were observed between EIT-PTT and BP (measured via an arterial line). Although the results of this research appeared to be very promising, they have to be carefully treated: the study was performed on one single animal model under well-controlled experimental conditions. New animal model studies, including more individuals and enlarging the amount of hemodynamic conditions are here required.

Another important limitation of the performed study was the use of an arterial line placed at the ascending aorta as a trigger to measure the genesis of pressure pulse. While this approach allowed demonstrating that pressure pulses could be detected at the descending aorta, it remains a highly invasive experimental technique. Non-invasive strategies to detect the opening of the aortic valve were listed in Section 4.3, and need to be further tested.

The final step, *i.e.* the investigation of the accuracy of the EIT-based approach to monitor BP in humans, is lacking as well. The fact that to date EIT recording platforms were limited in number and rarely used on humans has impeded performing such experiments. With the deployment of new EIT machines expected for the following years (see Table 2.11) this task should be facilitated soon.

On the use of the chest sensor to measure central PWV and BP

The accuracy of a novel potentially-cheap chest sensor to continuously measure central PWV was studied in Chapter 5. This sensor was conceived to be built of a set of mature monitoring technologies, facilitating thus its rapid introduction in an industrialization process. Although this thesis showed on a large population of healthy and hypertensive subjects that central PWV values as measured by the chest sensor correlate to central PWV

values as measured by standard clinical tools, a final experimental step is to be performed yet: an additional large population experimental campaign is required to assess the accuracy of the chest sensor on tracking continuous BP changes for each subject. In other words: currently for each enrolled subject one single PWV value was measured. A new study is required now in which for each enrolled subject a plurality of measurements are performed, each measurement being related to a different hemodynamic condition. Nevertheless, Annex 4 provides first experimental evidence on the accuracy of the chest sensor on continuously monitoring BP on one human subject.

6.3. Conclusions

In conclusion, the present thesis demonstrated that there exist technological solutions for the continuous non-occlusive measurement of BP in ambulatory.

In particular, the family of technologies based on the so-called PWV principle was highlighted as a potential candidate that might answer the clinicians and patients demand of a BP monitoring device that is non-occlusive, unobtrusive, unsupervised, accurate, continuous… and that can be used in ambulatory.

Furthermore, this thesis introduced, developed and tested two novel PWV-based technologies to monitor BP on both: human and animal models. The obtained experimental results point at the feasibility of both solutions, and encourage to further proceed with the implantation of these technologies.

Referring now to the opening sentence of the introduction chapter, the results presented in this thesis might help to hear in the near future one saying:

"*Four days ago my doctor gave me this chest belt, and believe me… I don't feel it at all!*"

References

[1] D. Barschdorff*, et al.*, "Noninvasive continuous blood pressure determination," presented at the XVI IMEKO World Congress, Wien, 2000.

[2] M. Y. M. Wong*, et al.*, "Can the Timing-Characteristics of Phonocardiographic Signal be Used for Cuffless Systolic Blood Pressure Estimation?," presented at the 28th IEEE EMBS Annual International Conference, New York, 2006.

[3] R. Mukkamala and R. J. Cohen, "A forward model-based validation of cardiovascular system identification," *Am J Physiol Heart Circ Physiol,* vol. 281, pp. H2714-30, Dec 2001.

[4] X. Y. Zhang and Y. T. Zhang, "A model-based study of relationship between timing of second heart sound and systolic blood pressure," *Conf Proc IEEE Eng Med Biol Soc,* vol. 1, pp. 1387-90, 2006.

[5] R. A. Payne*, et al.*, "Pulse transit time measured from the ECG: an unreliable marker of beat-to-beat blood pressure," *J Appl Physiol,* vol. 100, pp. 136-41, Jan 2006.

Curriculum Vitae

Josep Maria Solà i Carós

Born on the 6th of June 1980

in Santa Coloma de Farners, Catalonia, Spain

Education

2006-2011: **ETHZ Swiss Federal Institute of Technology Zurich** – Zurich

CSEM Centre Suisse d'Electronique et Microtechnique – Neuchâtel

PhD Studies (Dr. sc. ETH) under the supervision of Prof. Dr. Ralph Müller and Dr. Olivier Chételat.

2003-2004: **Sony International (GmbH) Europe** – Stuttgart

UPC Universitat Politècnica de Catalunya – Barcelona

Master Thesis under the supervision of Prof. Dr. Climent Nadeu, and Dr. Vicky Lam. Thesis topic: Environmental Robust Feature Extraction for Speech Detection. Obtained honor degree

2001-2004: **TALP Research Center for technologies and applications in language and speech** - Barcelona

European Master in Language and Speech

1997-2004: **UPC Universitat Politècnica de Catalunya** – Barcelona

M. Sc. Telecommunications

Professional experience

2004-2011: **CSEM Centre Suisse d'Electronique et Microtechnique** – Neuchâtel

R&D biomedical engineer and PhD student.

2003-2004: **Sony International (GmbH) Europe** – Stuttgart

R&D biomedical engineer and master student.

2001-2003: **UPC Universitat Politècnica de Catalunya** – Barcelona

Research assistant

Awards and honors

2010: Swisslaser Best Poster Award for a young researcher in the field of Biomedical Photonics, Biomedical Photonics Network – CH

2009: The very best research published in Physiological Measurement in 2009, IOP Science – UK

2004: Master thesis honor degree by Universitat Politècnica de Catalunya – ES

2003: Winning team of ELGRA students contest on parabolic flight campaigns - NL

Selected publications and patents

Peer-reviewed journal publications

2011 **J. Solà**, O. Chételat, C. Sartori, Y. Allemann and S. F. Rimoldi, "Chest Pulse Wave Velocity : a Novel Approach to Assess Arterial Stiffness," *IEEE Trans Biomed Eng*, vol 58, pp. 215-23, Jan 2011. Impact factor: 2.154

2011 **J. Solà**, A. Adler, A. Santos, G. Tusman, F. Suárez Sipmann and S. H. Böhm, "Non-invasive monitoring of central blood pressure by Electrical Impedance Tomography (EIT): first experimental evidence," *Med & Biol Eng & Comp*, vol 49, pp. 409-15, Mar 2011. Impact factor: 1.757

2011 S. Maisch, S. H. Böhm, **J. Solà**, M. S. Goepfert, J. C. Kubitz, H. P. Ridder, A. Goetz and D. A. Reuter, "Heart-Lung Interactions Measured by Electrical Impedance Tomography", Critical Care in Medicine, Epub ahead of print, 9 June 2011. Impact factor: 6.373

2009 **J. Solà**, R. Vetter, Ph. Renevey, O. Chételat, C. Sartori and S. F. Rimoldi, "Parametric estimation of pulse arrival time: a robust approach to pulse wave velocity," *Physiol Meas*, vol. 30, pp. 603-15, Jul 2009. **Awarded as "the very best research published in Physiological Measurement in 2009"**. Impact factor: 1.43

Peer-reviewed book chapters

2010 **J. Solà**, Y. Allemann and S. F. Rimoldi, "Ambulatory monitoring of the cardiovascular system: the role of Pulse Wave Velocity," *New Developments in Biomedical Engineering*, I-Tech Education and Publishing, Vienna, Austria, 2010, ISBN 978-943-7619-57-1

Conference papers

2010 **J. Solà**, O. Chételat, M. Bertschi and S. F. Rimoldi, "Reflective photo-plethysmography for the non-invasive unsupervised measurement of arterial stiffness," Proc. Yearly meeting of the Biomedical Photonic Network (BMPN) 2010, Bern. **Awarded by the "Swisslaser Best Poster Award for a young researcher in the field of Biomedical Photonics"**.

2009 **J. Solà** and S. F. Rimoldi, "Continuous Non-invasive Monitoring of Blood Pressure," Proc. DARPA Workshop on CNIMBP 2009, Coronado, DARPA

2008 **J. Solà**, O. Chételat and J. Luprano, "Continuous monitoring of cardiovascular responses," Proc. EMBS 2008, 1423-26, Vancouver, IEEE

Patents

2011 **J. Solà**, J. X. Brunner, D. Ferrario, A. Adler and M. Proença, "Method and apparatus for the non-invasive measurement of Pulse Transit Times (PTT)," PCT/EP2011/061753, 11 July 2011.

2011 **J. Solà** and J. X. Brunner, "Method and Apparatus for Time-Based Analysis of Electrical Impedance Tomography Data," PCT/EP2011/061757, 11 July 2011.

2011 **J. Solà** and S. F. Rimoldi, "Sensor device and method for measuring and determining a pulse arrival time value," PCT/EP2011/054834, May 2011.

2009 **J. Solà** and H.A. Loeliger, "Method and apparatus for a continuous non-invasive and non-obtrusive monitoring of blood pressure," US 2009/0163821 A1, 25 June 2009 & EP 2 074 942 A1, 01 May 2009

Annex 1 – Modified first generation of Pulse Wave Velocity-based techniques for the assessment of Blood Pressure (generation #1b).

Partly adapted from:

Method and apparatus for a continuous non-invasive and non-occlusive monitoring of blood pressure

Josep Solà[1] and Hans-Andrea Loeliger[2]

[1]CSEM – Centre Suisse d'Electronique et de Microtechnique, Neuchâtel, Switzerland

[2]ISI - Institute für Signal- und Informationsverarbeiting, ETHZ - Swiss Federal Institute of Technology, Zurich, Switzerland

Published in:

European Patent Office (2009), EP 2 074 942 A1

US Patent Office (2009), 2009/0163821 A1

Initial research works of the current thesis aimed at improving existing PWV-based techniques to measure BP. Accordingly, a novel technique was suggested from a theoretical point of view, yet lacking of extensive experimental evidence. The material provided in this annex has been adapted from [1] and [2] and aims at drawing a guideline for future research. For a review of the PWV-based BP estimation see Section 2.6.5.

As described in Section 2.6.5, state-of-the-art PWV-based BP measurement techniques require frequent recalibrations via inflation brachial cuffs. The goal of this modified first generation of techniques is to reduce the frequency of such intermittent re-calibrations. Assuming that the major source of calibration modifications are changes of radius and stiffness of conduit arteries, the proposed technique compensates for these changes without necessitating additional calibrations. In order to do so, the technique requires the continuous measurement of both PWV and Cardiac Output (CO), and assumes a Moens-Korteweg-like model of pulse wave propagation together with a Poiseuille's model of fluidic resistance.

This research starts by analyzing the sources of errors that might induce to a need of recalibration of the PWV-BP relationship. Two hypothesis are initially analyzed: on the one hand the fact that the assumptions underlying Moens-Korteweg model (see Section 2.6.2) might deviate from the actual biomechanics encountered in the arterial tree; especially in

small arteries, the viscosity of blood and the thickness of the arterial wall introduce important perturbations to the predicted pulse wave velocities [3]. In 1960 Bergel studied and quantified this model discrepancies and upper-bounded it to values up to 25% [4].

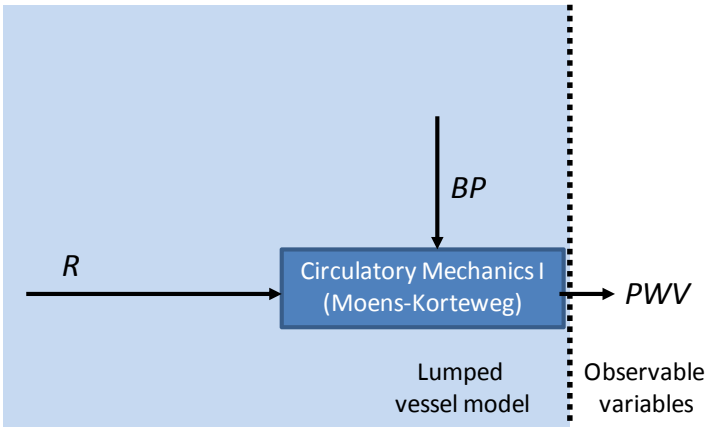

Figure 7.1: According to the Moens-Korteweg model, *PWV* depends on both Blood Pressure (*BP*) and the diameter (d) of the vessel segment. Accordingly we claim that in order to use *PWV* as a surrogate marker of *BP*, additional information on d must be provided to the model.

However, because the propagation of pressure pulses in which this techniques is interested mostly occurs in large to medium size vessels (i. e. thin arteries), the effects of the exposed deviations might be minor in experimental setups. On the other hand, the second hypothesis against the adequacy of using Moens-Korteweg equation (Equation 21) as a surrogate of BP is the non-stationarity of the $h/\rho R$ term. State-of-the-art techniques rely on the assumption of the existence of a deterministic PWV-BP calibration function, i.e. intrinsically assuming a fixed value of $h/\rho R$. In muscular arteries, or any peripheral artery, the validity of such an assumption would pass through a complete blockage of vasomotor activity during experimental setups. Unfortunately, in a living cardiovascular system, the vascular tone, and thus the diameter and the thickness of arteries, are continuously regulated in order to achieve cardiovascular homeostasis (see Section 2.1.2). Some recent studies have measured the modifications of diameter in human arteries during different cardio vascular adaptations in-vivo. In [5], for instance, the change in diameter of radial artery is assessed by echo-Doppler techniques: during the recordings, the diameter of the radial artery was found to increase from 2mm to 2.2mm (10% increase). In [6] researchers induced postural modifications to subjects while measuring the changes in diameter of the carotid artery by an ultrasound imaging technique. An increase from 6 to 7mm (16% increase) of diameter was found when pressure was increased by 30mmHg. Furthermore, this hypothesis is confirmed by the conclusions drawn by Payne et al. in [7], i.e. *it would appear inappropriate to use PTT* (i.e. *PWV*) *as a predictor of Systolic Blood Pressure in all persones, particulary for assessing changes due to vasoactive drugs*.

According to the exposed facts, we conclude that the inadequacy of pulse wave velocity as a surrogate estimate of arterial blood pressure in *in-vivo* setups is mainly caused by the vasomotor activity inherent to the arterial tree. Indeed, we shall assume that *PWV* includes information on both the transmural pressure (expected effect) and the vasomotor activity

(parasite effect) of all the segments of the arterial tree involved in the measurement. In the following, we exploit this assumption in order to develop a novel observer of coordinated cardiovascular responses.

Because Pulse Wave Velocity contains information on both arterial pressure and vasomotor activity, we hypothesize that additional information sources are required to obtain an accurate understanding of its relationship to arterial blood pressure. The question arisen is 'what sources would allow resolving our observation problem under the restricted constraints of *in-vivo* measuring setups'.

For doing so, we develop a high-level model of the circulatory mechanics involved in the determination of PWV. We start by lumping the different segments of the arterial tree involved in our measurement setup into a single and homogeneous theoretical vessel that fulfills the assumptions of Moens-Korteweg model of pulse wave propagation (Equation 21). We then assign the influences of arterial blood pressure and vasomotor activity on the setting of *PWV* through the Moens-Korteweg equation. In particular, we consider the influence of changes in vessel radius (R) and blood pressure (BP) on the setting of *PWV* as (see Figure 7.1):

$$\mathrm{PWV}=f_{CM1}(BP,R,K_0)$$

Equation 63

where K_0 depicts a calibration factor. Note that according to the Moens-Korteweg equation, the suggested model assumes the radius of the artery and *BP* to be the main vasomotion-modified variables, and sets h and ρ to be constant values represented by the scalar calibration factor K_0.

In order to resolve the model, *i.e.* to determine the dependency of *PWV* to *BP* independently of *R*, additional information sources are required. In order to do so, we introduce the concept of Systemic Vascular Resistance, or S*VR* as depicted in Section 2.1. In a Poiseuille's sense [3], *SVR* is the impediment to blood flow exerted by systemic vessels. The notion of *SVR* has been criticized by several authors because of the fact that the systemic circulatory system weakly fulfills Poiseuille's conditions ([3] provides a detailed review of these weaknesses). Nevertheless, the concept of *SVR* remains of interest in the sense that it facilitates the understanding of the influence of vasomotor activity in the establishment of *BP* [8], and that it provides a simplified analytical model of the relationship between vessel diameter and flow impediment [9].

In particular, assuming central venous pressure to be small in comparison with *BP*, one defines:

$$SVR=\frac{BP}{CO}$$

Equation 64

where *CO* stands for Cardiac Output, i.e. the volume of blood transferred from the left ventricle to the aorta par minute. Hence, assuming *CO* to be expressed in mL/min and *BP* in mmHg, *SVR* has the empirical units of mmHg/mL/min.

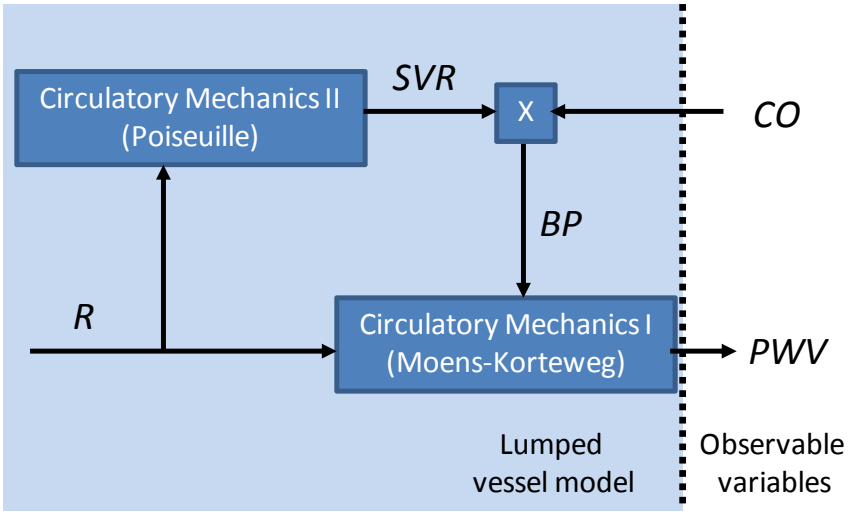

Figure 7.2: Lumped model of a segment of the arterial tree including the Moens-Korteweg model of pulse wave propagation, and a Poiseuille model of fluidic resistance. Given a measurement of Cardiac Output (*CO*) and Pulse Wave Velocity (*PWV*), the model supports resolving the internal variables: Blood Pressure (*BP*) and Vascular Resistance (*SVR*).

We recall that our goal is to resolve the dependency of *PWV* to *BP*. Poiseuille's equation plays now an important role since it provides a relationship between *SVR* and the diameter of our lumped vessel, *i.e*.

$$\mathrm{SVR}=f_{CM2}(R,K_1)$$

Equation 65

being K_1 a calibration factor depending on blood viscosity. Introducing Equation 63 and Equation 65 into the cardiovascular model of Figure 7.1 one obtains the extended model illustrated in Figure 7.2.

From a formal perspective, one might criticize the proposed model arguing the weakness of the joint applicability of Moens-Korteweg and Poiseuille's equations to systemic vessels. Further research is needed to analyze the consequences of matching both equations. Still, in the following, we assume both equations to be applicable to our theoretical lumped vessel.

The model of the theoretical lumped vessel as it is illustrated in Figure 7.2 comprehends two observable variables: *CO* and *PWV*. Recall that the main goal of this technique is to develop a method to estimate the hidden variable BP (and SVR) from these observable variables. We will here demonstrate the solvability of the model and the uniqueness of the solution, given a set of observations (*CO*, *PWV*). Because of the monotonic decreasing properties of

$f_{CM2}(R, K_1)$ with respect to *R*, and the monotonic decreasing properties of $f_{CM1}(BP, R, K_0)$ with respect to both *BP* and *R*, given a set of observations (*CO*,*PWV*) and a set of calibration factors (K_0, K_1) there is a unique possible solution *R*. Then, according to the model, given *R* and *CO*, the values of both *SVR* and *BP* are intrinsically determined.

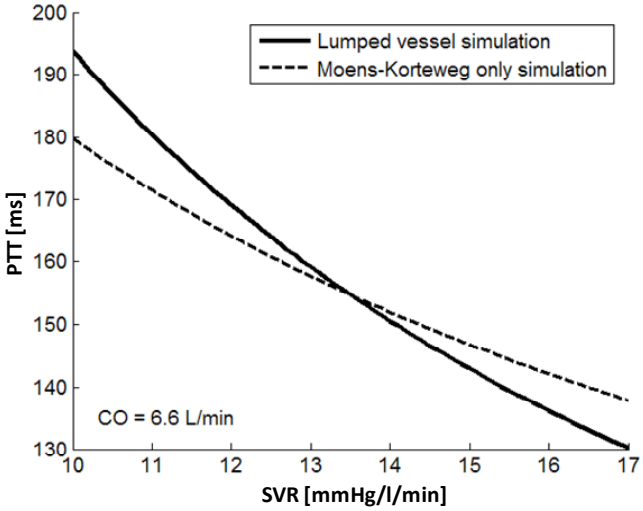

Figure 7.3: Expected Pulse Transit Time (*PTT*) values at different vasomotor conditions given a fixed Cardiac Output (*CO*) of 6.6 L/min. Comparison of expected values according to state-of-the-art Moens-Korteweg model and the novel lumped vessel model.

Figure 7.3 depicts a simulated example of model solution. Given a measured value of *CO* (*e.g.* 6.6 L/min), we simulate the expected Pulse Transit Time (i.e. $PTT = k/PWV$) computed for different hypothesized *SVR* values. Then, searching for the actual measured *PTT* in the simulated curve, one obtains the most likely *SVR* hypothesis. Note the uniqueness of the *SVR* solution.

Figure 7.3 displays as well the simulated results in the special case where $f_{CM2}(R, K_1)$ is considered to be constant with respect to *R*, i.e. the case where the Moens-Korteweg equations is used alone, as it is the case in state-of-the-art approaches. In particular, the simulation assumes a constant *SVR* value of 13.5 mmHg/l/min. In this setup, the expected *PTT* value differs in the worst cases by 15 ms. Comparing now this simulated error with the regression lines proposed in [7], we predict that the use of Moens-Korteweg equations alone might induce *BP* estimation errors of up to ±8 mmHg.

In summary, the proposed technique consists on estimating the most likely underlying *BP* value of a cardiovascular system, by measuring the variables *CO* and *PWV* and solving:

$$\hat{R} = \mathrm{argmin}_R |PWV - f_{CM1}(CO\ f_{CM2}(R, K_1), R, K_0)|$$

$$\mathrm{BP} = \mathrm{CO}\ f_{CM2}(\hat{R}, K_1)$$

Equation 66

Or in a more compact manner:

$$\widehat{BP} = \text{argmin}_{BP} \left| PWV - \widehat{PWV}(BP, CO, K_0, K_1) \right|$$

Equation 67

where :

- K_0, K_1 are two constant values, calibrated once during the initialization phase.
- and $\widehat{PWV}(BP, CO, K_0, K_1)$ is the predicted *PWV* value given the two calibration constants, the measured *CO* and the hypothesized *BP.*

To date the accuracy of the proposed new technique has been validated on limited pilot experiments [1]. Further research on the implementation and limitation issues of the approach is required before promoting it further. For the current thesis, the focus of the research works is now moved into the second generation of PWV-based BP-estimation techniques, which is expected to overcome the need of vasomotion compensation by measuring PWV directly in elastic arteries.

References

[1] J. Sola*, et al.*, "Continuous monitoring of coordinated cardiovascular responses," *Conf Proc IEEE Eng Med Biol Soc,* vol. 2008, pp. 1423-6, 2008.

[2] J. Solà and H.-A. Loeliger, "Method and apparatus for a continuous non-invasive and non-occlusive monitoring of blood pressure," 2009.

[3] W. W. Nichols and M. F. O'Rourke, *McDonald's Blood Flow in Arteries*. Oxford: Oxford University Press, 2005.

[4] D. H. Bergel, "The dynamic elastic properties of the arterial wall," *J Physiol,* vol. 156, pp. 458-69, May 1961.

[5] G. Grassi*, et al.*, "Sympathetic modulation of radial artery compliance in congestive heart failure," *Hypertension,* vol. 26, pp. 348-54, Aug 1995.

[6] C. D. Steinback*, et al.*, "Carotid distensibility, baroreflex sensitivity, and orthostatic stress," *J Appl Physiol,* vol. 99, pp. 64-70, Jul 2005.

[7] R. A. Payne*, et al.*, "Pulse transit time measured from the ECG: an unreliable marker of beat-to-beat blood pressure," *J Appl Physiol,* vol. 100, pp. 136-41, Jan 2006.

[8] J. Hisdal*, et al.*, "Regulation of arterial blood pressure in humans during isometric muscle contraction and lower body negative pressure," *Eur J Appl Physiol,* vol. 91, pp. 336-41, Mar 2004.

[9] J. R. Levick, *An introduction to Cardiovascular Physiology*, Fourth ed. New York: Arnold Publishers, 2003.

Annex 2 – A frequency tour to ensemble averaging

Section 2.7.4 describes the use of ensemble averaging technique to denoise $\mathrm{ICG}(t)$ time series under the assumption that ICG signals could be modeled by a basic ICG pattern $p(t)$ repeated in time with a periodicity determined by heart rate, and to whom a zero-mean noise had been added (see Equation 40). Assuming that an *a-priori* estimate of heart beat occurrence times T_n was available, the ensemble-average estimate of $p(t)$ was defined by Equation 41.

In this annex we further justify the interest of applying ensemble averaging techniques from a frequency domain perspective (see Figure 8.1). In particular, we aim at demonstrating that the ensemble averaged time series $\hat{p}(t)$ corresponds to a very-narrow comb pass-band filter version of $p(t)$, with central filter frequencies determined by the heart rate frequency and its harmonics.

We start by redefining $\hat{p}(t)$ as the convolution of $\mathrm{ICG}(t)$ with a train of Dirac delta functions. It is then easy to demonstrate that such re-definition is indeed an especial case of $\hat{p}(t)$ as defined in Equation 41, where $w(t)$ has now constant amplitude values:

$$\begin{aligned}\hat{p}(\mathrm{t}) &= \mathrm{ICG}(\mathrm{t}) * \frac{1}{N}\sum_n \delta(t - T_n) = \frac{1}{N}\int \mathrm{ICG}(\tau)\sum_n \delta(t - \tau - T_n)\, d\tau \\ &= \frac{1}{N}\sum_n \int \mathrm{ICG}(\tau)\delta(t - \tau - T_n) d\tau = \frac{1}{N}\sum_n \mathrm{ICG}(t - T_n)\end{aligned}$$

Equation 68

Therefore, from the proposed new perspective, ensemble averaging corresponds to the convolution of the raw ICG signal with a train of Dirac delta functions whose periodicity is determined by T_n. In order to illustrate the behavior of such operator, assume now that no variability is present in heart rate, *i.e.* $T_n = T, \forall n,$ then Equation 68 becomes in the Fourier domain:

$$\begin{aligned}\mathrm{F}\{\hat{p}(\mathrm{t})\} &= \mathrm{F}\left\{\mathrm{ICG}(\mathrm{t}) * \frac{1}{N}\sum_n \delta(t - T)\right\} = \mathrm{F}\{\mathrm{ICG}(\mathrm{t})\}\,\mathrm{F}\left\{\frac{1}{N}\sum_n \delta(t - T)\right\} \\ &= \frac{1}{NT}\mathrm{ICG}(\mathrm{f})\sum_k \delta\left(f - \frac{k}{T}\right)\end{aligned}$$

Equation 69

In other words, in the frequency domain the ensemble-averaged estimate of $p(t)$ corresponds to the Fourier transform of ICG, *i.e.* $\mathrm{ICG}(\mathrm{f})$, sampled at the frequencies $f = \frac{k}{T}, k = 1 \ldots K$. Hence, $\hat{p}(\mathrm{t})$ is a very-narrow band-pass filtered version of $\mathrm{ICG}(\mathrm{t})$, and in particular, is a comb-filtered version of $\mathrm{ICG}(\mathrm{t})$ with filter band pass frequencies corresponding to the heart rate (and its harmonics) frequencies.

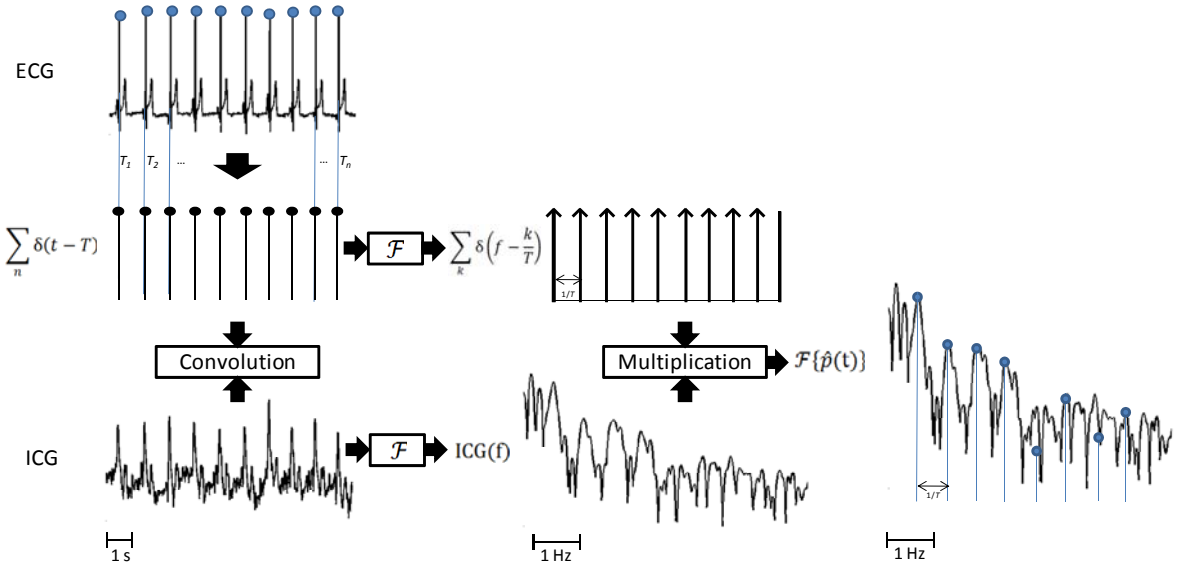

Figure 8.1: Frequency domain interpretation of the ensemble averaging of ICG time series: the Fourier transform of $\hat{p}(t)$ depicts the multiplication of the Fourier transform of ICG by a very-narrow comb filter with central frequencies centered at the harmonics of heart rate.

For the sake of clarity the current development was performed assuming no variability in heart rate frequency. However, in reality heart rate variability is intrinsic to any living cardiovascular system (see Section 2.1.2). Therefore, a major benefit of using ensemble averaging techniques is that the comb filtering described in Equation 69 takes into account such variability, by "sampling" the raw $\mathrm{ICG}(t)$ at the correct delayed T_n time values. Note that conventional comb filter designs are not capable of coping with such variability.

Annex 3 – Orders of magnitude for thoracic tissue electrical impedance: experimental evidence

Section 2.7.5 describes the use of Electrical Impedance Tomography (EIT) for the generation of sequences of images depicting thoracic impedance changes along the cardiac and respiratory cycle: any monitoring technique based on the analysis of body bio-impedances relies on the fact that different tissues will present different electrical impedance characteristics. Surprisingly, no consensus on the orders of magnitude of tissue impedance values for thoracic biological tissues has been reached to date. Current data lacks of homogeneity in the measurement setups: published studies are related to different electrode configurations, frequency ranges, tissue temperatures, and are performed both *in vivo* and *in vitro*, and on human and animal tissues. The goal of this annex is to provide experimental data on a homogenized set of measurements of the orders of magnitude of tissue resistivities present within the thoracic cavity.

Accordingly, we performed a systematic measurement campaign: using a high precision LCR meter (Instek LCR-821) we assessed *ex vivo* the resistivity of several pig tissues at different electrical current frequencies. Seven hours after animal death each biological tissue was placed between two copper-coated electrodes, and its complex resistance (Z) was measured. After correcting for tissue-electrode contact surface (A) and sample length (l), a resistivity value (ρ) was calculated as:

$$\rho = Z\frac{A}{l}$$

Equation 70

Table 9.1 depicts resistivity values for the measured thoracic organs, tissues and structures. A comparison to tissue resistivities extracted from a meta-analysis of published data [1] is provided as well. It is in particular interesting to note the large disagreement on resistivity values for lungs and bones between our measurements and published values: in our opinion it is difficult to interpret how a collapsed lung could present similar resistivity values as chest muscles do (200 Ω.cm**)**. New measured resistivities appear to be physiologically more consistent: note that collapsed lung resistivity (2742 Ω.cm) is about four times higher than chest muscle resistivity (537 Ω.cm). Figure 9.1 illustrates an example of the calculated impedance values, distributed in a typical human thoracic cavity shape.

Table 9.1: Typical values of resistivity for biological tissues present within the thoracic cavity of a pig, measured at 50 kHz and 100 kHz. Comparison to values from a meta-analysis study is provided as well.

Biological tissue	Measured resistivity		From [1]
Resistivities in [Ω.cm]	**F=50 kHz**	**F=100 kHz**	**F=100 kHz**
Collapsed lung	3179	2742	200
Inflated lung	6210	5732	-
Bone	950	921	5.10^7
Chest wall muscle	672	537	200
Full chest wall	1373	1258	-
Rib, with muscular interstice	855	689	-
Heart (filled with blood)	532	448	-
Heart wall	551	454	-
Skin (without fat)	3194	3075	$500- 10^5$
Skin (with 4mm fat)	2407	2369	-
Fat			7000
Blood	-	-	< 200

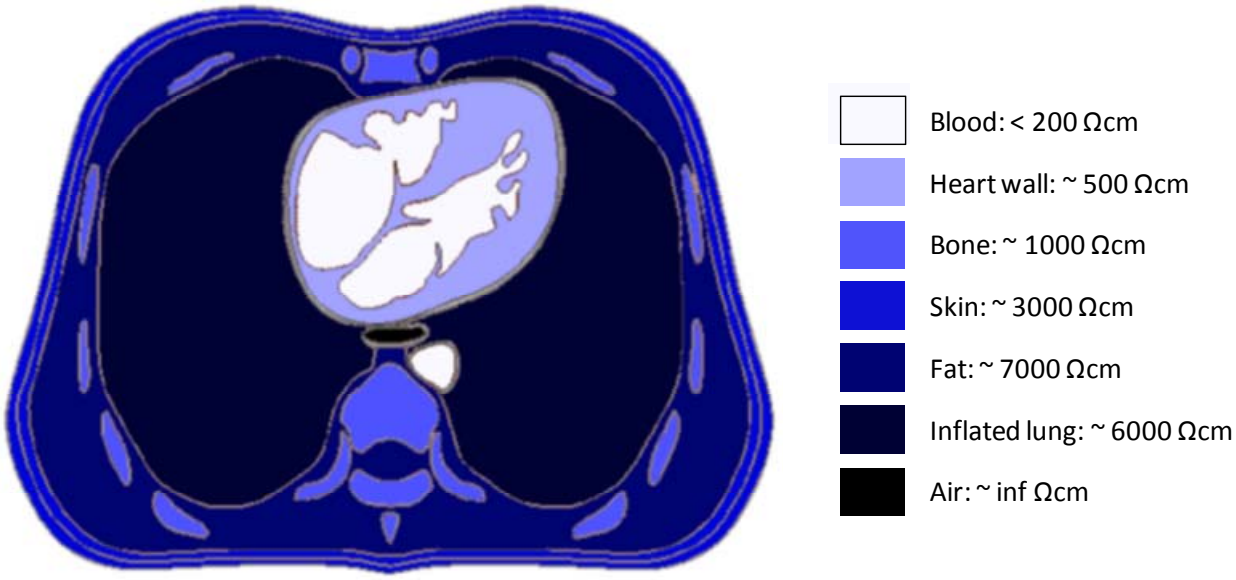

Figure 9.1: Distribution of isotropic impedance volumes within a human thoracic cavity. Impedance values depict order of magnitudes only, according to CSEM measured values and [1]. Thoracic image is adapted from [2].

References

[1] T. J. Faes*, et al.*, "The electric resistivity of human tissues (100 Hz-10 MHz): a meta-analysis of review studies," *Physiol Meas,* vol. 20, pp. R1-10, Nov 1999.

[2] J. Malmivuo and R. Plonsey, *Bioelectromagnetism - Principles and Applications of Bioelectric and Biomagnetic Fields*. New York: Oxford University Press, 1995.

Annex 4 – Continuous non-occlusive monitor of Blood Pressure in humans using a chest sensor: first experimental evidence

Adapted from:

A Chest sensor for Continuous Measurement of Blood Pressure and Arterial Stiffness

Josep Solà[1] and Olivier Chételat[1]

[1]CSEM – Centre Suisse d'Electronique et de Microtechnique, Neuchâtel, Switzerland

Published in:

CSEM Scientific reports of 2010

After demonstrating that the chest sensor was capable of providing central Pulse Transit Time (PTT) values in basal conditions in a cohort of 31 normo- and hypertensive subjects (see Chapter 5), its ability to track continuous changes of BP is here investigated.

Figure 10.1: Example of cardiovascular measurement setup, in collaboration with the Swiss Cardiovascular Center in Bern.

A 60 minutes experiment was performed on an adult male, in collaboration with the Swiss Cardiovascular Center in Bern. Continuous BP values were simultaneously acquired by the novel chest sensor, and an occlusive measurement device placed on the finger (Portapres, FMS, The Netherlands). Figure 10.1 illustrates a typical cardiovascular measurement setup.

The goal of this experiment was to induce fast measurable changes of BP by performing several cardiovascular maneuvers, and assess the accuracy of the chest sensor to track these changes. In particular, four maneuvers were used:

- Mental stress: a series of arithmetic operations was proposed to the subject, requiring fast and accurate verbal answering. BP was expected to increase due to increased activity of the sympathetic nervous system.
- Hand grip: the subject was required to perform a sustained handgrip on one hand, at 20% of his maximal force. BP was expected to increase due to increased activity of the sympathetic nervous system as well.
- Cold stress: subject's left hand was immersed in cold water. BP was expected to increase due to increased peripheral resistance (peripheral vasoconstriction).
- NO: nitroglycerine was administrated to the subject by inhalation. This maneuver was expected to induce a vasodilatation of peripheral arteries, while keeping stabilized BP conditions (control maneuver).

Figure 10.2 illustrates the results of the 60-minute experiment. Across the different cardiovascular maneuvers, the chest BP sensor was capable of tracking BP variations as provided by the reference measurement system. BP calibration was performed by applying a linear fitting of PTT data points to simultaneously-measured BP values. The observed different time and amplitude dynamics of the estimated values are due to differences in the measurement principles of the Portapres and CSEM systems. Note that during NO administration chest BP estimations remained stable, pointing to the fact that the chest sensor might be robust against peripheral vasomotion phenomena (as hypothesized by Chapter 5).

For this experiment, the chest sensor reached an accuracy level equivalent to the BHS category Grade B (see Section 2.3).

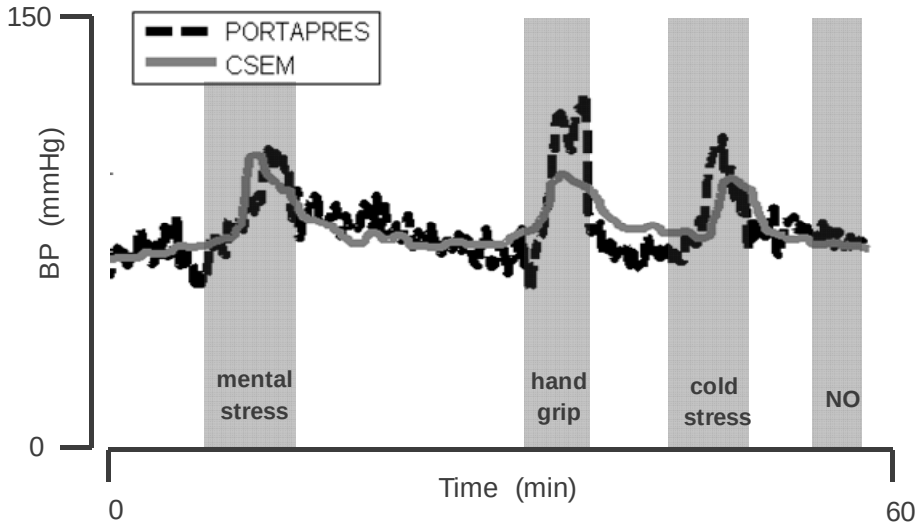

Figure 10.2: Example of 60 minutes of BP monitoring involving several cardiovascular maneuvers. Portapres is a reference occlusive BP monitor placed on the finger, and CSEM depicts BP estimations performed by the non-occlusive chest sensor.